PHASE PROPERTIES OF SEMICONDUCTOR AND TRANSITION METAL MATERIALS FROM EXPERIMENTAL AND COMPUTATIONAL PRINCIPLES

By

DAVID LEE BROWN

A DISSERTATION PRESENTED TO THE GRADUATE SCHOOL
OF THE UNIVERSITY OF FLORIDA IN PARTIAL FULFILLMENT
OF THE REQUIREMENTS FOR THE DEGREE OF
DOCTOR OF PHILOSOPHY

UNIVERSITY OF FLORIDA

2020

Et non fuit pluvia in tenebris, sed longe venerunt

ACKNOWLEDGMENTS

Firstly, I would like to thank the McKnight Doctoral Fellowship, for the financial support in completing my dissertation. I would like to thank my first mentor Dr. James Zavislan for introducing me to photonics and instrument construction. Dr. Henry Zmuda for support during my time in ECE, which allowed me to graduate. Dr. Johan Eicholz and Dr. Micheal Hartman, who, during their Ph.D. candidacy, supported my study during my time at LIGO. In particular, Dr. Johan Eicholz's comments on my proposal that helped me win the NRC RAP postdoc fellowship. I would like to thank Michelle Fullertron, Josh Paul, Stephen Xie, and the rest of the Phillpot and Hennig groups for the scientific discussions that created my first paper. Lastly, I appreciate my Chair and Co-Chair Dr. Simon Phillpot and Dr. Kevin Jones for the scientific support in pursuit of the PhD.

TABLE OF CONTENTS

LIST OF TABLES

LIST OF FIGURES

Abstract of Dissertation Presented to the Graduate School
of the University of Florida in Partial Fulfillment of the
Requirements for the Degree of Doctor of Philosophy

PHASE PROPERTIES OF SEMICONDUCTOR AND TRANSITION METAL MATERIALS FROM EXPERIMENTAL AND COMPUTATIONAL PRINCIPLES

By

David Lee Brown

May 2020

Chair: Kevin Jones
Cochair: Simon Phillpot
Major: Material Science and Engineering

For the scaling of Moore's Law, new thin film materials have to accommodate lower contact resistance, and higher strain for improved carrier mobility. These material properties have become the limiting factor for device scaling. In recent years, highly doped Si:P and Si:As films have been studied for providing high dopant activation and source-drain stressors for nMOS devices. The epitaxial tensile strain is believed to be caused by vacancy stabilized Si_3P_4 and Si_3As_4 phases. For reduction of contact resistance, a silicide is embedded between the source-drain and metal contact. Titanium disilicide ($TiSi_2$) is a ubiquitous low contact resistance material used for complementary metal oxide devices (CMOS), for its thermal budget, oxidation resistance, and contact defect nature with silicon devices, but the introduction of Ge for compressive strain in pMOS channels causes a ternary reaction with titanium disilicide. It warrants further study of $Ti(Si_{1-x}Ge_x)_2$ for industry applications. In this work, A combination of experiment and computation is used for developing knowledge of these films. Epitaxial strain stability of vacancy stabilized Si_3P_4, Si_3As_4, Ge_3P_4, and Ge_3As_4 phases is studied from first-principles using electronic-structure calculations at the level of density functional theory. A simulation of electron energy loss spectroscopy (EELS), based on the structural relaxation of the vacancy stabilized Si_3P_4 phase, is compared to the experimental profile of highly doped Si:P films. Computational methods are also applied to the study of $Ti(Si_{1-x}Ge_x)_2$ allotropes (C40, C49, and C54 structures). The defect

formation and lattice stabilities are studied with pure phases of $TiSi_2$ and $TiGe_2$ structures, and $TiSi_2$-$TiGe_2$ pseudobinary thermodynamics is simulated using cluster and Monte Carlo methods. The $Ti(Si_{1-x}Ge_x)_2$ computational study is compared with experimental phase mixing post nanosecond laser anneals. As mentioned before, a fundamental understanding of these films is necessary for the continued scaling of Moore's Law. These studies develop essential knowledge for integrating these films into semiconductor process flow.

CHAPTER 1
INTRODUCTION

1.1 Motivation

Society is influenced by the transition of technologies from fundamental discovery to commercialized product. A corner-stone for a successful transition is determined by the materials available for the technology. The transistor is one such device with its success deriving from its materials. The transistor controls the flow of a large signal with a much smaller signal, and it's the foundation of all computer logic due to controllable on-off states. Transistor devices went from the size of a room during the Apollo program to the size of a wristwatch. The early form of this device was the vacuum tube. A vacuum tube transistor requires high power such that heat dissipation reduced the lifespan of the device, and technicians would frequently replace tubes due to burn out. Also, the vacuum tube transistors' size made computers impractical for the consumer. A new materials perspective would be necessary to replace the vacuum tube. In the 1930's, the quantum theory of solids was well understood, so industrial scientists began searching for a solid-state alternative. Until the late 1940's, the only materials available for solid-state transistors were copper oxide, lead sulfide, and cadmium sulfide. The inconsistent stoichiometric ratios and impurities of these materials made performance of semiconductor devices unpredictable, so the field could be refereed to an art not a science. Eventually, the need for RADAR motivated process improvements of silicon and germanium by Dupont. Silicon and germanium crystals generated rectified signals at gigahertz frequencies. Bell Labs would follow with applying these crystals to transistors. Russel Ohl would develop the understanding of p-type and n-type doping based on the periodic table and p-n junctions in 1940. Afterward, William Shockley derived the theory for solid state transistors, but he could not develop working device until John Bardeen and Walter Brattain handled the engineering and development.[1] The solid-state transistor replaced vacuum tubes and the next challenge became device density.

Moore's law has been the model for transistor density since the 1970's. This law is the observation that the number of transistors in an integrated circuit approximately doubles every two years. The increased number of transistors allows an electronic device to perform more functions; the electronic devices are capable of more memory with faster responsiveness. However, device scaling, size reduction of the transistor, has become more difficult, and new markets have emerged to pressure the industry for more performance at lower power. The introduction of big data and cloud computing require always-on devices with instant data retrieval. The mobile market has placed pressure to have increased smart phone function with decreased power consumption. Combining cloud computing and mobile devices with sensors is called the Internet-of-Things (IoT), and IoT is expected to dominate technology markets in the coming years. IoT will need to provide instant data and always-on performance. These expectations need to be achieved with limited resources between memory, power, and speed.[2]

In the past, device scaling introduced more memory and speed at lower powers implicitly with complementary metal–oxide–semiconductor (CMOS) transistors. CMOS is conceptualized as an on or off switch. This switching has an energy cost, shown in eq. 1-1, is the product of gate capacitance and power supply voltage for CMOS.[3]

$$P = \frac{C_L V_{DD}^2}{2} \tag{1-1}$$

The scaling down of planar CMOS devices reduces the gate length and capacitance. The reduced gate length increases the responsiveness of the device, and it allowed for more transistors on a chip. Down to 22nm planar devices, device scaling reduced the capacitance for less power consumption per switch event.[3]

To keep up with demand, 2016 was the last year for planar device architectures (excluding power electronics) because the architecture cannot be further scaled to meet these market demands.[2] The industry is moving to new device architectures such as finFETs, for its improved gate control. All-around gate devices will replace finFETS, which further improves electrostatics gate control and enables further scaling. However, device scaling has introduced

new problems, and these problems reduce the performance return with reducing device size. These problems include new parasitic resistances such as contact resistance. A four percent per year performance drop is expected beyond 2018.[2] Therefore, device scaling alone will not be enough to keep up with demand. A materials science perspective of these challenges is necessary for meeting future device expectations.[2]

1.2 Transistor Technology

The CMOS device is composed of an n-type (nMOS) and a p-type (pMOS) transistor. As the name implies, the nMOS and pMOS work in a complementary to produce stable output voltages which improves the on-off characteristics.[4] Together, these devices form a logic inverter which flips the logic input state. A voltage-high input signals a voltage-low output (off-state) while a voltage-low input triggers a voltage-high output (off-state). The inverter can be modeled as an infinite off-resistance or finite on-resistance (see fig. 1). The inverter is the fundamental component of all microprocessors, memory, field programmable gate array (FPGA), and arithmetic logic unit (ALU).

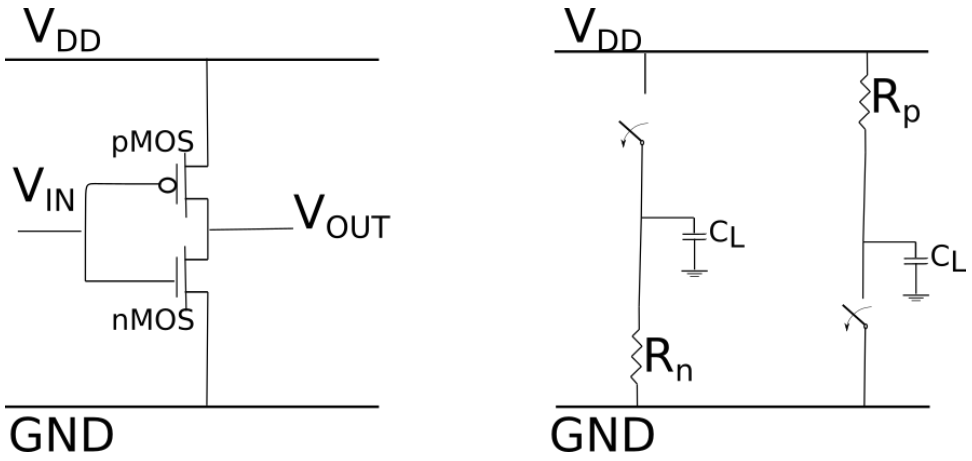

Figure 1-1. CMOS inverter switch schematic model (left) with pMOS and nMOS. The RC model (right) conceptualizes the switching behavior. When the switch is active, the nMOS capacitor is set to voltage VDD, and the pMOS capacitor is shorted to ground.

This complementary relationship of nMOS and pMOS originates from the ability of nMOS to efficiently pull to GND and pMOS to efficiently pull to V_{DD}. Independently, the cMOS and

pMOS transistors can produce all the required logic. However, the schematic layout of fig. 1 ensures the output signal does not oscillate after a switch. Thus, this complementary behavior motivates the use of n-type and p-type semiconductor materials simultaneously.

From the resistance-capacitance (RC) model, the time constant dictates the responsiveness of the CMOS.

$$\tau_{NMOS} = R_N C_L \tag{1-2}$$

$$\tau_{PMOS} = R_P C_L \tag{1-3}$$

The capacitance, C_L, is related to the power per switch and the time constant, so it dictates the switching speed and power. The CMOS capacitance is strongly related to device dimensions, and the capacitance decreases with size scaling. Therefore, Reducing the capacitance has been the main focus of the industry through size scaling. However, aggressive size scaling is reaching a limit on the expected improvement for two main reasons. Size scaling does not reduce the resistance in the RC model, and new parasitic resistances have been introduced due to size scaling (e.g., contact resistance ($\Omega - cm^2$)).[4]

CMOS is operated in the saturation region so that the current across the transistor is constant. Ideally, the current across the transistors needs to be sensitive to the gate voltage. More sensitivity insures optimal on-off characteristics of the device. A figure of merit relates the currents sensitivity to gate voltage change called transconductance g_m:

$$g_m = -\sqrt{2\mu_n C_L \frac{W}{L} I_D} \tag{1-4}$$

Where μ_n is the carrier mobility, C_L is the capacitance of the oxide layer; W/L is related to device dimensions; I_D is the current across the device. The variable of interest is the carrier mobility. A large transconductance is ideal for device performance, which improves with higher mobility.

1.2.1 The Future: 3-D Architectures

To increase the number of transistors on a chip, device scaling is still a primary focus. Table 1-1 shows the consistent reduction of gate length to create more logic bits and faster

devices. The 3-D architecture devices provide advantages over planar architectures. The 3-D architectures enables more potential for scaling with improved electrostatic control of the channel. Device scaling increases the risk of quantum tunneling of the channel. The quantum tunneling of an electron causes a device to always be in the on-state (or 1 for binary code). The 3-D architecture increases the potential against quantum tunneling.

Table 1-1. The decreasing gate length since 2016 to the projected gate length architectures[2]

Year	2016	2018	2020	2022	2024	2026
Gate Length	15.3	12.8	10.6	8.9	7.4	5.9

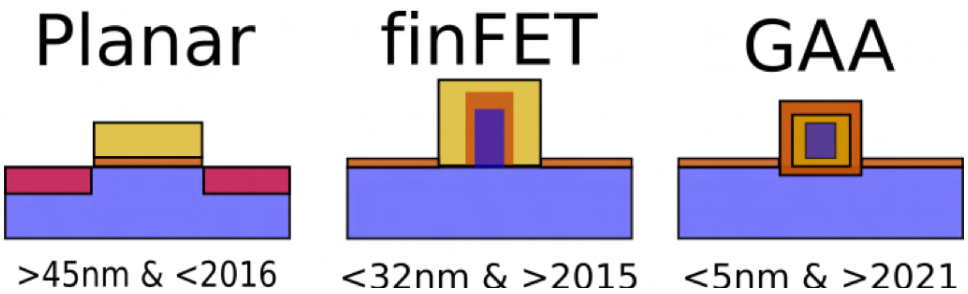

Figure 1-2. Architecture evolution of the transistor illustrating the past 2-d planar device, the modern 3-d fin-field effect-transistor (finFET), and the future gate all around device architecture (GGA).

The electrostatic control of a transistor can be improved using the finFET, which is the first generation of 3-D architecture devices. The improved electrostatic control also exhibits an additional benefit of reducing the leakage current (picoamp current still flows in the off-state). Figure 1-2 is a simplified illustration for contrasting the 2-D and 3-D devices. The finFET is currently the most ubiquitous device architecture; the planar architecture is being phased out in computer transistor devices. Beyond the finFET, horizontal gate-all-around devices will dominate for their continued improvement on electrostatic control; beyond 2021 this architecture will be vertical to continue increasing the density of transistors.

However, even with 3-D architectures, the expected performance increase of doubling the transistor density will drop 4% per year. This issue is due to the higher order physics such as contact resistance. Therefore, methods that will reduce parasitic resistance and increase carrier

mobility are necessary for the future of semiconductor devices. A materials science perspective is needed to introduce materials which achieves these goals.

1.2.2 Strain Engineering

The carrier mobility of a CMOS device loosely dictates device performance. Epitaxial strain has a direct benefit to carrier mobility due to alteration of a carrier's effective mass. The concept of effective mass must be presented to understand how strain on a Si channel improves device performance. The effective mass is related the interaction of the carrier's mass with environmental forces. Since electrons are wave-like, movement across a crystal can be described as a group velocity. Utilizing the Lorentz force law and Newton's law with the first derivative of the electron group velocity. The effective mass of the electron can be related to the curvature of the energy band structure E vs k in eq. 1-5. The complete derivation can be viewed in textbooks of semiconductor physics.[5]

$$\frac{1}{(m_n^*)_{\text{ij}}} = \hbar^{-2}\frac{\partial E(k)}{\partial k_i \partial k_j} \tag{1-5}$$

Where i and j represent the indices of the crystal orientation, m_n^* is the effective mass of the electron. The effective mass of an electron is proportional to the curvature of the energy band structure. About the conduction band minimum, a large curvature indicates a small effective mass while a small curvature indicates large effective mass. Next, the connection between the effective mass and carrier mobility is developed from a qualitative model.

From Drude's electron transport model in eq. 1-6, the carrier mobility is related to the drift velocity and average collision in a uniform electric field. The carrier is scattered at a mean time interval, and the carrier must accelerate in the field again. Drude's model relates mobility and effective mass by:

$$\mu = \frac{q\tau}{m_n^*} \tag{1-6}$$

Where τ is the mean interval time, q is the electron charge. From the model, it's clear that a small effective mass is desired to achieve higher mobility. Therefore, the band warping can reduce the effective mass and increase carrier mobility.

The introduction of strain engineering yields current enhancements for pMOS and nMOS of >50% and 32%, respectively.[6] A local epitaxial film is grown in the source/drain region to provide tensile or compressive strain on the channel. The channel strain affects holes and electrons differently; holes require compressive strain for enhancement, while electrons require tensile strain for enhancement. For pMOS enhancement, $Si_{1-x}Ge_x$ is epitaxially grown underneath the channel, inducing compressive strain. For nMOS enhancement, $Si_{1-x}C_x$ is epitaxially grown underneath the channel inducing tensile stress (see fig. 3).[7, 8]

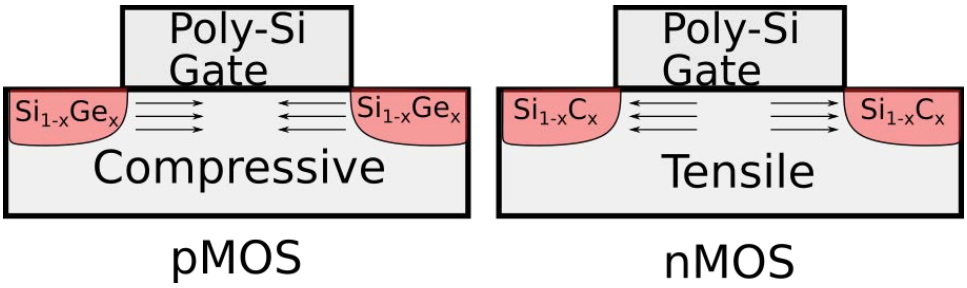

Figure 1-3. A planar device illustrates the approach to applying strain engineering on CMOS device channels. The pMOS channel is placed under compressive strain for hole mobility enhancement, and the nMOS channel is placed under tensile strain for electron mobility enhancement.

The compressive strain on a channel is found to enhance hole mobility at low and high strains. In contrast, electron enhancement for nMOS transistors requires high stress at least 1 GPa.[8] For nMOS, introducing a tensile strain greater then 1 GPa has been a challenge for the semiconductor industry. In the past, a ubiquitous method used selective epitaxial growth (SEG) to introduce cubic $Si_{1-x}C_x$.[9] The lattice constant of cubic $Si_{1-x}C_x$ is less than Si. Thus, this epitaxial layer introduces tensile strain on Si. However, intrinsic Si:C does not provide carriers for conduction, and dopants are epitaxially grown with $Si_{1-x}C_x$ producing Si:CP.[10] This material has been the most promising material for tensile strain. However, the introduction of 22nm devices has made contact resistance larger than the S/D channel resistance.[2] The contact resistance is a limiting factor for device performance. This resistance is lowered with higher carrier concentration, but the Si:CP material has problems with providing more carriers. The carbon and phosphorous compete for substitution sites, so the dopant solubility of silicon

is reduced. Higher concentration of phosphorous reduces the thermal budget creating carbon precipitates. These precipitates increase the sheet resistance beyond the acceptable limit.[11] To continue reducing contact resistance, New highly doped (HD) materials such as HD Si:P and HD Si:As are the focus of research for replacing Si:CP.

1.2.3 Contact Resistance

A conceptualization of contact resistance requires a brief overview of metal-semiconductor contacts. The Schottkey-Mott model is the widely used theory for metal-semiconductor interface. When the metal and semiconductor contact, a depletion region forms in the semiconductor and forms a barrier through which the electrons must tunnel (see fig. 1-4). The theory states that the electron barrier height of the interface is the difference between the metal work function and the electron affinity of the semiconductor. The Coulombic charge of the electron is denoted as q. Equation 1-7 shows the barrier height that forms; this is illustrated of the equation is shown in fig 1-4.

$$\phi_B = \phi_m - q\chi_s \tag{1-7}$$

The Schottkey-Mott model has two different contact resistance types the Ohmic ($\phi < q\chi_s$)and Shottky contact ($\phi > q\chi_s$). The Ohmic contact case is of interest for semiconductor devices due to carrier enhancement. In this case, the electrons flow from the metal to the semiconductor, and the conductivity of the semiconductor improves near the interface which only acts as a resistor. This Ohmic contact occurs when the semiconductor is highly doped, which greatly reduces the width of the depletion region. With sufficient doping, quantum tunneling becomes the dominant mechanism for carrier transport across the boundary. The model inaccurately predicts the barrier height when interfacing with different metals. This inaccuracy is a phenomenon called Fermi level pinning, in which the barrier is locked to the Fermi level.

Where the depletion region becomes thin, the contact resistance, ρ_c, can be derived from the electron diffusion model. Contact resistance is expressed in units of $\Omega - cm$ in eq. 1-8.

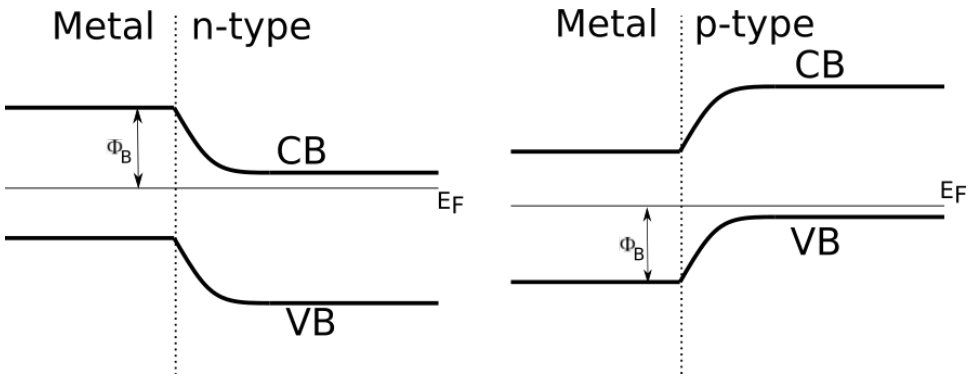

Figure 1-4. Band bending illustrated for metal-semiconductor interface for both p-type and n-type. The valence bands and conductance band curve creating a depletion region that electrons must tunnel.

$$\rho_c = \rho_0 \exp\left(\frac{2\phi_B}{\hbar}\sqrt{\frac{\epsilon_s m^*}{N_D}}\right) \tag{1-8}$$

From this equation, it is apparent that the contact resistance is dependent on the barrier hight, dopant density, and effective mass. Theses properties can be changed to reduce contact resistance from a materials science perspective. The effective mass m* can be altered by straining materials; the barrier height can be altered by placing a silicide between the metal-semiconductor interface since it has a more favorable barrier height. Materials such as HD Si:P, HD Si:As, and Ti($Si_{1-x}Ge_x$)$_2$ are among the candidates to reduce contact resistance.

1.3 Thin-film Growth of Semiconductor Devices

Whether Chemical Vapor Deposition (CVD) or Physical Vapor Deposition (PVD) all growth processes share the same goal, taking an pure initial state to a final state of a desired film with useful properties. The challenge of growth processes is understanding the phase reactions at the surface for each component.

Thin films can be grown by physically (PVD) and chemically (CVD). PVD methods rely on physisorption that the precursor gas starts as a solid in a container and is heated into the gas phase. CVD methods imply that the reactant was stored as a gas such as silane, phosphine, or arsine. Both methods share adsorption, desorption, and surface diffusion as the driving force for forming films.

The gas molecules in the chamber have some kinetic energy that can be modeled by the ideal gas law. The gases in the chamber do not coalesce due to the kinetic energy being greater than the interactions. Therefore, in order for these molecules to be adsorbed, the forces from surface of the substrate must overcome the kinetic energy. Sometimes another inert gas will be co-flowed to lower the kinetic speeds of the precursor gas providing control to the adsorption. Once the molecules adsorb onto the surface a lattice gas forms. Lattice gases refer to adatoms randomly diffusing across the surface of the substrate. These adatoms will eventually meet and collect to form a seed nucleus which can grow until a complete layer is reacted.

Most films are grown using gas phase precursors, but the solid reaction is worth discussion in this chapter due to the experiments on the Ti-$Si_{1-x}Ge_x$ solid reaction. Silicides are still routinely grown using solid-phase reaction with a metal-semiconductor interface. The reaction begins with the metal and semiconductor atoms diffusing across the interface. Typically, the starting nucleus is a metal rich phase at the boundary. The reaction continues until the metal rich phase forms a complete layer separating the metal and semiconductor pure phases.

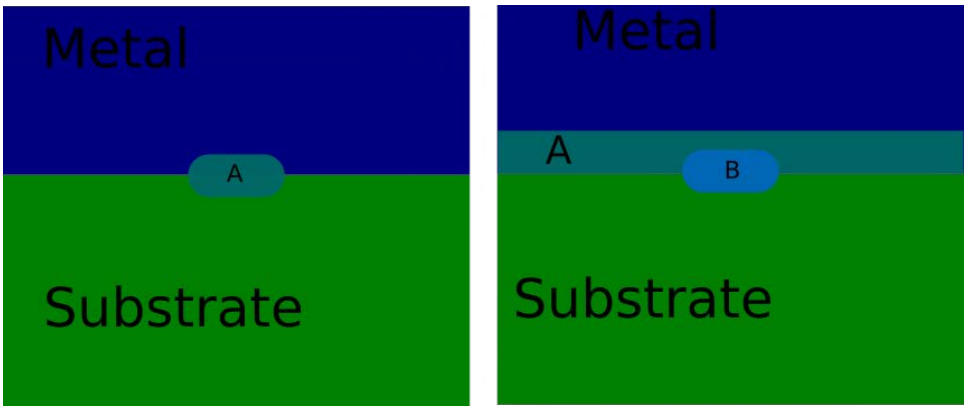

Figure 1-5. Simple illustration of a solid-phase reaction. The reaction starts with a metal rich nucleation region denoted A (left). When the reaction forms a layer, a new nucleated phase, denoted B, forms inside the metal rich layer (right).

The diffusion of the semiconductor and metal atoms becomes increasingly damped. When the diffusion barrier becomes too high, a stable phase will begin to nucleate. Eventually, the

more stable phase will fully form becoming the new barrier between the semiconductor and metal.

1.4 Cyclic Deposition Etch and Co-flow growth processes

Highly doped (HD) Si:P and Si:As films refer to dopant concentrations of As and P above the Si solid solubility limit that is $>1.11\text{x}10^{20}$ cm^{-3}.[12] This limit for Si systems occurs in equilibrium growth conditions, so Si films with dopant concentration above this limit are due to non-equilibrium growth methods. For this work, these methods are known as the cyclic-deposition etch (CDE) and co-flow processes, which are performed using low pressure chemical vapor deposition (LPCVD). The difference between CDE and co-flow is that CDE is performed in cyclic steps, while co-flow is when the CDE steps are performed simultaneously. The CDE process requires the CVD chamber to be purged, so the process is slower than co-flow. However, co-flow has a trade-off such that it produces higher resistivity films.[11] The discussion of this section will focus on CDE.

The sequence of CDE is as follows: a few nm of the desired material is gown using precursor gasses of high-order silane (e.g., disilane or trisilane). The high-order silane gases are known to achieve high growth rates at lower temperatures.[13] Once a few nm is deposited, the chamber is purged of the precursor gas. The wafer will have regions of dielectric photoresist, which only allow growth of amorphous or poly-crystalline films. In the next step, a selective etchant, is introduced to etch the non-crystalline regions leaving active regions. Finally, the chamber is purged again, and the growth step begins again. CDE is performed at reduced pressures (20 Torr) and temperatures between 500°C to 700°C. The low temperature is key to grow highly doped films in which the surface diffusion of the dopant is less than the film growth rate. If this condition is met, the film growth quenches the dopant, enabling high doping. Also, a lower temperature increases the etch rate of amorphous and poly-crystalline layers.[14] The co-flow and CDE processes do require different precursor gases for film growth. The co-flow process utilizes dichlorosilane (DCS) while the CDE process uses silicore (a

proprietary high-order silane Si_3H_8). Both methods may use HCl or Cl_2 with a GeH_4 catalyzer for the etchant step.

Additional differences in growth process are apparent for HD Si:P and HD Si:As. The growth of HD Si:P uses the precursor gas of phosphine (PH_3) during the growth step. However, the growth of HD Si:As films uses different precursor gases. Unlike HD Si:P growth, HD Si:As is successful with low order silane (SiH_4) with arsine (AsH_3) gas. Borot et al. reports total As concentrations up to 1.9×10^{21} cm^{-3} with These precursor gases.[15]

1.5 Highly Doped Si:P and Si:As Films

A film's strain on a Si channel induces carrier enhancement: Si:CP films achieve this carrier enhancement for nMOS. However, the Si:CP films fail in preventing parasitic contact resistance for future device scaling. To reduce contact resistance, the activated doping is increased, which requires greater concentrations of dopants during growth. The phosphorus and carbon need to be on a Si substitution site. If these atoms are substitutions, the carbon reduces the lattice constant while the P contributes to conductivity. However, C and P compete for substitution reducing silicon's solubility of the dopants. Thus, the likelihood of precipitation increases, which increases the sheet resistance beyond tolerance. This sheet resistance increase gives the HD Si:P and HD Si:As films a major advantage over Si:CP films. Not only do the films provide similar strain, HD Si:P and HD Si:As films are capable of dopant concentrations above the Si solubility limit without competition.

The contact resistance of HD Si:P is record breaking with values measured down to 1×10^{-9} $\Omega - cm$. This low contact resistance has been measured in HD Si:P/$TiSi_2$ junctions.[16] ultra-low contact resistance is achieved using $NiSi_2$ silicide with an improved thermal budget. However, $NiSi_2$ comes at the cost of a contact resistance at an order of magnitude higher than TiSi2.[17] Contact resistance studies of HD Si:As films have yet to be performed with silicide junctions.

The focus of the study for HD Si:P films is address the question as to why the strain is comparable to $Si_{1-x}C_x$. Currently, the reason for the strain is unresolved, with several

possible causes: the presence of a phase, defect cluster, or doping concentration.[11, 18, 19] The discussions originate from rocking curve high-resolution x-ray diffraction (RC-HRXRD) experiments. The instrument is locked to the (004) interplanar spacing, and the epitaxial strain is derived by a relationship to Bragg's law. This relationship is given by eq. 1-9.

$$\frac{c_{HDSi:P}^{strained} - c_{Si)}}{c_{Si}} = \frac{a_{Si}\Delta\theta}{2\lambda} \tag{1-9}$$

Where $\Delta\theta$ is the difference between the (004) peak to the epitaxial satellite peak, $c_{HDSi:P}^{strained}$ strained is the lattice constant of the epitaxial layer; c_{Si} is the lattice constant of the Si substrate; λ is the wavelength of the incident x-ray; a_{Si} is the lattice constant of Si. Once the epitaxial strain is measured, Vegard's law is applied between the silicon and epitaxial lattice. This equation assumes the lattice constant of two constituents is approximately equal to the rule of mixture. The predicted strain from Vegard's law agrees with the HRXRD experimental results, but this strain agreement is not enough evidence to prove the presence of pseudocubic phase.

HD Si:P films have been laser annealed between the temperatures of $900°C - 1300°C$. The tensile strain has been found to be stable up to $1200°C$; the reduction in strain is believed to be the dissolving of the pseudocubic, and the phosphorous begins to dissolve into the Si bulk. The phase has been observed releasing interstitials.[20] The high activation comes from a millisecond laser annealing. Laser annealing is different from rapid thermal annealing due to its rapid undercooling. The laser heats a small area with more directions for heat transfer. The rapid cooling allows for dopants to be quenched on Si sites before diffusing into a deactivation site or cluster.

It's a known value that 0.5% of phosphorous doping creates 0.0001nm lattice contraction,[21] and the calculated XRD peak is 500 arc second for 2.8x10^{21} cm^{-3}. The observed strain for HD Si:P is measured at 2000 arcsec at the same concentration.[22] Due to the disagreement in peak position, previous works have claimed that phosphorus doping alone does not account for

the strain. A complete discussion of the disagreement between P concentration and strain can be found in the dissertation of Weinrich.[23]

CHAPTER 2
OVERVIEW OF COMPUTATIONAL METHODS

The main computational technique used in this work is Density Functional Theory (DFT). The Debye temperature and lattice structure of phases are computed with DFT for electron energy loss (EELS) simulation; these are compared with experimental results in Chapter 5. In Chapter 6, the material properties of TiS_2 and $TiGe_2$ are analyzed with DFT. The Bader charge analysis package requires the charge density of the material from DFT. The epitaxial stability of Si-P, Si-As, Ge-P, and Ge-As systems is calculated by introducing strain on the lattice structures. Therefore, a brief overview of DFT and functionals is presented for this chapter. All the computational techniques depend on the calculations of DFT, but each technique will be discussed separately the following sections.

2.1 Density Functional Theory

Quantum theory has been one of the most widely successful theories in scientific history; its cornerstone is Schrodinger's equation. However, the Schrodinger equation is only solvable for a small number of one or two-body systems. Even something as simple as a three-body problem is generally not solvable. Moreover, even if a many-body problem could be solved, the equation would require an unrealistically large computational load. DFT is a reformulation of quantum mechanics in a form suitable for the computation of the electronic properties of condensed phases. This reformulation is built on the Hohenberg and Kohn (HK) theorems[24]. The first HK theorem states that the total energy of a system of electrons is given exactly as a function of the total electron density, ρ, and that the ground state of a system of electrons is the same as the ground state determined as a function of electron density alone. This theorem allows the physical properties to be a function of electron density in 3-D space. The second HK theorem states that there exists a total energy $E[\rho]$ that can be minimized to obtain a ground state total energy, $E[\rho_0]$. However, the HK theorems do not describe the functional form of the electron density itself or provide guidance as to how to obtain it.

Nevertheless, these theorems provide a basis for computational approaches to obtain approximations to the electron density. Specifically, the Kohn-Sham (KS) method provides an iterative approach for computers to efficiently analyze multi-electron systems quantum mechanically. The KS method defines the total energy of a system from the following sum:[24–27]

$$E[\rho] = E_{KE}[\rho] + E_c[\rho] + E_E X[\rho] + E_{XC}[\rho] \tag{2-1}$$

Where $E_{KE}[\rho]$ represents the electron kinetic energy, $E_C[\rho]$ represents the Coulombic electron energy; $E_{EX}[\rho]$ represents the external energy on the system; $E_{XC}[\rho]$ represents the energy from the electron-electron interactions, known as the exchange-correlation functional. Every term in the KS potential can be given analytically except for the exchange-correlation energy. It is, therefore, necessary to develop approximations for these non-classical interactions. The two most common approximations are the local density approximation (LDA)[28] and the generalized gradient approximation (GGA)[29]. LDA, $E[\rho]_{xc}^{LDA} = \int e_{xc}^{hom}(\rho(r))d^3r$, only considers the energy of a homogenous electron gas at a position r. The GGA, $E[\rho]_{xc}^{GGA} = \int e_{xc}^{hom}(\rho(r), \Delta\rho(r))d^3r$, includes the local gradient of the electron gas. While GGA is more sophisticated, it does not necessarily mean that GGA is more accurate than LDA; thus, both approximations may be used on a system for comparison. For example, LDA has a tendency to under-predict the lattice constant(s) of a crystal, while GGA has a tendency to over-predict them. While for some systems one or both approximations yield good estimates of the electronic bandgap, for other systems they give poor agreement with experiment. In extreme cases, they predict insulating materials to be metals.[30] This is generally a problem for systems with highly correlated with d and f electrons, and has motivated research to develop exchange-correlation functionals beyond LDA and GGA. Fortunately, we do not consider f-electron systems in this work. Here, therefore, we use a form of GGA called the Perdue-Burke-Ernzerhof generalized gradient approximation (PBE-GGA) functional, and a more

sophisticated meth, the Strongly Constrained and Appropriately Normed (SCAN) functional, discussed in the next section.

2.2 SCAN Functional a Meta-GGA

The shortcomings of the LDA and GGA functionals have inspired the development of "beyond GGA" methods.[31] This discussion will focus on one category of methods known as meta-GGAs, and in particular the SCAN semilocal density functional.

The exact form for $E_{XC}[\rho]$ is not known, but over the fifty-five years of DFT, the pieces of the exchange-correlation have been identified and are introduced as additional terms. Each additional term addresses a physical constraint on the functional and may be a series expansion[32]. An unknown parameter is associated with each term; the numerical values of the parameters are unknown and must be determined.[31] Semi-empirical density functionals are the oldest approach and are still utilized for fitting the parameters with known molecular and atomic properties. Ideally, a density functional would be universal, providing accurate and precise results for all materials systems, including molecules and solids. However, in general, a fitting performed for a molecular system will not yield accurate results for a solid-state system, and vice versa.[33]

This problem has motivated the development of non-empirical meta-GGA functionals, where the GGA provides the local parameters for the semilocal functional. The meta-GGA approach has two distinct advantages: desirable computational efficiency and additional accuracy, coming from the incorporation of the second derivative of the gradient of the electron density.[34] A non-empirical meta-GGA does not require successful fitting to known molecular or atomic properties, but the functional does have to produce the correct properties to be deemed successful.

The level of sophistication of the exchange-correlation term can be described in terms of the rungs of a "Jacobs ladder,"[35]. This is illustrated in the equation:

$$E_{xc}[\rho_\uparrow, \rho_\downarrow] = \int dr^3 \rho(r) \epsilon_{xc}(\rho_\uparrow, \rho_\downarrow, \nabla\rho_\downarrow, \nabla\rho_\uparrow, \tau_\uparrow, \tau_\downarrow) \tag{2-2}$$

Where ρ represents the electron densities with arrows denoting spin, and τ represents the kinetic energy density. The specific form of ϵ_{xc} yields the various density functional approximations; for example, the LDA functional represents the first rung in which only the electron densities $(\rho_\uparrow, \rho_\downarrow)$ are considered, while the GGA represents the second rung of Jacob's ladder, by incorporating the gradient $(\nabla\rho_\downarrow, \nabla\rho_\uparrow)$. The kinetic energy density, $(\tau_\uparrow, \tau_\downarrow)$, is the second derivative of the energy gradient, the third rung component. Though the meta-GGA employs all three rungs, it does not solve the exchange-correlation problem of DFT because the meta-GGAs have a finite interaction potential at the nucleus for ground-state electron densities.[34, 35]

There are various types of meta-GGAs. Each type places constraints on the density functional based on known features of the exchange-correlation functional. While the details of each meta-GGA are not within the scope of this work, the SCAN functional is used extensively in this work. Thus, a brief discussion of the SCAN functional follows.

Ultimately, what sets the SCAN functional apart from other meta-GGA functionals is that it obeys all 17 known exchange-correlation constraints. One such constraint, satisfied even by LDA, is the Lieb-Oxford lower bound.[36] This constraint is represented by the inequality $E_{xc}[\rho] \leq BE_x^{LDA}[\rho]$, Where the B is a parameter that can be fitted using a semiempirical method, or its bounds determined analytically. For example, Levy and Perdew[29] proposed $1.93 < B < 2.273$. The Lieb-Oxford lower bound is a constraint that has been known for a long time. Though there may be new constraints identified in the future, SCAN is a novel functional in that it satisfies the 17 known constraints.

The exchange-correlation potential is broken into two parts: the exchange part and the correlation part. There are six known exchange and six known correlation constraints, with an additional five being on the sum of the two parts. These are discussed in more detail in the works of Sun et al.[37, 38] All meta-GGA functionals are based on the following equation for

the exchange-correlation.

$$
\begin{aligned}
E_{xc}[\rho_\uparrow, \rho_\downarrow] &= E_x[\rho_\uparrow, \rho_\downarrow] + E_c[\rho_\uparrow, \rho_\downarrow] \\
&= \int dr^3 \rho \epsilon_x(\rho_\uparrow, \nabla\rho_\downarrow, \nabla\rho_\uparrow, \rho_\downarrow, \tau_\uparrow, \tau_\downarrow) F_x(\nabla\rho_\downarrow, \nabla\rho_\uparrow, \rho_\downarrow, \alpha) \\
&\quad + \int dr^3 \rho \epsilon_c(\rho_\uparrow, \nabla\rho_\downarrow, \nabla\rho_\uparrow, \rho_\downarrow, \tau_\uparrow, \tau_\downarrow) F_c(\nabla\rho_\downarrow, \nabla\rho_\uparrow, \rho_\downarrow, \alpha)
\end{aligned}
\tag{2-3}
$$

As stated earlier, the exchange-correlation functional can be expressed as a sum of the exchange term and the correlation term to more easily manage the functional. $F_x(\nabla\rho_\downarrow, \nabla\rho_\uparrow, \rho_\downarrow, \alpha)$ and $F_c(\nabla\rho_\downarrow, \nabla\rho_\uparrow, \rho_\downarrow, \alpha)$ are the exchange and correlation enhancement factors, and are the key component for introducing constraints to the approximate exchange-correlation functional.[34, 38] α is a constant that represents the covalent ($\alpha \approx 0$), metallic ($\alpha \approx 1$), and weak ($\alpha \gg 1$) bonds. These enhancement factors are comprised of interpolated, extrapolated, and coefficients terms and enforce the constraints placed on the functional.[37] Ideally, a meta-GGA should be bounded by the constraint for all-electron densities and α.

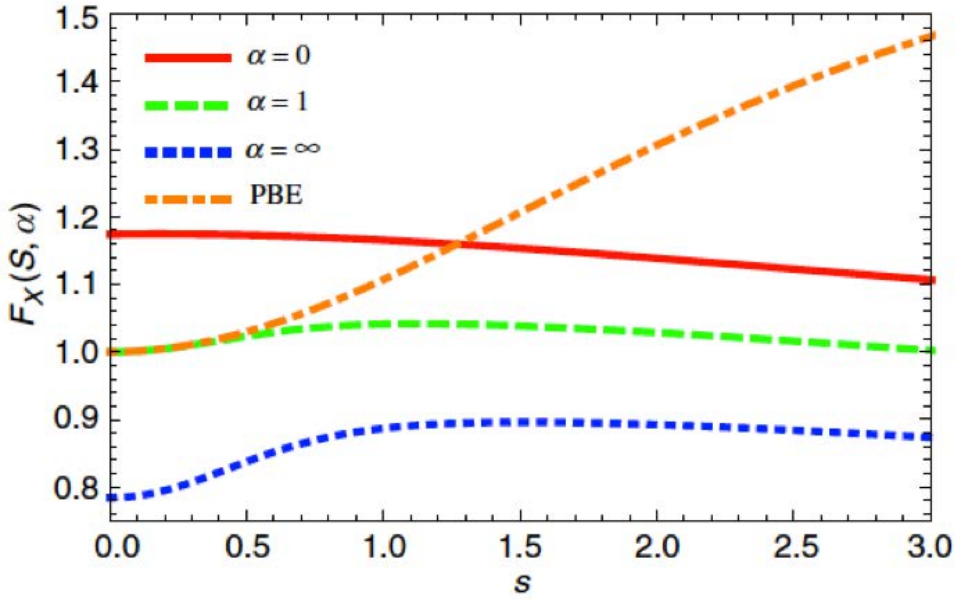

Figure 2-1. The enhancement factor of the SCAN functional compared to PBE-GGA for a spin unpolarized system. The PBE-GGA functional diverges as $S \to \infty$. Note, the x-axis labeled S is a dimensionless parameter representing the electron density gradient ($\nabla\rho_\downarrow, \nabla\rho_\uparrow$).[37]

For example, SCAN obeys the rigorous spin-unpolarized density bound[39] of $F_x \leq 1.174$ for all-electron densities and α. This exchange enhancement factor is the optimal lower bound for the exchange energy of a two-electron interaction. PBE-GGA fails to obey this constraint (see Fig. 2-1) for higher electron density gradients, and Sun et al.[37, 38] found this failure to be present for other meta-GGA functionals, such as TPSS and revTPSS. Conversely, the SCAN functional was found to obey the two-electron Lieb-Oxford bound while other functionals failed to. SCAN's derivation satisfying all constraints establishes the potential for outperforming all prior meta-GGA and in some reported cases, more sophisticated and computationally more expensive, hybrid functionals.

Previous works[40, 41] show that SCAN improves geometries and energies of diversely bonded materials (i.e. covalent, metallic, ionic, hydrogen, and van der Waals) over LDA and GGA. Remsing et al. studied the structure and dynamics of liquid silicon based on the choice of density functional.[42] They compared SCAN, LDA, and PBE-GGA functionals performance on the semiconductor-to-metal transition, specifically the Si melt. The success was mostly due to SCANs' accuracy of simultaneous metallic and covalent bonds during the melt transition. Therefore, the SCAN functional was chosen for this work to provide more accurate results for materials containing transition metal and semiconductor atoms.

2.3 Phonon Simulation

Thanks to the introduction of modern high-performance computing and DFT, the thermodynamic properties calculated from DFT often match experimental results well. This accuracy is achieved with a combination of DFT and phonon software packages.

2.3.1 Harmonic Approximation

When a DFT calculation is performed, the results are the ion positions at 0 K. This is a significant limitation because all experiments are performed at $T > 0K$. However, this limitation can be addressed, at least in part, by determining the thermodynamics properties at elevated temperatures via phonon analysis. Two basic assumptions underpin this analysis. First, the ionic positions given from DFT relaxation can be interpreted as the equilibrium location

of the atoms. That is, an ion is no longer to be viewed as having a fixed to a position but as oscillating about that position with a small amplitude. The second assumption is that these oscillations are not large enough to be interpreted as diffusion; that is, the oscillation is far less than the interatomic spacing. These underpinning assumptions are needed for the harmonic approximation and more sophisticated phonon approximations.[43]

The notation of the Phonopy package will be used for the following equations.[44] The atoms move from their equilibrium positions $r(lk)$ with displacement $u(lk)$, where l and k are the labels of unit cells and atoms in each unit cell, respectively. The potential energy of a crystal is a function of the displacements of atoms and defined as Φ. It can be represented as a Taylor expansion.

$$\Phi = \Phi_0 + \sum_{lk}\sum_{\alpha}\Phi_\alpha(lk)u_\alpha(lk) + \frac{1}{2}\sum_{lk,l'k'}\sum_{\alpha\beta}\Phi_{\alpha\beta}(lk,l'k')u_\alpha(lk)u_\beta(l'k') \tag{2-4}$$

$\Phi_\alpha(lk)$ and $\Phi_{\alpha\beta}(lk,l'k')$ are the first and second-order force constants, respectively. The first three terms of the potential energy Taylor expansion are known as the harmonic approximation component.

Expressing the first order forces as $F_\alpha(lk) - \dfrac{\partial\Phi}{\partial u_\alpha(lk)}$, the second-order force constant can be obtained by the equation:

$$\frac{\partial^2\Phi}{u_\alpha(lk)u_\beta(l'k')} = -\frac{\partial F_\alpha(lk)}{\partial u_\beta(l'k')} \tag{2-5}$$

From here, the equation is solved using eigenvalues of the dynamical matrix by the set of equations:

$$D(q)e_{qj} = \omega_{qj}^2 e_{qj} \tag{2-6}$$

$$D_{kk'}^{\alpha\beta}(q) = \sum_{l}{}' \frac{\Phi_{\alpha\beta}(0k,k'l')}{\sqrt{m_k m_{k'}}}\exp ih\cdot[r(l'k') - r(0k)] \tag{2-7}$$

Where $D(q)$ is the Hermitian dynamical matrix, m_k is the mass of the kth atom, j is the phonon band index, and ω_{qj}^2 and e_{qj} are the phonon eigenvalues (frequency squared) and polarization, respectively. The sign of the phonon eigenvalues is an important tool for

determining the dynamical stability of the phase. Specifically, the frequency is the square root of the eigen value. If the eigen value is negative, then the frequency is imaginary, leading to an exponentially increasing amplitude with time from $\exp(-i(i)) = \exp \omega t$.

From the Bose-Einstein distribution in statistical mechanics, the total energy of phonon frequencies over the Brillouin zone can be determined as:

$$E = \sum_{qj} \hbar\omega_{qj}(\frac{1}{2} + \frac{1}{\exp \frac{\hbar\omega_{qj}}{k_b T} - 1}) \tag{2-8}$$

The total energy includes the zero-point energy term $\sum_{qj} \hbar\omega_{qj}\frac{1}{2}$ which represents the quantum-mechanical ground state vibrational energy of the crystal. The vibrational contributions to the thermodynamic properties, such as constant volume heat capacity (C_v), Helmholtz free energy (F), and entropy (S), can be computed as derivatives of the total energy; this it, in terms of of phonon frequencies. The complete derivation of the harmonic approximation and its relationship to thermodynamic equations can be found in textbooks.[43, 45] yielding:

$$C_\nu = k_b \sum (\frac{\hbar\omega}{k_b T})^2 \frac{\exp \frac{\hbar\omega}{k_b T}}{(\exp \frac{\hbar\omega}{k_b T} - 1)^2} \tag{2-9}$$

$$F = \frac{1}{2} \sum \hbar\omega + k_b T[1 - \exp \frac{-\hbar\omega}{k_b T}] \tag{2-10}$$

$$S = \frac{1}{2T} \sum \hbar\omega \cot \frac{\hbar\omega}{2k_b T} - k_b \sum ln[2 \sinh \frac{\hbar\omega}{2k_b T}] \tag{2-11}$$

2.3.2 Quasi-Harmonic Approximation

The harmonic approximation is applied to different volumes of contraction and expansion within 1% of the lattice constant for implementing the quasi-harmonic approximation.
The phonon frequencies are affected by changing volumes of the material; therefore, the thermodynamic properties are also affected. Calculating phonon frequencies and total energy at each volume yields the Gibbs free energy, so the equilibrium Gibbs energy is calculated from the

transformation equation:[46, 47]:

$$G(T,p) = \min_{v} \left[F(T,V) + pV\right] \tag{2-12}$$

This equation states the Gibbs free energy is found at the volume corresponding to the lowest energy point of the system. Figure 2-2 illustrates the process of calculating the Gibbs free energy with each point represented by $F(T,V) = E_{el} + F_{ph}(T,V)$.

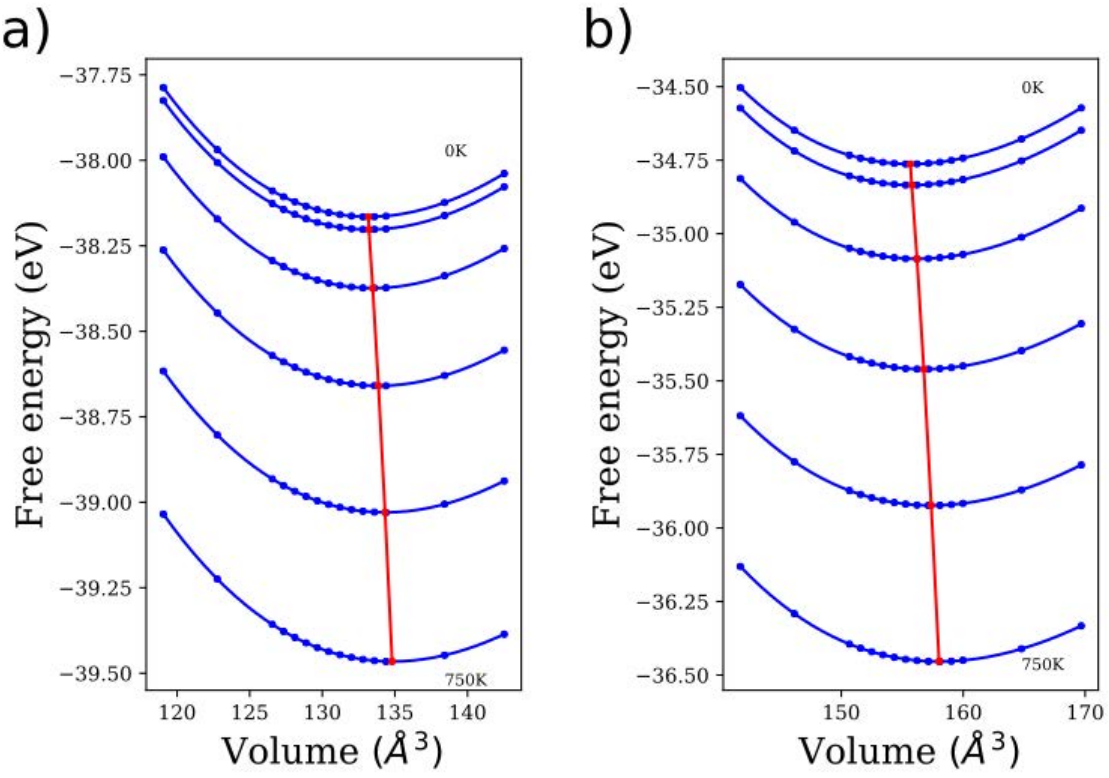

Figure 2-2. $F(T,V) = E_{el} + F_{ph}(T,V)$ pseudocubic Si_3P_4 (a) and Si_3As_4 (b) with respect to volume and temperature. Blue circles represent total energy of that volume calculated from DFT while blue line represents state-variable fit between the points. The red line traces the minimum energy points at each temperature.

The energy from DFT is calculated for each volume at 0 K added to energy calculated from the phonon frequencies to give the Helmholtz free. The volume dependent Helmholtz energies are fitted with an equation of states to determine the minimum at each temperature. This yields the temperature-dependent volume, phonon frequencies and phonon contributions

to the thermodynamic properties. This quasi-harmonic approximation typically yields reasonably accurate predictions for thermal expansion for temperatures up to about two-thirds the melting point of the phase. In the case of the pseudocubic phases, the temperature range chosen was 0 K to 750 K, based on the melting point of silicon, since the melting point of pseudocubics is unknown.

2.4 Real Space Multiple Scattering Theory

Electron Energy Loss Spectroscopy (EELS) is a technique that measures the energies of fast traveling electrons after inelastic scattering within a thin material (typically 15 nm). The fast electron, traveling at 70% of the speed of light for standard scanning transmission electron microscopy (STEM) or transmission electron microscopy (TEM) configurations, inelastically scatters with a core electron that is excited to the conduction band of the material. The instrumentation of EELS measures the scattered electrons' energies. The instrumentation will be discussed in Chapter 3. There are no qualitative techniques for analyzing EELS spectra, so ab initio methods are utilized to interpret the experimental data.[48] This section will focus on the theory for computational prediction.

EELS spectra of core electrons are given by Fermi's golden rule equation which accounts for the initial and final states of the electron-hole post scattering:

$$S(q,\omega) = \sum |< f \mid \exp iq \cdot r \mid i >|^2 \, \delta(\omega + E_i - E_f) \tag{2-13}$$

$$\frac{d^2\sigma}{d\Omega d\omega} = 4(\frac{\gamma}{a_0})^2 q^{-4} \frac{k'}{k} S(q,\omega) \tag{2-14}$$

Where $\frac{d^2\sigma}{d\Omega d\omega}$ represents a double-differential scattering cross-section (DDSC) with respect to the scattering angle Ω and energy loss ω. The DDSC represents the probability of observing an electron. E_i and E_f are the initial and final state energies of the electron; $s(q,\omega)$ is the dynamical state structure with respect to energy loss, ω, and the momentum transfer direction, $q \cdot k$ is the wave vector of the incoming electron, and k is the wave vector of the scattered electron.

The use of Fermi's golden rule was the first attempt to calculate x-ray absorption spectroscopy (XAS) spectra and, by extension, EELS signal. The immediate problem for calculating the scattering from Fermi's golden rule is that the choice of initial and final states is ambiguous. Commonly, the initial state is chosen to be the ground state and the final state is chosen to be a screened core-hole.[48] These choices allows application of Fermi's golden rule in DFT with the advantage of full-wave potentials; the screened core-hole is treated as a Z+1 defect. However, it showed wide oscillations after the initial excitation, yielding poor results (as shown in Fig. 2-3). Due to the self-interaction of defects across the periodic boundaries, the oscillation error worsens, requiring supercell convergence.

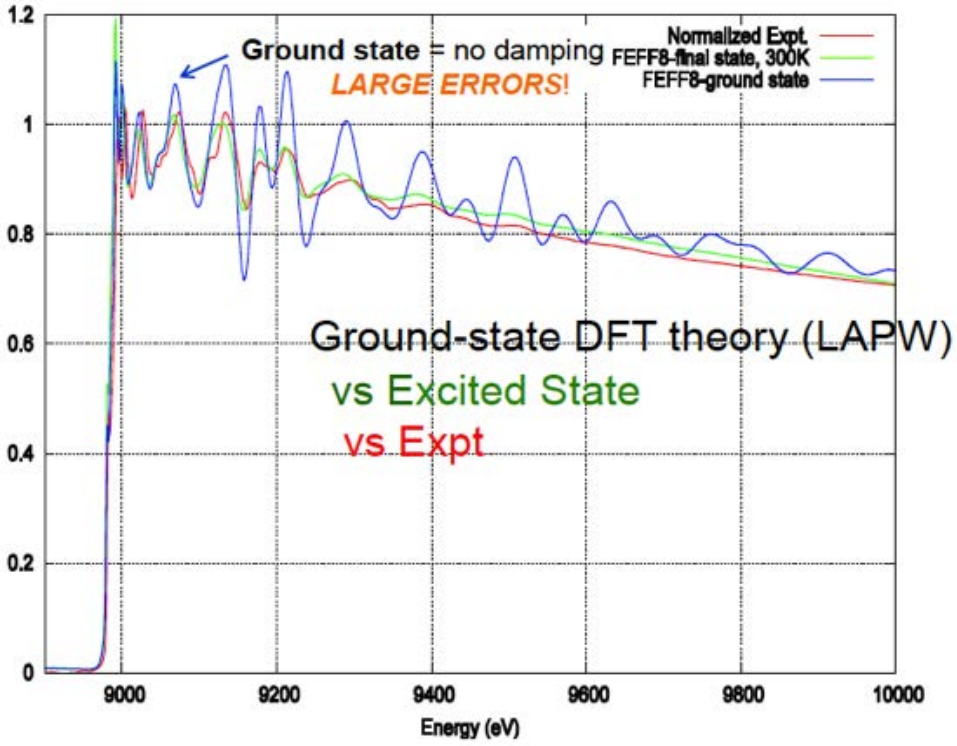

Figure 2-3. Plot comparing experimental EELS spectra with RSMS (using FEFF9) and Z+1 (using LAPW WIEN2K) methods.[49]

Real Space Multiple Scattering (RSMS) is an approach that solves the above problems and is the modern theory utilized for computing EELS scattering.[50] The RSMS scattering solution uses a Green's function approach, which contains the Hamiltonian of the particle's

final state and an imaginary component representing decay of the excited particle:

$$\sigma(\omega) = -\frac{4\pi}{c\omega} Im \sum <| \ i \ | \ iq \cdot r^* G(\omega + E_i) q \cdot r \ | \ i > \theta(E_i - E_f + \hbar\omega) \tag{2-15}$$

With the assumption that low-q values dominate, $e^(iqr)$ in Fermi's equation can be simplified to the dipole term, proportional to q r. The definition of an initial particle state is necessary for computing EELS scattering; this initial state is assumed to be the ground state calculated from DFT. Due to its relationship with DFT, the RSMS theory is regarded as a quasi-particle approximation in which a single particle is considered inside an electron density. The Hamiltonian describing RSMS is reminiscent of DFT.[48, 50]

$$H = h_{ke} + h_c + h_{ex} + \sum (E_{e-h}) \tag{2-16}$$

$$\sum E_{e-h} \equiv V_{xc} \tag{2-17}$$

There is a Hamiltonian term within RSMS, $\sum E_{e-h}$, which describes the excited core electron. This term is similar to the exchange-correlation functional, and these terms are equal for energies near the excitation edge of the atom (e.g. K-edge, L_1,L_2,L_3-edges). The terms diverge due to the self-energy $\sum E_{e-h}$ dependence on total energy, damping, and extrinsic losses in the final state. For solids, the Hedin-Lundqvist (H-L) model is used for approximating the self-energy $\sum E_{e-h}$. The H-L model is derived from the LDA of density functional theory; that is, the model is based on the plasmon-pole model for an electron gas and is based on a dynamically screened exchange operator.

2.5 Muffin-Tin Potential

For this work, the FEFF9 package was used for EELS simulation, FEFF9 self-consistently converges electrons in the same manner as DFT packages such as VASP, CASTEP, and WIEN2K. However, FEFF9 uses muffin tin potentials, which are not a full-wave potential.[51]

Muffin Tin orbitals are defined as:[49].

$$V(r) = \begin{cases} V(\mid r - R \mid) & \mid r - R \mid < r_o \\ Const. \quad \text{else} \end{cases} \tag{2-18}$$

This potential represents an ion within some defined radius r, and the potential for an atom is developed by matching solutions with the Schrodinger's equation. The muffin-tin potential is divided into two parts: the region inside some spherically symmetrical surface is defined by a spherical function of the potential. The internal region is represented by a linear combination of spherical harmonics and eigenfunctions. The region outside the sphere is held to a constant potential. This region is typically represented as a Fourier series constant.

Muffin tin potentials require little computation expense, and the potentials were widely used in the 1970s because they made calculations feasible. The muffin-tin potential is useful for closely packed or metallic systems; however, the approximation becomes very poor for covalently bonded systems such as Si. Another issue is the strong dependence on the choice of radius. If a radius is not standardized between calculations, the result will be different for each calculation.

Software packages, such as WIEN2K, can use RSMS with a full-potential (linearized) augmented plane-wave method. However, at the time of this work, EELS simulation with modern full-wave potentials was in beta testing. The FEFF9 simulation package calculated the EELS spectrums, which still uses muffin-tin potentials for self-consistent convergence.[52] This work uses the FEFF9 package with muffin-tin potentials for covalent pseudocubic material.

2.6 Cluster Expansion Method

First-principles achieve an accurate description of thermodynamic properties for alloys. However, these methods require tedious work for writing input files for software tools and monitoring the process and post-processing. Therefore, calculating the thermodynamics for numerous alloys requires an unreasonable amount of time, and thus limits practical

implementation. The cluster expansion method utilized in the Alloy Theoretic Automated Toolkit (ATAT) simplifies the process by introducing decision rules for alloy configuration.

The main advantage of the cluster expansion is its good convergence with a small number of known energy configurations; so, it is a computationally inexpensive algorithm. This fast convergence is important for the combining cluster expansion method with DFT: cluster energy is used for regression fit to determine the unknown interaction parameter J.

The cluster expansion method, a generalization of the Ising Hamiltonian, consists of a parent lattice where each site, denoted i, takes the value of A or B for a binary alloy. These discrete variables represent an atom, and the atom site is allowed to interact with its neighbors. When this model is generalized to an arbitrary multi-component system, it is known as the cluster expansion method[53, 54] and yields the equation .

$$E(\sigma) = \sum m_\alpha J_\alpha \langle \prod_{i\epsilon\beta} \sigma_i \rangle \tag{2-19}$$

$E(\sigma)$ is the energy represented as a polynomial expansion; σ_i is an occupation variable representing each site of the lattice; α is a lattice configuration or cluster of the parent lattice; the average $\langle \prod_{i\epsilon\beta} \sigma_i \rangle$ is taken over all β, being clusters related to α by symmetry; J_α is the expansion body coefficient which represents the energetics of the alloy; and, the multiplicities m_α indicates the number of clusters that are equivalent to α.

One advantage, the cluster expansion equation is that when appropriately summed for all α, can represent any energy of configuration σ. Another advantage is that the cluster expansion converges quickly with a small number of known energy configurations, so it's a computationally inexpensive algorithm. This fast convergence is important for combining cluster expansion with DFT. Cluster energy is used for regression fit to determine the unknown interaction parameter J_α. Fitting the energies from DFT is known as the structure inversion method (SIM).

Fitting the energies from DFT is known as the structure inversion method (SIM). SIM relates the configuration of the cluster to the enthalpy of the system. This is an inversion

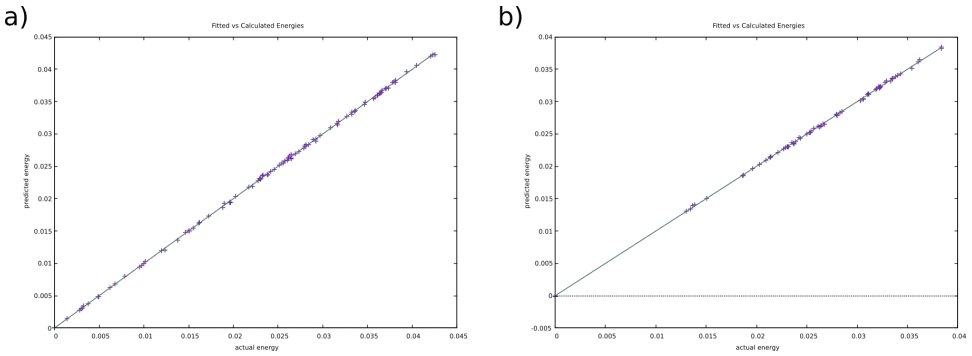

Figure 2-4. The fitted vs. calculated energies for $TiSi_2$-$TiGe_2$ pseudobinary mixture of C49 (a) and C54(b). The teal plot is a line with a slope value of one. Ideally, the fitted to predicted energy values should yield a ratio of one.

of the cluster method equation such that J_α becomes a function of total energy from DFT. For SIM to work, the interaction energy is assumed to operate at short distances, which is an accurate assumption. The predicted energy from cluster expansion and the energy from DFT form a line with a slope of unity, as shown in Fig. 2-4.

2.7 Special Quasirandom Structures

Randomly oriented phases are important in materials engineering as they have numerous applications. Therefore, a method for generating random structures efficiently would be valuable. Of course, one such method manually replaces the atomic sites of a binary alloy. However, this method creates two problems: the positions of the atoms in the alloy will deviate from a truly random structure, and a manual method will become unrealistic for structures requiring a larger number of atoms, such as $Mg_{0.75}Li_{0.25}$ requiring 128 sites. The random $Mg_{0.75}Li_{0.25}$ image of Fig. 2-5 was constructed using SQS for this section.

A method for mimicking an infinite random alloy with a finite supercell is called the special quasirandom structure (SQS) algorithm. It is expected that a supercell approximation of an infinite random alloy will have spurious periodic errors. SQS assumes that interactions between distant neighbors are less than between close neighbors. Therefore, it only considers the first few neighbor cells inside a defined radius, and the periodicity errors from approximating a random alloy with a supercell only occur between neighbors at greater distances.[55] Like

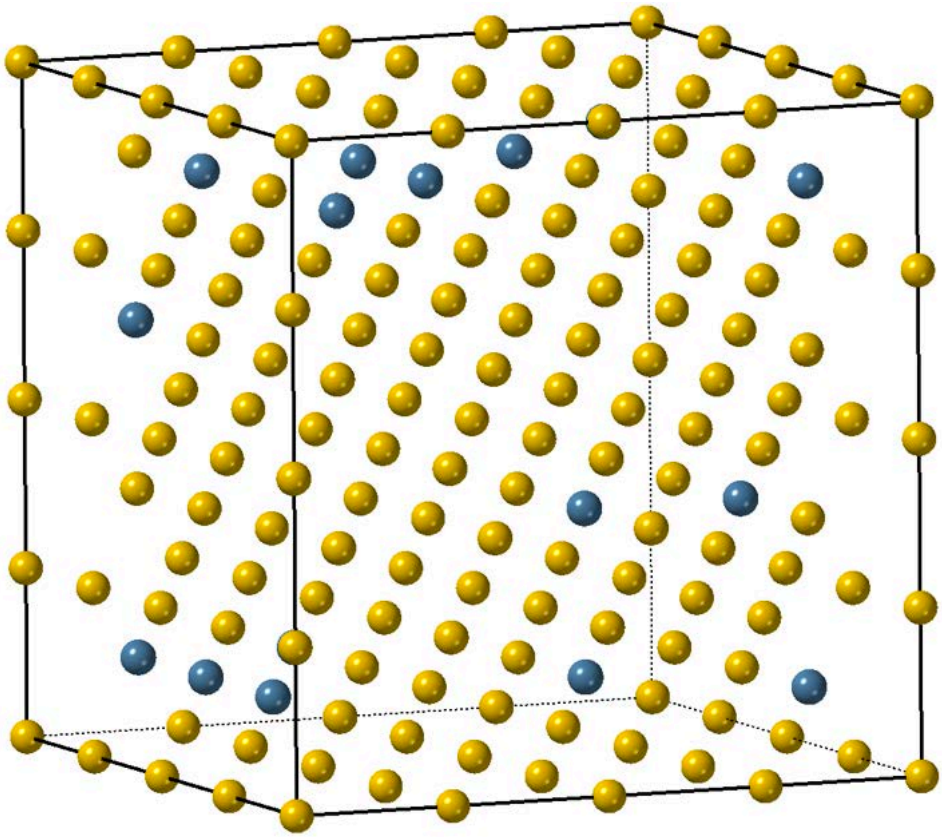

Figure 2-5. $Mg_{0.75}Li_{0.25}$ after relaxing at the level of density functional theory. The structure was generated using the special quasirandom structure algorithm.

the cluster expansion method, SQS builds on the theory of the Ising model, such that sites occupied by A carry a value of $+1$ while sites occupied by B carry a value of -1.[56, 57].

$$\prod_{f}(\sigma) = \frac{1}{D_f N}\sum_{l}\prod_{f}(l,\sigma) \tag{2-20}$$

For a binary alloy, a configuration σ is discretized into components of $f = (k, m)$ where pairs of atoms are k=2, triplets k=3, with neighbor mth neighbor distances. N represents the total number of atoms, and D_f represents the total number of f = (k,m) per site. The lattice average (also known as the correlation function) is denoted by the left-hand side of the equation.

$$\langle p\rangle = \sum_{k,m} D_{k,m}\langle \prod_{f=k,m}(\sigma)\rangle p_{k,m} \tag{2-21}$$

Unlike the cluster expansion method, SQS does not correlate the configuration of the random alloy to a DFT total energy. $p_{k,m}$ represents the interaction parameter of $f = (k, m)$, and the left hand side of the equation is the average of a physical property. $< P >$ is compared with a truly random average $< P^{avg} >$ such that the following objective function can be minimized.

$$Q = -\omega L + \sum \mid \Delta P(\sigma) \mid \tag{2-22}$$

ω is a user-specified weight while L is the largest length that satisfies $(\sigma) = 0$ for all clusters. $\Delta P(\sigma) = P(\sigma) - P(\sigma^{rnd})$. $P(\sigma^{rnd})$ is calculated from the knowledge that the truly random system site occupations are independent. This equation ensures that the stochastic search will converge for multicomponent systems and is the defining quality that distinguishes the method utilized by ATAT.[57] Each new SQS system is tested with the objective function. If the new SQS further minimizes Q, the SQS enters a simulated annealing loop based on a Monte Carlo scheme. With a probability proportional to $exp(-Q/T)$, a jump to a new supercell shape is made or two atoms in the same cell permute. After the anneal loops, the best SQS is tested in the same manner again then kept or replaced.

The SQS software, as implemented in the ATAT package, optimizes the shape of the supercell and the lattice site occupation of atoms. The method is not sensitive to starting supercell structure, and is capable of managing multi-component and multi-sublattice systems with minimum input from the user. In this dissertation, this software is used to calculate the enthalpy of mixing for pseudobinary $Ti(Si_{1-x}Ge_x)_2$ phases.

2.8 Bader Analysis

The atomic charge is an important property of molecules and crystals, especially for charge transfer behavior between atoms, i.e. ionic bonds. However, the atomic charge is not an observable in quantum mechanics, which inhibits a clear definition of charge from DFT. DFT outputs an overall spatially dependent charge density, so it is unclear how to partition this continuous charge such that a single charge value can be attributed to one atom over another.

There have been several proposals for handling the partitioning, ranging from the older scheme of Mulliken population analysis to the more modern Bader and Hirshfield analysis; this work utilizes the Bader analysis scheme.

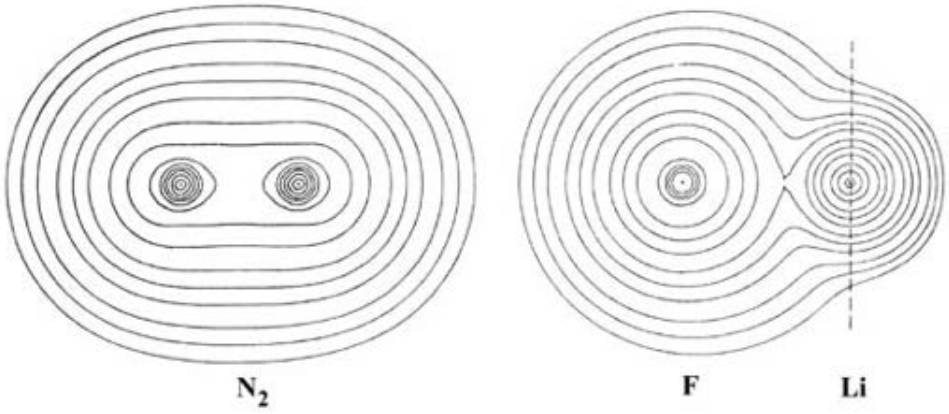

Figure 2-6. $Mg_{0.75}Li_{0.25}$ Contour maps of covalently bonded N (left) and ionically bonded F-Li (right) at equilibrium distance. The lines to the right of the Li dashed line represents the unbounded charge density.

The algorithm for applying Bader analysis to the charge density output of DFT is beyond the scope of this study, but the general concept is illustrated in this section and in Fig. 2-6 as N_2 and LiF charge density contours. A subsystem containing a nucleus is determined as the surface formed at which there is no flux in the gradient vector field. Bader analysis utilizes one vector equation $\nabla\rho(r_s)n(r_s) = 0$; $n(r_s)$ is a unit normal vector to the surface r_s.

The concept is very simple, but the challenge is algorithm implementation. Due to potentially large charge density files, Bader analysis codes are optimized software algorithms for quickly determining these subspaces, also called Bader volumes.[58–61]

One important note, DFT software does not always include the core electrons in calculations since core electrons contribute little to the bonding. If the core electrons are not included in the charge density file, the Bader analysis code will determine an incorrect atomic charge. Once the core electrons are included in the DFT calculation, Bader analysis will generate the correct charge within the Bader volume. Bader analysis is used for qualitatively

describing the charge transfer in this work. The method is applied to the perfect and defect allotropes of $TiGe_2$ and $TiSi_2$.

CHAPTER 3
OVERVIEW OF EXPERIMENTAL METHODS

3.1 Sample Preparation for Electrical and Micrograph Characterization

This chapter covers the experimental methods utilized in this work. All materials of this work are grown on (001) oriented p-type Si. The HD Si:P films in chapter 4 are grown with chemical vapor deposition (CVD), and the $Si_{1-x}Ge_x$ films in chapter 6 are grown with CVD as well. The HD Si:P and $Si_{1-x}Ge_x$ films are grown at Applied Materials in Santa Clara, Ca on a Applied Materials® Centura® tool.

The experiments of chapter 7 require additional steps for characterization. After $Si_{1-x}Ge_x$ films are deposited on Si, physical vapor deposition electron-beam evaporator PVD E-Beam deposits 5 nm of Ti, and then a layer of 3 nm of TiN is deposited with Atomic Layer Deposition (ALD). The PVD E-Beam tool is a University of Florida Nanoscale Research Center tool (NRF). ALD is performed at NRF on a Cambrdige Nano Fiji 200. The TiN layer has two purposes. First, the TiN layer buffers the Ti-$Si_{1-x}Ge_x$ solid reaction from the atmosphere during nanosecond (ns) laser annealing. However, this protection is not absolute since the TiN will eventually oxidize.[62] Second, the TiN is a dielectric where the index of refraction helps couple the laser light energy into the solid-state reaction. Otherwise, the dramatic difference in index of refraction between Ti and air would cause an additional reflection from the reaction.

Once laser annealed, the TiN/Ti(unreacted)/$Ti(Si_{1-x}Ge_x)_2$ samples are etched to remove TiN and unreacted Ti. The amorphous TiN deposition may cause confusion of interpreting the electron diffraction patterns generated, and TiN being an insulator may raise the sheet resistance of the $Ti(Si_{1-x}Ge_x)_2$ films of interest. Another disruption in sheet resistance measurement is the Ti itself. Not all the Ti will react with the $Si_{1-x}Ge_x$, so a layer of Ti will remain to skew the measurement. For these reasons, the films are etched for 10-15 minutes in a mixture of NH_4OH:H_2O_2:H_2O at 70°C. This recipe removes the TiN film and unreacted Ti after annealing while preserving the $Ti(Si_{1-x}Ge_x)_2$ layer.

Microstructural characterization is necessary for determining the presence of extended defects and phases. An electron beam is capable of achieving images beyond the resolution limit of optical microscopy. These micrograph images are produced using a transmission electron microscope (TEM) which can resolve features as small as 2.7 pm at 200 keV electron beam potentials.[63] The FEI Tecnai F20 S/TEM was the TEM used for this work and its resolution is closer to 250 pm. The material samples need to be electron transparent, which necessitates sample preparation. The samples are prepared in two ways: the first is a cross-sectional TEM (XTEM) sample, which allows a TEM instrument to image the sample from the side. This view-point allows for the detection of extended defects, surface uniformity, precipitation, layer thickness, and energy-dispersive x-ray spectroscopy (EDS). The second is a plan-view TEM (PTEM) sample, which provides the view-point from the top of the sample. PTEM will be used for electron diffraction to detect different allotropes of $Ti(Si_{1-x}Ge_x)_2$.

3.1.1 XTEM Sample Preparation

The XTEM sample process requires extensive use of a dual-beam focused ion beam (FIB) tool. Since ion imaging induces sample damage, a dual-beam FIB tool utilizes scanning electron microscopy (SEM) imaging, so ion imaging damage is minimized. Ion imaging would degrade or destroy the sample of interest. This setup is especially crucial for electron energy loss spectroscopy (EELS) sample preparation, which requires an XTEM sample preparation. For EELS, the sample must be thinner than typical XTEM preparation to reduce plasmon scattering noise. The use of ion imaging during the thinning steps will damage the XTEM sample. The FEI Helios NanoLab 600 dual beam is used for XTEM samples.

XTEM sample preparation begins with a black marker to introduce carbon on the surface (see fig. 3-1). The carbon temporarily protects the surface from ion damage and charge accumulation. The charge accumulation causes pattern distortion during the ion milling due to Coulombic forces.[64] A subsequent layer of platinum is deposited on the surface at a thickness of 2 um. The platinum layer provides long term protection of the surface, and it is crucial for final thinning. Following deposition, the FIB mills a stepped depth pattern with a

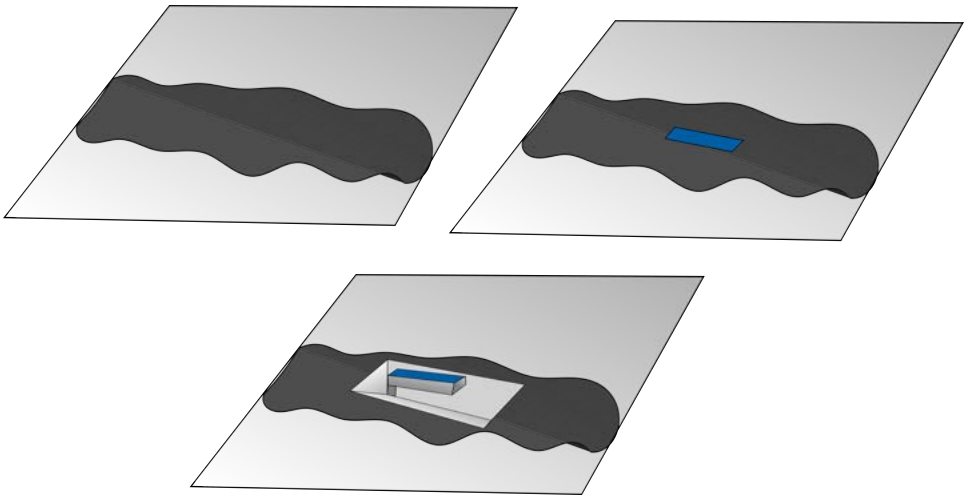

Figure 3-1. A brief illustration of lamella sample preparation, the preparation begins with a coating of carbon on the surface. A subsequent layer of platinum (blue) is deposited to protect the surface during ion milling. The area around the platinum is milled, leaving a section to support the lamella.

deeper depth near the surface of interest. This mill pattern is performed on the other side, to expose a lamellar sample. The lamella is cut with an "L" shaped pattern, so one side is detached from the bulk with the other side still supported. A micromanipulator is attached using decomposition of organometallic platinum on the free side of the lamella. Finally, the material which attaches the lamella to the bulk is cut, then the lamella is lifted out of the bulk. The lamellar sample is attached to molybdenum or copper (molybdenum grids needed for EELS thinning) grids with platinum. Once the lamella is secured onto the grid, a final thinning sequence is followed, as described in Schaffer et al.[65] For conventional TEM imaging, the lamella is thinned below a 100 nm thickness. However, more sophisticated techniques such as high-resolution transmission electron microscopy (HRTEM) or EELS may require more thinning.

3.1.2 PTEM Sample Preparation

PTEM sample preparation does not require the use of an expensive FIB instrument as in XTEM. However, sample preparation is a long and strenuous process that requires multiple levels of personal protection equipment (PPE). The outcome of the sample preparation is

etching the center of a 1 cm x 1 cm square sample until puncture, so the edges of the hole formed are electron transparent.

The process starts with mounting the sample on to a glass slide typically used for optical microscopes. The silicon is bonded to the glass with Crystalbond™ and a hot plate at 110ºC. The sample is slightly agitated while in contact with the Crystalbond™ to remove air bubbles. After cooling, the sample is adequately reinforced by the slide and crystal bond, which prevents chipping or cracking. The slide is mounted on a VCR group model no. V100 coring drill. The coring tool produces a circular sample with a diameter of 3 mm. After coring, the left-over sample is heated to melt the Crystalbond™ then the circular sample is cleaned to remove Crystalbond™ (a sequence is acetone then isopropanol).

Using Crystalbond™ and a hot plate, the samples are mounted on an aluminum cylinder. The surface of interest is mounted to the cylinder to protect it for TEM. A solution of water and 15 um alumina powder is mixed on a 400-grit polishing pad. The backside is polished down to under 100 um with a uniform thickness. Again, the sample is removed using a hot plate and cleaned to remove Crystalbond™.

Paraffin wax is liquified using the hot plate for application to the sample. The sample front-side is coated with liquified paraffin wax to protect it from the acid etch. Once the front side is protected, the sample is mounted on a custom Teflon™ stub. These stubs have a backside mount for a diode light pipe that shines light through the sample after puncture; This light pipe signals puncture to stop the acid etch. The backside of the sample is carefully coated with paraffin wax to leave an exposed circle in the center. Figure 2 illustrates the wax coating necessary for the acid etch step.

The sample is placed in a drip etcher that uses a mixture of 25% hydrofluoric acid (HF) and 75% nitric acid (HNO_3). The HF etches the SiO_2 native oxide that forms on a silicon surface while the HNO3 prevents hydrogen passivation; hydrogen passivation, a consequence of the HF etch, slows the formation of the native oxide. The backside of the sample is acid-etched (see fig. 3-2) until the sample is punctured, which takes up to seven minutes.

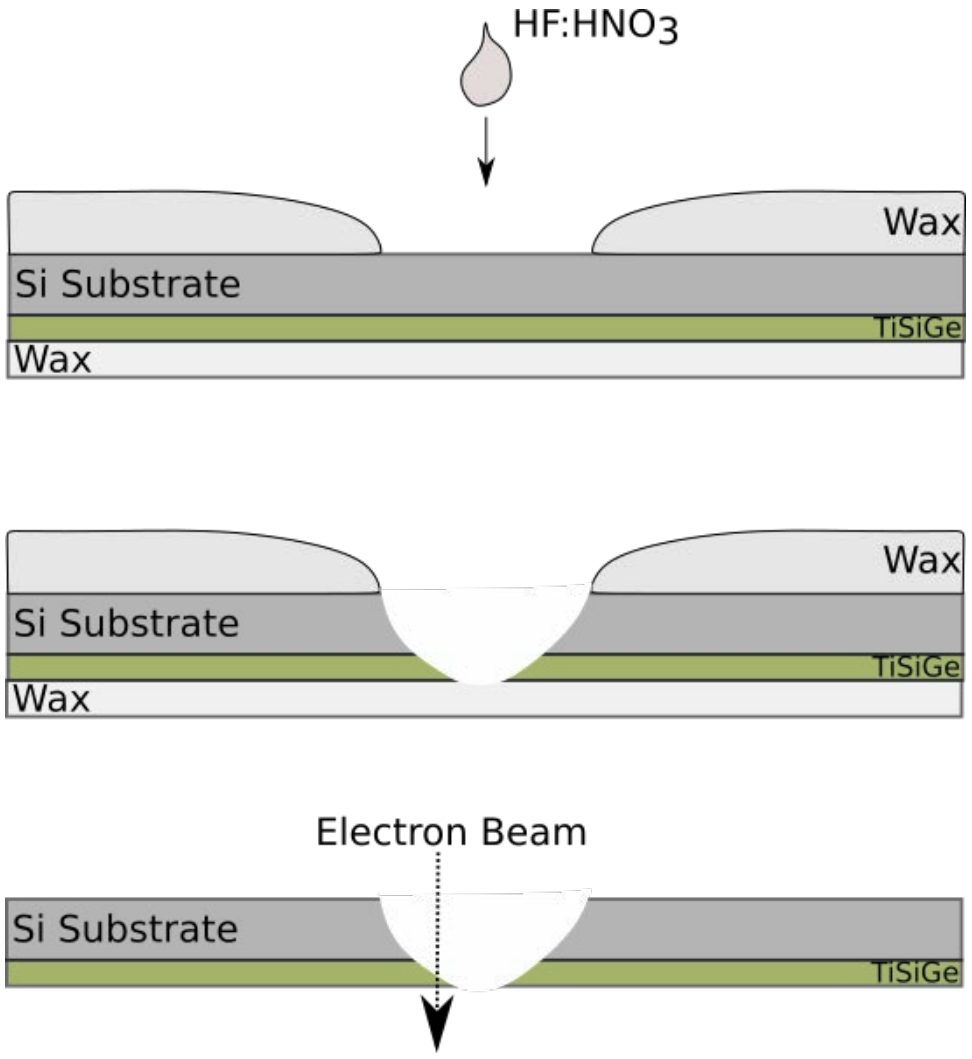

Figure 3-2. The front side is coated with paraffin wax to protect the $Ti(Si_{1-x}Ge_x)_2$ layer from acid etching. The backside is coated with wax, but the center exposed. Droplets of acid slowly etch the Si substrate until puncture. Once etching is complete, heptane removes the wax for TEM.

Once light shines through the puncture, the etch drip is stopped, and the stub is submerged in water to dilute the acid. The wax mounting the sample to the stub is carefully removed using a scalpel. Once the sample is free from the stub, it is submerged in heptane to remove the excess wax from the sample then qualified under an optical microscope. The application of paraffin wax on the backside dictates the quality of the etch. If the wax is not uniformly applied, the acid mixture etches more of the sample and damages the $Ti(Si_{1-x}Ge_x)_2$ film (see fig. 3-3).

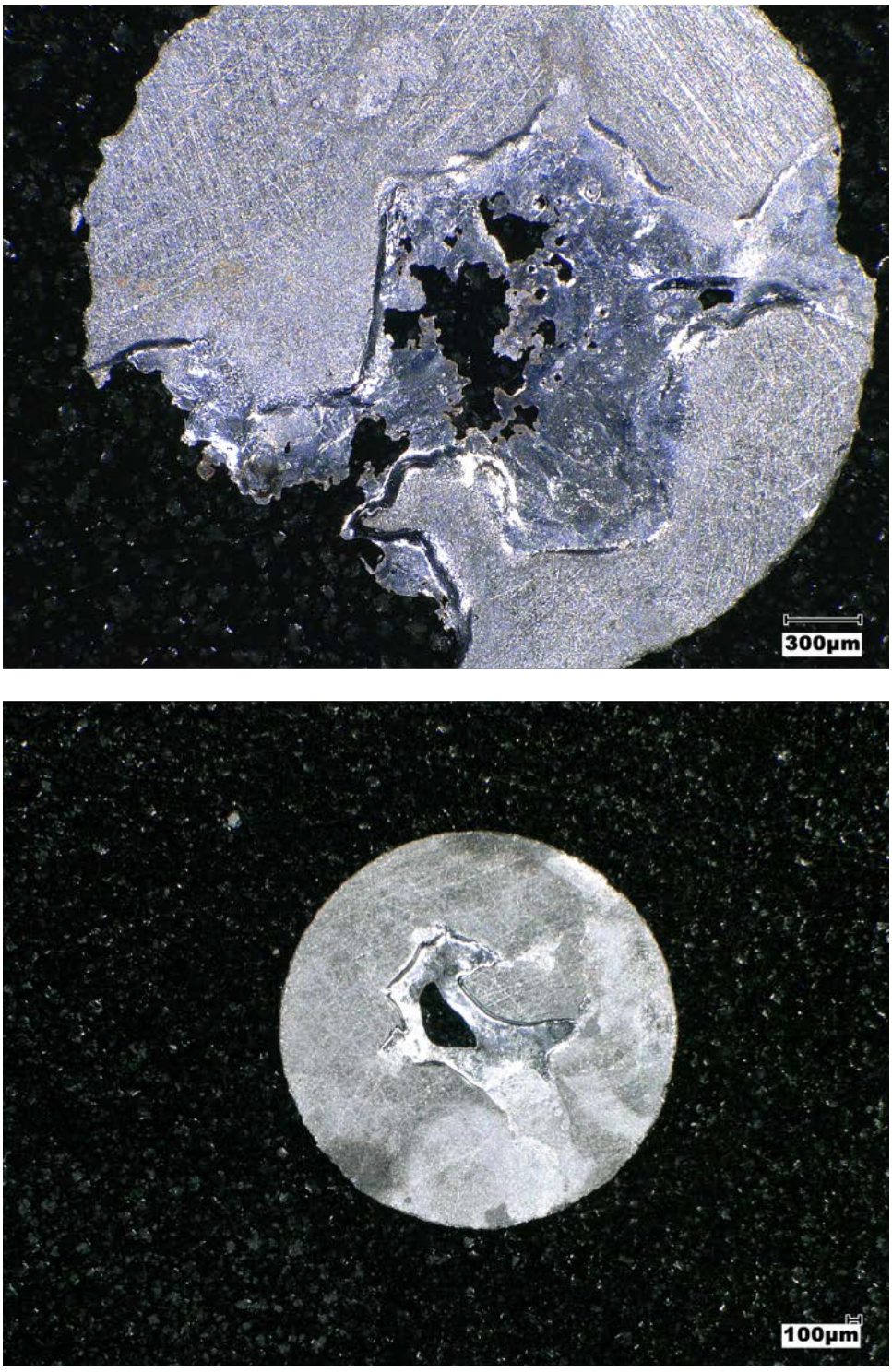

Figure 3-3. optical images after the cored samples are drip etched. The top image shows the result of improper wax coating of the sample, while the bottom image is the result of a properly coated sample. Both images are of the backside.

3.2 Electron Energy Loss Spectroscopy

Electron Energy Loss Spectroscopy (EELS) is a core-level spectroscopy technique capable of chemical, structural, and electronic analysis.[66] The technique measures the loss of kinetic energy of an inelastically scattered electron from the sample. The inelastic electron excites a core electron into the conduction band (well above the Fermi level), leaving behind an electron-hole pair in the sample. EELS is performed using TEM or scanning transmission electron microscopy (STEM) configurations, but STEM has proven to be a more powerful technique since it can produce EELS maps at atomic resolutions.[67, 68]

The EELS instrument has several major components comprising the energy-loss spectrometer; these components being the electron monochromator, magnetic prism, and energy selecting slit.[66] The electron monochromator is the most important component of the resolution of STEM. Reason being, the electron gun outputs electrons with a spread of energy value dictated by $\Delta E_s = 2.45(k_b T_s)$, which subsequently reduces the spatial resolution of the instrument.[66] The energy dispersion also has the additional hindrance of dictating the energy resolution limit of EELS. An electron monochromator is based on a Wien filter, though with a multitude of unique designs. This filter employs perpendicular magnetic (x-axis) and electrostatic fields (y-axis), with both fields being perpendicular to the electron (z-axis). These fields introduce a cyclotron frequency on the electron such that an electron with the desired energy starting at $x = y = 0$ at the input ends at $x = y = 0$. An electron with a higher or lower kinetic energy entering the Wien filter at $x = y = 0$ will exit at $x \neq 0$. The aperture blocks undesired kinetic energy electrons.

After the energy-loss electrons leave the sample, the electrons are collected and focused onto the detector using a magnetic prism. The electron experiences a radius of curvature by a magnetic field described by $R = ((\gamma m_0)/eB)v$.[69] The exit aperture determines the trade-off between energy resolution and signal-to-noise ratio of the experiment (see fig. 3-4). Finally, a scintillator transforms the electron into photons with a subsequent photomultiplier tube for detection.

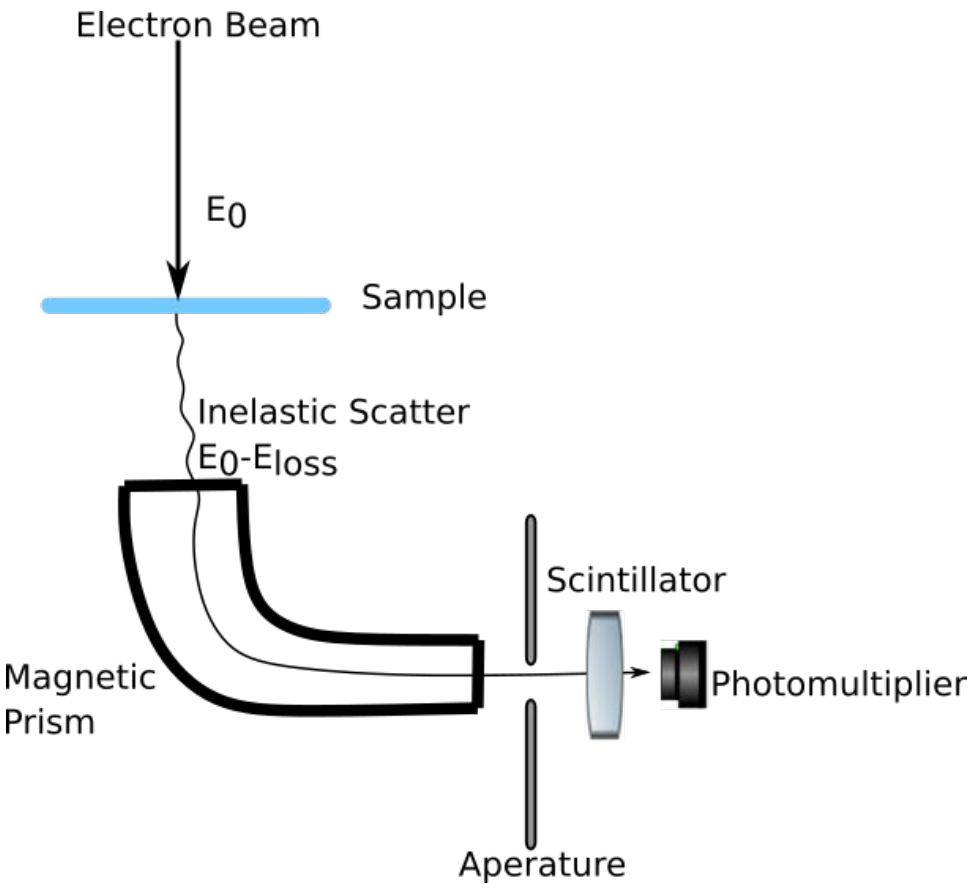

Figure 3-4. A simple illustration of an EELS attachment to the output of the TEM. EELS is comprised of an electron prism to separate the inelastically scattered electrons and an aperture. The detector is a scintillator with optical fibers to guide flashes of light on to a photomultiplier tube.

The EELS spectrum is broken into two parts named the energy loss near edge structure (ELNES) and the extended electron energy loss fine structure (EXELFS). Figure 3-5 shows a typical energy loss spectrum of up to 600 eV. The ionization edge at 400 eV represents the energy for a core electron to be excited above the Fermi level or ionization of the K shell. This edge is useful for determining the atomic species present in the sample. After the first ionization edge, oscillations are observed within 50 eV, which represents ELNES region. This region is useful for mapping the conduction band density of states of the material. The oscillations are sensitive to the nearest neighbor atoms of a material, and this region provides fingerprinting of phases. ELNES has become a well-understood spectrum, but the spectrum

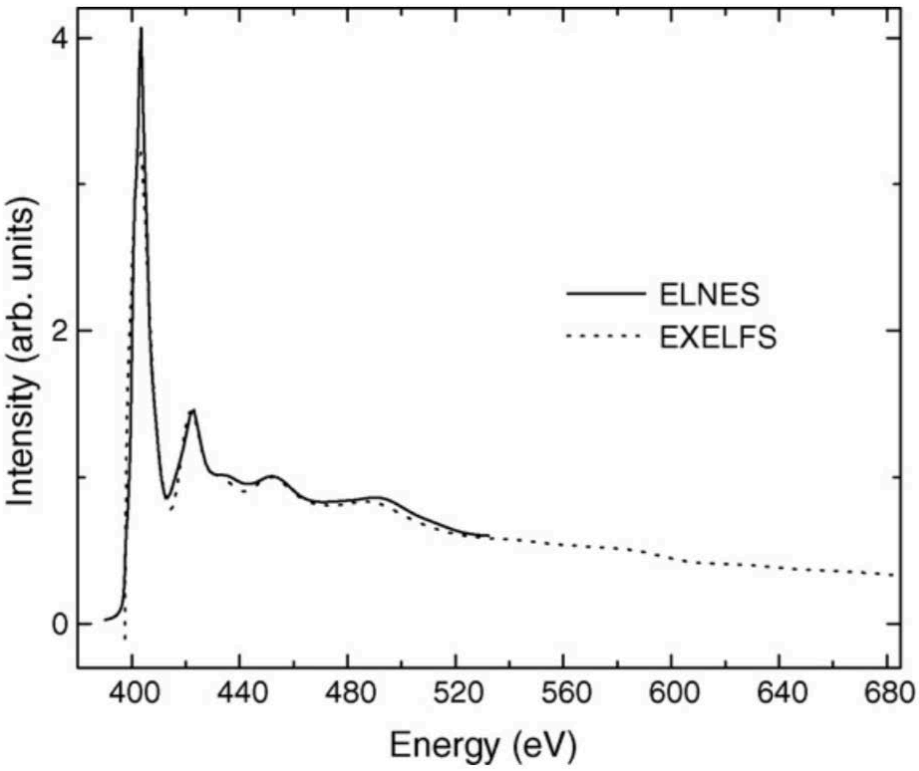

Figure 3-5. The typical energy loss spectrum of EELS with the core excitation edge at 400 eV (e.g., the Nitrogen k-edge). The ELNES and EXELFS spectrums are overlapped. [49]

cannot be analyzed using qualitative techniques. A computational compenent is required to understand ELNES.

On the other hand, EXELFs is a spectrum under active research since its relationship to the material is poorly understood. The reason being that the EXELFS structure is sensitive to the material's wave function (i.e., local bonding). This scattering regime becomes dominant beyond 100 eV of the ionization edge. The spectrum peaks become smoother and more spread apart due to the core electron, since it is within the conduction band, behaving more like a free-electron.

Like X-ray absorption fine structure XAFS, EXELFS is a multi-scattering technique. The final state of the local structure is influenced by the outgoing wavefunction of the electron and backscatter of the local atoms. Unlike EXAFS, EXELFS has a superior spatial resolution for

investigating complex nanophases. However, for more heavier atoms, the electron counts from the k-edge are below the noise floor because the scattering cross-section is too low.

3.3 EDS

Energy dispersive X-ray spectroscopy (EDS) is a technique with some relationship with EELS. When the transmitting electrons inelastically scatter with a core electron of the atom, the electron is excited into the conduction, leaving a hole in the core. The excited electron in the conduction band eventually decays back into the core. When the hole is filled, the energy difference is emitted as an X-ray of a characteristic wavelength, and the statistics of the emitted x-ray determines the atoms species and concentration.[70] EDS is operated as an attachment of a TEM instrument like EELS.

The x-rays are converted into a voltage using a Si detector with a drifted Li to compensate for impurities. An incoming electron generates an electron-hole pair for every 3.76 eV of radiation. A bias voltage causes the holes and electrons to travel to opposite ends of the crystal. The charge from the bias is measured and converted to a voltage pulse, and the voltage pulse generated is related to the energy of the photon that was created and thus the atomic species in the sample.

3.4 Van Der Pauw

Widely used in the semiconductor industry, Van Der Pauw method is a technique for measuring the sheet resistance or resistivity. This method is different from the four-point probe, which only provides resistivity in the sensing direction. Van Der Pauw determines the resistivity of any arbitrary shape. The shape must be 2-D, so the film must be infinitesimally thin compared to the surface dimensions.[71] The typical schematic uses a square shape with four contact points total at each corner. Two contacts are connected to a current source while the other two contacts measure the voltage such that $R = \frac{V}{I}$.

Van der Pauw states there exists two characteristic resistances RA and RB which represent two source probe configurations in figure 3-6. These two resistances are related to the sheet

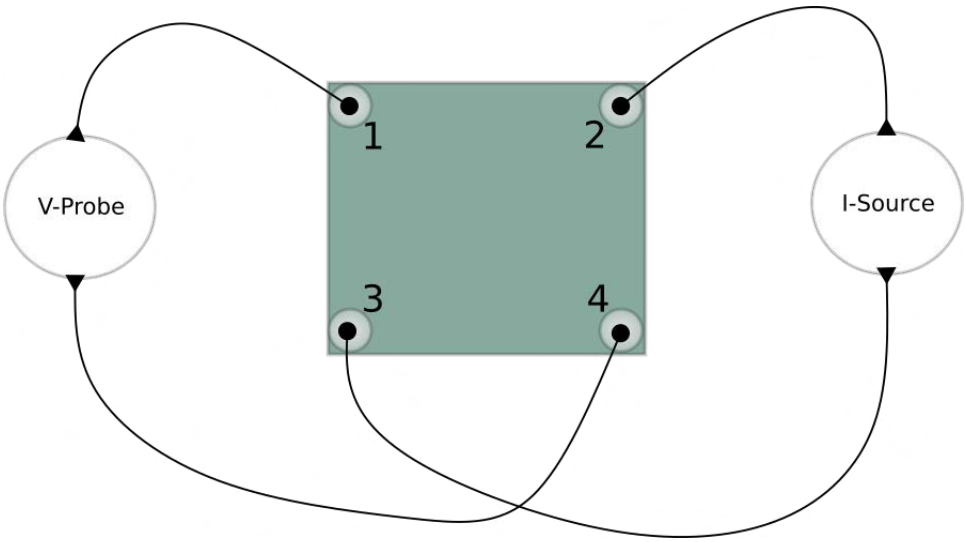

Figure 3-6. Schematic of the Van Der Paul layout on a sample for measurement. Two probes are the current source on the sample, while the other two are the voltage probes. The points one, two, three, and four alternates between probe and source.

resistance by the van der pauw equation.

$$exp\frac{-\pi R_A}{R_S} + exp\frac{-\pi R_B}{R_S} = 1 \tag{3-1}$$

The sheet resistance can be solved numerically then related to resistivity by $\rho = R_s\frac{A}{l}$. Where A represents the area of the surface, l represents the sample thickness, which is in the micrometer or nanometer regime. This equation was solved numerically in MATLAB using data from a semiconductor analyzer instrument.

3.5 High Resolution X-Ray Diffraction

The application of x-ray diffraction (XRD) is among the oldest characterization techniques of materials. If the structure of the material is unknown, Bragg's law can be applied to determine the structure. For this work, a Cu k source is used for exposing the sample while the x-ray angle between the source and sample is altered. The detector position is angle locked to the sample. The outputted data from the experiment is a function of source angle that is related to Bragg's law for determining lattice spacing (see fig. 3-7).

$$n\lambda = 2d\sin\theta \tag{3-2}$$

$$d = \frac{a}{\sqrt{h^2 + k^2 + l^2}} \tag{3-3}$$

Where n is the order of the interference, λ is the wavelength of the source, a is the lattice constant of the cubic structure, and h, k, and l represent the miller indices of the lattice plane. The interatomic spacing equation given above is for a simple cubic structure in eq. 3-3; for non-cubic systems, the interatomic lattice spacing may become increasingly complex.

High-resolution x-ray diffraction (HRXRD) utilizes x-ray optics for improving angle resolution down to the arcsecond regime. This resolution is necessary for measuring thin epitaxial films. HRXRD can measure structural and defect information such as composition, layer thickness, strain, surface damage, dislocation density, and inhomogeneity.[72] To achieve these measurements, X-ray optics are employed for collimation of the beam and remove deviation from the chosen wavelength. The most modern approach is to focus and collimate the beam in two different axes: One axis is collimated using parabolic mirror optics, taking advantage of total external reflection of X-rays. The other perpendicular axis of the X-ray will be focused using an ellipsoidal mirror. These subsequent optics are known as specular optics because the components take advantage of the total external reflection of X-ray beams. To improve spectral linewidth of the X-ray source, a monochromator is introduced which is a crystal comprised of material such as Si or Ge. The monochromator crystal disperses the spectral components of the crystal source enabling filtering of the desired wavelength.

HRXRD optics is especially crucial for the rocking curve (see fig. 8) for thin-film measurements. Rocking curve high-resolution x-ray spectroscopy (RC-HRXRD) enables the measurement of strain for thin epitaxial films at post-growth. RC-HRXRD is performed by keeping the source and detector centered on the sample, and the sample is tilted to perform a theta scan.

An important parameter for thin epitaxial films is strain at post growth; it varys with gas pressures and other conditions during growth For epitaxial thin films, the strain is biaxial being compressive or tensile perpendicular to the interface with the substrate. The strain is a value which deviates from the relaxed value of the crystal; therefore, the strain can be derived by the

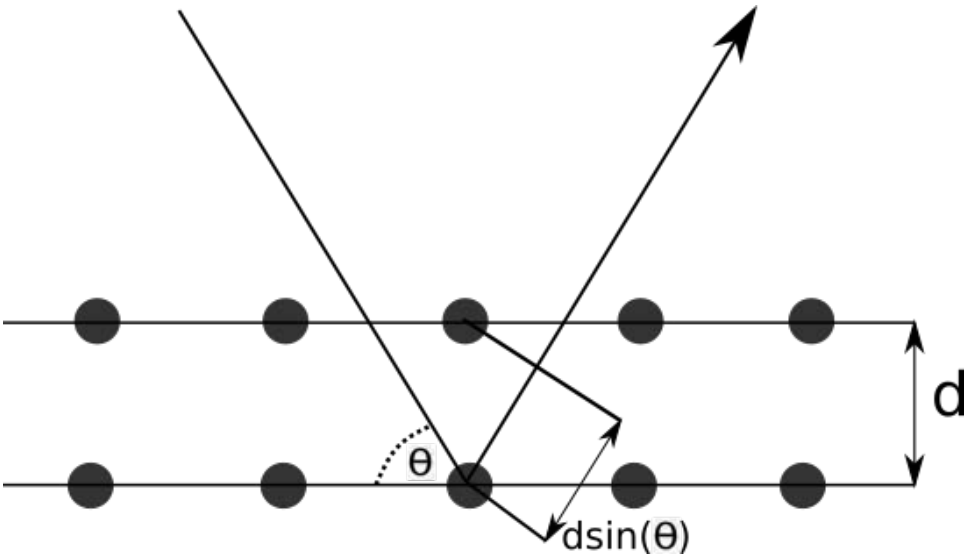

Figure 3-7. x-ray reflection inside the crystal will experience constructive interference with the x-ray reflected at the surface. The relationship of the interference is known as Bragg's Law, and it is observed as a peak in the XRD spectrum.

derivative form of Bragg's law.

$$\epsilon = -\cot\theta d\theta \tag{3-4}$$

ϵ represents the strain experienced by the thin film. Therefore, the location of the epitaxial layer peak on a 2θ plot measures strain. For films grown on Si, RC-HRXRD is performed on the (004) plane for a non-zero structure factor. The parallel substrate plane creates a sharp peak fo pure silicon at zero. The pseudomorphic film on the Si generates a broad secondary peak on the plot to the right. The position of the secondary peak is related to strain of the film. If the peak is at smaller angles, the film is compressively strained ($d\theta$ is positive), while a peak at greater angles relates to tension ($d\theta$ is negative).

3.6 Secondary Ion Mass Spectrometry

Secondary ion mass Spectrometry (SIMS) is the most versatile tool for semiconductor characterization. SIMS destructively removes material from the surface of a sample with some portion scattering at an angle. These scattered ions are collected with a mass spectrometer. A majority of the ions ejected are neutral and cannot be detected, but about 1% are charged. The mass-to-charge ratio of these ions is measured by the mass spectrometer.[71]

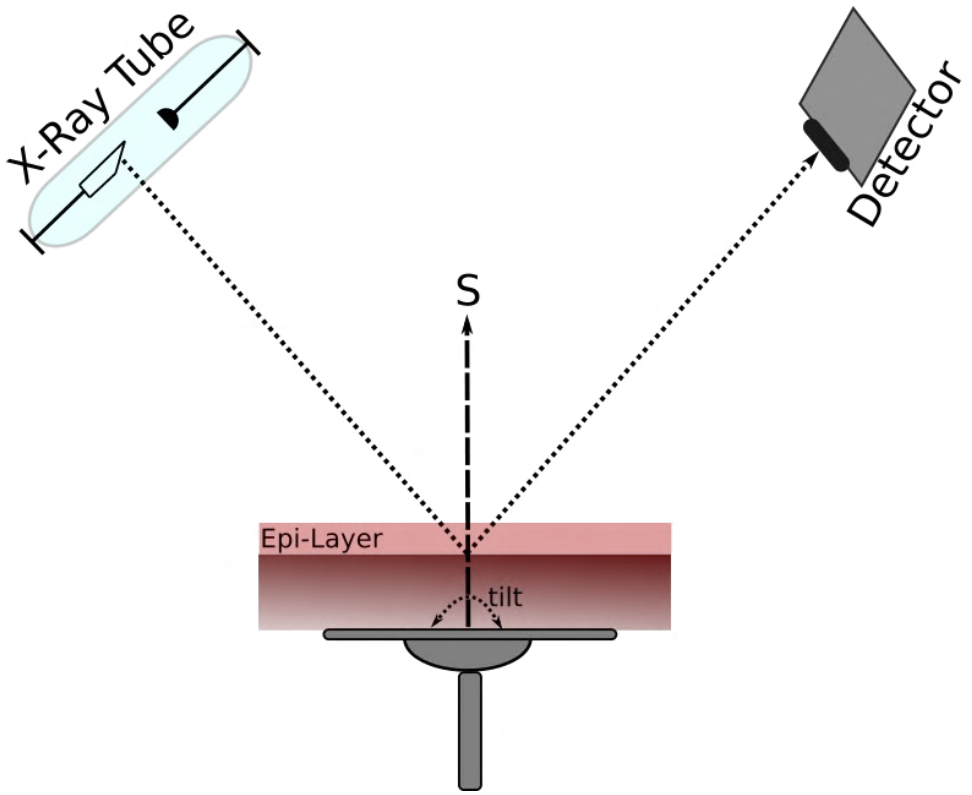

Figure 3-8. A simple illustration of RCXRD showing an X-ray tube as a source for the system and a detector containing a scintillator and photomultiplier tube. The detector and source remain stationary while the sample is tilted. This setup is known as a double-axis transverse scan.

The mass spectrometer consists of an electrostatic and a magnetic component. For the electrostatic component, parallel plates are placed at a potential V with the ions following a radius of curvature r_V. The potential across the plates only allows ions with specific energy to pass. For the magnetic component, the ions pass through a magnetic field B, which causes the ions to follow a radius of curvature r_B. The mass-to-charge ratio from the two components follows the equation.

$$\frac{m}{q} = \frac{B^2 r_B^2 d}{V r_v} \tag{3-5}$$

Where m is the mass of the ion, q is the charge of the ion, d is the distance of the parallel plates. The application for SIMS is dopant profiling. Sims can determine the atomic species present post-growth along with the concentration and depth profile. SIMS is useful for analyzing the diffusion behavior after anneals.

3.7 Rapid Thermal Annealing

Rapid thermal heating is the dominant technology since the 1980's for activating semiconductor dopants. By radiative block-body heating, rapid thermal annealing is a process developed to minimize the thermal budget by reducing the time at a given temperature. The original motivation of the technology was to reduce transient enhanced diffusion for improved control of the profile depth. Now, the applications have expanded to oxidation, silicidation, film densification, chemical vapor deposition, and epitaxial growth.

In this work, the system used is a AG associates Heatpulse 4100 capable of heating rates up to 200 °C/s and a maximum temperature of 1100°C. A thermocouples is sandwiched between two coupon silicon wafers which is connected to a proportional integrated derivative (PID) controller to determine temperature as a function of lamp power.

CHAPTER 4
STABILITY OF PSEUDOCUBIC III-V SEMICONDUCTORS

4.1 Background

The continuous decrease in contact area of semiconductor devices requires further increases in the doping of the semiconductors in order to mitigate the increase of contact resistance. New approaches are needed to provide high doping for lower contact resistance and high strain for improved carrier mobility.[2] Silicon doped with carbon and phosphorous (Si:CP) has been the material of choice, with the thin film providing tensile strain for electron mobility enhancement. However, because of the solubility limits in silicon, only a limited concentration of carbon and phosphorous dopants is possible using conventional epitaxial growth methods. At high dopant concentrations, the C and P compete for substitution sites causing two problems: the C is more likely to precipitate, and the P activation is limited by the C concentration. New methods of chemical vapor deposition (CVD) have enabled the growth of highly doped Si:P[73, 74] which provides a strain comparable to Si:CP. These methods may use low temperature, low pressure cyclic deposition etch processing, which commonly uses Si_3H_8, as the precursor or high temperature, high pressure co-flow processing which utilizes dichlorosilane ($Si_2Cl_2H_2$).[74] By employing this complex growth scheme it has been shown that phosphorus can be introduced at concentrations up to 10% with no visible signs of extended defects.[11, 22, 75] A record low contact resistance has been achieved with this material via the use of a post growth anneal.[75] While, the origin of the strain and the positions of the phosphorus in the lattice have not been firmly established, the presence of a dispersed non-equilibrium Si:P phase was suggested in earlier works.[11]

Evidence for the presence of such pseudocubic Si_3P_4 phases has only appeared recently. Ye et al. analyzed CVD grown highly doped (HD) Si:P with Rocking Curve High Resolution X-ray Diffraction (RC HRXRD).[11, 22, 76] They concluded that the observed strain arose from phosphorus atoms clustered locally into pseudocubic Si_3P_4 complexes. Based on Hall effect and TEM data, Weinrich concluded that HD Si:P contained substitutional phosphorous,

clusters of phosphorous vacancies, and clusters of phosphorus interstitials clusters (PIC's).[18, 23] Dhayalan et al. inferred the existence of a Si monovacancy surrounded by phosphorus from positron annihilation spectroscopy showing an excess of vacancies. However, they also concluded that the observed strain does not require the presence of Si_3P_4 complexes, but can be explained by phosphorous doping alone.[19, 20] Although others have found that the Si_3P_4 complexes is necessary to explain the strain.[18]

Density Functional Theory (DFT) studies of pseudocubic form of Si_3P_4, have shown it to have a negative enthalpy of formation.[77] Based on these calculations and the HRXRD results, these clusters have been proposed as the mechanism of accommodation of the excess phosphorus.[22] These DFT studies also examined Si_3As_4, Ge_3As_4, and Ge_3P_4, and also showed they too have negative enthalpies of formation.[77] In a single unit cell of silicon, this phase can be viewed as a cluster of four phosphorus atoms around a vacancy, or a Si_3P_4 defect. DFT calculations show that the Si_3P_4 defect is stable at high phosphorous concentrations. [78, 79] Previous studies have not explored the possibility of Si_3P_4 growing epitaxially as a submicroscopic ordered phase; that is a phase on the length scale below that resolvable by TEM. This chapter, therefore, analyzes the thermodynamic stability of these defective zinc blende structures with respect to the known phases by constructing free-energy convex hulls[21, 80–83] of the binary systems. In addition, the effect of epitaxial strain from the Si and Ge substrates and volumetric strain on the extended phases is also studied.

4.2 Computational Methods

The DFT calculations use the plane-wave method as implemented in Vienna Ab initio Simulation Package (VASP). The Generalized Gradient Approximation (GGA) is used for the exchange-correlation effects.[24–27] Pseudopotentials are described by the projector augmented wave (PAW) method.[24–27] A supercell of 2x2x2 conventional unit cells is used for convex hull calculations. A 3x3x3 Monkhorst-Pack k-points mesh is used for the Brillouin zone sampling. The converged plane wave cutoff energies are 310 eV, 290 eV, 300 eV, and 350 eV for Si_3P_4, Si_3As_4, Ge_3P_4, and Ge_3As_4, respectively. For unconstrained bulk calculations, the cell

parameters and atomic positions are relaxed simultaneously until the force on each atom is less than 0.01 eV/Å, and the components of stress are less than 0.02 GPa.

The thermodynamic properties of pseudocubic Si_3P_4 was calculated using the Phonopy package.[47] The GGA potential was exclusively used due to close agreement of GGA and SCAN for mechanical properties. The phonon band structures are calculated using the Non-Analytical Correction (NAC) and Debye model. For the Quasi-Harmonic Approximation, density-functional perturbation theory (DFPT) with a supercell approach of 2x2x2 was performed in VASP. The lattice constants for volume change was chosen within 1% of compression and expansion. QHA is valid up to 2/3 the melting temperature; however, the melting temperature of these pseudocubic materials is unknown, so a temperature cutoff of 800 K was chosen based on the Si-P equilibrium diagram.

To mimic the strain effect of epitaxial growth, A supercell for each phase was chosen such that the lattice would be commensurate with the substrate material. The supercell lattice in the a, b directions (i.e. normal to the growth direction) are set to those of Si or Ge. The cell parameters are relaxed in the direction normal to the epitaxial plane (c-direction) only, and the atomic positions are relaxed to the same force limit. In order to consider a precipitate, the supercell is again made commensurate with the substrate material, and the supercell lattice parameters in all three directions are fixed to those of the Si or Ge matrix in which it is embedded, and only atomic relaxations are allowed. In all calculations, the atom positions are optimized such that the force on every atom is small. The interface between the substrate and phases are not included in the calculations. The d-orbital electrons are included in the Ge potential.[84]

4.3 Epitaxial Stability of Pseudocubic III-V Semiconductors

As Figure 4-1 shows, The Si_3P_4 structure is like the zincblende structure but with the atom at the center of one face absent; we designate this plane as (100). This means that from a crystallographic point of view the structure is tetragonal. However, the three lattice constants for the Si_3P_4 phase are essentially the same (a=b=5.0929 Å, c=5.0928 Å); that is,

the structure can be considered as pseudocubic. The near equality of the lattice parameters arises from the atomic relaxation of the P atoms. These calculated lattice constants are consistent with the film strain determined from RC HRXRD.[11, 74]

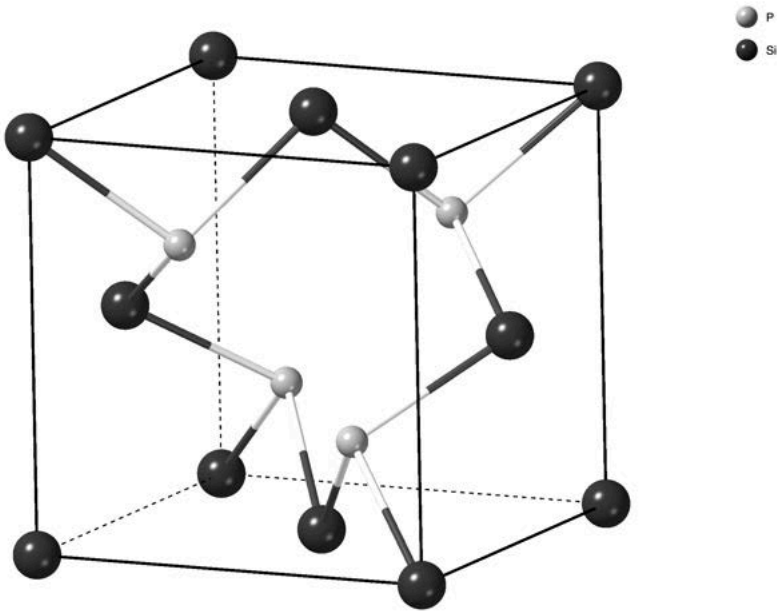

Figure 4-1. Structure of pseudocubic Si_3P_4 is a defective zinc blende structure; note the absence of Si atoms (black) on the front and back faces of the cube. The P atoms (Gray) are in the interior of the unit cell.

Other compositions are also present in the Si-P binary system. In particular, the stable SiP and SiP_2 phases have been studied experimentally; microscopy has found them to be orthorhombic in silicon films.[85, 86] From solid reaction and ion implantation studies, the SiP and SiP_2 form as precipitates in Si films at high P concentrations. Though SiP and SiP_2 precipitate at high P concentrations, HD Si:P layers are grown far from equilibrium at low temperatures (400°C-500°C)[11, 22] well below the much higher temperatures where the equilibrium SiP and SiP_2 phases are typically observed (900°C-1400°C).[21, 80, 81] These compositions form the convex hull of this work, so they provide reference for the stability of Si_3P_4. The pseudocubic Si_3P_4 structure has not been observed experimentally in TEM. However, its structure is similar to that of silicon, so it would not be expected to be visible

using high resolution or high angular dark field STEM microscopy. The only indications for the existence of a Si_3P_4 material are the earlier DFT calculations.[11, 87]

The energy of the Si:P system as a function of composition is shown in Figure 2(a). The red squares are the data for the stress-free system; the red line is the associated convex hull. This shows that the SiP and SiP_2 phases are stable. The Si_3P_4 pseudocubic structure lies 45 meV above the convex hull. Based on the analysis of a 29,902 inorganic materials. Sun et al. identified 70 meV as being an upper limit for metastability for most materials.[88] That is, if a structure lies more than 70 meV above the convex hull it is likely to decompose; if it lies less than 70 meV above the convex hull there is some chance that it will be metastable, most particularly if the metastable phase was actually the stable phase at some point in the processing history of the structure. Thus, though energetically disfavored to decomposition relative to the SiP and SiP_2 phases, the Si_3P_4 might show metastability.

For epitaxy on a Si substrate (open green symbols and green line), there is only a small increase in energy for the SiP and SiP_2 phases, but a larger increase in energy for Si_3P_4. It now lies 101 meV above the convex hull; based on the analysis of Sun et al., it is likely to be unstable relative to SiP and SiP_2. The germanium substrate (open blue) has a larger effect on the stability. In particular, while SiP_2 remains stable, SiP is only marginally stable, lying essentially on the line between Si and SiP_2. Epitaxy on Ge further increases Si_3P_4 above the convex hull (198 meV), increasing its driving force to decomposition. The corresponding precipitate cases show that SiP and SiP_2 are again stable for a Si matrix, while only SiP is stable for the germanium matrix. Thus, for all cases considered, the energy of Si_3P_4 is above the convex hull (169 meV for the Si matrix and 602 meV for the Ge matrix) and it can be expected to decompose under these conditions. We thus conclude that strain does not stabilize the Si_3P_4 pseudocubic phase.

Although they have not been explored experimentally, it is of interest to characterize the corresponding energetics for the Si:As, Ge:P and Ge:As systems. Figure 2(b) illustrates the stability for the Si:As system. The convex hull for Si:As is similar to that of Si:P for the bulk.

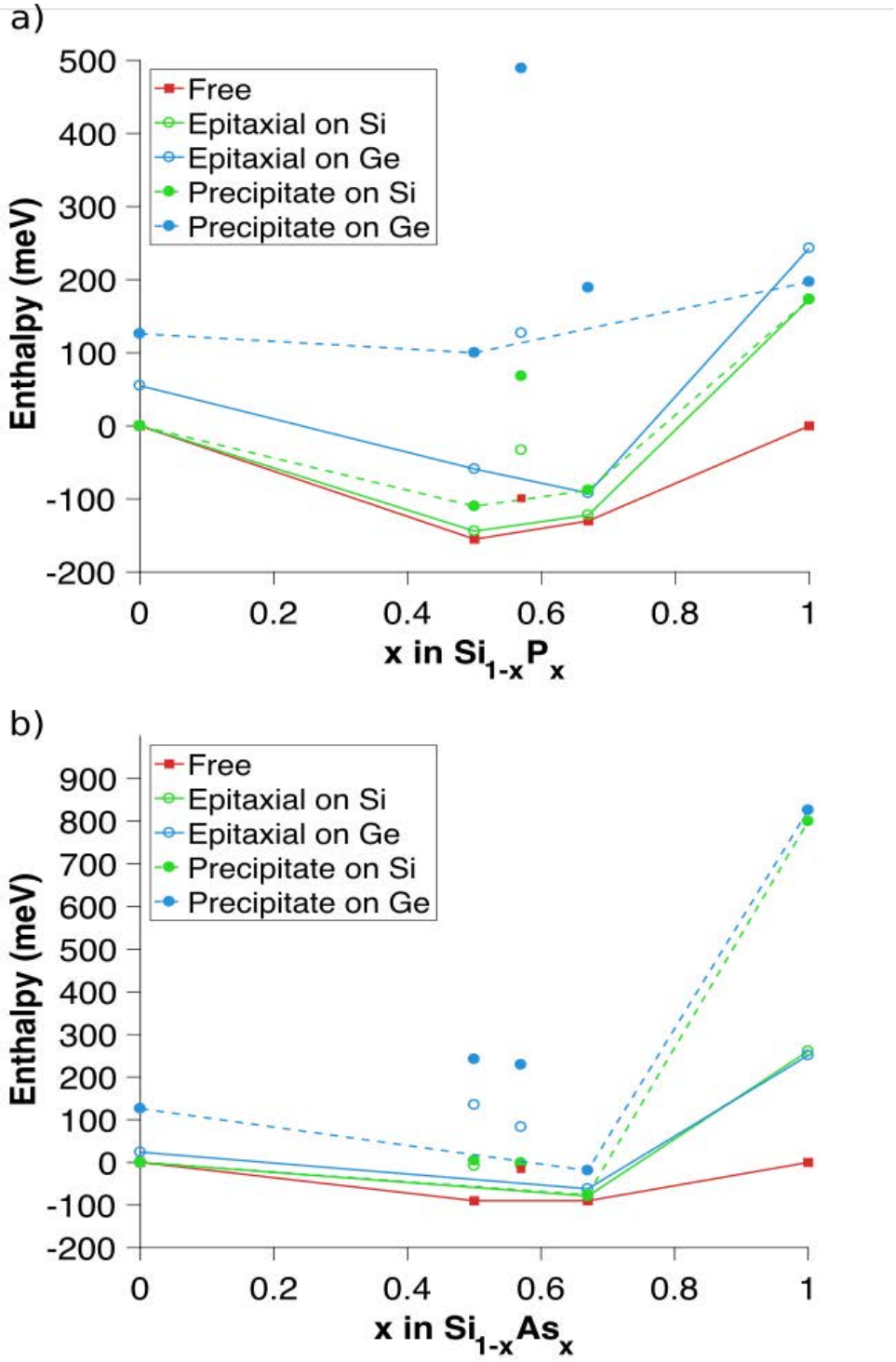

Figure 4-2. Stabilty of Six, Si_3x_4, Six_2 in the bulk (red squares), on a Si sustrate (green circles) and on Ge substrate (blue circles) for (a) Si:P (i.e., x=P), (b) Si:As (i.e., x=As). For the epitaxial case, a hollow circle is used, and a filled circle for the precipitate case. Note that the energy scales are not all the same.

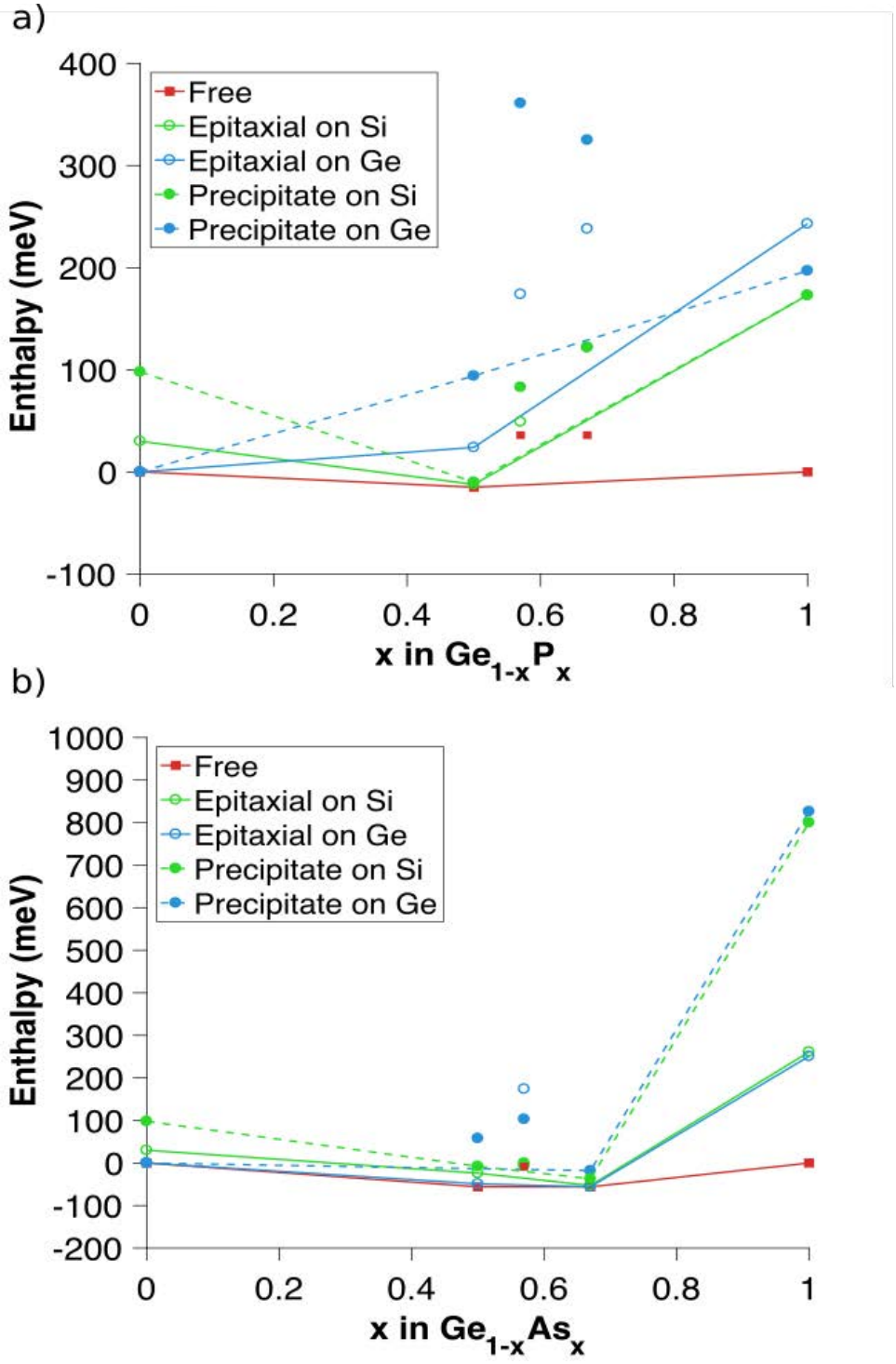

Figure 4-3. Stabilty of Gex, Ge_3x_4, Gex_2 in the bulk (red squares), on a Si sustrate (green circles) and on Ge substrate (blue circles) for (a) Ge:P (i.e., x=P), (b) Ge:As (i.e., x=As). For the epitaxial case, a hollow circle is used, and a filled circle for the precipitate case. Note that the energy scales are not all the same.

For the unstrained system, as for the Si:P system, the SiAs and $SiAs_2$ are stable, with Si_3As_4 lying 74 meV above the convex hull. For epitaxy on a Si substrate, only the $SiAs_2$ phase is stable. $SiAs_2$ remains stable as a precipitate in Si and is marginally stable as a precipitate in Ge. Interestingly for both epitaxial and volumetric strain, the Si_3As_4 is closer to the convex hull (62 and 66 meV respectively). These are close to the limit of metastability, so it is possible, though unlikely, that they could be present. For epitaxial and volumetric strain in Ge, the Si_3As_4 is 180 and 227 meV above the convex hull respectively and thus is predicted to be unstable.

Previous computational work on the GeP phase was not found, so the SiP structure was used as a prototype, and the lattice constants for GeP are comparable to the XRD data of Wadsten et al.[82] The GeP_2 phase was constructed based on previous computational work which found the tetragonal phase to be the most stable structure.[89] The bulk Ge:P system shows a stable GeP phase with a small formation energy and unstable GeP_2 and Ge_3P_4 phases. The Ge_3P_4 phase lies 48 meV above the convex hull and thus might be metastable. All of the strain conditions on a Si substrate stabilize the GeP phase relative to the stress-free condition. The epitaxial strain on Si increases the energy of the Ge_3P_4 to 63 meV above the convex hull, while the volumetric strain increases it further to 97 meV. The epitaxial strain from a Ge substrate increases the metastability of Ge_3P_4 to 119 meV, but this is reduced to 66 meV under volumetric strain.

Finally, in the absence of strain, GeAs and $GeAs_2$ are very weakly stable, Ge_3As_4 lies 48 meV above the convex hull. The energy of $GeAs_2$ is only weakly affected by the strain and remains stable for both epitaxial and precipitate conditions. For silicon epitaxy, GeAs lies just above the convex hull, while it is marginally stable as a precipitate in Si. Most interestingly, the effect of a Si substrate changes energies in such a way that the Ge_3As_4 lies 20 meV above the convex hull for both epitaxial and volumetric strain conditions. It is thus possible that metastable Ge_3As_4 could be present.

4.4 Thermodynamics of Pseudocubic III-V Semiconductors

This section focuses on the thermodynamic properties of the pseudocubic in the bulk cases. As these materials have not been successfully grown as bulk crystal, the thermodynamic results of this section are computational predictions. In the case of HD Si:As and Si:P films, These phases may only form dispersed complexes, but knowledge of the behavior of bulk material may be expanded for predictions of the behavior of the films. Though the lattice and electronic structures have been well studied computationally, Thermodynamic properties have been neglected in previous works, and this section fills in this gap with computational methods.

Before the epitaxial or bulk cases could be explored, it is necessary to establish a baseline: first, the structure must be calculated such that it matches with previous works. The mechanical properties of Table 4-1 were found to be in close agreement with most previous works.

Material	Lattice Constant (Å)	Bulk Modulus (GPa)
Si_3P_4	5.01 5.091[77] 5.027[90]	69.63 69.60[90]
Si_3As_4	5.37 5.38[77] 5.36[90] 5.37[91]	57.62 59.7[77]
Ge_3P_4	5.236 5.264[77]	72.56 54.5[77]
Ge_3As_4	5.531 5.523[77] 5.327[90] 5.499[91] 5.116[92]	60.34 46.3[77] 58.77[90] 59.58[91]

Table 4-1. The relaxed lattice constants for the semiconductor pseudocubic study.

The bulk modulus was calculated by fitting the Murnaghan equation of state equation to the data, which relates the internal energy of the lattice with physical parameters such as bulk modulus.[93] The bulk modulus fit is an essential first step for showing the fidelity of this work. Figure 4-4 was generated by expanding and contracting the volume of the pseudocubic unit cell up to 1%. The parabolic shape of the data shows a well-converged setup for the calculations.

The phonon bandstructure provides support for the dynamical stability of the phase. A crystal is stable if the potential energy increases with atomic displacements. A negative eigenvalue represents an instability of the crystal structure, so a simulated displacement does not have an associated restoring force on the atom. A negative eigenvalue may also indicate a phase change, so phonon stability was checked at each volume change for QHA

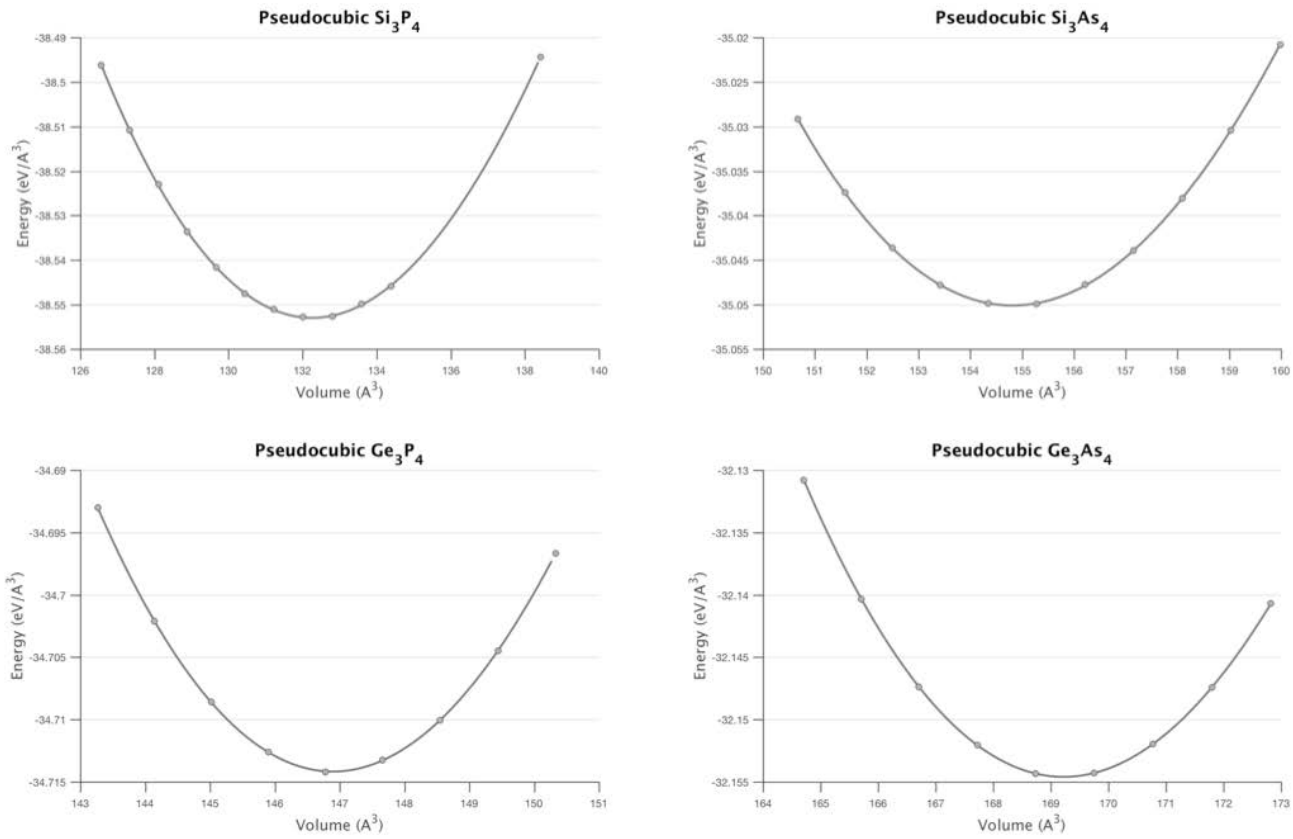

Figure 4-4. The Murnaghan state variable fit to total energy data shows convergence for system.

calculations. Like defect calculations, the supercell used for thermodynamical calculations must be converged. The convergence of the supercell was based on the Debye temperature for pure Silicon and Germanium, so the phase is considered to converge when a supercell increase shows little change of the Debye temperature; The supercell used for bulk calculations was 2x2x2. The high symmetry points chosen were for an FCC lattice.[94]

The dissimilar masses, 74.92 u for arsenic and 30.96 for phosphorus, have a wide gap between the acoustic and optical modes. The similar masses do not show this splitting, so the phonon bandstructure calculations at equilibrium were performed with the non-analytical correction (NAC). Except for the silicon arsenide, a splitting of the transversal and longitudinal optical modes occur at the gamma symmetry point.

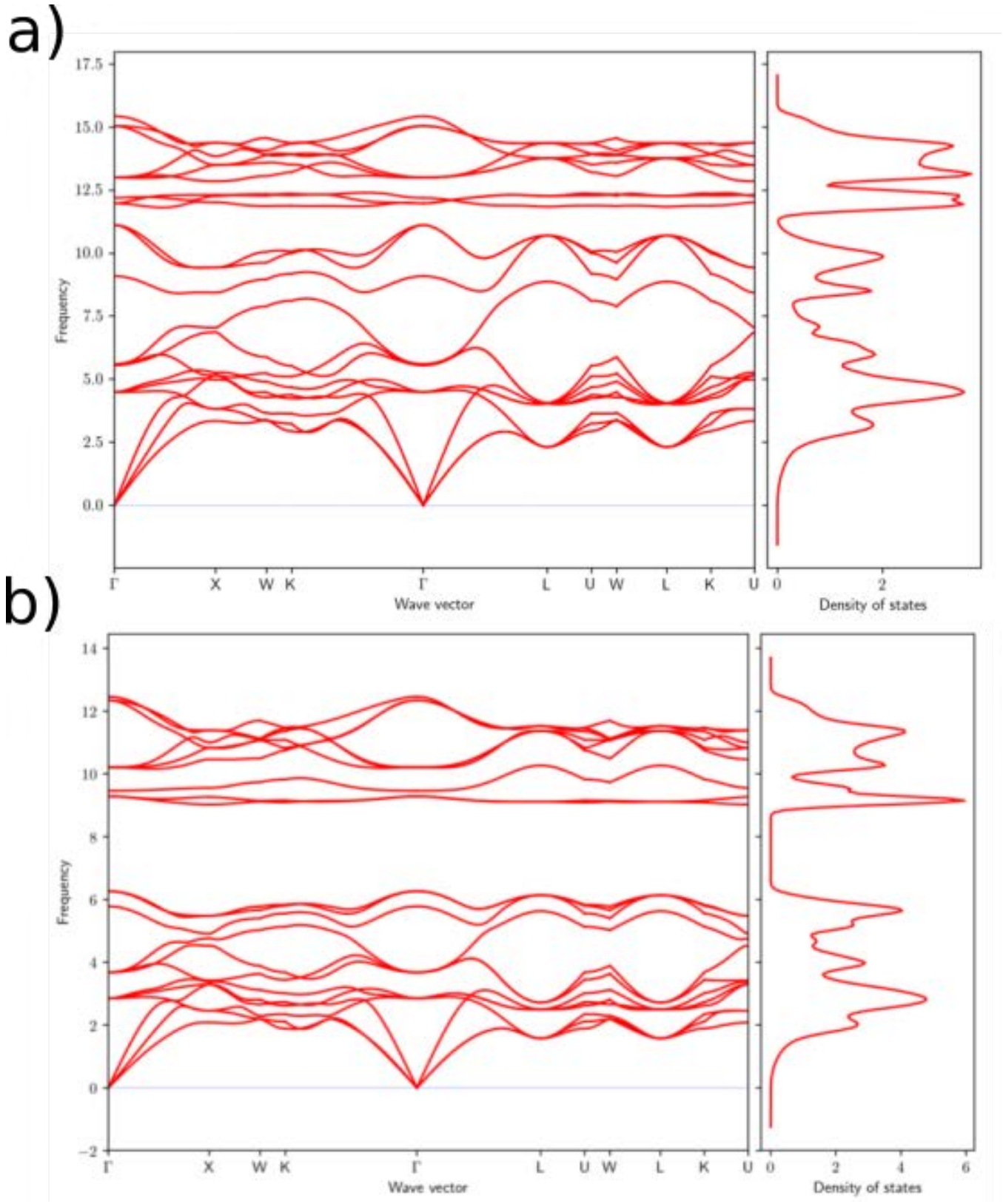

Figure 4-5. Phonon bandstructure and density of states for Si_3P_4 (a) and Si_3As_4 (b).

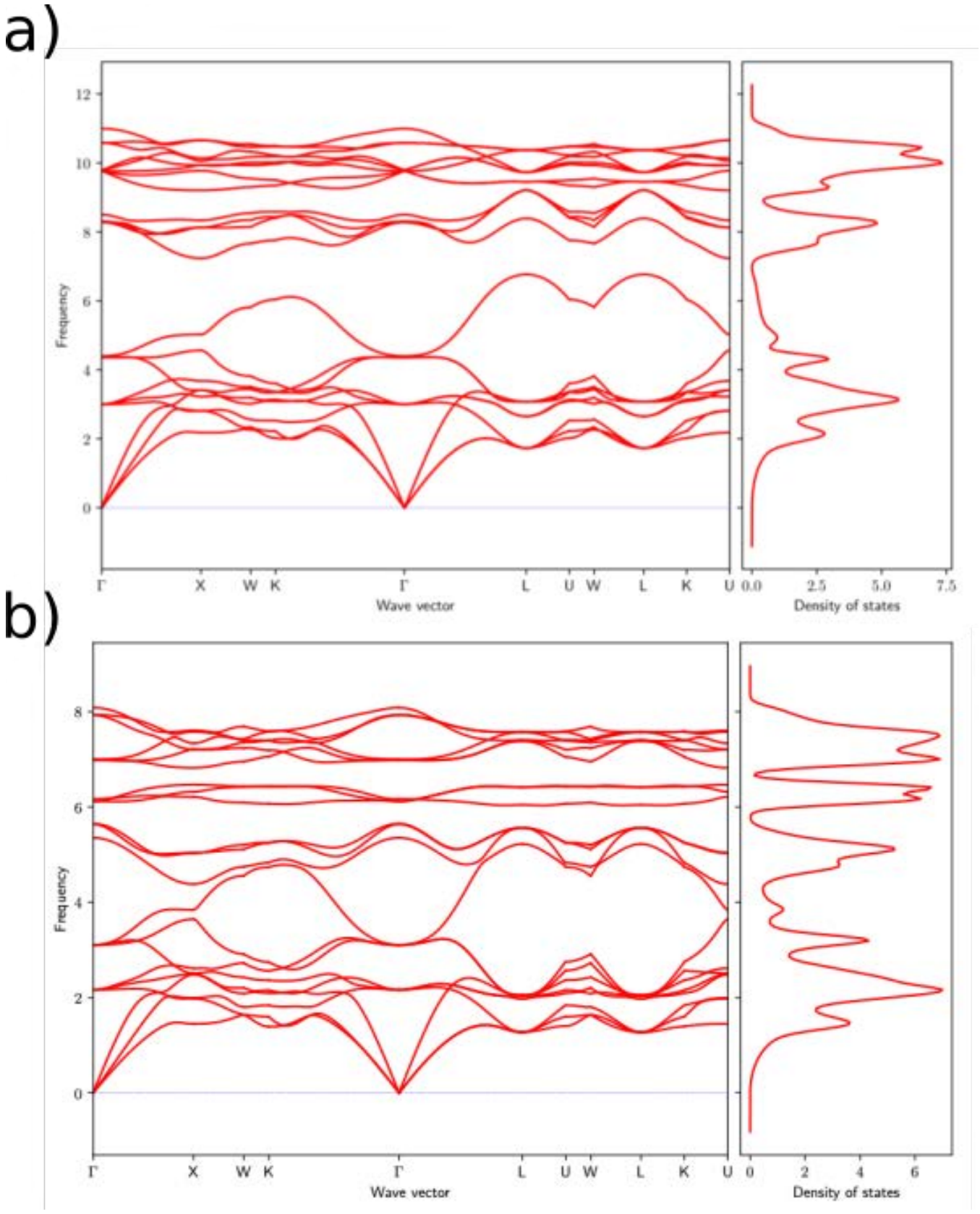

Figure 4-6. Phonon bandstructure and density of states for Ge_3P_4 (a) and Ge_3As_4 (b).

From the phonon DOS calculations, the lower phonon frequencies are fit to the Debye model up to ¼ the maximum phonon frequency. The fitted function is parabolic parabolic function, $D(\gamma) = a\gamma^2$, when $a = \frac{6\pi^2 N \frac{1}{3}}{V}$ is the fitted variable representing Debye frequency. The Debye temperature is is the temperature of a crystals' highest order mode. It's a routinely measured quantity for experimentalists due to its direct relationship with properties such as specific heat, and lattice enthalpy.[43] The calculation of Debye temperature for the pseudocubic structure is relevant for Debye-Waller factors. These calculations are essential for introducing phonon scattering of electrons for EXELFS simulation.[95]

Figure 4-7 shows the calculation of Debye temperature with the corresponding cohesive energy of the crystal. Debye temperature is a rough measure of bond strength of a material, so the cohesive energy of the crystal was calculated for self-consistency. The cohesive energy calculated is accurate for low temperatures near 0 K. Therefore, Eq. 4-1 represents the energy necessary to separate a crystal into basic atomic parts. Its the total energy of the lattice structure divided by the total number of atoms. Each atomic component, represented as i, is isolated in a vacuum. DFT is used to calculate the total energy of the isolated atom with the spin-polarized correction by Vosko, Wilk and Nusair scheme.[39]

$$E^{coh} = \frac{E_{tot}}{N} - \sum E_i(r \longrightarrow \infty) \tag{4-1}$$

The Germanium and Silicon crystal calculations was compared with experimental data, so the fidelity of the work is supported.[43] With consideration of the pseudocubic phases, a pattern of reducing cohesive energy with Debye temperature is observed. The larger atoms increase the stress on the FCC lattice bonds, which corresponds with decreasing cohesive energy and Debye temperature.

From Fig. 4-7, The bonding between the Ge-P atoms is stronger than the Ge-As, but the enthalpy of formation of these phases shows Ge_3P_4 to be unstable above the 0 eV line. The reason is associated with the elastic stress energy for the formation from reference phases.

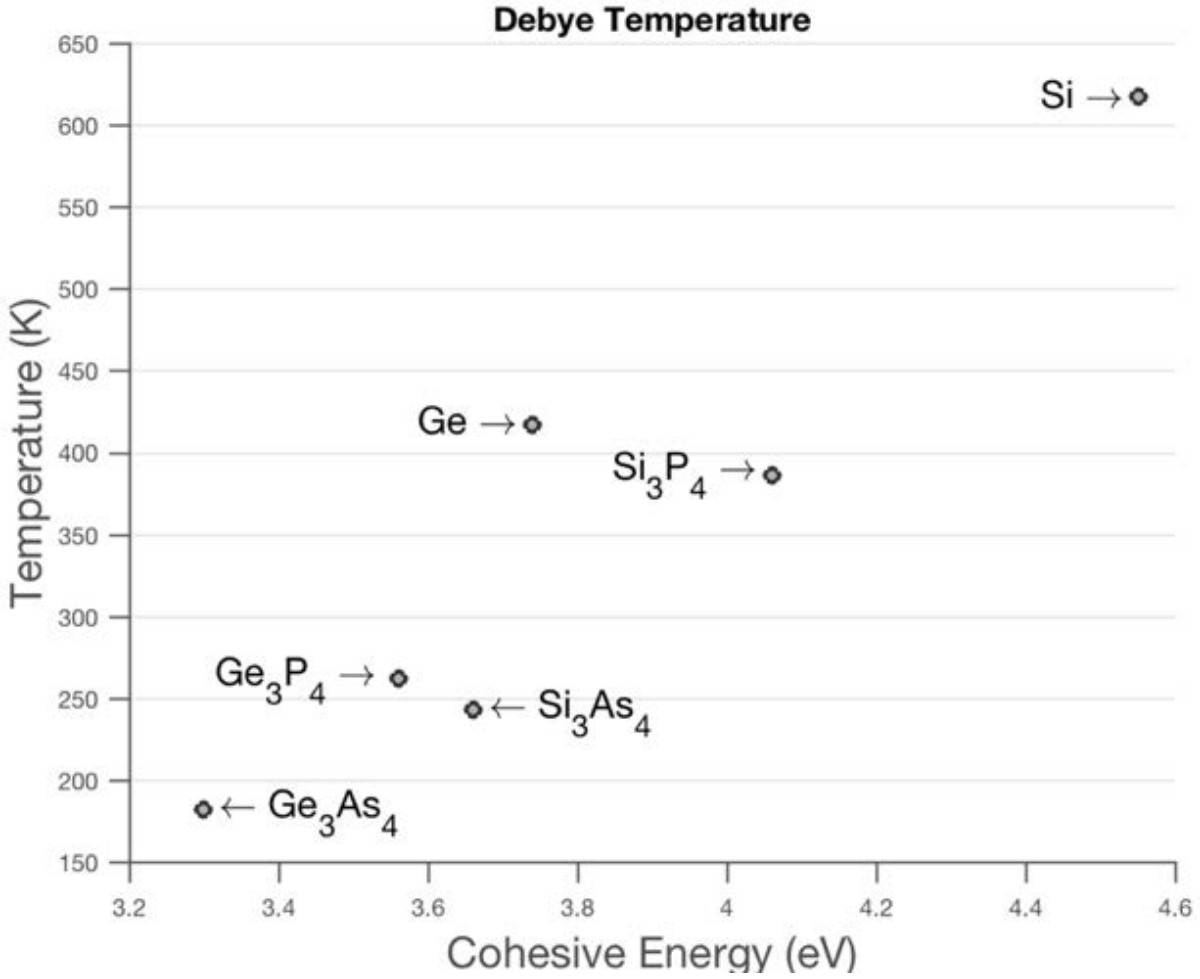

Figure 4-7. The Debye temperature plotted with the cohesive energy of the pseudocubic phases. The calculated cohesive energies are positive for comparison with experimental data.

The enthalpy of formation can be broken into two terms, $\Delta H = \Delta E_{chem} + \Delta E_{microstructure}$, the first term being the internal bonding energy of the lattice while the second term represent energy from the change of angle and distance of bonds from the pure phase components. The enthalpy from the bonding does not overcome the microstructural stress of the phase. The weaker bonds for the pseudocubic show a thermal expansion similar to a metal. This behavior is not a surprise due to its low Debye temperature. The thermal conductivity was calculated using QHA, and it provides a self-consistency check. The Debye temperature provides a point when specific heat converges to the Dulong-Petite limit.

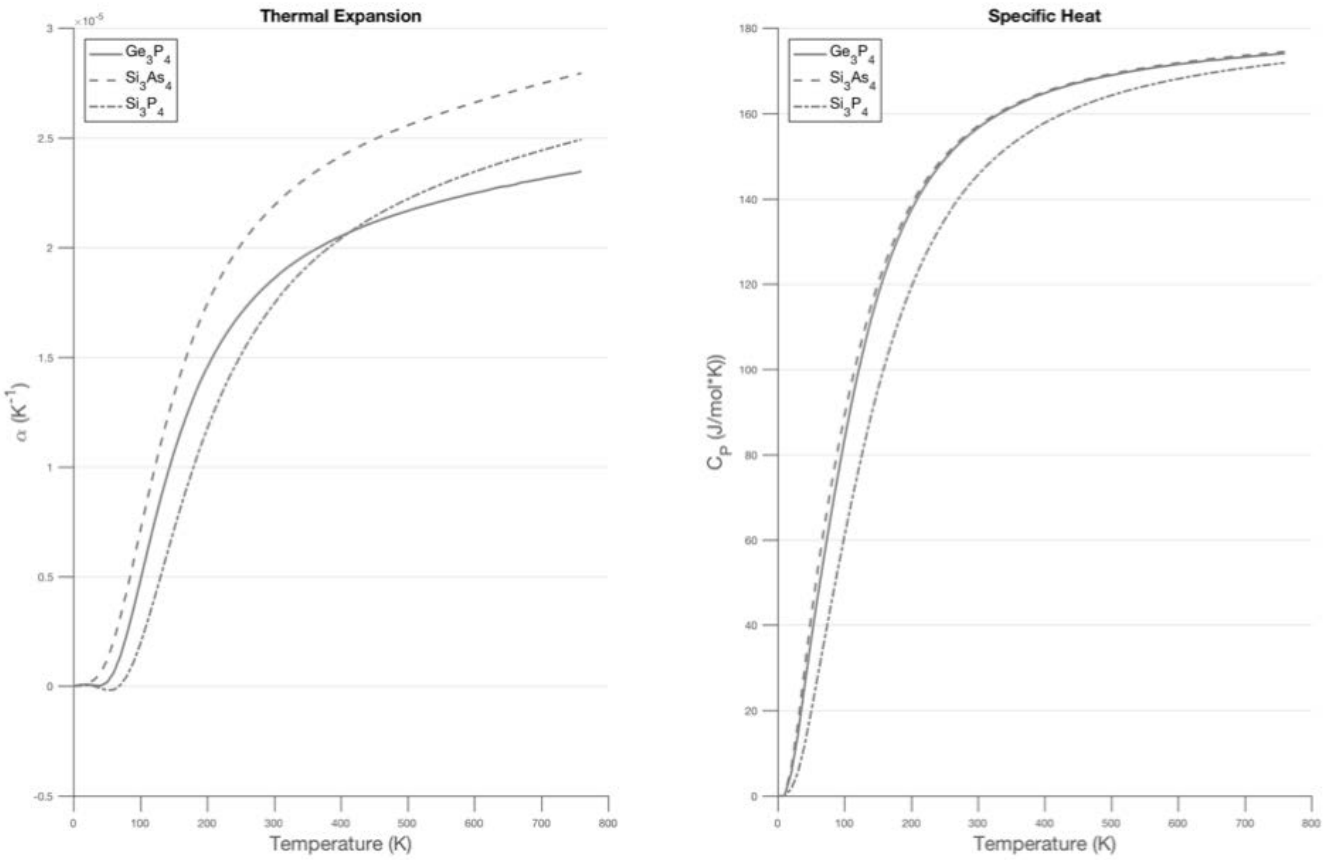

Figure 4-8. The thermal expansion and specific heat calculated from the quasiharmonic approximation. The specific heat (right panel) shows the self-consistency of the equations; the inflection point before the Dulong-Petite limit matching the calculated Debye Temperatures. The thermal expansion of the pseudocubics is more metallic, which is cause by the weak bonds of the pseudocubics.

4.5 Discussion

Overall, A_3B_4 (A=Si, Ge; B= P, As) stoichiometries are not predicted to be thermodynamically stable either in bulk or under epitaxial or volumetric strain in either Ge or Si. However, the metastability, as measured by the distance above the convex hull, is small enough in some cases that their manifestation under some processing conditions cannot be ruled out.

This work shows that an extended ordered phase of Si_3P_4 is not thermodynamically favored. The stability decreases with epitaxial and volumetric strain, such that the ordered pseudocubic phase has a thermodynamic driving force for decomposition. No precipitates

or extended defects are observed with microscopy techniques; Therefore, the experimentally observed strain does not appear to be associated with lattice mixing between submicroscopic Si_3P_4 and silicon, but rather the formation of a concentration of randomly dispersed Si_3P_4 complexes. This scenario is likely to play out in the Si:As, Ge:P and Ge:As systems also. Consistent with this conclusion EXAFS experiments have concluded the existence of As_4V defects in Si:As at temperatures below 750°C.[96] Positron annihilation spectroscopy has also concluded the existence of vacancy centered arsenic defects post-growth.[97]

HD Ge:As films have not yet been grown. However, Milazzo et al. ion implanted Ge wafers with arsenic above the solubility limit; these wafers were then laser annealed to achieve a similar highly doped Ge:As film on a Ge wafer.[98, 99] Their RC HRXRD work found an epitaxial compressive strain layer. Based on our lattice calculations, a tensile strain is expected for a Ge substrate, and the pseudocubic Ge_3As_4 enthalpy of formation is above 0 eV for all cases. We therefore conclude that a defect complex other than Ge_3AS_4 must be causing the compressive strain of the film.[98, 99] Highly doped Ge:P film has not been grown on Si or Ge. However, this work does not predict a pseudocubic phase will form.

The silicide is vulnerable to stress in post-annealing steps. These pseudocubic phases provide a high strain for the industry but shows a high thermal expansion behavior. This work predicts a potential processing challenge for the implementation of these films. Contact between these films and a silicide induces cracking of the silicide in the post process. These defects generate an increase of contact resistance beyond tolerance. The predicted material behavior of these films poses a challenge for the semiconductor industry. A mechanical stability problem does introduce process challenges to devices, so these films are grown with the thermal expansion behavior in mind. For example, silicides reduced contact resistance, but silicides are vulnerable to stress in post-annealing steps with thermal expansion mismatch.[100] These pseudocubic phases exhibit metallic like thermal expansion, so this works predicts a potential processing challenge for the implementation of these films. Based on these

calculations, contact between these films and a silicide will generate defects at the silicide interface. These mechanical stresses alter the electrical characteristics of a silicide.[101]

4.6 Chapter Summary

In conclusion, DFT calculations have shown that submicroscopic pseudocubic phases of Si:P, Si:As, Ge:P and Ge:As are not thermodynamically stable as epitaxial films on or as precipitates in Si or Ge. It is possible, though unlikely, that the ordered pseudocubic phase of Si_3P_4 could be metastable under Si epitaxial conditions. It is also predicted that the submicroscopic pseudocubic Ge_3As_4 and Ge_3P_4 phases are not energetically favorable in the bulk unstrained case. If these films were experimentally grown under strained conditions, an ordered submicroscopic pseudocubic phase is also not predicted to form. For the first time, the GeP phase was found to be stable, and the lattice constants within agreement of XRD experiments. However, the GeP_2 tetragonal phase was not found to be stable in the bulk calculations, and the Ge:P system was not found to have any stable phases for epitaxial systems.

CHAPTER 5
STEM MODE EELS OF HIGHLY DOPED SI:P FILMS

5.1 Background

Chapter 4 showed the pseudocubic phases Si_3As_4, Si_3P_4, Ge_3P_4, and Ge_3As_4 are unstable as submicroscopic nanophases. Therefore, subsequent studies need to study the films from a defect clustering perspective. There are three primary types of clusters: interstitial, vacancy, and substitutional clusters as well as the definition of a Si_3P_4 nanophase(see Fig. 5-1). Recent computational and experimental studies have investigated the existence of these clusters in highly doped (HD) Si:P films and to some extent in HD Si:As films.[18, 78, 79, 97] Simulation supports the formation of P_4V as the stable cluster.[19, 20] Although simulation does not support the epitaxial Si_3P_4 nanophase (ie the clustering of P_4V clusters), an experimental determination would still be valuable. As defined in chapter 4, the submicroscopic nanophase is below the resolution limit of a TEM. Figure 5-2 shows an artistic representation of the P_4V defect in a Si supercell, and a subsequent illustration of the Si_3P_4 submicroscopic nanophase, which is a clustering of P_4V defects. This chapter will focus on a single experimental approach that attempts to detect a submicroscopic nanophase or a defect cluster in HD Si:P films.

The substitution or vacancy cluster defects (of P and As on a Si lattice site) are present as the nearest neighbor to Si or a vacancy at the center of the sublattice. The substitution defect clusters are deactivated due to the proximity of the dopants, so the dopants comprising the cluster do not contribute electrons. The vacancy defect clusters look similar to the substitution clusters, but the dopant atoms cluster around a vacancy site (V_{Si}), and these defects are also not electrically activated.

As mentioned in chapter 4, high through put DFT calculations have ascertained the binding and formation energies of an assortment of pure and mixed P and As clusters.[78, 79] The calculations of Sahli et al. reference with isolated defects of vacancy or dopants within a Si supercell. The idea of these reference energies was to compare the point defects of P, As, vacancies, and interstitial preference for being isolated or clustered. This reference is different

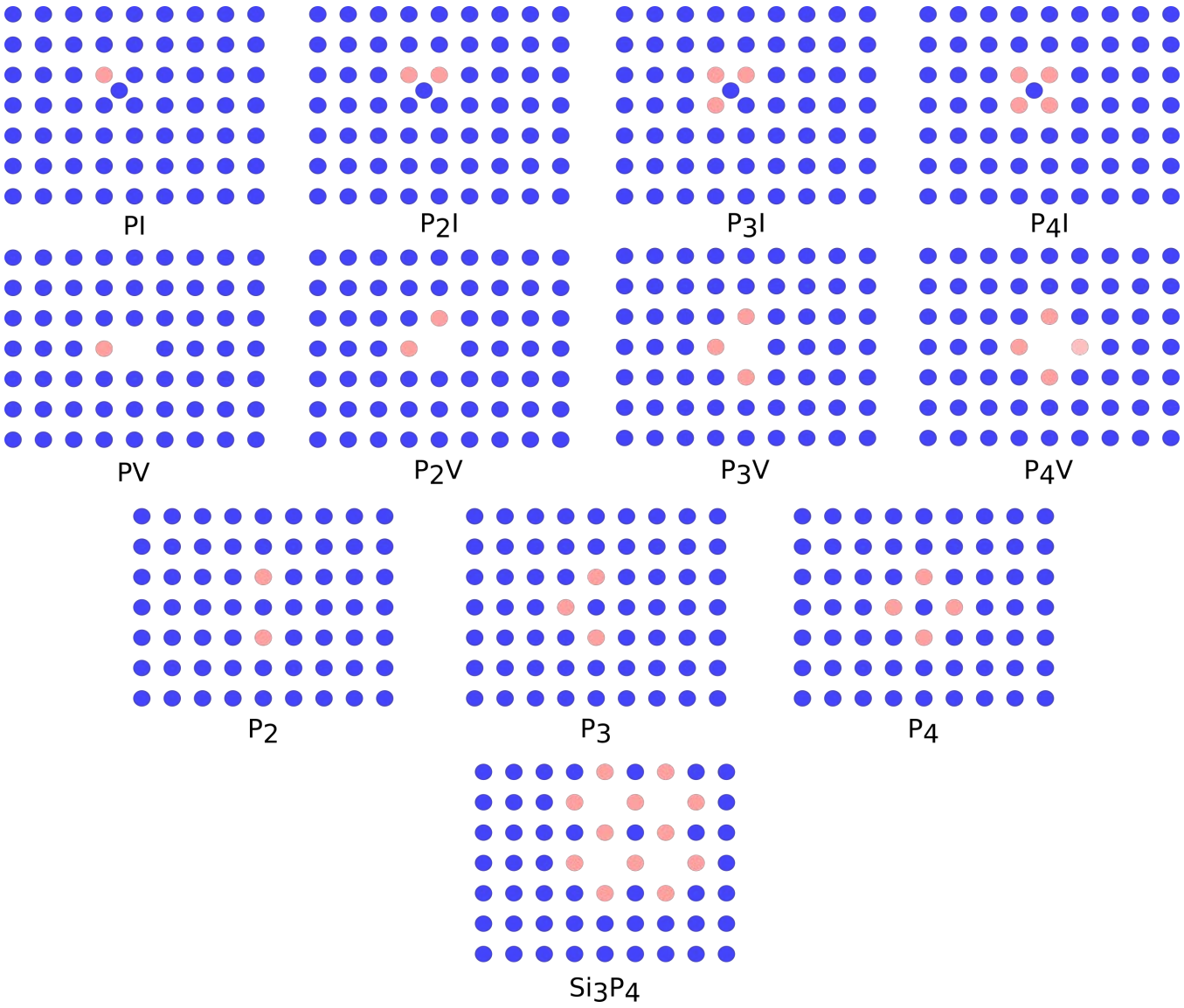

Figure 5-1. A 2D illustration of the interstitial, vacancy, and substitutional defect clusters and nanophase of Si_3P_4. Pink circles represent the dopant clustering around a Si atom (blue) or a vacancy. The substitution defect clusters are within the nearest neighbor distance of a Si atom, and these substitutions are considered too close to its same atom to contribute an electron (not activated). The interstitial Si atoms sit on the split-<110> position. The nanophase Si_3P_4 is a clustering of P_4V defect clusters.

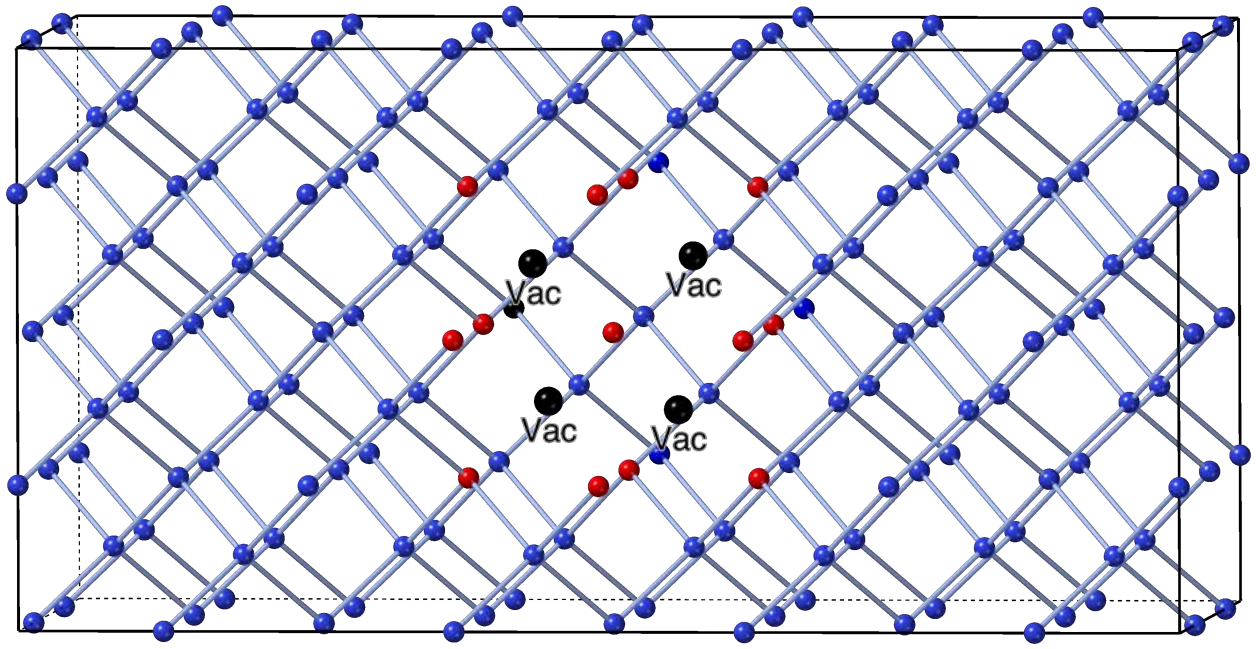

Figure 5-2. A 3D illustration of a P_4V defect (a) and a submicroscopic nanophase of Si_3P_4 (b). Inside an arbitrary Si supercell, The bottom panel represents the P_4V defects clustering into the nanophase.

from the mainstream methods, which references the pure phases of the defect components, in this case, pure Si, P, and As phases. Sahli et al. performed these calculations for all three cluster sites. However, high through put methods trade accuracy for speed. This work applies the same method but with a focus on accuracy. A Si supercell of 3x3x3 with cluster defects relevant to HD Si:P and Si:As films (e.g., As_4V and P_4V) was calculated to check the trend of Sahli et al.[78] Figure 5-3 was found show a deviation from the high through-put work, but the trend for the clustered defects did not change. Both works show the vacancy centered defects favorably increasing with dopant clustering, while Si centered substitution defects decrease with

dopant clustering. The formation energy suggests a spontaneous formation of the As_3V, As_4V, and P_4V cluster defects.

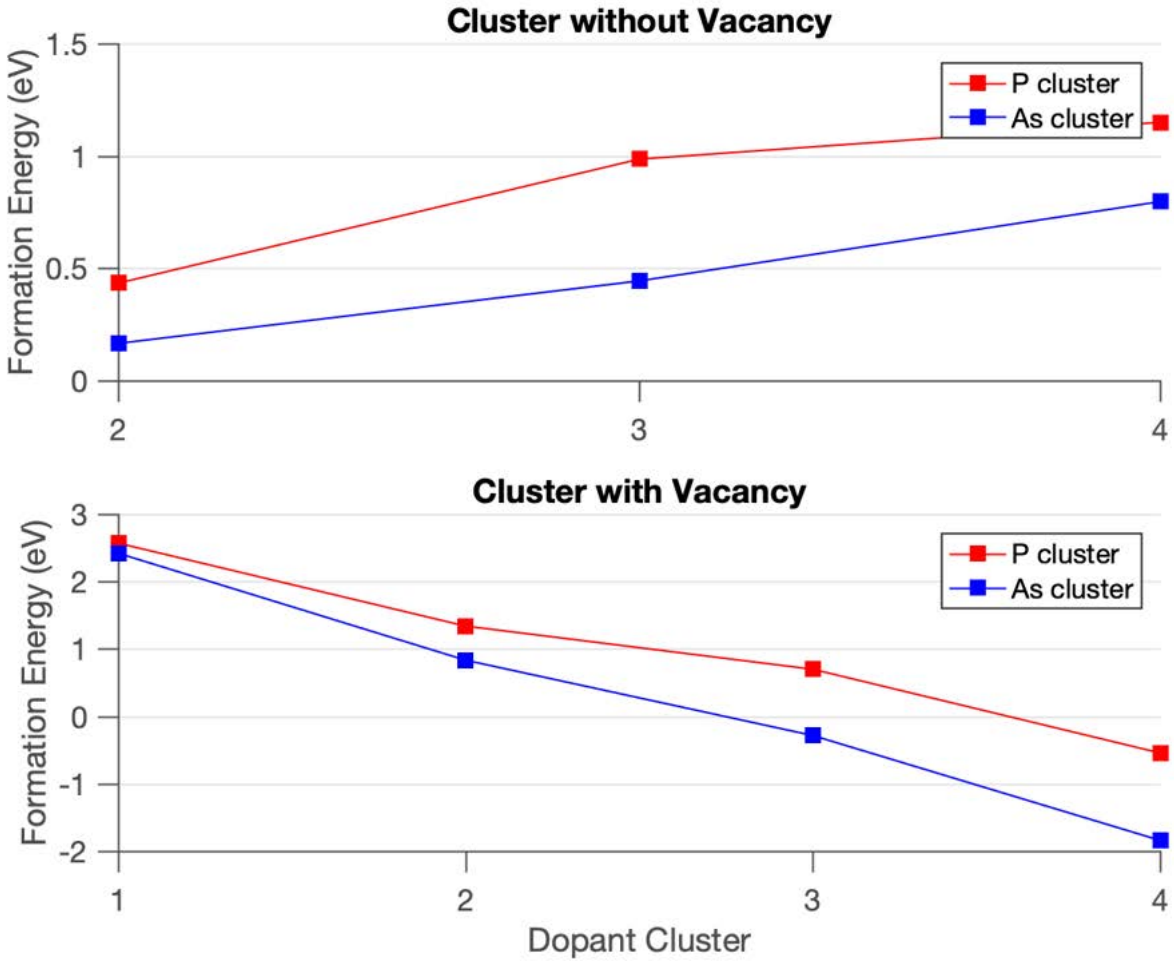

Figure 5-3. Plot of the formation of energy as a function of the number of dopant atoms in the cluster. The plot shows a trend for the formation energy of the substitution cluster defect and the vacancy center. The dopant clustering around a Si atom increases the formation energy while dopants around the vacancy decrease it.

A recent study by Weinrich et al. examined the properties of these HD Si:P films.[18] The films studied were low doped (LD) Si:P with of 5.0 x 10^{20} cm^{-3} to high doped (HD) Si:P films with concentrations of 4.4 x 10^{21} cm^{-3}. The films were highly activated by millisecond laser anneal at 1200°C; the subsequent thermal deactivation behavior was studied. A range of subsequent anneal times, up to 30 min, at temperatures between 700°C and 900°C by rapid thermal anneal (RTA) were performed with no significant diffusion, as confirmed by secondary

ion mass spectroscopy (SIMS). Due to the lack of diffusion, changes in sheet resistance cannot be attributed to a loss of phosphorous in the films. The study found that the LD Si:P films maintain electrical activity under significantly longer anneal times and higher temperatures compared to HD Si:P. The activation energy barrier for the deactivation was found for HD Si:P to be half that LD Si:P. Additionally, it was found that activation of HD Si:P films was found to recover with a subsequent ms laser anneal after the deactivation anneals.

Microstructural analysis using TEM found no extended defects or precipitates for RTA up to 2 min, and strain analysis from rocking curve high-resolution x-ray diffraction (RC-HRXRD) did not show a release of strain with deactivation. Therefore, the transition of dopant atoms between substitutional lattice sites and interstitial sites does not appear to participate in the observed activation and deactivation process. A following experiment in the same work utilized a marker layer as an indicator of point defect flux. A time series of RTA at a temperature of 700°C was performed at HD Si:P concentrations of 2.9 x 10^{21} cm^{-3}. The diffusion of the marker layer was found to be much greater than the control sample. This interstitial flux suggests the HD Si:P films release a significant number of interstitials during deactivation. Therefore, The HD Si:P layers may be simultaneously grown with a high concentration of interstitials and vacancy clusters.

Based on the assumption that P_4V is present in the films and having verified the absence of precipitation, two mechanisms for the deactivation have been proposed. The first proposed mechanism by Rossel and Dhalyan et al.[19, 102] involves the breakup and reforming of vacancy clusters. The P_4V cluster partially or fully disassociates during laser annealing releasing free P atoms for activation and release of a vacancy. The observed deactivation process is due to the phosphorous re-clustering around the vacancy. At high laser temperatures, a free Si interstitial annihilates the vacancy center, and a second self interstitial enables the disassociation of substitutional P_4 cluster defects. The second mechanism considers the existence of Phosphorus interstitial clusters (PICs).[18] From the marker layer experiments[18] and previously reported work of Keys et al.,[103, 104] it was

suggested that PICs grow simultaneously with P_4V clusters in the HD Si:P films. PICs dissolve allowing the P to become an electrically active on substitutional sites, and a self-interstitial (Si_I) defect is the result of the activation. The reverse occurs during the deactivation anneals. Both of the discussed mechanisms require a high concentration of PICs or Si_I, and the effect of high interstitial concentrations on strain is unknown. Also, the role of the P_4V cluster on strain is still unknown. DFT calculations have suggested the strain could be due to the Si-P bond lengths, which means the P_4V defect does not introduce significant strain but instead is simply the means of accommodating P at concentrations above the solubility limit with no precipitation.

The previously mentioned works do not support or disprove the presence of other defect clusters being present (e.g., PV, P_2V, and P_3V) which based on DFT could be stable.[78, 79] Therefore, a spectroscopy method sensitive to the local bonding structure, such as electron energy loss spectroscopy (EELS), is desirable for determining if these clusters or a dispersed Si_3P_4 nanophase exist. A probe corrected scanning transmission electron microscope (STEM) enables atomic-level resolution of material for micrographs and EELS maps.[105] Moreover, the EELS spectra produced are sensitive to the local bond structure of an atomic species at these resolutions. The spectra due to the local structure can be simulated and compared with experiment for local bonding determination.[106]

Weinrich et al. attempted EELS to determine the local bond structure types in the HD Si:P film.[23] In an attempt to maximized the P_4V signal, the highest P concentration of 4.4 x 10^{21} cm^{-3} was prepared for spectra collection prior to any post-growth annealing. The analysis was conducted on a JEOL JEM ARM200CF aberration-corrected TEM at an accelerating voltage of 200 kV. The EELS instrument was operated in TEM mode since the film is known to be uniform. Also, STEM instruments may suffer from stage drift, which can cause a shift of detection statistics in the spectra.[107] The energy loss range chosen was for the phosphorus $L_{1,2,3}$-edge. Figure 2 shows the collected spectra of the HD Si:P layer. A sharp initial peak from $L_{2,3}$ excitation at 99 eV is indicative of the Si atoms present in the film followed by

the delayed peaks of Si $L_{2,3}$ peak, and the Si L_1-edge is weakly visible at 132 eV. The peak at 127 eV is the P $L_{2,3}$-edge, and the P L_1-edge is not visible in the spectrum. As described in textbooks,[66] the low energy loss region is the energy loss near edge structure (ELNES) spectra, which fingerprints the presence of atomic species. The spectrum beyond 160 eV is the extended energy loss fine structure (EXELFS) region, which is sensitive to the local bonding structure. This region is observed as oscillations, and the expected oscillation the EXELFS spectrum is not present in the plot (only a smooth decay). Weinrich et al. concluded that EELS could not resolve the clustering of the vacancy complexes. At the time of the experiment, the instrument was not equipped with an electron monochromator, so the energy resolution of the instrument was >350 meV. The conclusions of the work stated that the local bonding structure might be achieved with better energy resolution. A better energy resolution (less than 1 meV) would allow the EXELFS spectrum to be compared with simulation.

The EELS results from Weinrich et al.[23] (see fig. 5-4) were transposed with FEFF9 ELNES simulation. The two computational spectrums are based on an early work for a pure Si_3P_4 phase and a single dopant P atom in a Si supercell. The isolated P atom calculation is based on the electron being scatted by the P atom, while Si_3P_4 is produced with electrons being scattered by Si. The choice of scattering atom allows both species to be summed; each spectrum is the sum of the $L_{1,2,3}$-edge excitations. The blue plot in the graph represents the calculated spectrum of a pure Si_3P_4 phase, and the yellow plot represents the spectrum of a single P atom substitution in a Si 3x3x3 supercell, and the supercell volume and ions were relaxed simultaneously. As reported by Sahli et al.,[78, 79] this calculation setup is equivalent to P doping concentrations of HD Si:P (1×10^{21} cm^{-3}). The experimental and theoretical spectra are normalized for comparison. The ELNES features in the experimental EELS are displayed with a corresponding colored arrow and letter. A (blue arrow) is the delayed peak of the Si atom, and B (red arrow) is the delayed peak of the P atom. C (green arrow) is the L_1-edge of the silicon atom; D (yellow arrow) is an arbitrary trough feature; E (purple arrow) is a peak feature which may correspond to a delayed P L_1-edge. The corresponding colored

arrows on the FEFF9 simulations attempt to point out similar features between experimental and theoretical ELNES. From visual inspection, The A and B peaks correspond with the delayed peak of the experiment; the B peak suggests the Si_3P_4 introduces additional scattering in the experiment. However, FEFF9 suggests a different location for the delayed peaks A and B. As discussed in chapter 2, FEFF9 simulation of covalently bonded systems is poor, and the software is designed for closed pack metals. The D and E peaks support the presence of a Si_3P_4 phase in the HD Si:P film, and the C peak is related to the Si atom chosen as the electron scatterer in the Si_3P_4 phase, so it only indicates the presence of silicon's L_1 edge. Therefore, every ELNES feature from the experiment corresponds with a peak from FEFF9.

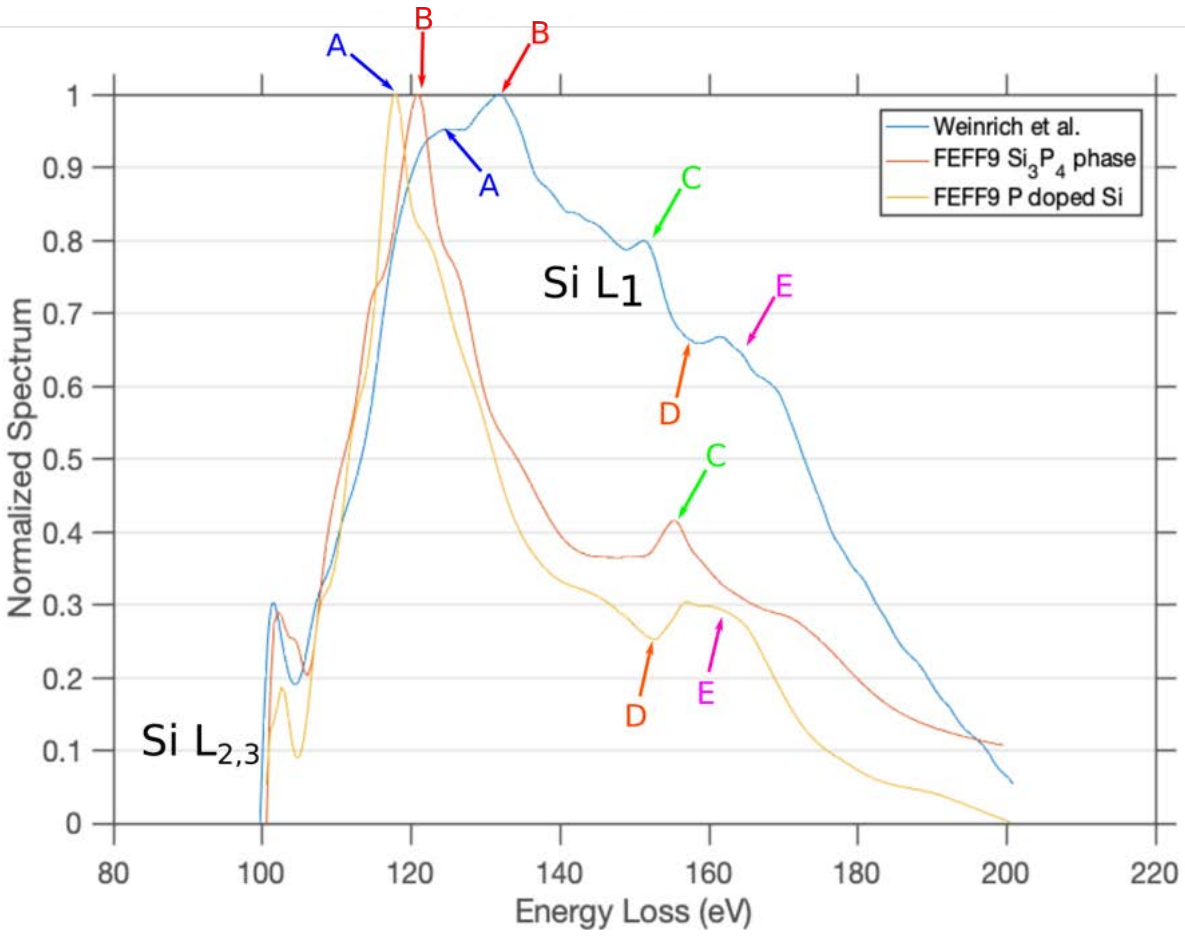

Figure 5-4. The Weinrich et al. EELS experiments on a JOEL aberration-corrected TEM compared to early FEFF9. The FEFF9 calculations are a pure Si_3P_4 phase, and a single P atom (substitution site) in a 3x3x3 Si supercell.

Though fig. 5-4 is promising, the energy shifts between the delayed maximum of the experimental and theoretical data are problematic, and it does not provide EXELFS details necessary for determining the local structure. However, the correspondence between peaks was enough to justify an experiment with a more advanced EELS system. A STEM with ultra-low stage drift and a 1 meV energy resolution monochromator might produce the necessary EXELFS spectra to determine if the P_4V complex exists.

Low doped (i.e., below the solubility limit) films of Si:As exhibit the same cluster types.[96] These defect clusters have been observed by extended x-ray absorption fine structure spectroscopy (EXAFS). EXAFS is a photon equivalent to EXELFS, which suggests if x-ray absorption spectroscopy (XAS) is a usable technique, then EELS should provide a similar result.[50] Moreover, the EELS simulation of FEFF9 is also built from the theory and code of EXAFS.[52] A brief discussion of EXAFS results of low doped Si:As films will serve as background for the EELS experiments on HD Si:P films.

Allain et al.[108] performed experiments on As doped samples ranging in concentration from $3x10^{16}$ – $5x10^{16}$ cm^{-2}. The samples were laser annealed for a fully activated layer, with another subsequent anneal to induce deactivation clusters. A deactivation model was developed to compare with an EXAFS spectrum, and a vacancy centered defect complex of As_mV was determined from model fitting. Temperatures below 550°C resulted in As complexes of up to 7 ± 4 atoms. With increasing annealing temperatures, the mean number of As atoms around a vacancy increased, but the large error margin prevented a conclusion of an increasing number of clustered As atoms. Allain et al. surmised that the As_mV complexes acted as embryos for precipitation at lower temperatures. A more recent study by Giubertoni et al.[109] utilized the FEFF8.4 package with structural parameters obtained from DFT. Samples were ion-implanted, ranging from $3x10^{14}$ – $3x10^{15}$ cm^{-2}. The complexes detected were AsV, As_2V, As_3V, and As_4V, and SiAs precipitates for the highest implanted samples. With increasing arsenic concentration, the fraction of AsV, As_2V, and As_4V complexes increased. The As_3V complex was found to be at its highest concentration at $1x10^{15}$ cm^{-2}. The success of these experiments for determining

the presence of complexes and precipitates suggests similar studies might work for the HD Si:P films.

The EXAFS experiments require a limited-access synchrotron facility. EELS is a more readily available technique as an attachment to a TEM instrument[48] However, EELS requires sample preparation with adequate thinning to reduce plasmon scattering. Also, the EXAFS experiments of Allain and Giubertoni et al. allowed for the K-edge spectrum to be measured. In EELS, the K-edge electron counts are too low for analysis, so the $L_{1,2,3}$-edges are collected from the sample instead, which increases the complexity of post-analysis.

The following experiment attempts to determine if the matched ELNES peaks in fig. 5-4 are real. If real, a gradual decrease of the matched experimental signal peaks from fig. 5-4 is expected to decrease with increased anneal times. The peaks should reduce corresponding to a reduction of nanophase scattering, and thus a reduction of electron counts. Secondly, the experiment attempts to resolve the EXELFS spectrum. If the EXELFS spectrum is compared with simulation, the spectrum will complement the ELNES. The two spectra comparison will help determine if the excess phosphorus exists in a dispersed nanophase composed of many clusters or isolated defect clusters.

5.2 Experimental Methods

HD Si:P films were grown with an epitaxial thickness of 80 nm on p-type 300 mm (001) Si wafers. The Applied MaterialsCenturareduced pressure chemical vapor deposition (RP-CVD) grew films at a high phosphorous concentration of $3.1e^{21}$ cm^{-3}. This concentration is chosen based on the extended defects observed for $4.4e^{21}$ cm^{-3} concentration samples with post anneals.[18] All samples were rapid thermal annealed (RTA) at 900°C, with times ranging from 30 s to 120 s. Based on work from Weinrich et al.[23] with laser surface annealing, an RTA temperature of 900°C was expected to dissolve the defect or phase, thus reducing strain. Rocking curve high-resolution x-ray diffraction (HRRC-XRD) was performed on annealed samples to measure changes in strain, which would signify if the complexes dissolved. Then, secondary ion mass spectrometry (SIMS) was performed on samples to corroborate with the

RC-XRD data. Evans Analytical performed SIMS using a Cs^+ source, and RC-HRXRD was performed with a JVX7300LSI.

The samples for EELS were prepared using an FEI Helios Nanolab dual beam SEM/FIB. The samples for STEM-based EELS are prepared in cross-section and were thinned to less than 15 nm for removing plasmon multi-scattering noise.[66] Figure 5-5 illustrates the thinning technique as described by Schaffer et al.[65] Samples were thinned in steps with the thickest part attached to the post; this step thinning method ensures the high strain of the film does not destroy the sample during the thinning process.

Figure 5-5. A simple illustration of the step thinning for making STEM cross-section samples. As the Si:P film is at a high-stress state, this method reduces the strain of the sample so that it may be thinned to 15 nm.

The STEM Nion U100 at Oakridge National Laboratory was used for the measurement of EELS. This tool was chosen for its superior energy resolution of 1 meV and low stage drifts during EELS map collection. Before loading, the samples were exposed to a 12-hour low-temperature bake to remove organics.

The University of Washington's FEFF9 package used for EELS simulation does not relax lattice structures. Therefore, relaxation was done by the density functional theory as implemented in the VASP software package. The Si_3P_4 pseudocubic was treated as a pure phase for the EELS simulations, and an isolate P atom inside a Si supercell was internally relaxed simultaneously with full volume relaxation. The Si_3P_4 phase's internal structure was also simultaneously relaxed with volume, but only in one direction to accurately represent epitaxial conditions. The energy cutoff has been converged to 340 eV with a 3x3x3 Monkhorst pack.

The FEFF9 EELS simulation package does not provide phonon contributions to EXELFS. Based on the phonon work described in chapter 4, phonon simulations are introduced for

EXELFS simulation using the correlated Debye-Waller factors. The Debye-Waller factors are essential for accurate oscillations in the EXELFS calculations. The Cornell spectrum analyzer package[110] was used for the extraction of the spectrum from the EELS maps and background subtraction. The Nion U100 collects high angle annular dark-field (HAADF) STEM in parallel with EELS. Figure 5-6 illustrates this process of parallel data collection from the Cornell spectrum analyzer package. Every image generated from the HAADF STEM data has a corresponding STEM-mode EELS map. The orange box in the EELS map picture represents an EELS spectrum requested from the software. A smaller collection square corresponds with a better resolution at the cost of lowering the signal-to-noise ratio. The background-subtracted spectrum was filtered using a Gaussian average scheme, so the random noise from the experiment could be removed.

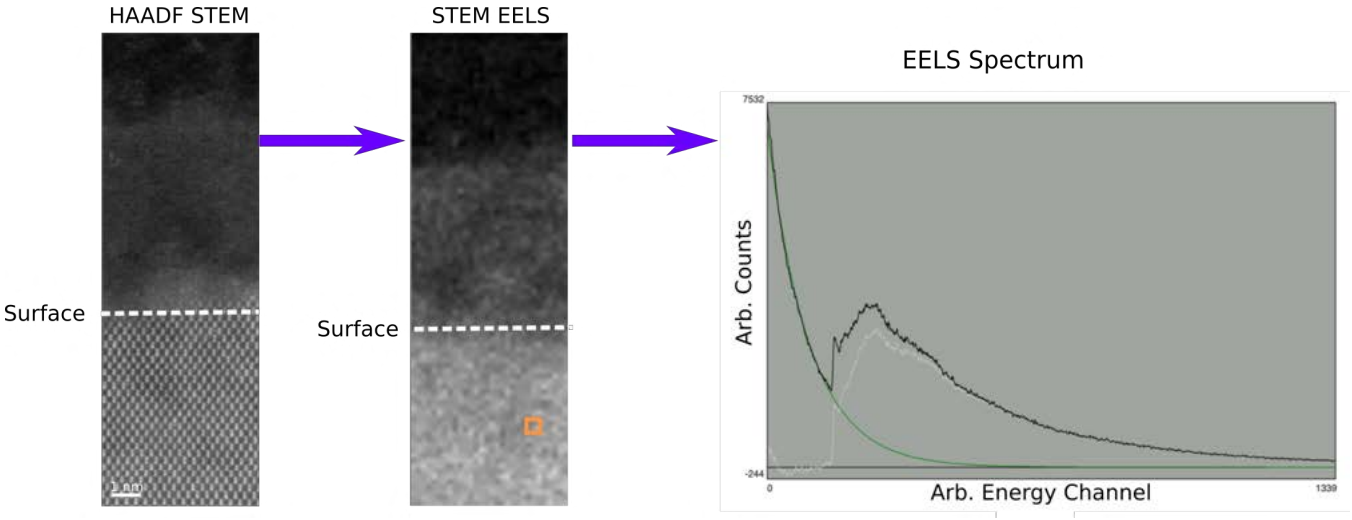

Figure 5-6. The EELS instrument raster the electron beam collecting STEM and EELS map in parallel. The orange square represents the area of the EELS spectrum for the plot. The final panel is the EELS spectrum extracted from the selected area. The EELS spectrum (black line) is subtracted based on an exponential fit (green line). A final spectrum is extracted with background noise removed for post-processing (white line).

5.3 Experimental Results

An RC-HRXRD coupled scan conducted on the (004) brag peak was performed to show the strain stability after post-annealing treatments. A series of $3.1x10^{21}$ cm_{-3} samples were

ms laser annealed prior to RTA anneal at increasing 30 s differences in time. The RC-HRXRD coupled scan sets the (004) peak to zero, so peaks at larger angles indicate strain (tensile or compressive strain). The control shows a strong peak at a high angle, which indicates a tensile strain present (see fig. 5-7). The subsequent samples exposed to longer heating times show a peak shift to lower Omega-2θ values, closer to the (004) peak, indicating a reduction of the film strain. Based on these results, it can be suggested that the defect causing strain is dissolving. The 90 s and 120 s anneal do not show a difference in strain shift.

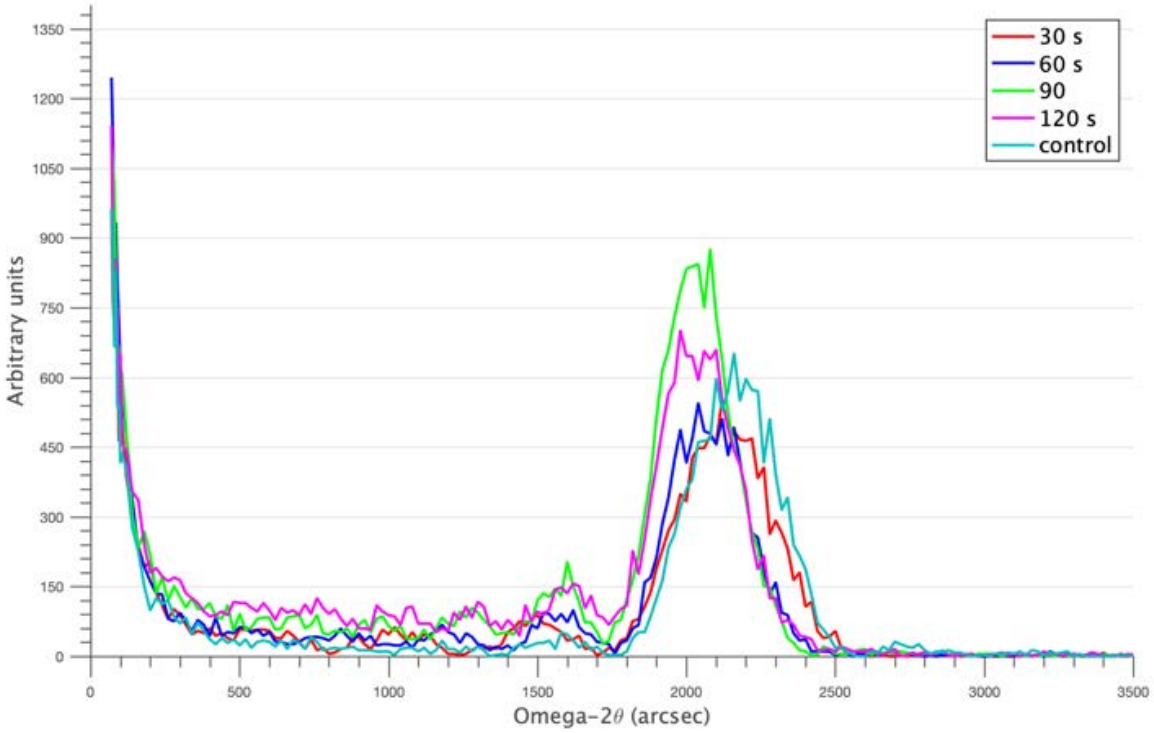

Figure 5-7. RC-HRXRD data on 3.1x10^{21} cm$_{-3}$ doped film for the EELS experiment. All samples were annealed at 900°C using a rapid thermal anneal tool. A strain reduction is observed between 30 s to 120 s.

The exponential decay relationships is compared with strain over time (see fig. 5-8). A highly activated HD Si:P layer has an active carrier concentration of 1x10^{21} cm^{-3} that decays to a stable concentration of 2.5x10^{20} cm^{-3}. The decay rate is calculated from an Arrhenius relationship with an energy barrier of 1.3 eV and a preexponential factor of 1.07x10^{6} s^{-1}. A

decay rate of 2.71 s^{-1} is calculated for HD Si:P at 900°C. The values for the model are taken from the work of weinrich et al.[18] The exponential decay model in fig. 5-8 (b) shows the P atoms are deactivated to the stable carrier concentration within 2 s time. When this decay model is compared to the strain in fig. 5-8 (a), the strain data continues to relax linerarly up to 90 s then the strain stays stable for 120 s. Therefore, the deactivation of P into PICs does not contribute to the strain relaxation observed over 120 s.

SIMS data provides a qualifying technique for the P concentration in the films. The SIMS results of (in fig. 5-9) show approximately a $3.1x10^{21}$ cm^{-3} P concentration in the film. SIMS also detects additional atom species in the film (e.g., O, Cl, N, and C), a result from the growth process of the films. The high concentration of Cl atoms is due to the HCl etchant used in the co-flow process. However, at the observed concentrations, their presence is benign. The oxygen peak at the surface sample indicates an oxide film growth, and it is corroborated with a peak of P atoms, which indicates piling up due to oxide growth.[111] For the 120 s anneal, no significant diffusion takes place during the anneal with the 80 nm thickness of the film visible (in fig. 5-9). Therefore, the reduction of the observed strain in fig. 7 is not correlated with a reduction of P concentration in the film. A reduction of EELS peaks would be related to dissolution of a cluster defect complex or submicroscopic Si_3P_4 nanophase.

Fig. 5-10 shows the micrograph images for $3.1x10^{21}$ cm^{-3} samples annealed at 900°C for 120 s. The images show a lack of P precipitation and extrinsic defects, indicating and changes during annealing are occurring on the sub microscopic scale. The TEM micrographs for shorter times also did not show signs of defects. The absence of defects at lower temperatures is expected, so the micrographs are not presented for brevity.

Figure 5-11 shows the simulated spectrum for the pseudocubic Si_3P_4, and the excitation for each band is close to the experimental values for Si and P. The simulated spectra were generated with more sophistication than simulations in Fig. 4. First, the spectra generated considers the phonon scattering with Debye-Waller factors. Lastly, the self-consistent loop of FEFF9 generates errors in the Fermi level (partly due to the muffin tin potential mentioned

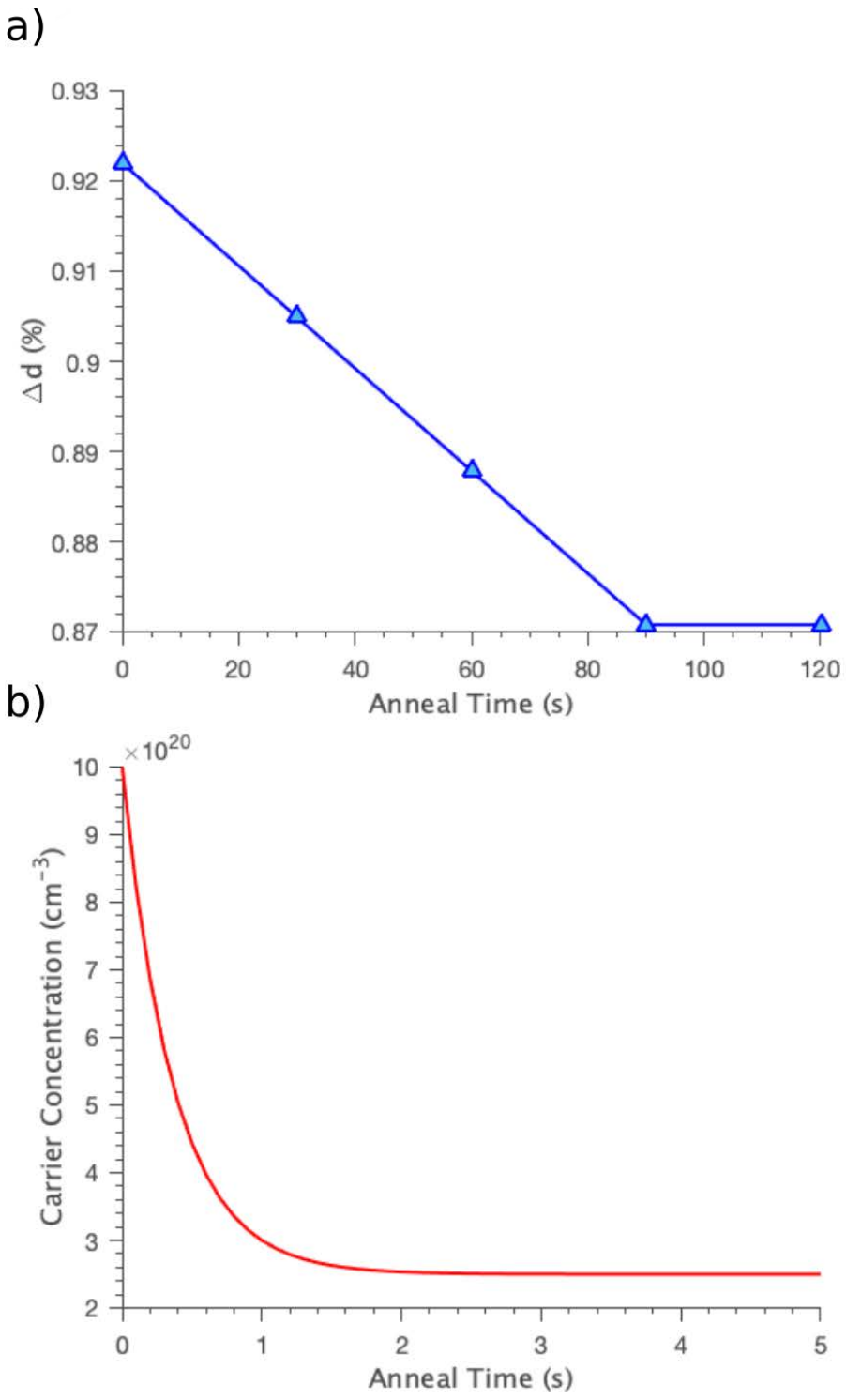

Figure 5-8. The calculated strain from RC-HRXRD (a) Shows a linear drop with annealing time until 90 s. The strain drop is directly compared to the calculated deactivation (b) of the film. The P is fully deactivated within 2 seconds of the anneal based on the model. Therefore, The strain drop over 120 s is not related to P atoms forming PICs.

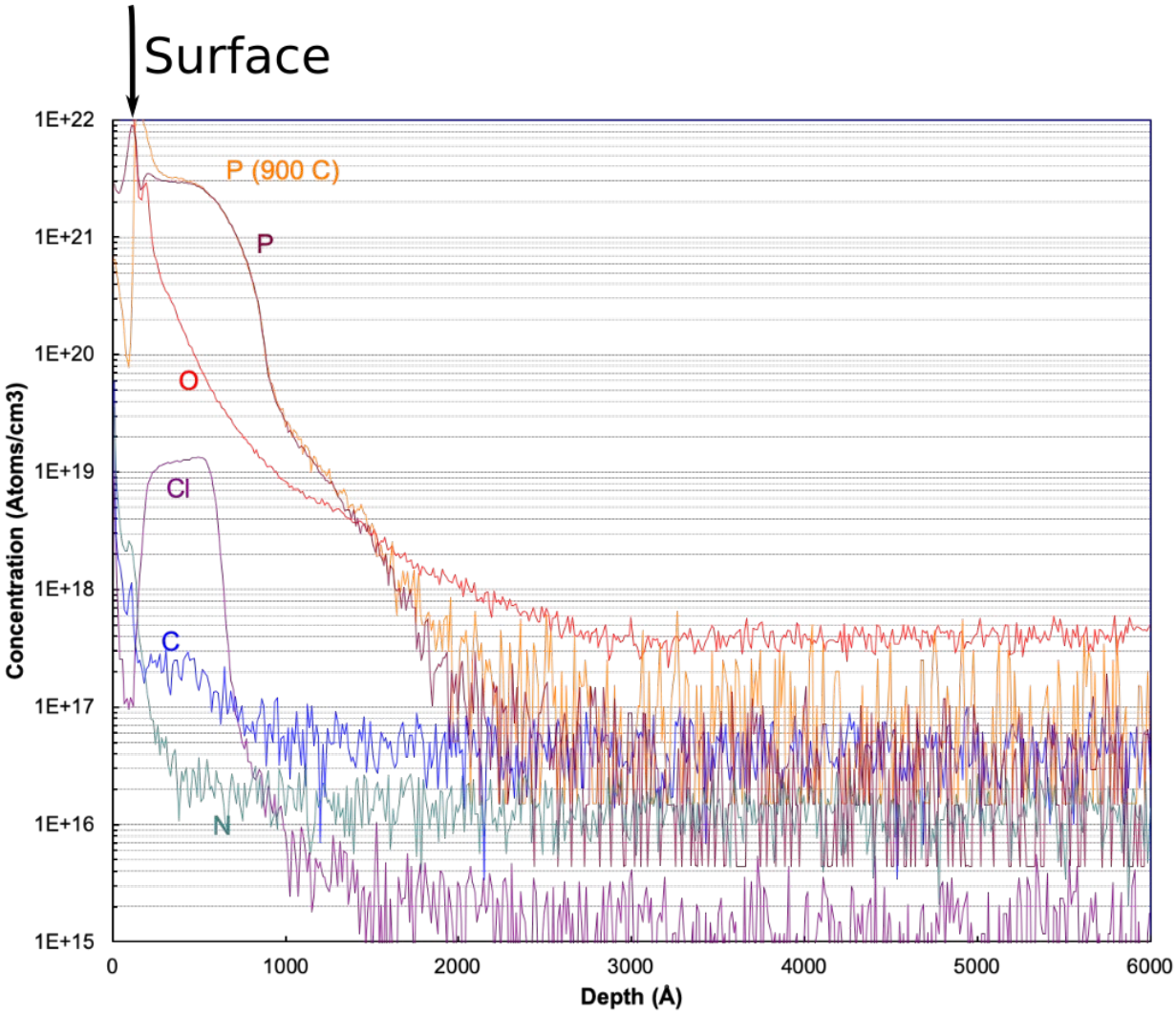

Figure 5-9. The SIMS data for the 120 s RTA annealing time at 900°C (orange). No significant diffusion of P is observed for the 3.1×10^{21} cm^{-3} doped films.

in chapter 2), so the Fermi level is shifted to the middle of the semiconductor bandgap. The agreement with the initial excitation demonstrates fidelity to the calculated results. After the initial excitation, the peaks developed are related to the scattering due to the core-hole state and lifetime specific to the material studied, so it provides a fingerprint for the material. The spreading of the peaks in the simulation is related to the built-in error of the FEFF9 package, which assumes error from the STEM instrument based on the aperture and collection angles. However, FEFF9 does not include spreading from the plasmon resonance of the material, so the spreading of the experimental results' peaks is significantly wider. Figure 5-11 (c) shows

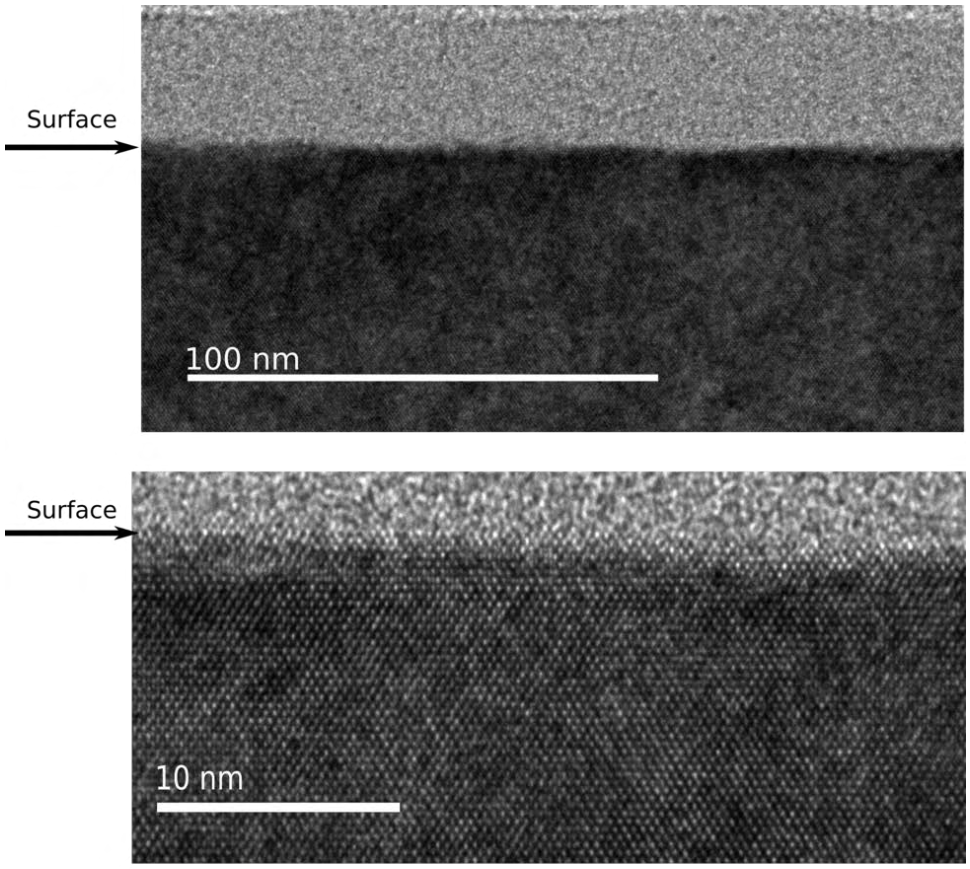

Figure 5-10. TEM micrographs of a 3.1×10^{21} cm^{-3} concentration sample (HDSiP layer is 80nm thick) heated with an RTA at 900°C for 120 s. The micrograph shows no precipitation or extrinsic defects present after annealing.

every calculated spectrum of Si and P superimposed. In this figure, the spectrum overlap is clearly visible.

Figure 5-12 shows a comparison between the spectrum for a single P doped Si cell and a pseudocubic phase. The scattering target is the P atom. The L_3-edge is chosen for comparison since it is the strongest signal in the EELS spectrum. The difference between the two spectra is subtle for both the ELNES and EXELFS regions. The p doped Si cell shows a single ELNES peak while the pseudocubic shows a slight splitting. In the EXELFS region, The p doped Si cell shows an oscillatory behavior while the pseudocubic shows a smooth decay. The subtle

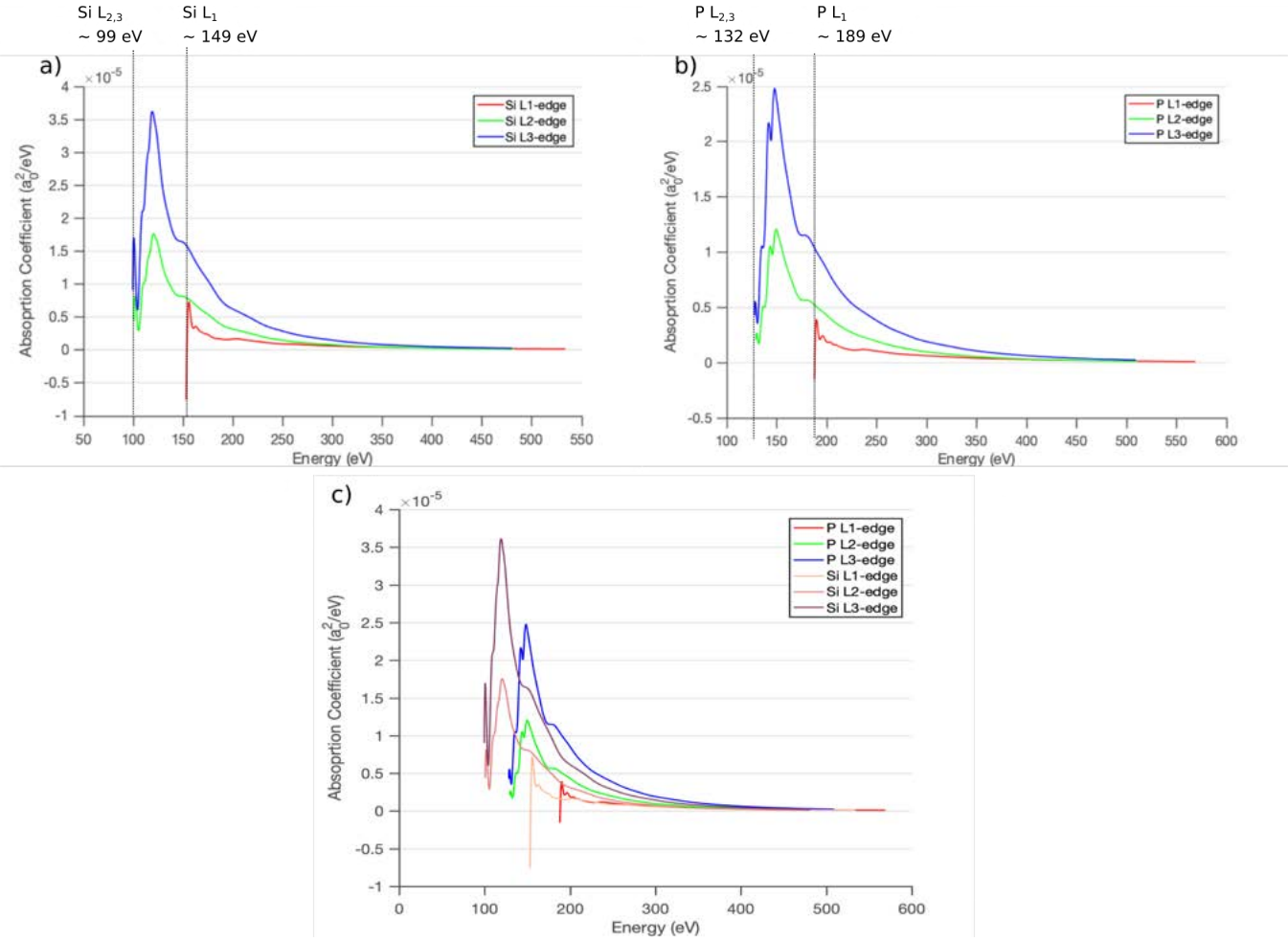

Figure 5-11. EXELFS simulation from the FEFF9 package for Si (a) and P (b) core-hole excitation. The spectrums are separated into $L_{1,2,3}$ core electron excitations. The simulation includes energy error spreading from the instrument, and the experimental values for the excitation edges denoted as a dotted vertical line. A superimpose figure (c) shows the oveelap of the Si and P scattering.[112]

difference between the two spectra justifies the need for a high energy resolution EELS system. However, These signals will be overwhelmed with the overlapping signal for Pure Si.

The EELS spectrum from experimental data is illustrated in Fig. 5-13 and 5-14; the aperture and collection angles were set to the same simulation parameters for peak broadening. In Fig. 5-14, A difference of counts is noticeable from the two spectrums but only related to the difference of the lamella thickness during sample preparation. The film spectrum shows more oscillatory noise due to the small cross-section of the EELS map selected. Larger collection areas are not used due to the stronger Si signal than P, and this spectrum eventually

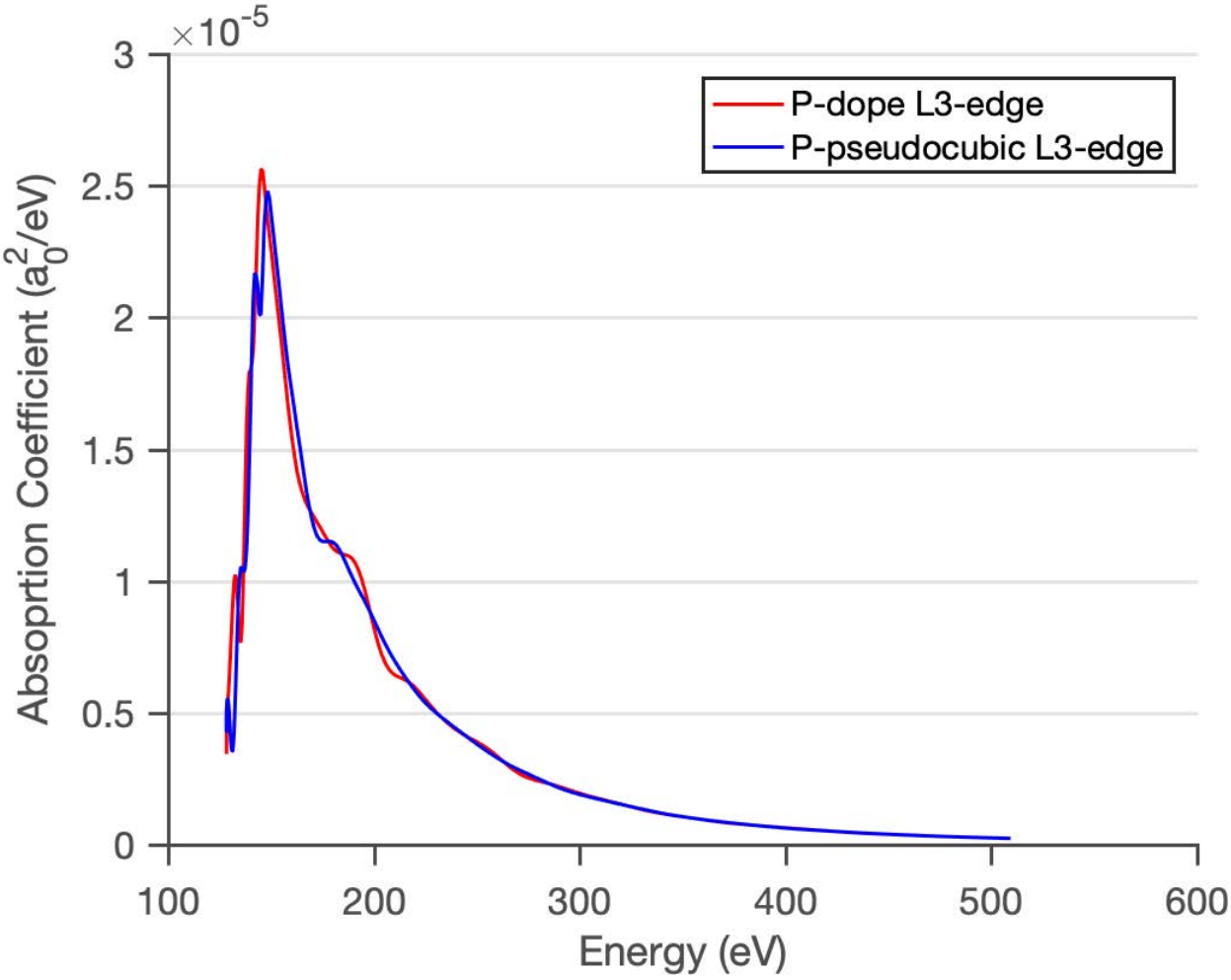

Figure 5-12. The FEFF9 calculation of the P L_3-edge. The calculated scattering of a single P doped Si cell and pseudocubic P is compared. The L_3-edge is the strongest signal observed in experiment soit was chosen for the comparison.

converges to Si like, with greater collection areas. Both spectrums begin at the Si $L_{2,3}$ excitation bands. For the Si control, the next excitation peak is expected for the spectrum with a L_1 peak visible at 127 eV. The spectrum of the film shows stark differences at the delayed peak (i.e., ELNES region). The film shows a splitting of the peak, which is related to fig. 5-11 (c); the peak is narrow compared to the Weinrich et al. experiment due to improved energy resolution. Figure 5-14 shows a direct comparison of the two experiments with this work showing resolvable peaks. The two spectra show a different decay of the tails. The difference

may be the different choices in aperature and collection angles between the instruments. Based on FEFF9 in fig. 9 (c), this peak splitting is indicative of the presence of P scattering.

The rough features for the film spectrum (above 150 eV) are related to the small collection area. As mentioned earlier, a small collection area was scanned across the EELS map until the peak splitting was visible. Unfortunately, this causes a reduction of signal-to-noise ratio, which causes the noise in the EXELFS region. The spectrum includes noise filtering, and additional filtering to remove the noise would degrade the EXELFS.

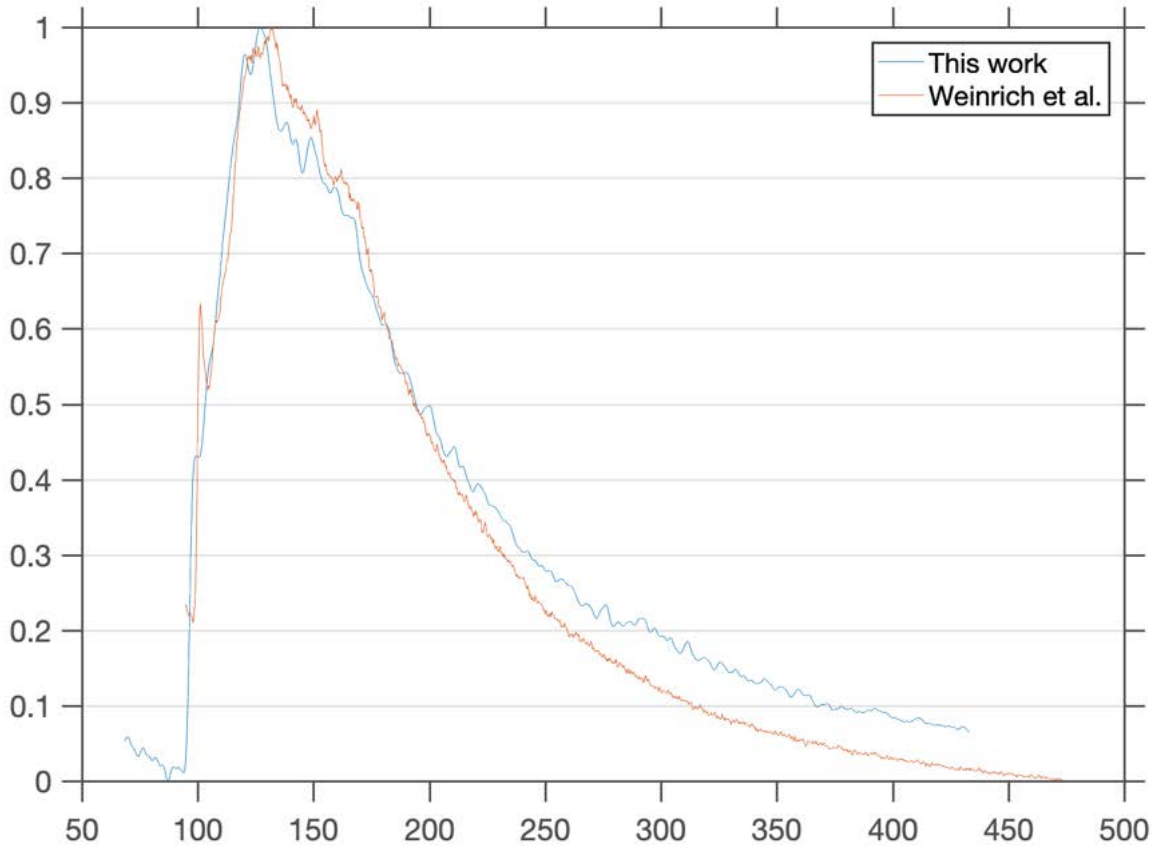

Figure 5-13. The experimental EELS spectrum of this work compared with Weinrich et al. This work shows finer peaks and features in the delay peak region. A noticeable difference is the difference of decay rates between the two spectrums. An explanation, The two experiments used different aperture and collection angles.

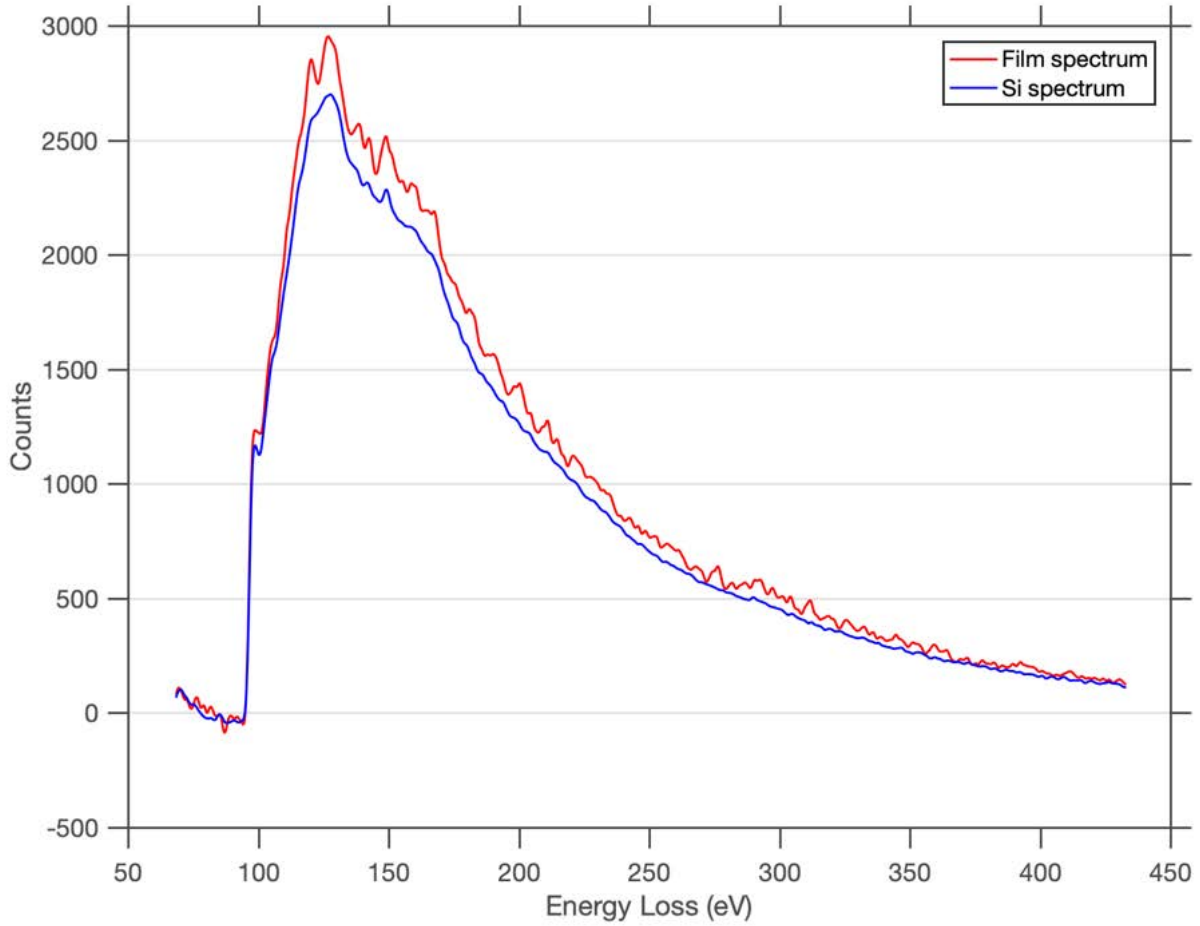

Figure 5-14. Experimental EELS spectrum comparison between the HD Si:P film and pure silicon. The Si spectrum is taken from the substrate.

5.4 Discussion

RTA shows that the strain is stable at high annealing temperatures up to 120 s at 900°C. The SIMS data shows the P atoms are not diffusing out of the layer during the annealing treatment. While the phosphorus concentration inside the layer is not changing, the high strain is still present based on RC-HRXRD. The data does show some reduction in strain, but it is not caused by P atoms diffusing out of the layer based on SIMS data. TEM micrographs show no visible defects, so the P atoms are still present in the film without visible defects or precipitates in the micrograph due to the dissolution of the strain. Therefore, the reduction of strain is related to the dissolution of cluster defects of PV, P_2V, P_3V or P_4V. Possibly, the

phosphorous atoms causing the strain reform into other non-electrically active defect cluster types. However, the data provided no evidence for what defects clusters are dissolving or the form the P atoms take after the dissolution.

To summarize, EELS spectra are broken into two regions: the first is the ELNES region, which fingerprints phases and atoms in the material. Second, EXELFS is the higher energy loss region sensitive to the local bonding structures. If a dispersed nanophase is present, a corresponding ELNES spectrum would be observed, and this signal would reduce with decreasing strain. If the vacancy defect clusters existed, a corresponding EXELFS signal would be present, and it could be corroborated with simulation. However, the EELS experiment did not provide data that could be used for either conclusion.

The EELS map was continuously scanned with the Cornell spectrum analyzer, and the film was found to have a splitting while the substrate lacked a splitting. A comparison of the experimental data and FEFF9 simulations show a peak splitting within the ELNES spectrum. This peak splitting was found to be related to Si-P bonding, showing the existence of a highly doped P film, but it did not provide evidence of a Si_3P_4 nanophase. The EXELFS spectrum which indicates more fine detail on local structure could not be resolved. Due to the Z number of Si a P being only one apart, the ELNES and EXELFS partly mix with the added complexity of L-edge mixing from two atomic species. Therefore, the deconvolution of the spectra is infeasible due to the strong excitation overlap.

5.5 Chapter Summary

For the experiment, EELS was performed on HD Si:P film. The EELS data showed a presence of P atoms, but the local clustering of the atoms could not be determined. The Z number of Si and P are too close, causing spectra to overlap, so the EXELFS spectrum could not be compared with theoretical simulations. While the conclusion is that EELS is not feasible for the application of HD Si:P films, the technique may be feasible for HD Si:As films due to the greater Z number difference between Si and As atoms. EXAFS has been successful in showing local cluster defect structures for LD Si:As films. The EXELFS from EELS can be

successful for understanding the origin of strain for HD Si:As structures. P and As atoms share similar chemical behaviors being on the same column in the periodic table. If these experiments could be performed, the results could be analogous for the HD Si:P films.

CHAPTER 6
LATTICE STABILITY AND POINT DEFECT FORMATION ENERGY OF $TISI_2$ AND $TIGE_2$ ALLOTROPES FROM FIRST-PRINCIPLES CALCULATIONS

6.1 Background

The continuing decrease in the feature size of microelectronic devices means that the contact resistance between the semiconductor and metal interconnects is becoming ever more important. An increase in contact resistance leads to a decrease in device performance. Methodologies have therefore been developed for reducing this contact resistance. One such method is the use of a silicide such as tungsten disilicide (WSi_2), titanium disilicide ($TiSi_2$), nickel disilicide ($NiSi_2$), or cobalt disilicide ($CoSi_2$). These silicides interface between the semiconductor (usually Si) and the contact metal as an additional layer. The silicide has a different work function from Si, so it reduces the Schottky barrier height between the metal and semiconductor, thus reducing contact resistance. Among the silicides, $TiSi_2$ is the ubiquitous low contact resistance silicide used for Complementary Metal Oxide Semiconductor (CMOS) devices because of its low thermal budget, and excellent oxidation resistance.[113, 114] Additionally, it has the added benefit of low defect concentration in the contact region with silicon. Two allotropes are of particular interest for $TiSi_2$: the low contact resistance C54 structure, and the high contact resistance C49 structure, with the C54 structure being the desired phase.[113–116] The C49 phase forms at lower temperatures and transforms into C54 at temperatures above 700 °C;[115, 116] this transformation has been the focus of much analysis. The C49 allotrope is observed at a lower temperature as the precursor phase, but is considered to be a metastable precursor phase to C54. Two different origins for this phase sequence have been proposed. In the first, the interfacial energies for $TiSi_2$/amorphous-TiSi and $TiSi_2$/Si interface are lower for the C49 structure than for the C54 structure. As a result, the C49 structure forms first.[117, 118] The second, argument is made based on the the majority atom experiencing twice the vacancy diffusion of the minority atom. In the case of the silicide, the Si atoms have greater mobility, and Si is known to be the dominant diffuser in

$TiSi_2$.[119][120] However, the mechanism by which this greater Si mobility causes C49 to be formed first, remains to be clarified.[115, 120, 121]

In addition to exploring why C49 is the precursor, several experiments have manipulated the environment of the C49-C54 solid reaction to understand the transformation from one to the other; these manipulations include introducing n-type and p-type dopant concentrations which tend to suppress the C49-C54 phase transformation by increasing the vacancy diffusion energy barrier.[122] Experiments have also altered the Ti deposition thickness: a decrease of Ti thickness correlates with an increase of the C49-C54 transformation energy barrier. This phenomenon has been called the "fine line effect," relating to the reduction of nucleation sites for C54.[123] From TEM micrographs, C54 has been observed to grow from the triple-point grain boundaries of C49, the concentration of which decreases with decreasing Ti thickness. Since device scaling requires thinner films, the very thin films will exacerbate the trend, making it even harder to form the C54 phase. It is thus desirable to investigate methodologies to reduce the C54 formation temperature.

The use of a third element has been shown to lower the temperature required for the formation of the C54 structure. Previous works have reported using Ta or Mo to form a ternary solid-state reaction to reduce the C54 formation temperature.[113, 121] However, introducing these metals would require an additional processing step for semiconductor devices. Fortunately, the introduction of Ge achieves the same effect using layers of $Si_{1-x}Ge_x$. This layer is grown as a co-flow process requiring only a single step.[16, 124–126]

The introduction of $Si_{1-x}Ge_x$ films at the source-drain regions introduces compressive strain in microdevices, thereby improving the hole mobility in the channel.[8] The $Si_{1-x}Ge_x$ films produce C49 and C54 allotropes of $Ti(Si_{1-x}Ge_x)_2$.[124, 127] Initially, it appears the Ti-$Si_{1-x}Ge_x$ solid reaction solves the prior problems: it the $Si_{1-x}Ge_x$ film provides the benefit of enhancing hole mobility and reducing the C49-C54 transformation temperature. Although Ge may reduce the C54 formation temperature, Ge segregation introduces an additional problem for thinner films of Ti: still require higher temperatures for complete C54 transformation. Specifically,

with increased temperature, the Ge segregation rate increases into the grain boundaries forming a region of $Si_{1-y}Ge_y$ (a different concentration from the $Si_{1-x}Ge_x$ film) extending from the surface to the substrate.[117] Additionally, Aldrich et al. found that the C49-C54 transformation energy barrier still increased for thinner Ti layers (less than 10nm thick). Therefore, the "fine-line effect" still plays a key role, and higher temperatures are needed for C54 formation. The Ge segregation worsens with increased temperature, so the Ge atoms at thinner Ti thickness introduce a new problem in addition to the "fine-line effect."[117] $Si_{1-x}Ge_x$ alloys will continue to be employed to introduce compressive strain, so an understanding of the $Ti(Si_{1-x}Ge_x)_2$ allotropes is beneficial for semiconductor processing.[126, 128]

Like $TiSi_2$, the $TiGe_2$ phase forms as C49 and C54 allotropes. However, in this case C49 is not observed as a precursor phase. The solid-phase reaction of Ti-Ge forms the precursor phase Ti_6Ge_5, with the C54 structure forming during the continued reaction of Ge with Ti_6Ge_5 through a nucleation process.[127, 129] However, metastable C49 has been synthesized using co-evaporation of $Ti_{0.33}Ge_{0.67}$ followed by crystallization to C49 at 315°C.[130] The metastability of the $TiGe_2$ C49 allotrope suggests that Ge plays a role in reducing favorability for C49, thereby reducing the C49-C54 transformation barrier.

This chapter will develop a theoretical understanding of the $TiGe_2$ phase, with the objective of more fully understanding why the Ti-$Si_{1-x}Ge_x$ reactions reduce the C54 formation temperature. Also, the lattice stability and defects in $TiSi_2$ and $TiGe_2$ will be characterized. A thermodynamic perspective of these solid-state reactions will be presented based on evidence from Density Functional Theory (DFT) calculations.

There exists a third allotrope of interest, the C40 structure. It has a lower electrical resistance than C49, and it transforms into C54 with subsequent annealing. Due to lattice mismatching, C49 cannot form with C40, so the high resistance of the C49 structure is bypassed. The C40 structure has been synthesized with laser pulse annealing, and characterized with Raman spectroscopy and transmission electron microscopy.[131–134] As it thus appears

that the formation of low resistance C54 might be achieved without the presence of the C49, analysis of the C40 structure is also included in this work.

6.2 Structure and Calculation Methods

A discussion of the silicide and germanide allotrope structures is vital for this work. The structures are illustrated in Fig. 6-1. The C49 has a base centered-orthorhombic (Fddd) structure. The C54 has a base centered orthorhombic type (Cmcm) structure. The C40 has a hexagonal type ($P62_22$) structure. The most noticeable structure difference between the three structures is in the periodic layering of Si/Ge. The C49 structure has two distinct bonding environments for the Si/Ge atoms. As Fig. 6-1 (c) shows, there is a Si/Ge monolayer with four-fold bonding in the plane. There is also a Ti-Si/Ge layer, in which the Si/Ge is covalently bonded with two nearest neighbors. The monolayer will be denoted as 4-NN for its four nearest Si/Ge neighbors, while the Ti-Si/Ge layer will be denoted as 2-NN for its two nearest Si/Ge. The other allotropes have higher symmetry than C49. Figure 6-1 (a) is the ab perspective of the C40 allotrope in which the hexagonal structure is evident. Figure 6-1 (b) from the bc perspective of C40 shows that the Si atoms have two nearest neighbor atoms and a periodic stacking. Figure 6-1 (d) shows that the Si atoms in C54 also have two nearest neighbors.

The Vienna Ab initio Simulation Package (VASP) is used for the electronic-structure calculations at the level of Density Functional Theory (DFT). The Generalized Gradient Method (GGA) and the Strongly Constrained and Appropriately Normed (SCAN) functional, described in more detail in Chapter 2, are used for the exchange-correlation in this work; SCAN is a new meta-GGA functional, which has proven to be well-suited for characterizing transition metal reactivity.[24–27, 29, 38, 56, 135, 136] The [3d 4s 4p] orbitals are included for the calculations with Ge potentials,[83] while the [3d 4p 4s] orbitals were included for the calculations with Ti potentials. The Si potential includes [2s 2p] orbitals.

The plane-wave cutoff used for relaxation was 520 eV, and the Monkhorst-Pack mesh method was used for Brillouin zone sampling.[137] The C49 structure was relaxed with a 10x3x10 k-point mesh, the C54 structure was relaxed with a 5x3x3 mesh, and the C40

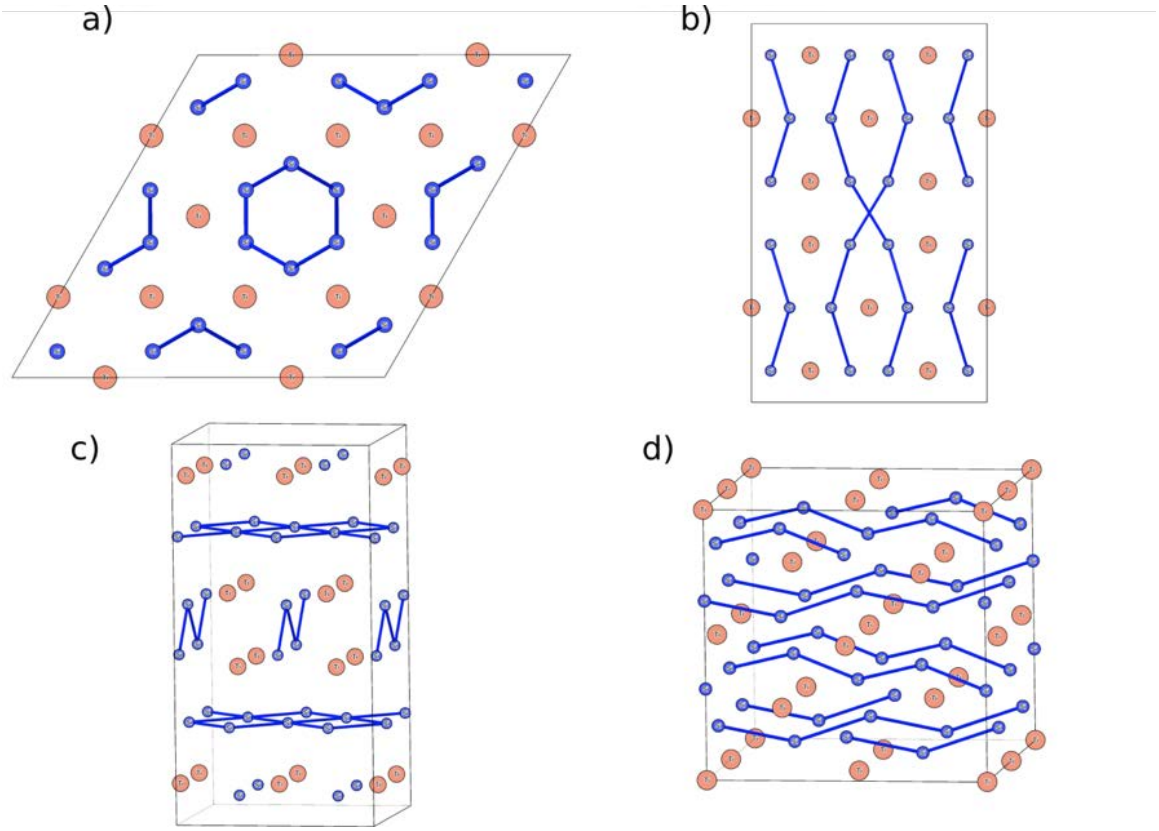

Figure 6-1. The hexagonal C40 structure from the (a) ab and (b) bc perspectives. The base-centered orthorhombic for C49 (b) showing two structurally different layers; the C54 (c) C49 face-centered orthorhombic structure; The silicon atoms represented as small circles (dark blue), and the titanium atoms are large circles (light orange).

structure was relaxed with a 9x9x5 mesh. These large k-point meshes are needed because of the small unit cell sizes, which are of different dimensions for each system. The supercell dimensions and ion positions were relaxed simultaneously until the force on each atom was less than 0.01 eV/Å, with components of stress less than 0.02 GPa. The space groups of the calculated structures were determined using the FINDSYM package.[138] The density of states and formation energies were calculated with the tetrahedron method[139] and a Methfessel-Paxton pre-convergence. [140] For the point defect calculations, the C54, C40, and C49 structures were relaxed using supercells of 3x2x2, 3x3x2, and 5x1x5 unit cells, respectively. These dimensions were chosen to yield approximately cubic supercells. The sampling scheme

for defect calculations was a 3x3x3 k-point sampling mesh. The interstitial positions were found using the MPInterfaces framework.[141]

The supercell dimensions were fixed for point defect calculations. While there are still defect-defect interactions between supercells, this fixed volume condition attempts to represent the conditions of an isolated defect.[54] $TiSi_2$ and $TiGe_2$ are conductors, so charged defect charges are not considered for this work. The defect formation energies are calculated using the standard equations:

$$Vacancy : \Delta H_f = E_{defect}[V_{SiorTi}] - E_{perfect} - \mu_{SiorTi} \tag{6-1}$$

$$Frenkel : \Delta H_f = E_{defect}[V_{SiorTi}] - E_{defect}[Si_i or Ti_i] - 2E_{perfect} \tag{6-2}$$

$$Substitution : \Delta H_f = E_{defect}[Si/Ti_{SiorTi}] - E_{perfect} + \mu_{SiorTi} - \mu_{SiorTi} \tag{6-3}$$

The chemical potentials μ_{Si}, μ_{Ge}, and μ_{Ti} reflect the reservoirs for atoms added and removed during the formation of the defect. These chemical potentials are taken as the energies per atom of the pure bulk elements, as calculated with DFT.

The isosurfaces of the charge density difference (CDD) are plotted around the atoms first coordination shell so that the charge transfer can be visualized based on $\Delta\rho_{diff}(r)$. The CDD is defined as the difference between the charge density of the ordered phase, $\rho_{phase}(r)$, and sum of the charge densities of the single element, $\rho_\alpha(r - r_\alpha)$ when the other elements are removed from the supercell: $\Delta\rho_{diff}(r) = \rho_{phase}(r) - \sum_\alpha \rho_\alpha(r - r_\alpha)$. This definition thus represents the charge redistribution when atoms are brought together to form the phase[142, 143]

A qualitative measure of the charge transfer is provided by Bader analysis. Here, the ionic bonding component and defect charge transfer is analyzed using the Bader analysis code from the Henkelman group.[58–61]

The importance of charge transfer for the enthalpy of formation of phases and defects was shown in Liu et al.[144] based on the extended Born model. This model considers partial polarization in a material. Like Liu et al., this work will study the C49 and C54 allotropes from

the extended Born model perspective. The extended Born model takes into account covalent bonds and partial charge transfer:[145]

$$\Delta H_f = \Delta H_{at} + (\Delta U_i - \Delta U_{ea}) + \Delta H_{el} + \Delta H_{cov} \tag{6-4}$$

The enthalpy of formation in Table 6-1 is represented as ΔH_f in the extended Born model. ΔH_{at} represents the covalent energy between atoms of the same element, taking into account that there is no charge transfer between like atoms. The electron affinity and ionization energy for the isolated atoms are represented by the second term $(\Delta U_i - \Delta U_{ea})$. ΔH_{el} is the electrostatic lattice energy for localized bonding, and ΔH_{cov} corresponds to the heat of formation of the covalent lattice of the crystal, which depends on valence electron orbitals and coordination.

There are multiple steps to evaluating eq. 6-4 In the first step, the binary alloy is cleaved such that its energy can be referenced to its pure components: this is the way that ΔH_f is calculated. In the second step, the atoms of the pure phases are disassociated into isolated atoms such that $\Delta H_t = \frac{E_{tot}}{N} - \sum_i E_i(r \to 0)$ (Described in Ch. 4). In the third step, these isolated atoms are ionized, enabling an estimate of the partial charge transfer. In the fourth step, the electrostatic attraction within the crystal is determined as $\Delta H_{el} = \frac{N_A \alpha q_i q_j e^2}{4\pi\epsilon_0 r_0}(1 - \frac{1}{n})$. Where N_A is Avogadro's constant, α is the Madelung constant for the specific crystal lattice; q_i and q_j are the partial charges of the anion and cation; e is the charge of the electron; r_0 is the interatomic distance between the cation and anion, and n is an empirical quantity for the distance dependence of repulsion. In the last step, the total effect is determined by subtraction. Though the partial charge is not quantitative from DFT, the extended Born model qualitatively shows the importance of ionic and covalent bond mixing of the lattice enthalpy.

Based on the extended Born model, it is essential to know the qualitative degree of partial charge transfer and covalent bond stability. The plot of the calculated density of states (DOS) yields insight into the covalent bond stability, while Bader analysis qualitatively describes the

importance of partial charge transfer. The conclusions provided from both techniques should be consistent with CDD.

6.3 Computational Results

The enthalpic calculations for the $TiSi_2$ C40, C49, and C54 allotropes are shown in Table 1-1. The $TiSi_2$ C49 system is the most stable structure. The calculations with the GGA functional predicts that its enthalpy is 7 meV per atom lower than that of C54; the SCAN functional predict it to be 5 meV per atom (SCAN) lower. The C49 structure is even more stable with respect to the C40 structure: by 22 meV per atom (GGA) and 32 meV per atom (SCAN). These results agree with those of Jain et al.[83] However, they do not agree with the results of Colinet et al.,[146] which are lower by 32 meV per atom for $TiSi_2$ C49 or 33 meV per atom for $TiSi_2$ C54. Both Colinet et al. and Jain et al. used PBE-GGA functional for energy calculations. Colinet et al. noted a difference of enthalpy of formation when compared to other works.

The enthalpies of formation for the $TiGe_2$ C49 and C40 allotropes have not been calculated in previous works. As a baseline, we have calculated the enthalpy of formation for the $TiGe_2$ C54 allotrope to compare with an earlier high throughput work.[84] In Table 1-1, the lowest energy allotrope of $TiGe_2$ is C54, with the enthalpies of the C49 and C40 structures both being 11 meV/atom higher for the PBE-GGA functional. The SCAN functional also predicts that the C54 structure is the most stable, with the C40 structure being 8 meV/atom higher than C49.

Sun et al. performed data mining from the Materials Project, and evaluated the influence of the chemistry and composition for various polymorphic compounds.[88] The upper limit of the convex hull for metastability was found to be 70 meV for most inorganic materials. That is, structures with enthalpies of formation above the convex hull by less than 70 meV have a significant chance of being metastable and, thus, may be manifested experimentally. Relating this insight to this work, the $TiGe_2$ C49 and $TiSi_2$ C40 allotropes are known metastable

Phase		Space Group	Functional	a	b	c	Enthalpy
$TiSi_2$							
	C40	P6_222	GGA	4.727	4.727	6.598	-535
			SCAN	4.707	4.707	6.543	-491
			GGA[146]	4.731	4.731	6.570	-497
	C49	Cmcm	GGA	3.548	13.568	3.578	-557
			SCAN	3.524	13.510	3.553	-523
			GGA[146]	3.541	13.617	3.576	-525
			GGA[83]	3.559	13.498	3.572	-562
	C54	Fddd	GGA	4.806	8.258	8.570	-550
			SCAN	4.786	8.230	8.490	-518
			GGA[146]	4.806	8.268	8.560	-517
			GGA[83]	4.809	8.260	8.567	-556
$TiGe_2$							
	C40	P6_222	GGA	4.959	4.959	6.822	-422
			SCAN	4.892	4.892	6.755	-444
	C49	Cmcm	GGA	3.689	14.320	3.714	-422
			SCAN	3.643	14.088	3.675	-452
	C54	Fddd	GGA	5.073	8.663	8.827	-433
			SCAN	5.021	8.525	8.716	-460
			GGA[83]	5.083	8.677	8.826	-414

Table 6-1. Structure and formation enthalpies of titanium disilicide and titanium digermanide structures. The table contains comparisons with previous works (i.e. Colinet et al.[146] And Jain et. al.[83]).

structures and indeed within 70 meV upper limit. On this basis, the $TiGe_2$ C40 structure is likely to be metastable also.

The concentrations of point defects, such as antisites and vacancies, impact the lattice stability and phase equilibria of intermetallic alloys.[143] Therefore, it is necessary to determine the formation energy of defects in $TiSi_2$ and $TiGe_2$. The interstitial sites for are illustrated in Figure 6-2. For the Frenkel defects, the interstitial site was as far away from the vacancy as the supercell dimensions would allow. The point defects energies of these systems are compiled in Table 6-2. Because of the inequivalence of the Si/Ge atom lattice sites in the C49 structure, the vacancy formation energies for the 2-NN and 4-NN sites are calculated separately.

For the C49 structure of $TiSi_2$, the lowest formation energy by far (0.31 eV) is for Ti_{Si} on the 2-NN site (i.e., within the TiSi layer); the corresponding value for a 4-NN site is 0.99 eV. The formation energies for a Si vacancy on the 2-NN sites are 0.83 eV and on the 4-NN

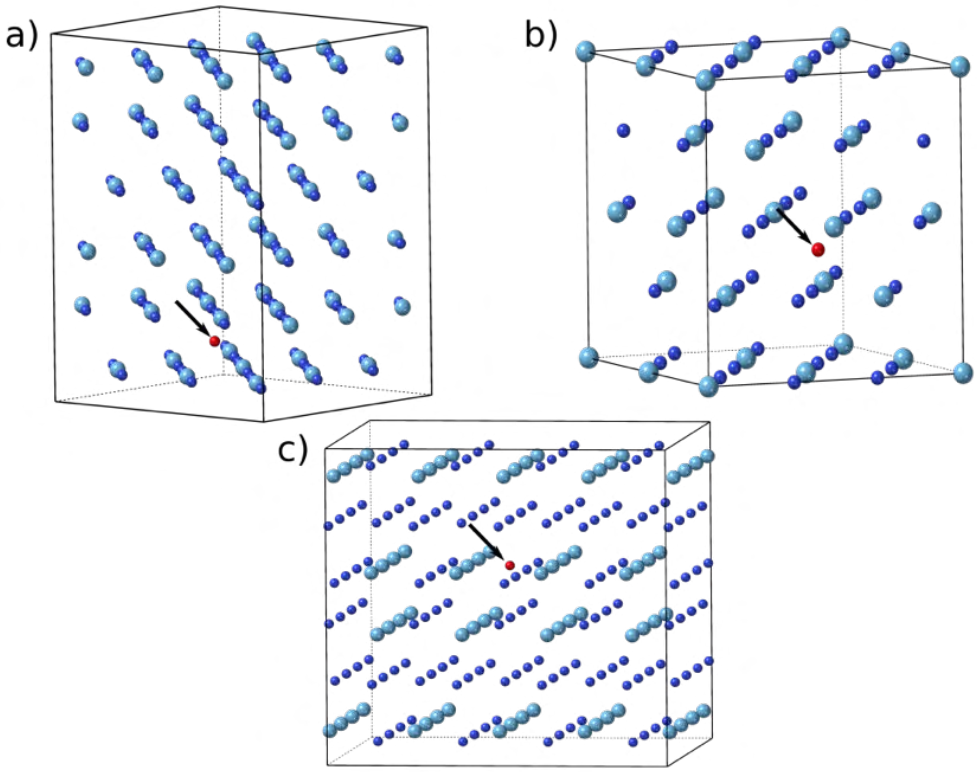

Figure 6-2. The interstitial site located for Frenkel and anti-Frenkel calculations for Ti and Si atoms in (a) C40, (b) C54, and (c) C49 structures. The interstitial site located for Frenkel and anti-Frenkel calculations for Ti and Si atoms in (a) C40, (b) C54, and (c) C49 structures.

Phase		$V_{Si/Ge}$	V_{Ti}	$Ti_{Si/Ge}$	$Ti_{Si/Ge}$	Frenkel	AntiFrenkel
$TiSi_2$							
C40		2.55	4.03	0.83	3.58	7.83	4.33
C49			2.71		4.34	6.49	
	2-NN	0.83	-	0.31	-	-	6.85
	4-NN	1.06	-	0.99	-	-	7.06
C54		2.49	3.85	0.95	4.26	7.50	7.28
$TiGe_2$							
C40		2.00	4.06	0.82	3.60	6.95	6.11
C49			1.87		3.40	6.49	
	2-NN	-0.004	-	-0.01	-	-	4.60
	4-NN	0.54	-	0.25	-	-	5.18
C54		1.53	2.95	0.37	3.74	7.35	6.27

Table 6-2. The formation energies for intrinsic point defects in eV calculated with PBE-GGA functional. Sites that are not relevant to the particular structure and defect are denoted by dashes.

sites are 1.06eV, respectively. The formation energy for V_{Ti} is 2.71 eV. The energies for Si_{Ti} and both the Frenkel and anti-Frenkel defects are all greater than 4 eV; thus, these defects are unlikely to be important. Moreover, these high Frenkel defect energies are consistent with the diffusion being a vacancy mechanism. From D'Heurle et al., the high Frenkel energy represents a closed pack structure suppressing interstitial diffusion.[120] Since the two lowest energies, Ti_{Si} and V_{Si}, both involve the loss of Si from the structure, these calculations predict that it is quite likely that C49 $TiSi_2$ will be Si deficient.

The defect energetics of the C40 and C54 structures are similar to each other with the enthalpy of formation of Ti_{Si} defect being less than 1 eV in both cases. Unlike the C49 structure, the formation energy of a Si vacancy is 2 eV or greater for both of these structures: these point defects are thus less likely to be important. Again, these structures may be Si deficient, but it is less likely than for the C49 structure.

Turning to the $TiGe_2$ structures, the formation energies of a titanium vacancy and the Frenkel and antiFrenkel energies are again high, and these defects are not likely to be relevant. Also, similar to $TiSi_2$, the Ti_{Ge} energy is the lowest defect energy for the C49, C54, and C40 structures, although in this case, it is considerably lower in the C54 structure (0.37 vs. 0.82 eV for the C40 structure). As in $TiSi_2$, the C49 structure again has the lowest defect formation energies.

The formation energy for Ti_{Ge} on the 2-NN sites is -0.01 eV, while the energy for a Si vacancy on the 4-NN site is -0.004eV. That is, the thermodynamically stable C49 $TiGe_2$ stoichiometry is predicted to be Ge deficient. These results can be compared with previous calculations. Using DFT with the GGA functional, Wang et al. found $E(V_{Si}) = 2.39$ eV and $E(V_{Ti}) = 2.40$ eV in the C54 structure.[147] The Table 6-2 value for the V_{Si} formation energy (2.51 eV) is close to their value. However, the formation energy for the titanium vacancy is larger (3.83 eV). This difference can be attributed to our calculations using a larger basis set for the Ti than that of Wang et al.; the presumption is that the larger basis set will result in a more reliable value of the defect energies.

Miglio et al. calculated defect formation energies for C49 with molecular dynamic (MD) simulations using a semiempirical tight binding interatomic potential.[148] However, their work only provided the formation energy for the 4-NN layer. They calculated the vacancy formation energy of Si to be 0.09 eV, which is considerably lower than this work's values of 0.85 and 1.06 eV. They determined the vacancy formation energy of Si in the C54 structure to be 1.41 eV[148], which is also lower than the 2.51 eV of this work. Given that DFT methods generally provide higher materials fidelity than tight-binding methods, this lack of agreement is not troubling.

A transition metal, such as Ti, has d-orbital valence shell, and the d-d bond is a significant contributor to the cohesive energy of the lattices.[149, 150] When an atom with an s and p shell, such as Si or Ge, is introduced into the transition metal lattice due to lattice expansion, reduces the bonds' contribution to lattice stability. In the case of silicide or germanide phases, a covalent hybridization between the transition metal d-orbital and the metalloid sp-orbital valence bands increases lattice stability. For this hybridization, the energy levels of the orbitals must overlap, and the crystal structure must have the correct symmetry to enable the hybridization. If the crystal does not have the correct symmetry, nonbonding states are created which do not contribute to stability. The interaction between Ti and Si atoms forms a bonding hybrid of the Ti d-orbitals and the p-orbitals, which increases stability. The hybrid bonding forms bonding orbitals below the Fermi level while antibonding and nonbonding orbitals form above the Fermi level. This behavior is observed in the total density of states plot as wide peaks above and below the Fermi level.

Although there is no bandgap, there is a region about the Fermi level which shows reduced electron density; this region has been called a pseudogap, and it arises from the bonding and anti-bonding associated with hybridization between atoms in the alloy.[151, 152] There are two important features to the pseudogap. First, the location of the Fermi level relative to the pseudogap provides insight into stability; second, the depth of the pseudogap well, at the Fermi level, is related to the strength of the covalent bonding.[151–155]

A Fermi level lower in energy than the pseudogap indicates unfilled bonding orbitals.[153, 154, 156] Previous works have noted the relative stability between $TiSi_2$ C49 and C54 structures based on the position of the Fermi level.[157][158–160] However, previous works have not plotted the DOS to determine relative stability between the $TiGe_2$ C49 and C54 structures, or the covalent stabilities between the $TiSi_2$ and $TiGe_2$ phases.

C49 has a DOS of 0.18 states per eV for C49, while C54 has 0.4 states per eV, indicating more electrons are localized in covalent bonds in the C49 structure. Also, the Fermi level for the C49 structure in Fig. 3 (a) is located at the minimum of the pseudogap, while the Fermi level for the C54 structure in Fig. 2 (b) is slightly below it. Therefore, based on the Fermi level position, the $TiSi_2$ C49 allotrope (filled orbitals) is expected to be more stable than the C54 structure (unfilled orbitals).[157][158–160]

Figures 6-3 (c) and (d) show the DOS for $TiGe_2$; this system shows a pseudogap as well. The Fermi level for C49 $TiGe_2$ is at the pseudogap minimum as it was for C49 $TiSi_2$. However, in contrast to $TiSi_2$ C54, The Fermi level for C54 $TiGe_2$ is now at the pseudogap minimum, so the C54 structure shows increased stability relative to $TiSi_2$. Therefore, unlike $TiSi_2$, C54 $TiGe_2$ has fully occupied bond orbitals since the Fermi level is shown in the pseudogap. Also, the DOS at the Fermi level for C49 $TiSi_2$ is 0.35 states per eV, while for C54 it is 0.31 states per eV. Based on the DOS in the pseudogap, it seems that the Ge interaction with Ti introduces additional hybridization thus stabilizing the structure. The DOS also suggests that the covalent bonding in C54 is stronger than in C49 $TiGe_2$.

The importance of an element's electronegativity for predicting alloy formation was first recognized by Miedema et al.[161] There is little difference in the Pauling's electronegativity of the elements: Ti (1.54), and Si (1.90) and Ge (2.01). The contribution of ionic bonding of a binary system, FI, as opposed to covalent bonding, is often estimated as $F_i = 1 - exp(-0.25\Delta X^2)$, where ΔX is the difference in the electronegativity of the components. This yields $F_i(TiSi_2) = 3.1\%$ and $F_i(TiGe_2) = 5.4\%$; this is, bonding for both systems is expected to be very largely covalent. Interestingly the ionic charges in fluorite-structured $NiSi_2$ were

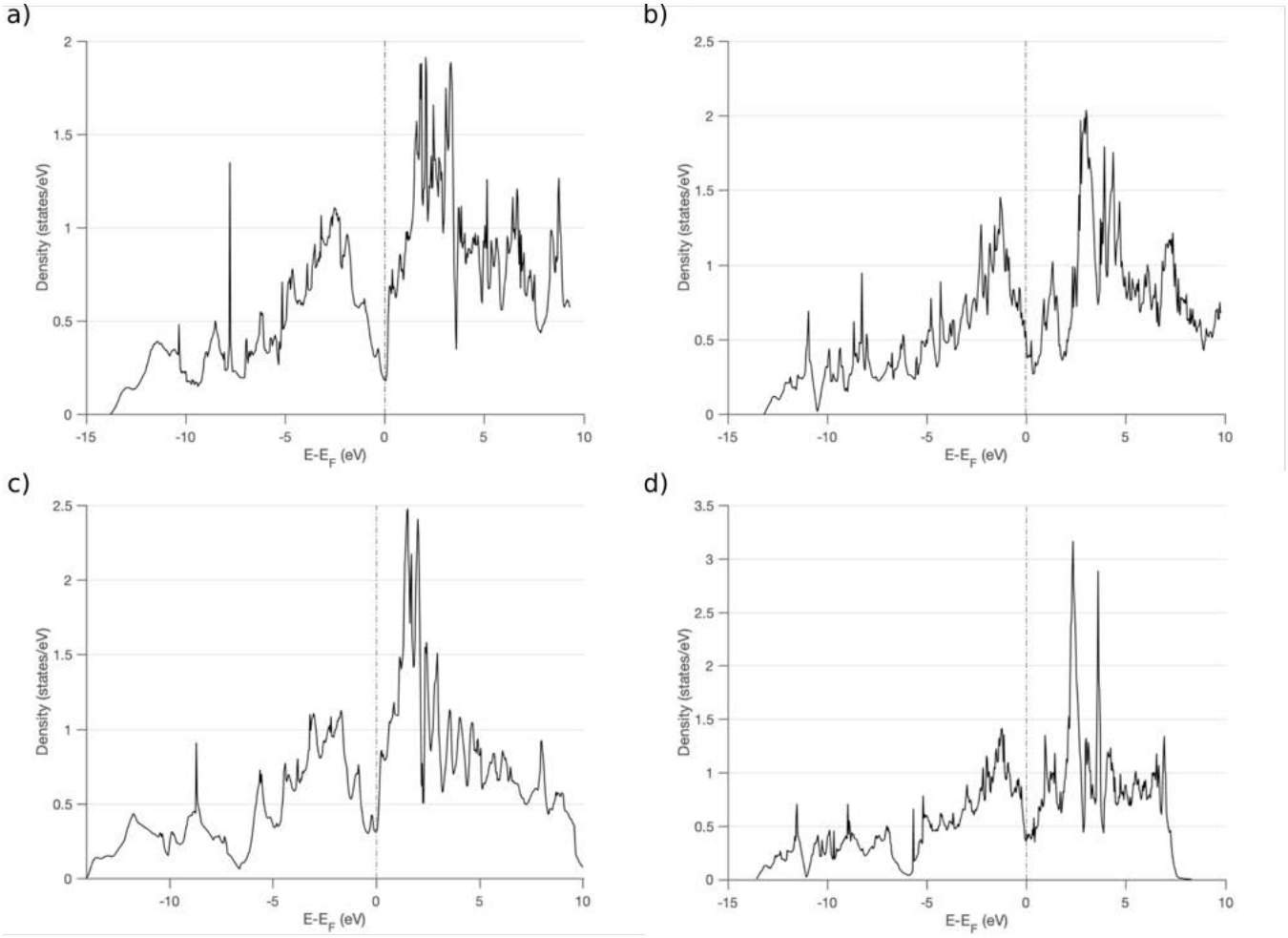

Figure 6-3. The DOS for: (a) C49 $TiSi_2$, (b) C54 $TiSi_2$, (c) C49 $TiGe_2$ and (d) C54 $TiGe_2$, calculated from SCAN functional and normalized by formula unit.

found to be +1.12 and -0.56 even though the electronegativity of Ni (1.91) is almost identical to that of Si.[162] To explicitly investigate the degree of covalency, we perform Bader analysis to determine the charge transfer in the silicide and germanide systems.

The charge transfer calculated from Bader analysis is given in Table 6-3. The C54 $TiSi_2$ phase shows significant ionicity, with the Ti atoms having charge +1.14e and Si atoms having charge -0.57e; interestingly, these are very similar to the values in $NiSi_2$. The C49 structure shows slightly lower ionicity. The Ti has a charge of +1.10e, while the 2-NN and 4-NN Si atoms have charges of -0.61e and -0.43e, respectively. The lower charge at the 4-NN site is presumably due to the covalent bonding with two additional neighbors.

Phase			Si	Ti
$TiSi_2$				
	C49			1.10e
		2-NN	-0.67e	
		4-NN	-0.43e	
	C54		-0.57e	1.14e
$TiGe_2$				
	C49			1.08e
		2-NN	-0.69e	
		4-NN	-0.39e	
	C54		-0.57e	1.14e

Table 6-3. Bader charges for TiSi2 and TiGe2

The charges in C54 $TiGe_2$ are identical to those in $TiSi_2$ despite the greater difference in the electronegativities. The C49 $TiGe_2$ structure also shows a very similar Ti charge to that in $TiSi_2$, but the apportionment of that charge to the 2-NN and 4-NN Si atoms is slightly different.

The charge transfer for C54 $TiSi_2$ was previously calculated by Wang et al.[147] They found the charge on Si to be -0.048e, which is less than 10% of the value determined here. Although this difference is large, variations of up to a factor of five have been seen for different methods.[144] In particular, this difference can be explained in terms of the choice of functionals and charge analysis type. Wang et al. determined the Mulliken charges using the GGA functional; the more accurate SCAN functional[136] was not available at that time. Mulliken charge analysis has been described as potentially unphysical due to the strong dependence of the charges obtained on the basis set.[163–165] The Bader charge analysis has the advantage of independence of basis set and convergence to a stable value. Therefore, we believe that the values determined here are more likely to be accurate.

As shown in $\Delta\rho_{diff}(r) = \rho_{phase}(r) - \sum_\alpha \rho_\alpha(r - r_\alpha)$, the charge density difference (CDD) is defined as the difference between the total charge density of the compound and constituent atoms. It therefore represents the charge redistribution when atoms are condensed to form a crystal. Thus, CDD is a valuable tool for assessing the degree of covalency and ionicity in

a bond. Like Bader analysis, CDD is a method based on charge density from DFT; so, the visualizations it generates complement the charge transfer calculations in Table 6-3.

Figures 6-3 through 6-6 show the CDD plots for each system, with the red regions represent charge accumulation, and the blue regions represent charge depletion. For the C49 allotrope, Figs. 6-3 (a) and (b) show a depletion region between the stacks; this forms the boundaries of the layered structure illustrated in Fig. 6-1 (a). The Ti atoms in Fig. 6-3 (a) show little direction of the charge accumulation, which indicates an absence of covalent bonding. These observations suggest that the layers are ionically bonded to each other, and charge depletion region contributes to the high sheet resistance measured for C49 films observed from experiments.[113–116]

Figure 6-3 (a) shows strong directional bonding between Si (blue) atoms through the center of the figure, which represents 3s-3p hybridization. Figure 6-3 (c) shows directional bonding between Ti (orange) atoms; the bonding is denoted by the red region with a definite ellipsoid shape, which represents 3d-3d bonding. Again, 3d-3d bondingis observed between Ti atoms in Fig. 6-3 (b). The regions between Ti and Si show charge depletion; so Fig. 6-3 suggests that there is no 3p-3d hybridization between the Si and Ti atoms. Bader analysis thus shows that the bonding between Ti and Si is due to partial charge transfer. We thus conclude that the observed pseudogap in the DOS is due to Si-Si and Ti-Ti covalent bonding.

In Fig. 6-3 (b), a blue depletion region is observed between the Ti and Si atoms with an anisotropic charge density for Ti. The reduced charge on the Ti atom represents the charge transfer to Si. Figure 6-3 (a) clearly shows more transfer of charge from the Ti to the 2-NN Si atoms than to the 4-NN Si atoms. This finding is not surprising due to the difference in the number of covalent bonds. Additionally, it is consistent with Bader analysis, which suggests that 2-NN takes more charge than 4-NN atoms.

For C54, charge accumulation is shown between Si atoms in Fig. 6-4 (a); three 3s-3p hybridization bonds link to three nearest neighbors. Figure 6-4 (b) shows d-d bonding between the Ti atoms, with the charge accumulation being isotropic for the center Ti atom. Figures

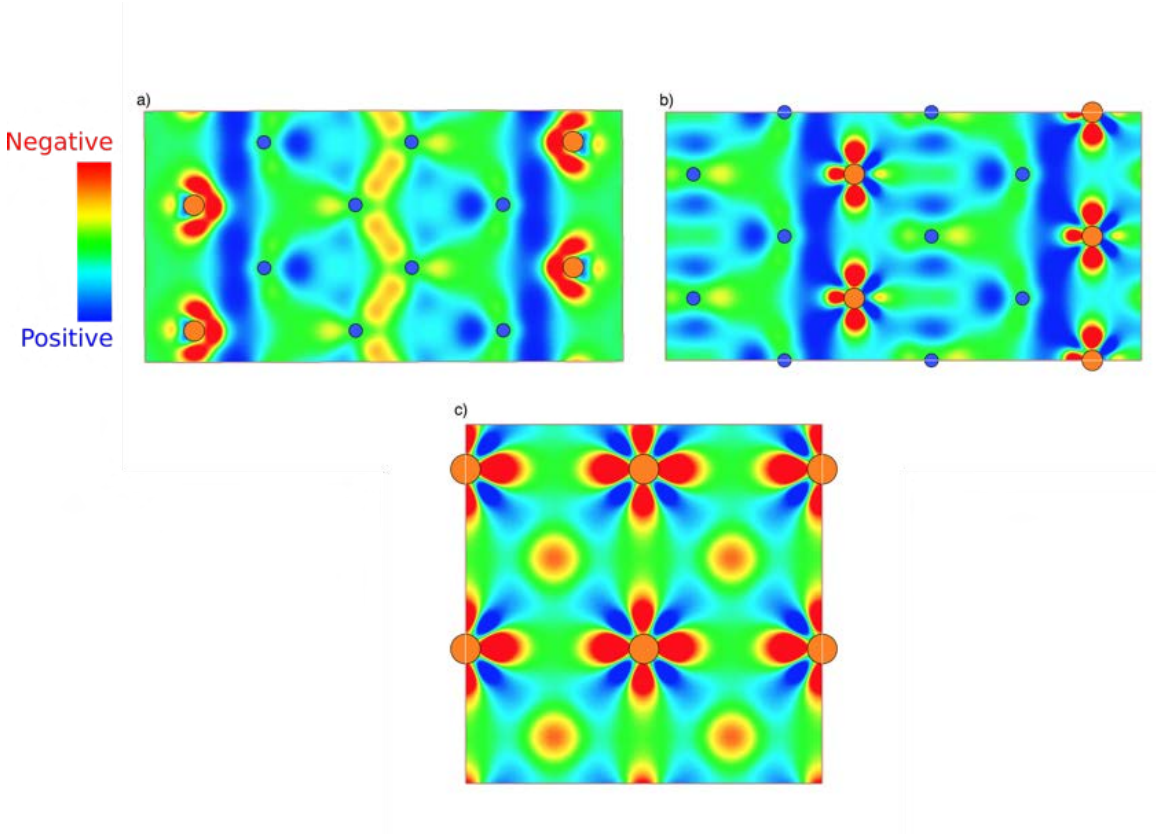

Figure 6-4. Charge density difference plot of C49 $TiSi_2$ looking into the (100) (a), (001) (b), and (010) (c) planes. Si (blue) and Ti (orange) atoms are located within the cross-section. The color legend represents the charge accumulation (red) and depletion (blue).

6-4 (a) and (c) show the charge depletion region around the Ti atoms, which relate to the charge transfer. The charge accumulation and depletion of the Ti atoms suggests an evenly distributed charge transfer to the Si atoms; this is consistent with Bader charge analysis in Table 6-3. No charge accumulation is observed between Ti and Si because the symmetry of the C54 structure does not allow Ti d-orbital hybridization with the Si p-orbitals.[152, 160] Figures 6-4 (b) and (c) show charge accumulation at the interstitial sites of C54. The differences between the $TiSi_2$ C54 and C49 structures are the isotropic charge transfer and the covalent bonds. C54 does not have the layer of 4-NN Si atoms, which suggests less hybridization. So, the reduction of hybridized bonding explains the increase of formation energy, and the reduction of covalent stability from the DOS plots.

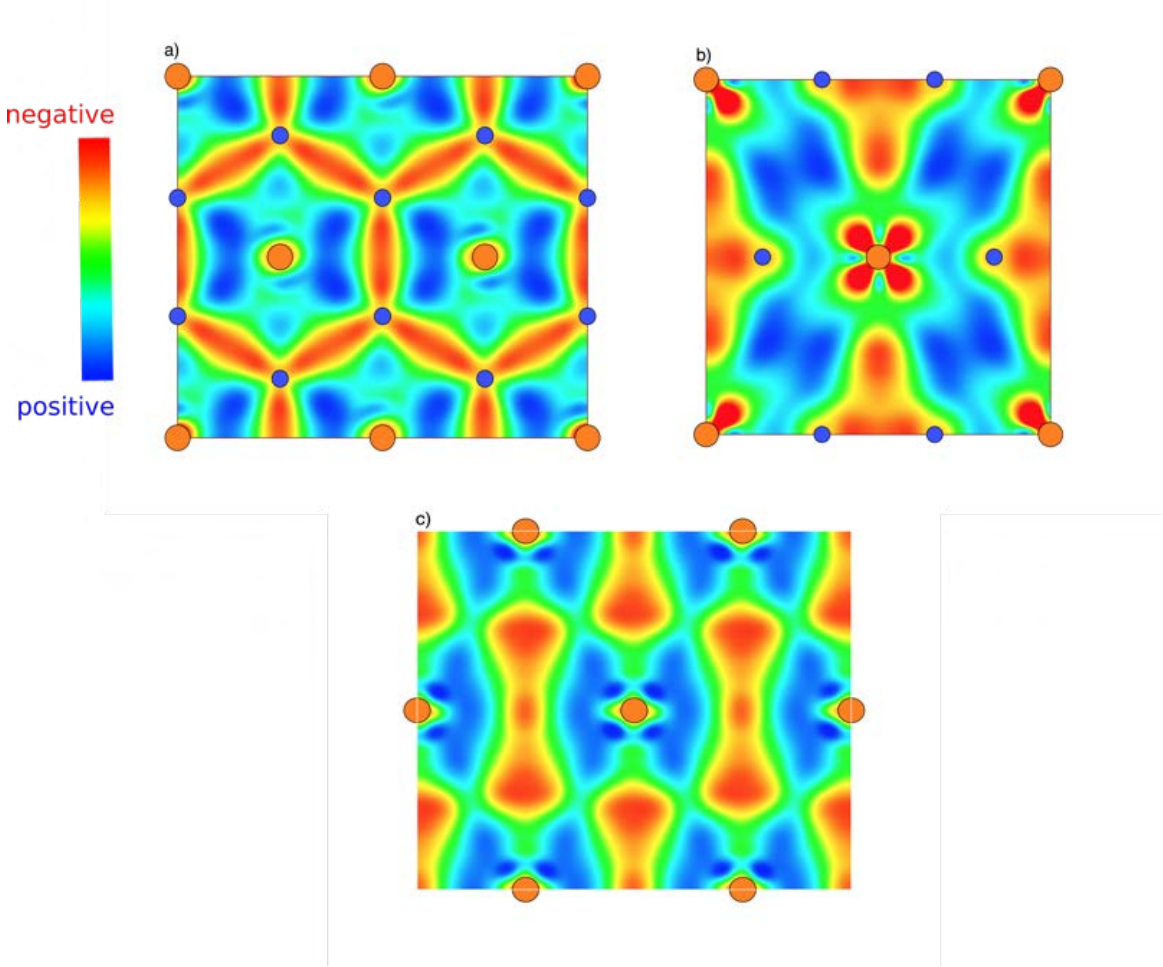

Figure 6-5. Charge density difference plots for the C54 $TiSi_2$ looking into the (001) (a), (100) (b), and (010) (c) planes. Si (blue) and Ti (orange) atoms are located within the cross-section. The color legend represents the charge accumulation (red) and depletion (blue).

From Bader analysis, The $TiGe_2$ and $TiSi_2$ allotropes show similar charge transfer; The Ti atom in the $TiGe_2$ and $TiSi_2$ C54 allotrope both transfer 1.14e, while the Ti atom in the C49 structure transfer 1.08e and 1.10e partial charge, respectively. This similarity is also evident in the CDD in Figs. 6-4 and 6-5. Charge accumulation is noticeable between the Ti atoms in $TiSi_2$ in Figs. 6-4 (b) and (c), indicating that 4d-4d hybridization also occurs for the C49 $TiGe_2$ system. In Fig. 6-5 (a), the same directional charge transfer is observed between the Ge atoms, which relate to 4s-4p hybridization. However, the accumulation region is broader than in C49 $TiSi_2$, indicating that the hybridized orbitals are less bound

than in $TiSi_2$. The introduction of the Ge atom increases the volume of the lattice structure which causes the d-orbital broadening. This broadening reduces the stability of the crystal; however, hybridization between a transition metal and metalloid lowers the energy of the crystal.[151, 152] Figures 6-5 (a) and (b) show charge accumulation between the Ge and Ti atoms indicating interaction; These panels suggest a 3s-3p hybridization between the unlike atoms.

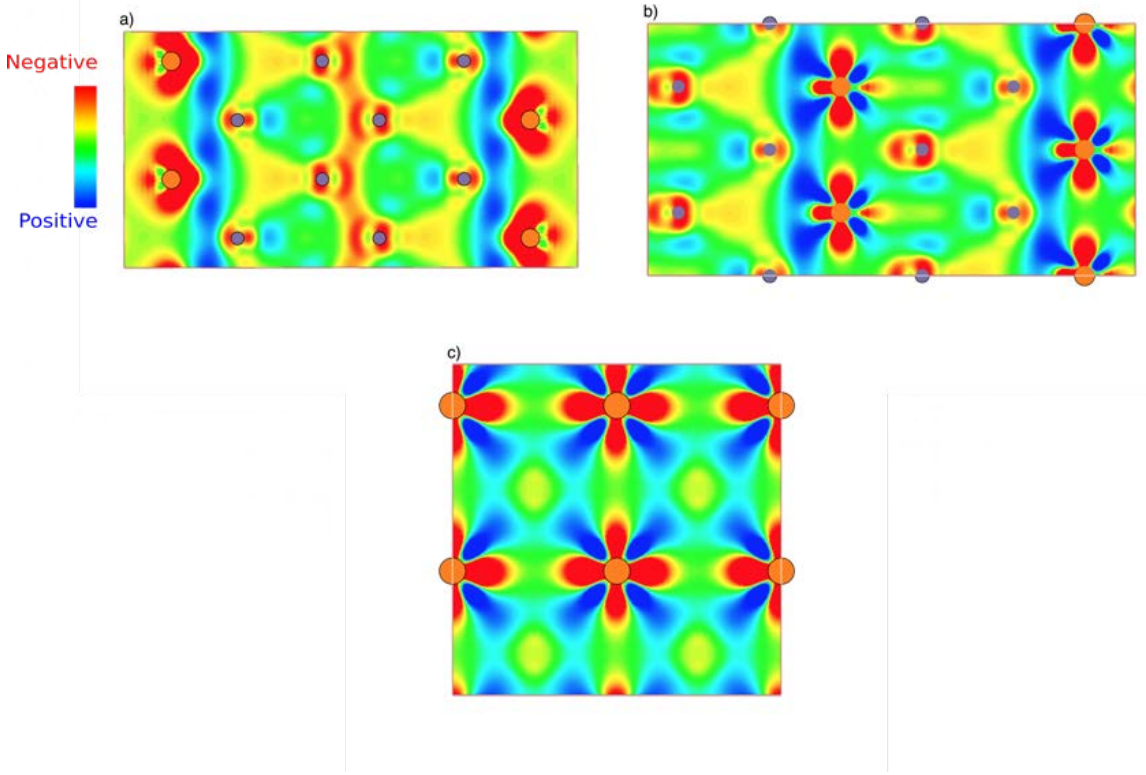

Figure 6-6. Charge density difference plots for the C49 $TiGe_2$ looking into the (001) (a), (100) (b), and (010) (c) planes. Ge (purple) and Ti (orange) atoms are located within the cross-section. The color legend represents the charge accumulation (red) and depletion (blue). The system shows similar electron density to C49 TiSi2, but more charge accumulation around the Ge atoms.

Figure 6-6 illustrates the CDD for $TiGe_2$ C54 allotrope; Figure 6-6 (a) shows the charge transfer between the Ti and Ge, and the 3d-3d hybridization between Ti atoms. The accumulation region between Ge atoms is wider than between Si atoms in Fig. 6-5 (a),

indicating that the electrons are less bound between Ge atoms. Like $TiGe_2$ C49, these findings point to hybridization between the Ti and Ge and are consistent with the stability inferred from the DOS. Unlike $TiSi_2$ C54, the 4s-4p hybridization lowers the formation energy for $TiGe_2$ C54. The reason for this is the interaction between Ti and Ge introduces more hybridization of orbitals than is present in $TiSi_2$ C54. The CDD plot for $TiGe_2$ C54 shows charge accumulation between the atoms supporting the increased interaction relative to $TiSi_2$ C54. Overall, the $TiGe_2$ bonding has more bonding similarities to the $NiSi_2$ and $CoSi_2$ than to $TiSi_2$.[162, 166]

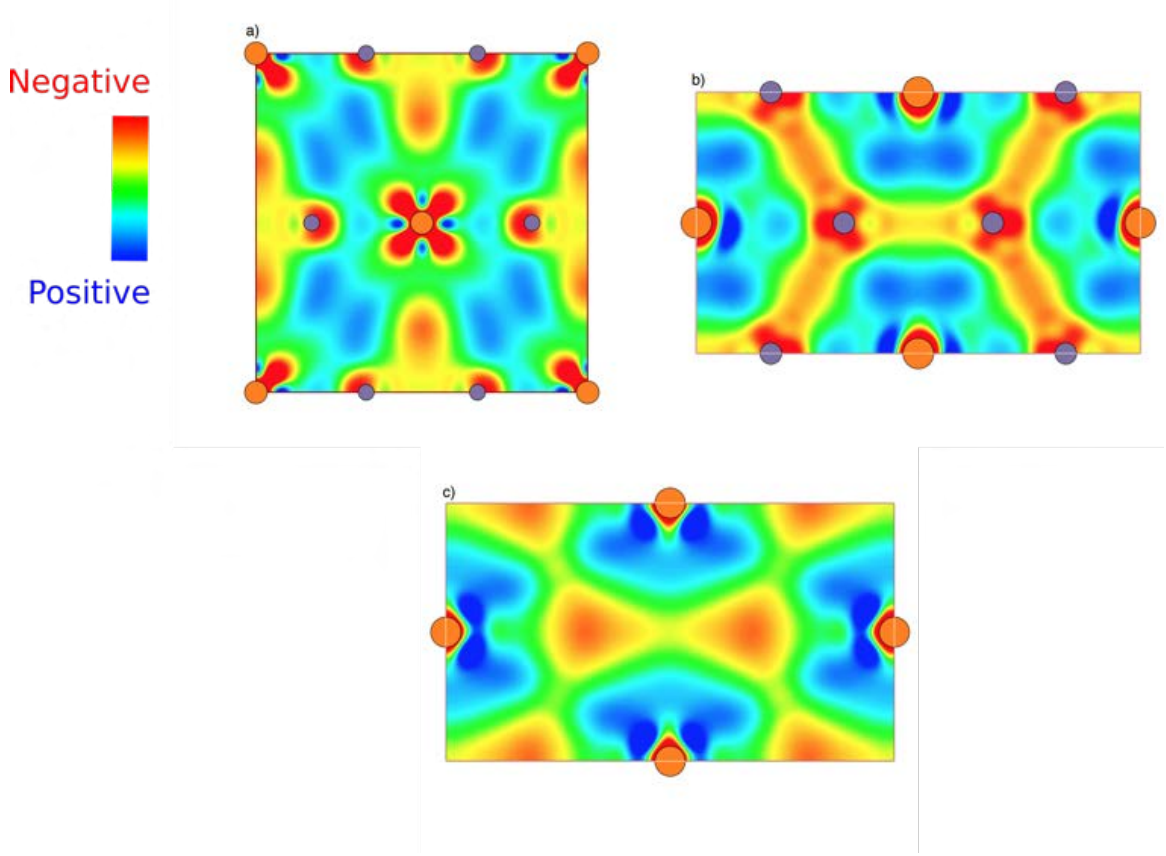

Figure 6-7. Charge density difference plots for the C54 TiGe2 looking into the (001) (a), (100) (b), and (010) (c) planes. Ge (purple) and Ti (orange) atoms are located within the cross-section. The color legend represents the charge accumulation (red) and depletion (blue). The system shows similar electron density to C49 TiSi2, but more charge accumulation around the Ge atoms.

For binary systems containing transition and non-transition metals with charge transfer, the point defect formation energies can be reduced with charge transfer between the anions

and cations[144]. As shown, the $TiGe_2$ and TSi_2 phases show a significant difference in formation energies for vacancies and substitution. The two phases also show partial charge transfer between Ti, Si, and Ge atoms. This partial charge transfer of these phases may be the reason for the low defect formation energies. Therefore, the partial charge transfer effect on stabilizing the $TiSi_2$ and $TiGe_2$ defects is explored with Bader analysis.

Bader analysis was performed to elucidate this relationship for the $TiSi_2$ allotropes. Only the nearest neighbor atoms around the defect are considered, so charge balance between these atoms is not expected. However, convergence was checked by matching the number of electrons in the potential files with the Bader analysis total electron output. The charge transfer was calculated in the same manner as the pure phase. The calculated total electron charge of an isolated atom species in the supercell subtracted the nearest neighbor defect atom. The difference determines the amount of charge gained or lost for the Ti (cation) and Si (anion) nearest neighbor.

Bader analysis is a limited tool for defect charge transfer for two reasons. First, as has been mentioned, it is a qualitative method. The second reason is related to the Bader volumes at the defects. For example, The effective total charge of a vacancy defect is expressed as $q_v = (q_{atom} - q_{vac}) - \sum_j \Delta q_j^{NN}$. Δq_j^{NN} is the charge difference of the nearest neighbors; these charges are listed in Tables 6-4 and 6-5. q_{atom} is the total charge of an isolated atom, which is trivial to determine. q_{vac} is the charge of the defect volume, which the atom once occupied. Though not always the case, the Bader analysis algorithms do not determine a Bader volume for defects and thus q_{vac} cannot be determined from the charge density, since the Bader algorithms are only designed to determine a volume related to an atom. With these problems in mind, the magnitude of partial charge transfer at the nearest neighbors will be used for an indirect measure of the Coulomb potential.

Table 6-4 shows the C49 $TiSi_2$ partial charge transfer of the nearest neighbor Si and Ti and the formation energy, with the defect energies for reference. Though the amount of charge transfer for the vacancy is unknown, it can be surmised that the region is electron depleted

Point Defect	Formation Energy (eV)	NN-Si Δq	NN-Ti Δq
V_{Si} 2-NN	0.83	-0.11e	0.38e
V_{Si} 4-NN	1.06	-0.45e	1.07e
V_{Ti}	2.71	-0.50e	1.05e
Ti_{Si} 2-NN	0.31	-0.57e	0.46e
Ti_{Si} 4-NN	0.99	-0.59e	0.9e
Si_{Ti}	4.34	-0.49e	1.1e

Table 6-4. Charge transfer from Bader analysis of the nearest neighbor atoms of the vacancy and substitution defects in C49 $TiSi_2$

Point Defect	Formation Energy (eV)	NN-Si Δq	NN-Ti Δq
V_{Si}	2.49	-0.51e	0.80e
V_{Ti}	3.85	-0.47e	0.87e
Ti_{Si}	0.95	-0.38e	0.72e
Si_{Ti}	4.26	-0.44e	0.92e

Table 6-5. Charge transfer from Bader analysis of the nearest neighbor atoms of the vacancy and substitution defects in C54 $TiSi_2$

and thus positive. The partial charge for both Ti_{Si} and Si_{Ti} substitution defects is positive. These values are 0.83e for the Ti substitution and 0.14e for the Si substitution. The positive defect center suggests that the nearest neighbor Ti introduces repulsive electrostatics, while the Ti substitution provides more electrostatic attraction with the nearest neighbor Si atoms. The Si nearest neighbor charges are similar, with the exception of V_{Si} 2-NN. The defects with formation energies below 1 eV show the smallest value for Ti charge: the V_{Si} 2-NN and Ti_{Si} 2-NN Ti charge values are 0.38e and 0.46e, respectively. These two defects have two nearest neighbor Si and four Ti atoms. The weighted partial charge becomes 1.52e for V_{Si} 2-NN and 1.84e for Ti_{Si} 2-NN. The Ti partial charge transfer for all defects above 1 eV is above 2.0e which suggests a lower Ti charge relates to lower formation energy.

Table 6-5 shows the C54 $TiSi_2$ partial charge transfer of nearest neighbor atoms. The Ti substitution yields a partial charge of 0.77e while the Si is 0.04e. The nearest neighbor Si partial charge is similar for all of the defects. The defect with the lowest formation energy is Ti_{Si}, which relates to a high Ti substitution partial charge and a lower positive nearest neighbor Ti charge.

The nearest neighbor Si interatomic distance is less than that for Ti for all cases, so its Coulombic potential contribution is greater than Ti nearest neighbors. The substitution defects show a higher positive partial charge for Ti than Si, which corresponds with lower formation energy. Due to the defect centers being positive, the positive nearest neighbor Ti contributes repulsive electrostatics, which does not stabilize defects. Also, lower positive partial charges for nearest neighbor Ti correspond with the lower formation energies.

To conclude, the partial charge transfer does affect the defect formation energies, but due to the limitations of Bader analysis, it is unclear how much the charge transfer reduces formation energy compared to lattice relaxation.

6.4 Discussion

The enthalpy of formation calculations for the $TiSi_2$ phase are mostly consistent with previous experimental and computational.[83, 116, 146, 167] The competition between the C49 and C54 has been the subject of much research. Previous experiments agree on the order of the formation, but the reasons for this order is debated. This work has shown the formation energy of C49 is lower than C54 and suggests some new arguments for the competition.

Via et al.[168] performed 460°C-540°C anneals on $TiSi_2$ C49 to introduce defects followed by an anneal to form C54. The activation energy for the transformation increased with defect concentration. They concluded that the transformation has a strong dependence on the point defect concentrations, and that this dependence is the reason for the inconsistent results on transformation kinetics among previous experiments. This dissertation's work supports the C49 allotrope as being much more defective compared to C54, consistent with the experiments.[167, 169] Therefore, this work suggests a component of the transformation competition is due to the low defect formation energies for $TiSi_2$ C49.

The V_{Si} and Ti_{Si} formation energies are considerably lower for the C49 structure than for C54; this suggests Ti-rich conditions for the C49 allotrope. Experiments support the C49 allotrope being Ti-rich near the Si interface, and these works show it co-exists with Ti-rich phases of Ti_5Si_3 and Ti_5Si_4.[170–172] The C49 allotrope being Ti-rich suggests that a wider

Ti concentration range is supported, which in turn could be a potential argument for why C49 forms first.

As mentioned above, the $TiGe_2$ system does not show a C49 precursor phase for the formation of C54.[127, 129] However, based on the work by Sun et al.,[88] this work's calculation for the $TiGe_2$ C49 energy is well below the upper limit for metastability. For the first time, this work showed the allotrope as potentially metastable; such metastability is consistent with experiment.[130]

The $TiGe_2$ C40 phase is not observed during the solid reaction, but this work combined with Sun et al. supports the possibility of the metastability of the structure. Experiments have shown the existing of the $TiSi_2$ C40 structure using nanosecond laser annealing experiments, in which the rapid cooling rate quenches metastable phases.[131–134, 173] Therefore, it seems possible that C40 $TiGe_2$ might be observable using the same nanosecond laser annealing techniques.

The point defect calculations of the $TiGe_2$ allotropes show a self-consistency and reflect TiSi2. The defects with formation energies below 1 eV for $TiSi_2$ are also low for $TiGe_2$, and both show a low substitution formation energy for Ti_{Si} and Ti_{Ge} but a higher energy for Si_{Ti} and Ge_{Ti}. The Frenkel defect formation energy is found to be high compared to the vacancy formation energy. This suggests the diffusion mechanism is likely to be vacancy dominant, which is experimentally supported for C54.[120] However, The C40 allotrope has never been synthesized, and the C49 has never been characterized, so this work provides predictions for these allotropes.

$Si_{1-x}Ge_x$ layers have become instrumental for introducing compressive strain to CMOS channels. These layers are coated with Ti for the creation of low contact resistance materials. These Ti-$Si_{1-x}Ge_x$ interfaces form the C54 structure of interest, but the $Ti(Si_{1-x}Ge_x)_2$ C54 structure forms at lower temperatures than $TiSi_2$ C54, which provides a higher thermal budget for semiconductor processing.[126]

This work has developed fundamental understanding of $TiGe_2$ C49 and C54 for applying to the $Ti(Si_{1-x}Ge_x)_2$ system: the C54 structure is the ground state structure because the Ge atom produces stable bonding orbitals. The extended Born model shows the stability of a binary alloy is a combination of ionic and covalent bonding. Based on these results, this work predicts that the Ge atom lowers the formation energy of the $Ti(Si_{1-x}Ge_x)_2$ C54. The defect formation energy is expected to be between those of the pure $TiSi_2$ and $TiGe_2$ binary phases, so C49 $Ti(Si_{1-x}Ge_x)_2$ should have a low defect formation energy and a higher concentration of defects. Extending the knowledge of defect concentration and activation energy, the C49-C54 $Ti(Si_{1-x}Ge_x)_2$ transformation is expected to express the same trend.

6.5 Chapter Summary

This work corroborates previous works in that $TiSi_2$ C49 is more thermodynamically stable than C54. The DOS plots show that the C54 covalent bonding is less stable than C49 due to unoccupied orbits. Bader analysis showed $TiSi_2$ to have charge transfer similar to $TiNi_2$. Based on the extended Born model, the stability of C54 must be dominated by the ionic bonding component.

An attempt is made to relate charge transfer with low defect formation energy. Bader analysis shows a trend of lower positive Ti partial charge with low formation energy. However, due to the limitations of Bader analysis, whether partial charge transfer or lattice relaxation is the dominant contributor could not be determined. The $TiGe_2$ allotropes are found to be similar to the $TiSi_2$ system in terms of charge transfer and defects. However, the most stable structure was found to be the C54 structure. This change in order of stability is consistent with differences in the DOS; the $TiGe_2$ C54 structures show fully occupied orbitals for stronger covalent bonding. The $TiGe_2$ C49 structure may not be the precursor phase for C54, but this work shows the allotrope to be metastable. Therefore, this work aligns with experiments suggesting increased favorability to form C54 $Ti(Si_{1-x}Ge_x)_2$ due to the C49 structure being less favorable for Ge. Also, The $TiGe_2$ C40 allotrope is shown to be metastable; but unlike C49, it has never been synthesized in the lab.

In conclusion, The $TiGe_2$ phase's ground state is the C54 allotrope, which supports the mixing of Ge with $TiSi_2$ will shift the thermodynamics to C54 favorability. The $TiGe_2$ C54 phase shows covalent bond stability, which is attributed to the lower formation energy. Thus, based on the work in this chapter, the introduction of Ge into $TiSi_2$ processing will stabilize the covalent bond and lower the enthalpy of formation.

CHAPTER 7
AB-INITIO CALCULATIONS OF TI($SI_{1-X}GE_X$)$_2$ C40, C49 AND C54 ALLOTROPES AND NANOSECOND LASER ANNEALING OF TI-($SI_{1-X}GE_X$)$_2$ BILAYERS

7.1 Background

The disilicide (e.g., $TiSi_2$) is formed from the heating of a bilayer system. The metal can be e-beam evaporated or sputtered on to a substrate to form the bilayer. The Ti-Si bilayer is heated to high temperatures to form the low contact resistance silicide. However, the high temperatures pose a problem for semiconductor processing since silicide formation is just one step of many. The additional high temperature heating can cause additional diffusion or other issues reducing yield. The introduction of rapid thermal annealing (RTA) allows the silicide to be formed within 60 seconds. Though the RTA reduces the anneal time, the RTA heats the whole wafer causing slower cooling. The semiconductor technology nodes continue to scale down (modern transistors are at the 7 nm scale), which demands more fine-tune control of heating. Also, highly doped films are paramount to reduce the contact resistance. The need for highly activated films to reduce contact resistance further reduces thermal budget due to deactivation. One approach for tackling thermal budget with silicides is reducing the transformation temperature of the silicide. The transformation temperature can be reduced with $Si_{1-x}Ge_x$ films that have the added benefit of providing compressive strain on the channel for enhanced carrier mobility. Additionally, the thermal budget can be improved using laser annealing. Unlike the RTA, laser annealing does not heat the whole wafer, thus provides more heating control. The laser heats a micron depth of material, so the substrate provides undercooling, which lowers the temperature at a much faster rate than RTA. This fast cooling rate enables high activation to be quenched before deactivation. If a combination between Ti($Si_{1-x}Ge_x$)$_2$ C54 transformation with laser annealing could be achieved, The semiconductor industry would have a new option for producing low contact resistance nMOS transistors that improves thermal budget.

The pMOS device has an additional problem, that is the p-type (commonly boron) solubility limit in Si is lower than n-type impurity doping.[174] thus, the solubility limit of

p-type limits contact resistance reduction of CMOS devices. $Si_{1-x}Ge_x$ can be applied as an intermediate layer between the Si and metal to remedy this issue. The $Si_{1-x}Ge_x$-Si interface conduction bands are aligned while the valence bands are offset. Furthermore, the band gap of $Si_{1-x}Ge_x$ is more narrow, which lowers the Schottky barrier height for p-type doping.[175] The barrier height can be further reduced with the introduction of a germanosilicide. However, previous experiments covering the metallization transformations into germanosilicides and electrical properties is limited compared to disilicides.

Figure 7-1 shows the accumulated work on sheet resistance thus far for $Ti(Si_{1-x}Ge_x)_2$ C49 and C54. In this figure, the high resistance C49 allotrope corresponds to a sheet resistance near 10 Ω/sq. The $Ti(Si_{1-x}Ge_x)_2$ C49 is formed between 500°C and 600°C, which is the general consensus for previous works.[176][125][177] A sheet resistance below 3 Ω/sq corresponds to the low resistance allotrope C54. The previous works reach a minimum sheet resistance then higher temperatures begin raising the sheet resistance. This increase in Fig. 7-1 is due to agglomeration of the germanosilicide and Ge segregation. Mostly, the works agree with solid reaction of Ti-$Si_{1-x}Ge_x$ bilayers. However, the work of Lai et al. measures the same sheet resistance but at higher temperatures. The lowest sheet resistance indicating the presence of C54 occurs at 800°C. The Lai et al. experiment utilized three layers: a capping Ti layer, a fully relaxed $Si_{1-x}Ge_x$, and a strained $Si_{1-y}Ge_y$ layer in contact with (001) Si substrate. The reason why the three layers raise the formation temperature is due to the additional strain that the $Si_{1-y}Ge_y$ layer introduces.

The solid reaction of Ti-$Si_{1-x}Ge_x$ bilayers has an additional processing challenge over disilicide formation: that is Ge segregation, this segregation process in $Si_{1-x}Ge_x$-Si heterojunctions is well known.[179] From TEM, SEM and XRD, Aldrich et al. studied the solid reaction of Ti-$Si_{1-x}Ge_x$ and observed the following sequence.[117, 176, 180] Once the Ti layer is fully reacted, the resulting germanosilicide layer has the same Ge and Si concentration as the substrate $Ti(Si_{1-x}Ge_x)_2$- $Si_{1-x}Ge_x$. The Si and Ge continue to diffuse into the germanosilicide layer and grain boundaries. The Si replaces the Ge in C54, and the Ge

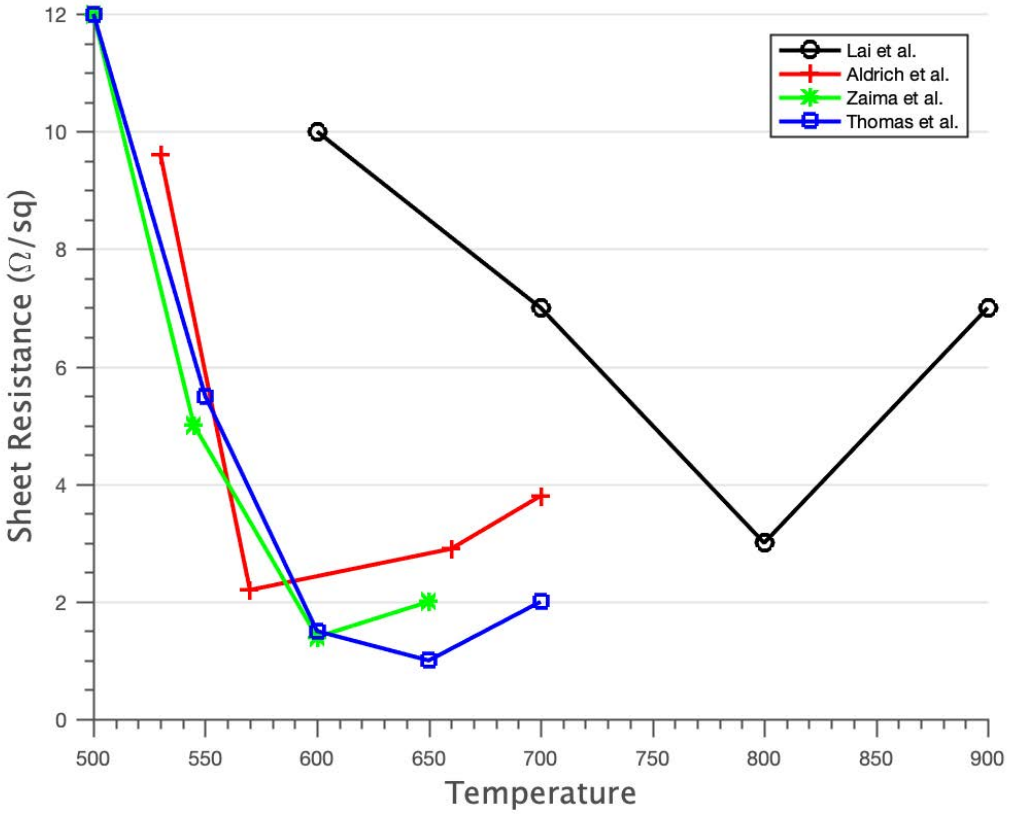

Figure 7-1. A compilation of previous experiments is shown for forming $Ti(Si_{1-x}Ge_x)_2$ C54. The outlier data of Lai et al. is due to the introduced strain during the transformation[176][125][177][178]

is driven to segregate into the grain boundaries. A Ge-rich $Si_{1-z}Ge_z$ alloy forms in the grain boundaries until islands are visible with SEM. After some time, $Si_{1-x}Ge_x$ substrate, $Ti(Si_{1-x}Ge_x)_2$ germanosilicide, and $Si_{1-z}Ge_z$ islands reach an equilibrium where $y<x<z$ represent the relative Ge concentrations. Aldrich et al. proposed a model based on the heat of formation for $TiSi_2$, $TiGe_2$, and $Ti(Si_{1-x}Ge_x)_2$ C54. The heat of formation for $TiSi_2$ C54 is lower than $TiGe_2$, so the driving force for Ge segregation is lowering crystal energy. The entropy of mixing was not included in the studies. The same segregation was observed for $Ti(Si_{1-x}Ge_x)_2$ C49 but at lower annealing temperatures ($<530°C$ for C49 and $>570°C$ for C54).[181] The reason for the different segregation temperatures between C49 and C54 is unknown.

Silicides have been synthesized with pulse lasers using bilayers of a metal and Si substrate. Most of the studies were performed in the melt regime with near-noble metals. Previous works found the composition and microstructure of the silicide are different when grown in a furnace than by RTA.[182] The reason for the difference from thermal heating is the heating and cooling rate of laser annealing (on the order of 10^{10} Ks^{-1}). These short pulses enable the formation of metastable materials; thus, laser annealing provides an avenue for time resolved phase formation experiments.[183] Laser annealing has formed a metastable structure of $TiSi_2$ C40, which can bypass the C49 structure forming a complete C54 layer.[131–133] Though most studies focus on the laser melt region; silicide formation has been reported with fluences well below melt.[182]

Chen et al.[184] reported the earliest synthesis of $TiSi_2$ C54 with laser annealing. The Ti film thickness was 35 nm deposited onto (001) Si substrate. The laser system was a Q-switched Nd:YAG laser with a pulse width of 155 ns and a repetition rate of 10 kHz. The scanning speed and spot size of the laser resulted in an exposure time between 0.25 and 2.5 ms. The laser annealing was performed in air ambient. A combination of TEM, EDS, and Raman results determined the presence of $TiSi_2$ C54 with unreacted Ti at the surface. Based on computer simulation, Chen et al. showed the temperature remained below the melting point of Ti and Si. Thus, a solid reaction process is responsible for C54 formation. The reaction kinetics was studied for both reaction and diffusion limited cases. The silicide growth was found to follow a diffusion limited process.

Lu et al.[185] performed laser synthesis of $TiSi_2$ C54 with both a c-Si and a-Si substrates. The Ti thickness was 35 nm with a TiN capping layer of 15 nm. A continuous wave CO_2 laser was utilized with an exposure time in the millisecond regime. The sheet resistance measurements were performed with C54 being measured below 3 Ω/sq at a fluence of 1.25 J/cm^2. XRD measurements confirmed that the fluence necessary for C54 transformation is reduced to 1 J/cm^2 for amorphous Si substrate.

In this work, both a computational and experimental component are applied to the $Ti(Si_{1-x}Ge_x)_2$ material. The computational portion investigates the role of Ge concentration in the C40 C49, and C54 allotropes. The effect of mixing energy with Ge concentration and temperature is explored from first principles. The experimental component exposes bilayers of Ti-$Si_{1-x}Ge_x$ with laser pulses. The experiment is a first attempt to apply nanosecond laser pulses to achieve solid reaction of Ti-$Si_{1-x}Ge_x$ into $Ti(Si_{1-x}Ge_x)_2$.

7.2 Computational Methods

The calculations performed in this chapter are at the level of density functional theory using the Vienna Ab initio Simulation Package (VASP). For the exchange-correlation, the Generalized Gradient Method (GGA) and the Strongly Constrained and Appropriately Normed (SCAN) functional are used for calculating the enthalpy of the pseudobinary allotropes.[24–27, 29, 38, 56, 135, 136] The [3d 4s 4p] orbitals are included for the calculations with Ge potentials, while the [3d 4s] orbitals were included for the calculations with Ti potentials. The Si potential included [2s 2p] orbitals. The plane-wave cutoff is 520 eV. The volume and ions is relaxed simultaneously until the force on each atom was less than 0.01 eV/Å and a stress less than 0.02 GPa. Due to the presence of Ti metal atoms, Methfessel-Paxton was necessary for electron minimization because metal atoms introduce variational electron occupancies.[140] The Methfessel-Paxton method calculates more accurate forces for phonon calculations. The smearing of the Methfessel-Paxton method was converged to 0.05 eV width. The smearing is converged when the free energy and total energy of the calculation differ by less than 1 meV per atom.[186]

The Alloy Theoretic Automated Toolkit (ATAT) package[187][188][189] was used to generate the enthalpies of formation for C40, C49, and C54 $Ti(Si_{1-x}Ge_x)_2$ allotropes. The $TiSi_2$ phase unit cell relaxed in Chapter 6 was transformed into a primitive unit cell (as required by the ATAT framework). This primitive unit cell was used as the prototype for the increasing Ge concentration from x=0 to 1. For predicted $Ti(Si_{1-x}Ge_xx)_2$ structures, A Monkhorst-Pack k-point mesh[137] was used with k-point per reciprocal atom (KPPRA) of density 10000.

The bulk $Si_{1-x}Ge_x$ phase is a random alloy with a solidus/liquidus phase boundary.[190] The determination of an ordered or random arrangement of Si and Ge in $Ti(Si_{1-x}Ge_x)_2$ has not been a subject of study. Therefore, to construct a random phase, the efficient Monte Carlo algorithm of the ATAT package[57] was used to generate a special quasirandom structure (SQS). A cubic supercell of 90 atoms was generated for concentrations of x=0.1 to 0.90 with the Ti atoms at static positions. Once the SQS was converged, the ions and volumes for each supercell were simultaneously relaxed using the VASP package. A 2x2x2 Monkhorst-Pack scheme was utilized for SQS relaxation.

The enthalpy of mixing for the SQS $Ti(Si_{1-x}Ge_x)_2$ pseudobinary is expressed for each allotrope by:

$$\Delta H_{mix} = E(Ti(Si_{1-x}Ge_x)_2) - (1-x)E(TiSi_2) - xE(TiGe_2) \tag{7-1}$$

Where $E(TiSi_2)$ and $E(TiGe_2)$ are the reference states of total energy per active site (Si and Ge sites). The $TiSi_2$ and $TiGe_2$ phases have the same crystal structure, so each $Ti(Si_{1-x}Ge_x)_2$ allotrope may show spinodal decomposition.[191]

This reference for enthalpy of mixing is the starting point for determining the spinodal transformation temperature. To calculate this temperature, the Gibbs free energy is related to the enthalpy:

$$\Delta G(x,T) = \Delta H_{mix} - S(x)T \tag{7-2}$$

Where ΔH_{mix} is calculated from DFT, T is the temperature, and $S(x)$ is the configurational entropy. If the Si and Ge atoms are random in $Ti(Si_{1-x}Ge_x)_2$, the configurational entropy is calculated.

$$S(x) = -k_b(xln(x) - (1-x)ln(1-x)) \tag{7-3}$$

where k_B is the Boltzmann constant, x is the Ge concentration. ΔH_{mix} is described as a regular solution given by:

$$\Delta H_{mix} = \Omega x(1-x) \tag{7-4}$$

Where Ω is the interaction parameter, this coefficient is related to the ordering of the pseudobinary system. The sign of the interaction parameter suggests how the Gibbs free energy is minimized. A Positive parameter suggests Si-Ge bonds lower the Gibbs free energy than Si-Si and Ge-Ge bonds.

The interaction parameter is unknown for all the $Ti(Si_{1-x}Ge_x)_2$ allotropes. To determine the coefficient, the total energy for each SQS concentration was calculated using DFT. Knowing the total energy for the pure phases, the data points enthalpy of mixing was calculated. The enthalpy of mixing function was fit to the data points from DFT using a linear regression fit. From here, the Gibbs free energy can be calculated as a functional of temperature and the spinodal decomposition of $Ti(Si_{1-x}Ge_x)_2$.

7.3 Computational Results

The enthalpy of formation for pseudobinary $Ti(Si_{1-x}Ge_x)_2$ for allotropes is displayed (see fig. 7-2). The enthalpy, as a function of Ge concentration, is reference to the $TiSi_2$ and $TiGe_2$ pure phases. Figure 7-2 (a) and (b) show the C40 allotropes for the PBE-GGA and SCAN functional, respectively. The energies appear to agree between the two functionals; except that, the SCAN functional determines some additional structures with lower formation energies than PBE-GGA. Both functionals show energy increase between Ge concentrations of 0 to 0.5, and a subsequent decrease between 0.5 and 1.0 concentration. This behavior is related to the references being the same structure, and it indicates spinodal decomposition. The C49 allotropes is displayed in Fig. 7-2 (c) and (d). For this structure, the PBE and SCAN functionals show a strong difference in energies. The structure with lowest formation energies for PBE-GGA, especially between 0.30 and 0.70, show a shift lower into lower energy for the SCAN functional. Furthermore, The SCAN functional predicts ground states for C49 at 0.5 concentration, which supports $Ti(Si_{1-x}Ge_x)_2$ as being an ordered phase. In Fig. 7-2 (d), a structure of 0.3 Ge concentration is close to the convex hull line, and its energy is less than 1 meV above the line. A final note, the SCAN functional suggest the C49 does not experience spinodal decomposition. However, the PBE-GGA also does not

support spinodal decomposition, but some structure energies are above zero, thus it cannot be ruled-out. The disagreement between the two functionals is attributed to the SCAN functional's superior ability to handle simultaneous bonding types. From Chapter 6, The $TiSi_2$ and $TiGe_2$ phases were found to have both a covalent and ionic component to the enthalpy of formation. Therefore, for C49, the SCAN functional may calculate stronger covalent bonding, which lowers enthalpy of formation. An additional study of the C49 $Ti(Si_{1-x}Ge_x)_2$, like that of chapter 6, should divulge why PBE-GGA and SCAN calculate different formation energies. Figure 7-2 (e) and (f) shows an agreement for C54 between SCAN and PBE-GGA. That is, a spinodal decomposition is supported to be observed in experiment. Looking at the lowest formation energies produced, the SCAN functional results of Fig. 7-2 (f) do show lower formation energies with some structures lowering by more than 5 meV per site. Though many structures show enthalpy above the pure phases, the results of Fig. 7-2 do not suggest that the Ge concentration reduces structure stability. The reference choice suggests the $TiSi_2$ and $TiGe_2$ exist in equilibrium. $Ti(Si_{1-x}Ge_x)_2$ is grown as a bilayer of Ti and $Si_{1-x}Ge_x$, which suggests a Ti-rich reference.[117, 180, 192, 193] The mixing enthalpy of $Ti(Si_{1-x}Ge_x)_2$ needs further study with other reference energy choices, so a complete picture of Ge role in $Ti(Si_{1-x}Ge_x)_2$ allotropes. results suggest the materials will tend toward spinodal decomposition (i.e., segregation). This behavior is the result of $TiSi_2$ and $TiGe_2$ having the same structures.[191]

The special quasirandom structure results using 90 atoms is shown in Fig. 7-2. The data shown is calculated from PBE-GGA, and the enthalpy of mixing is imposed on the data from Fig. 7-2 (a), (c), and (e). The red line represents the linear regression fit of $\Delta H_{mix} = \Omega x(1-x)$, where Ω is the unknown interaction parameter to be fit. The error of the fit between the quasirandom structure and curve is due to two major components: the PBE-GGA formation energy being influenced[194] by the presence of both semiconductor and metallic atoms, and the quasirandom structure not being truly random. Figure 7-3 (a) shows Both the ordered and quasirandom structures support spinodal decomposition of $Ti(Si_{1-x}Ge_x)_2$

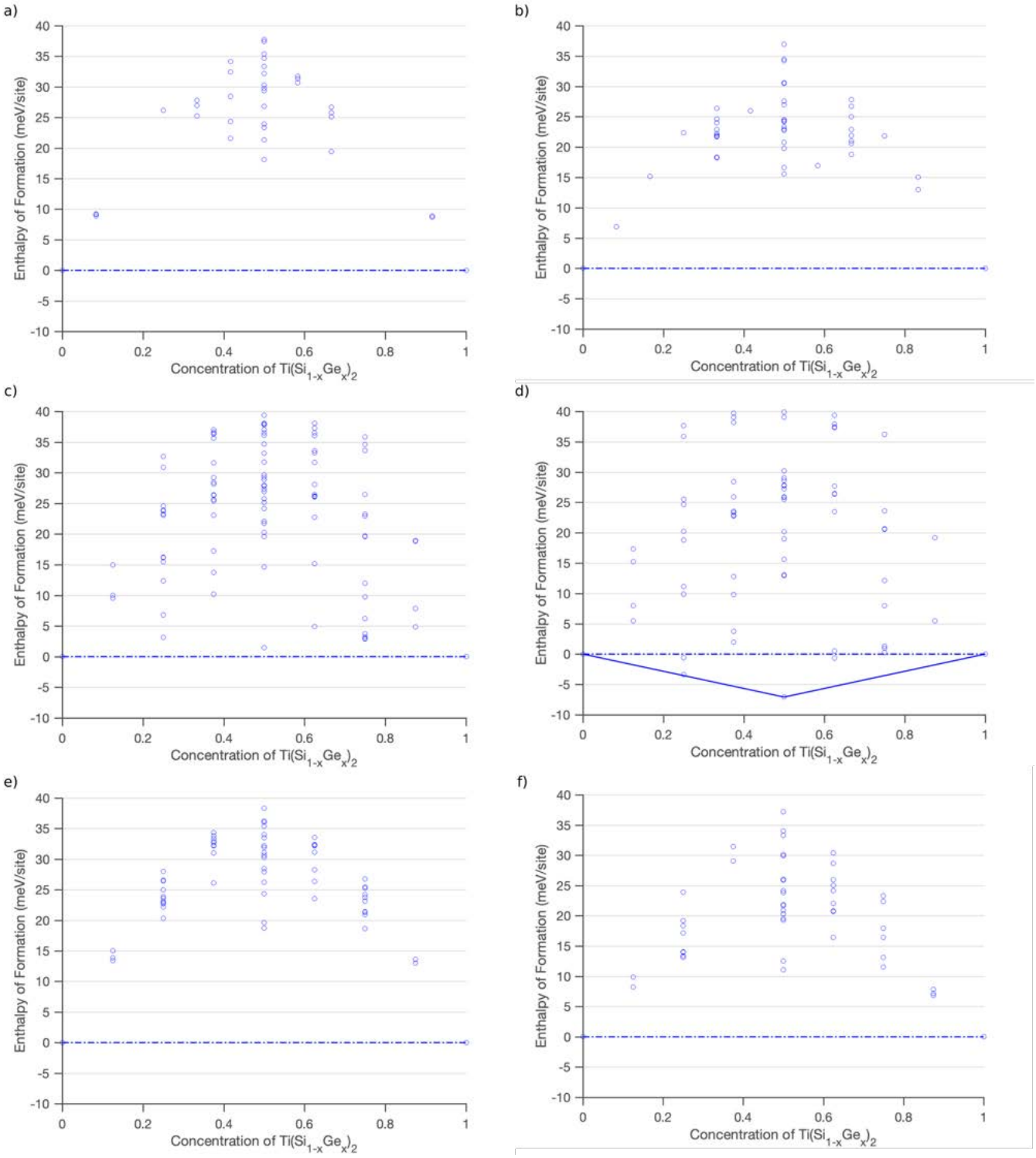

Figure 7-2. Pseudobinary enthalpy of mixing for $Ti(Si_{1-x}Ge_x)_2$ allotropes with both the PBE (a, c, and e) and SCAN (b, d, and f) functionals shown. The data shown is the energy as calculated by VASP for numerous ordered structures. The functionals appear to agree for C40 (a and b) and C54 (e and f) structures.

C40. Also, the enthalpy energy for quasirandom structures are not the lowest energies for all concentrations. Focusing on the enthalpy fit, the quasirandom structures have a lower energy for concentrations of Ge around 0.10 and 0.9. The C49 quasirandom energies in Fig. 7-3 (b) support a spinodal decomposition. However, the concentrations closer to 0.5 are among the highest energies for C49. This result suggest the C49 structure is more likely to be ordered. The result for the C54 allotrope is shown in Fig. 7-3 (d). The C54 allotrope shows a similar trend as C40. The ordered structures approach concentrations of 0.5 are much lower than the quasirandom structures, and the ordered and quasirandom structures support a spinodal decomposition.

Figure 7-4 (a), (b), and (c) show plots generated from the regular solution model for $Ti(Si_{1-x}Ge_x)_2$ C40, C49, and C54. These figures are generated with adding the logarithmic contribution of entropy $-S(x)T$ to the fitted enthalpy of mixing. The resulting Gibbs energy of mixing for C40 in Fig. 7-4 (a) shows a spinodal region starting at room temperature. This downward curvature about 0.5 concentration suggests a uphill diffusion mechanism. This suggests a non-uniform concentration of solute Ge atoms as the atoms diffuse from high concentrations to low concentrations. Thus, the Ge atoms will unmix forming regions of $Ti(Si_{1-a}Ge_a)_2$ and $Ti(Si_{1-b}Ge_b)_2$. The $Ti(Si_{1-a}Ge_a)_2$ and $Ti(Si_{1-b}Ge_b)_2$ represent two simultaneous concentrations of $Ti(Si_{1-x}Ge_x)_2$. The uphill diffusion ends for temperatures above 700 K. The C49 (see Fig. 7-4 b) and C54 (see Fig. 7-4 c) show the same spinodal behavior with uphill diffusion stopping above 700 K. However, the energy calculations for C49 does not support a disordered phase, so the spinodal behavior is not likely to be observed.

7.4 Experimental Methods

Epitaxial c-$Si_{1-x}Ge_x$ ($x = 0.1$, 0.2, and 0.3) films is grown on (001) Si substrate with a thickness of 45 nm. To create a Ti-$Si_{1-x}Ge_x$ bilayer, e-beam evaporation deposited 5 nm of Ti, and a subsequent 3nm layer of TiN is deposited using atomic layer deposition. The purpose of TiN is to protect the Ti layer from oxidation during nanosecond laser annealing in an air ambient environment. The sheet resistance of the samples is measured with Van Der Pauw

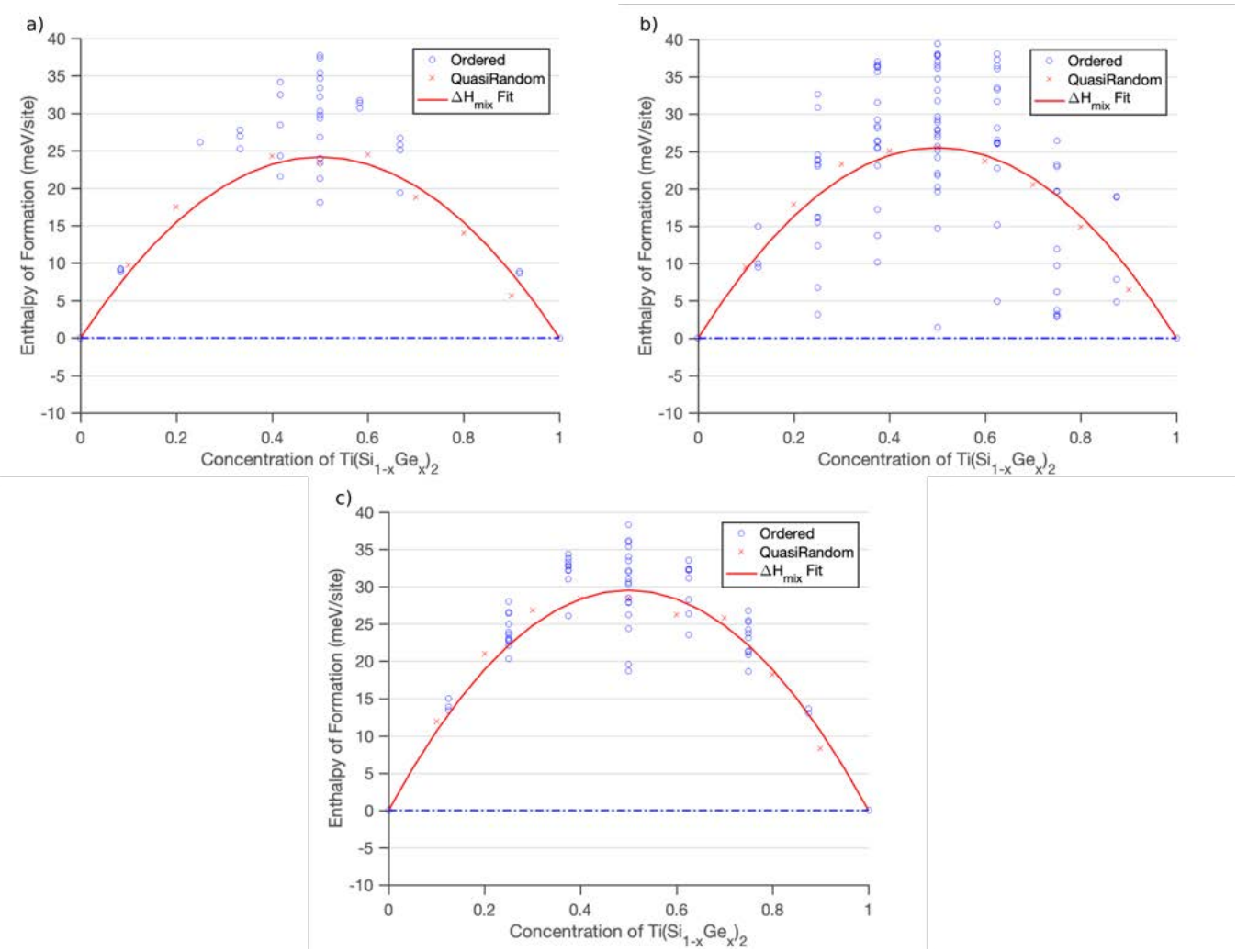

Figure 7-3. The Enthalpy of Mixing from SQS cells is shown for $Ti(Si_{1-x}Ge_x)2$ C40 (a), C49 (b), and C54 (d). The calculated enthalpy, as implemented by DFT, is shown (red x) imposed on the ordered enthalpy data (blue open circles) of Fig. 1. The red line is the fitted enthalpy of mix for a random system.

method. The Van Der Pauw equation was solved numerically to determine sheet resistance. For accurate sheet resistance measurement, the samples are first wet etched in diluted HF (100:1) for 30 seconds due to TiN forming a thin oxide.[62] Subsequently, the films are wet etched in SC-1 clean (NH3HO:H2O2:H20) for 15 minutes to remove the TiN and Ti. The samples were cross-section using a FEI Helios nanolab 600 dual beam FIB/SEM. The SEM function of the Nanolab 600 is used for the SEM surface images post-etch. Micrographs of the samples is done with a FEI Tecnai F20 S/TEM instrument.

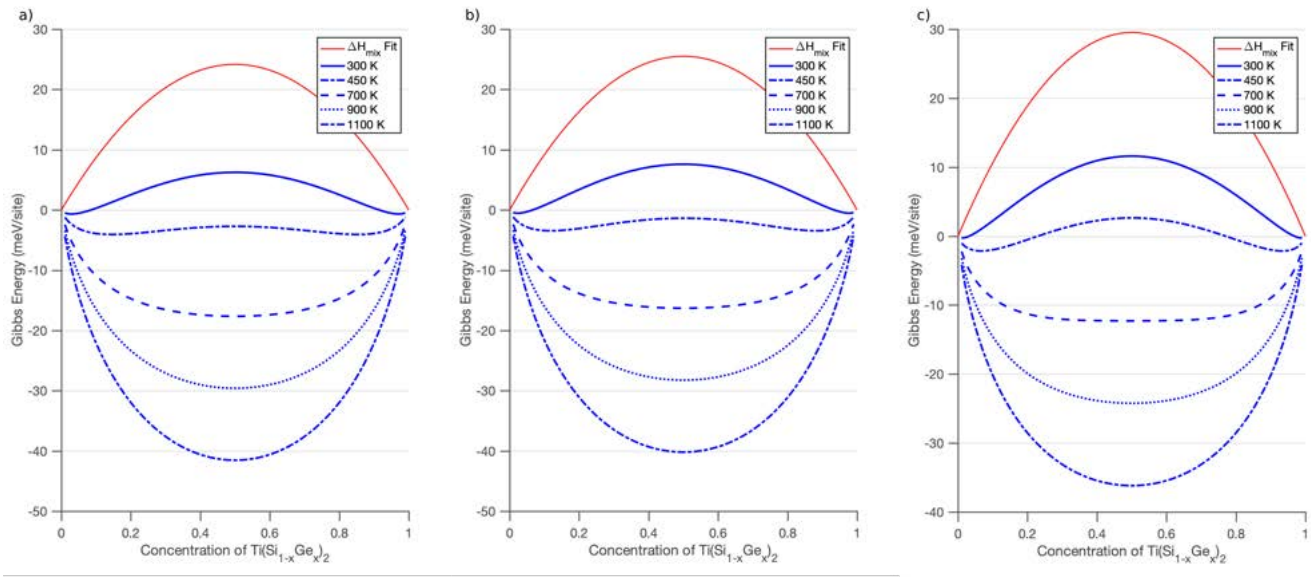

Figure 7-4. The Gibbs free energy of mixing for the pseudobinary system. The quasirandom structures show spinodal decomposition, shown as the red line, for $Ti(Si_{1-x}Ge_x)_2$ C40, (a) C49, (b) and C54 (c).

The nanosecond laser anneals are performed on an in-house instrument assembled for this work. The system utilizes two 1.2 J Q-switched Nd:YAG lasers with a second harmonic generation crystal for 532 nm laser. The two lasers output a 1 ns pulse. The lasers were built by continuum to output multiple modes to increase beam divergence. The increased divergence reduces the speckle (interference pattern) on the exposed sample. The power of the two lasers is controlled with motorized quarter-wave plates and a polarized beam splitter; the rejected laser energy is deposited into a laser beam dump. The two laser beams enter a pulse stretcher setup, which expands the pulse width to 48 ns. After the pulse stretcher, the beam is paralyzed with a 1 cm separation into an engineered diffuser and microlens array. The engineered diffuser increases the beam divergence, and the microlens array transforms the laser beam profile from a Gaussian profile to a square flat-top profile. Finally, a square aperture removes higher-order excitations of the microlens array. The two parallel square beams are focused onto the sample (the two beams are focused such that they are superimposed) with a 1 cm x 1 cm profile. The system loses 50% of the laser energy to reduce speckle and produce a square profile, and the

pulse stretcher efficiency is 83%. The maximum laser fluence which can be deposited into the sample is 600 mJ/cm^2.

The following model enables the calculation of temperature as related to the laser energy absorbed by the exposed sample. The model was developed for metals with free-electrons absorbing the energy due to the inverse Bremsstrahlung. However, the model can be used to describe pure silicon ablation.[195] In the nanosecond laser regime, the laser pulse duration is long in comparison with electron-phonon coupling time, or the amount of time need for the electron to transfer energy to the material's phonons. In this case, the electron temperature is equal to the phonon temperature ($T = T_e = T_p$).[195] This model enables a rough approximation of the temperature experienced by the c-$Si_{1-x}Ge_x$ layer. The penetration depth of the laser energy can be approximated with the relation $l_p = \sqrt{\alpha^2 \tau_{pulse}}$.[196] Where α^2 is the coefficient of thermal diffusivity, τ_{pulse} is the pulse width of the laser. Once the depth of energy penetration is known, the absorbed energy per pulse can be related to a temperature jump from room temperature. This relationship is given with the equation $E_{film} = \rho A l_p C_p \Delta T$. Where A is the area of the laser profile (1 cm x 1 cm square), C_p is the specific heat capacity; ρ is the mass density. The material parameters for c-$Si_{1-x}Ge_x$ calculations are taken from Schaffler et al.[197][190]

One downside of laser annealing is the sample never experiences a constant temperature like furnace or RTA methods. This behavior is due to the rapid heating and cooling rates, which anneals the material far from equilibrium. Therefore, Arrhenius plots cannot be applied to laser annealing with accuracy. Analytical models can be applied to laser annealing to determine an effective temperature.[196][198] This work does not calculate an effective temperature using ordinary differential equation models. An approximate temperature is determined with calculating the amount energy needed to raise the temperature above room temperature.

Chen et al. states the laser annealing of $TiSi_2$ is a diffusion limited process while the fluence is below the melt regime.[184] Therefore, the thickness of Ti transformed into a silicide

is given by the integral.

$$x^2 = A \int_0^t \exp -\frac{E_a}{k_b T(t)} \tag{7-5}$$

Where A is pre-exponential material constant, k_b is the Boltzman constant; E_a is the activation energy; $T(t)$ is the temperature as a function of time. The integral equation represents the amount of Ti transformed during a single laser pulse. In this work, The relationship between laser pulse and $T(t)$ is as follows: An approximate laser pulse is constructed using a linear combination of two gaussian functions. The constants of the two pulses are altered until a single pulse of 48 ns is constructed, and the maximum fluence of the experiment is represented by the function. The equation $E_{film} = \rho A l_p C_p \Delta T$ is used to replace the fluence of the constructed pulse with an effective temperature. The constructed pulse is applied to the integral and solved using numerical methods.

7.5 Experimental Results

The samples are irradiated at different pulse numbers, fluence, and Ge concentration. All the samples shown were wet etched for 15-20 minutes with SC-1 clean. Figure 7-4 shows the response of the material at different fluences. All samples in Fig. 7-4 are performed at a constant number of 90 pulses with a width of 48 ns. The 10% Ge concentration does not show a pattern with fluence, and this concentration does not show low sheet resistance comparable to the previous works in Fig. 7-1. The lowest fluence of 345 mJ/cm^2 is measured with a sheet resistance of 28 Ω/sq. An increase of fluence to 375 mJ/cm^2 drops the sheet resistance to 18 Ω/sq, which is the lowest sheet resistance among the samples. A subsequent fluence increase to 400 mJ/cm^2 raises the sheet resistance 36 Ω/sq. The sheet resistance drops again at 475 mJ/cm^2. The sheet resistance for the 30% Ge concentration follows a similar oscillatory pattern with sheet resistances between 32 to 44 Ω/sq. Based on previous works, The expected sheet resistance of a C49 structure should be under 10 Ω/sq while the C54 would measure close to 1 Ω/sq. Figure 7-4 suggests no formation of Ti($Si_{1-x}Ge_x$)$_2$ C49 or C54 allotropes at any fluence range below 475 mJ/cm^2. Also, No evidence suggests a relationship between Ge concentration and sheet resistance from these samples.

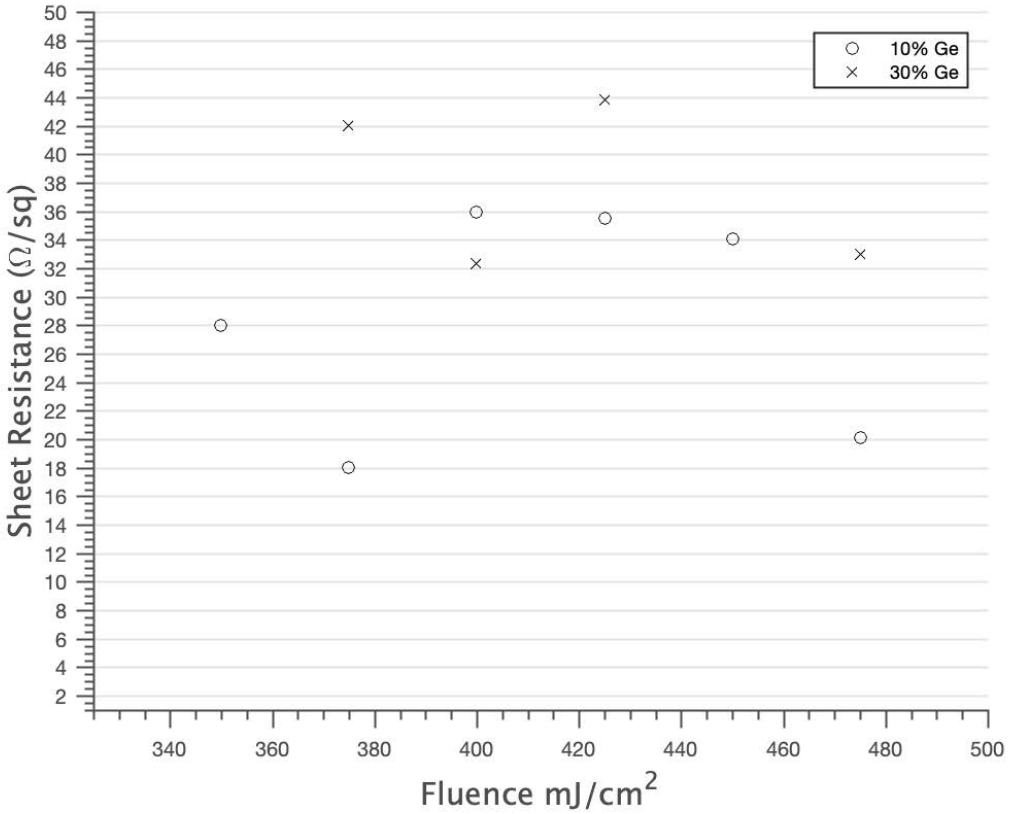

Figure 7-5. The sheet resistant measurements performed on 10% and 30% Ge with 90 pulses at 48 ns. The fluences range from 350 to 475 mJ/cm^2. The figure suggests the Ti($Si_{1-x}Ge_x$)$_2$ C49 or C54 allotropes are not forming within the film.

Figure 7-5 shows a laser annealed sample exposed to 475 mJ/cm^2 with 48 ns pulses. This sample is exposed to 90 pulses at this fluence. The control sample in Fig. 7-5 (a) shows the three layers deposited on c-$Si_{0.8}Ge_{0.2}$. The figure shows the 5nm of Ti deposited and the 3 nm of TiN. As a byproduct of sample preparation, Pt is visble at the top of the panel. In Fig. 7-5 (b), the TiN is not present for the laser annealed sample due to the etch process for electrical characterization. This sample is exposed to a solution of NH3OH:H2O2:H2O (i.e., SC-1 clean) for less than five minutes. The wet etch solution is selective towards TiN and Ti metal, so the solution is routinely used to expose silicides. The wet etch exposure time only removed most of the TiN. From the micrograph, the 5 nm of Ti is still present suggesting the Ti was left unreacted. The white layer visible between Ti and $Si_{0.8}Ge_{0.2}$ is a focusing artifact

of the TEM. This white layer can be removed with altering the TEM focus. A successful phase transformation occurs when interdiffusion of Ti, Si, and Ge into a critical concentration. The micrograph does not show a reduction of Ti. However, the c-$Si_{0.8}Ge_{0.2}$ is visible as an amorphous layer, which indicates melt. Therefore, from the micrograph, the fluence is too high for observing solid reaction between the layers.

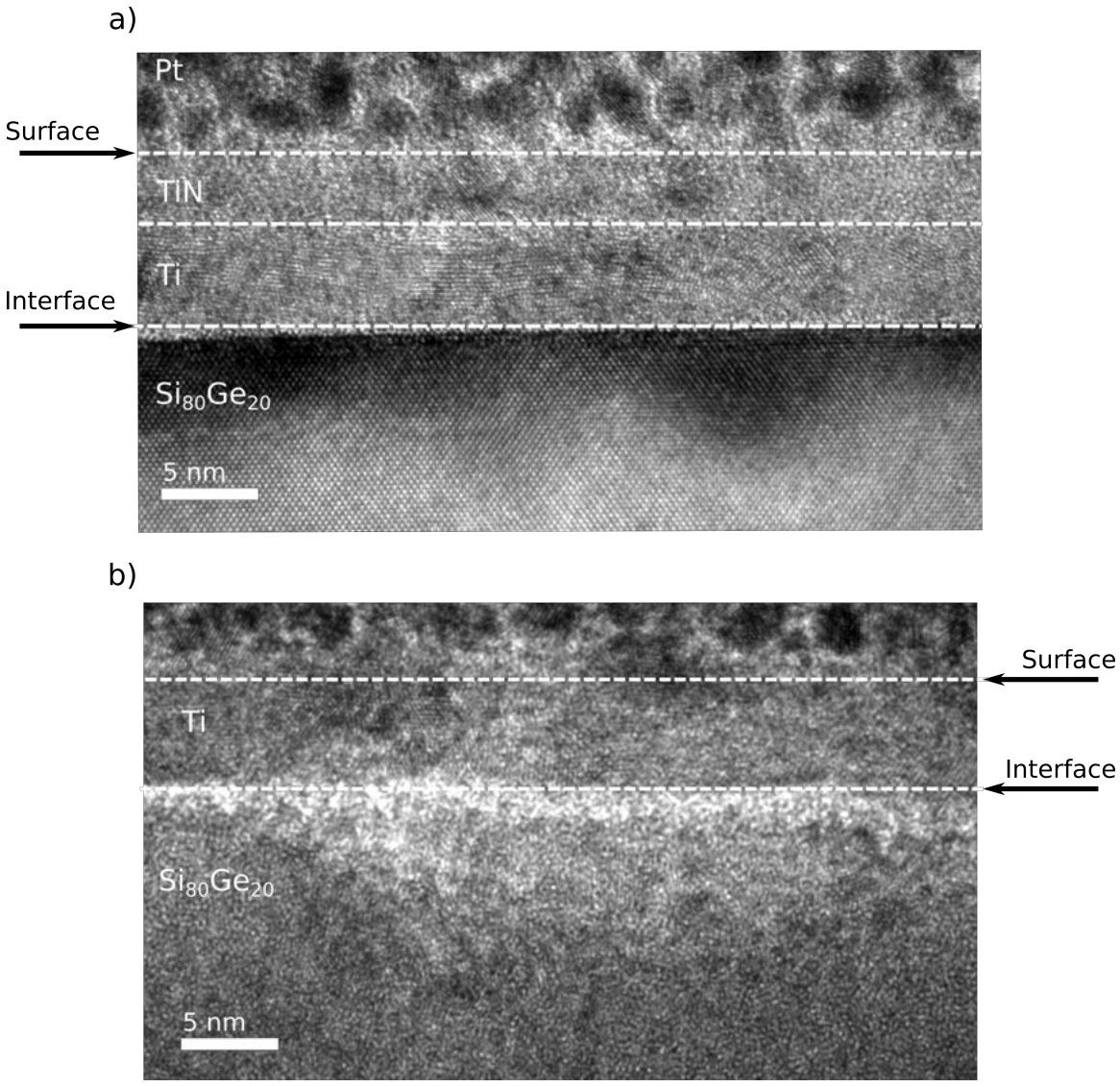

Figure 7-6. A XTEM micrograph of a ns laser annealed sample (a) is compared with the control sample (b). The laser annealed sample is exposed to 90 pulses with a 48 ns pulse width and 475 mJ/cm^2 fluence. The TiN layer is lost for the exposed sample due to a five minute SC-1 clean etch.

Figure 7-5 (b) suggests a 475 mJ/cm^2 fluence induces melt of the semiconductor layer. Therefore, the minimum melt fluence is an important parameter to determine. To find the melt fluence, the number of pulses is reduced to one pulse (this work arbitrarily chose five pulses). If the layer melts, a ripple pattern will be observable in SEM. Samples are exposed with a series of fluences ranging from 400 mJ/cm^2 to 500 mJ/cm^2. Two samples are shown in Fig. 7-6 At two fluences. Figure 7 (a) is five pulses of 430 mJ/cm^2, and fig. 7-6 (b) represents a fluence of 500 mJ/cm^2. Neither SEM micrograph show ripples, which indicates no melt. Since no ripples are observed at 500 mJ/cm^2, No ripples should be observed for the lower fluence samples, and figure 7-5 (a) supports the conclusion that lower fluences will not show ripples. The indication that no melt during the exposure directly contradicts the micrograph results of fig. 7-5 (b). The micrographs do show regions of lighter contrasts. These regions are the remaining Ti after the etch. Some samples show different amounts of left-over Ti. Thus, the remaining Ti explains the deviation for sheet resistance observed in Fig. 7-4.

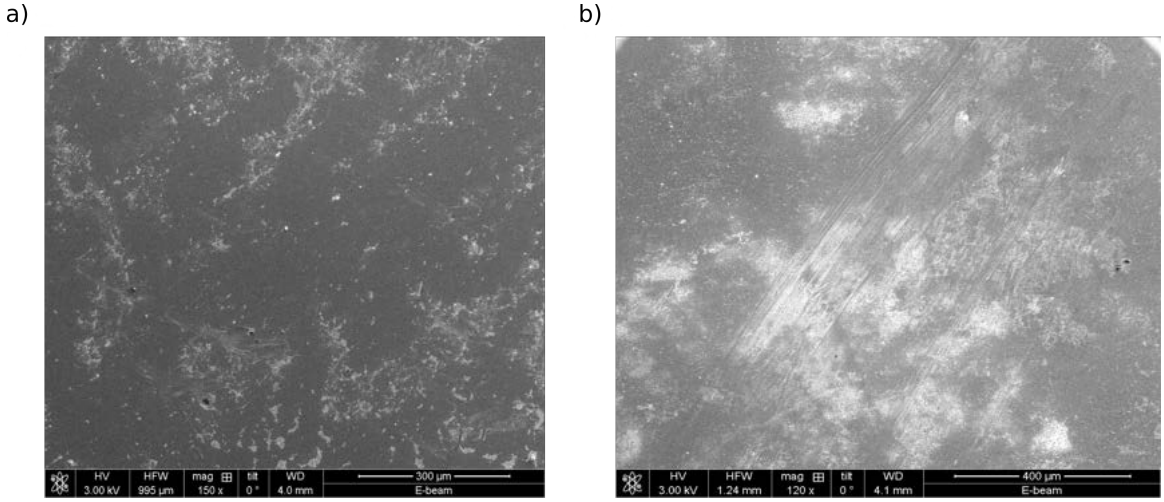

Figure 7-7. The SEM micrographs fo 430 mJ/cm^2 (a) and 500 mJ/cm^2 (b) laser annealed samples. No ripples are observed in the micrographs so no melt. The light contrast regions are due to remaining Ti post-etch.

Since no melt is observed, the next experiment focused searching for the number of pulses necessary to observe a solid reaction. A diffusion limited continuum model is applied with the transformation time being the laser pulse width. The laser pulse width is not an

accurate depiction of the temperature within the sample. Once the sample is exposed, the heat dissipates quickly, but the heat lasts beyond the time of the laser pulse. The activation energy for the Ti to fully transform into C54 is taken from Lee et al. The work of Lee et al. used an infrared laser with millisecond pulse width, and the experimentally determined transformation energy is 2.01 eV. Combining the activation energy with a diffusion-controlled model, A transformation width of 0.14 Angstroms is calculated for every laser pulse exposure. Though this value is not physical, this result is applied to determine the total number of pulses needed to transform 5 nm of Ti. Since the laser setup is 5 Hz, the heat is assumed to dissipated completely from each strike. Therefore, the number of laser strikes expected is 500 pulses. The fluence for the experiment is 500 mJ/cm^2 due to melt not being observed in SEM.

The electrical measurement is displayed in fig. 7-7 while the micrographs are visible in fig. 7-8. The electrical data is within the same range as the fig. 7-4 experiments. The highest sheet resistance is 48 Ω/sq with 100 pulses, and the lowest is 32 Ω/sq with 500 pulses. The 1000 pulse samples shows a slight increase of resistance to 42 Ω/sq. The electrical data results suggests no germanosilicide is forming during the laser anneal. The micrographs are shown in Fig. 7-8 with both panels showing the 500 pulse sample. The micrographs show a dramatic presence of surface features. Atomic force microscopy is need for a complete analysis, but the TEM suggests laser induced periodic surface structures (LIPSS). The presence LIPSS is related to two parameters of an experiment: the fluence is too high and/or the number of pulses is too high. Since this was not observed in SEM for 500 mmJ/cm^2, LIPSS is present due to the number of pulses.

7.6 Discussion

The first computational work on Ti$(Si_{1-x}Ge_x)_2$ allotropes is presented in this work. This work shows the C40 and C54 allotropes are more likely to be disordered while the C49 allotrope is ordered. To further compare the quasirandom and ordered structures, the phonon contribution to free energy is suggested to be a future work. A phonon study would provide additional evidence on whether or not the allotropes' lowest energy is ordered or disordered.

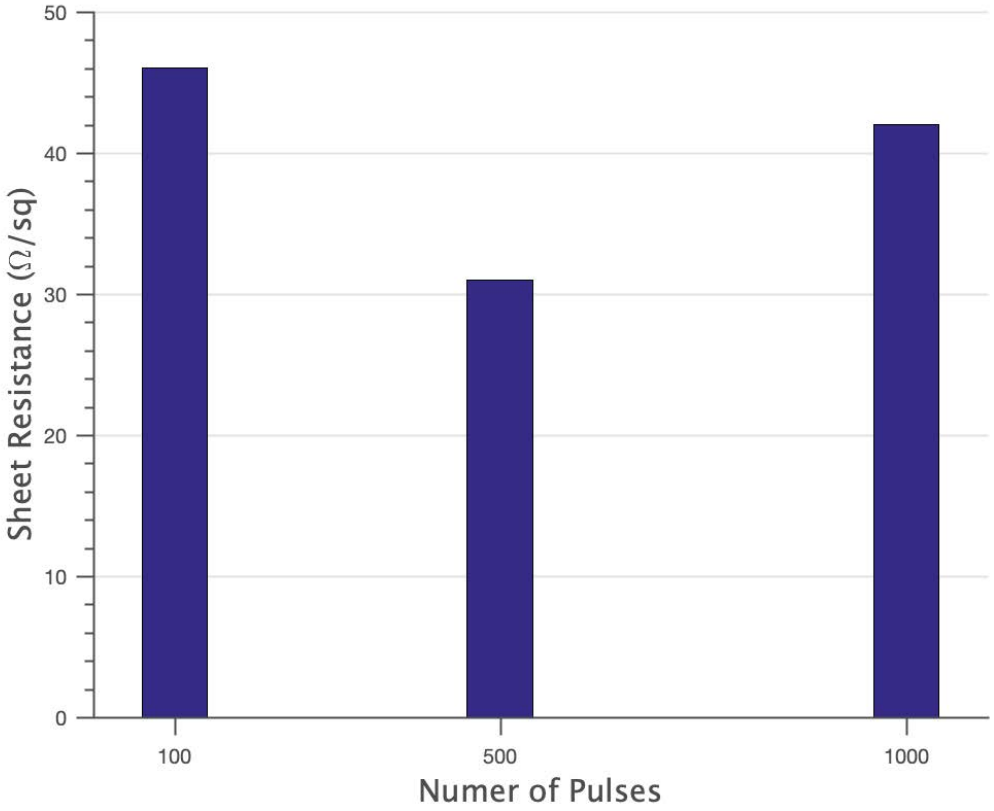

Figure 7-8. A bar graph relating the number of pulses that the samples is exposed and the resulting sheet resistance. All three samples are exposed to a fluence of 500 mJ/cm^2.

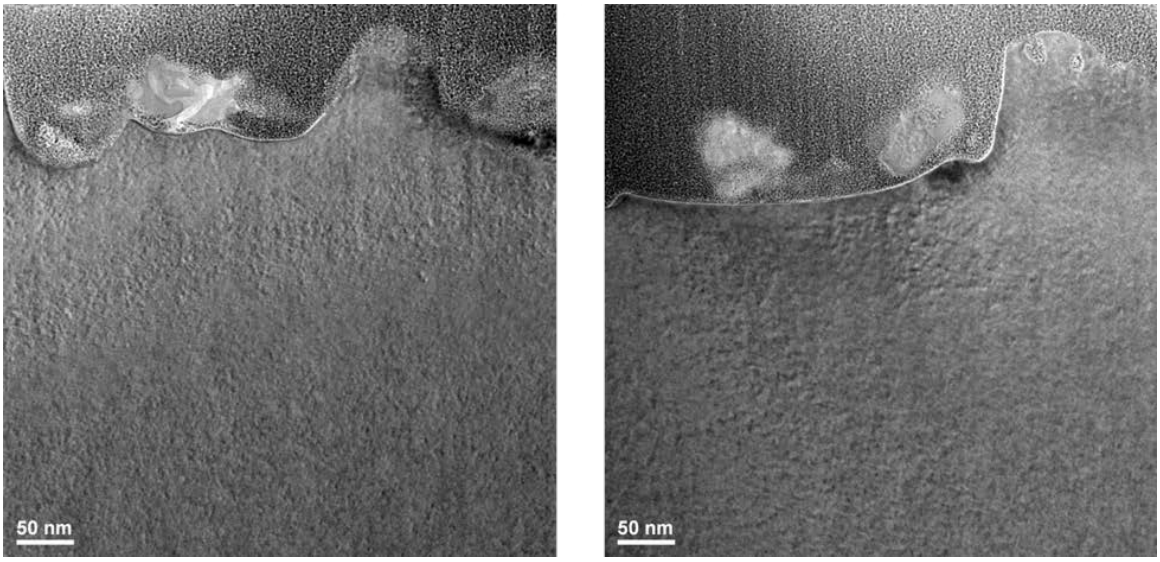

Figure 7-9. The TEM micrographs of a sample nanosecond laser annealed with a 500 pulse exposure at fluence of 500 mJ/cm^2.

As mentioned earlier, the work by Aldrich et al. showed the $Ti(Si_{1-x}Ge_x)_2$ phase segregates into a Si-rich $Ti(Si_{1-y}Ge_y)_2$ and Ge-rich $Si_{1-z}Ge_z$ phases. This phase segregation was observed for both the C49 and C54 allotropes.[180][192] This work does not use the references enabling a direct comparison. However, this work does suggest the Ge segregates to from two different compositions for the C54 structure. The phase segregation suggests the Ge-rich $Si_{1-z}Ge_z$ phase has a lower chemical potential than Ge-rich $Ti(Si_{1-y}Ge_y)_2$. Future work should include references for studying this phase segregation directly.

This work attempted several process approaches to from the allotropes of $Ti(Si_{1-x}Ge_x)_2$ with nanosecond laser annealing. No prior studies include nanosecond laser anneal formation of $Ti(Si_{1-x}Ge_x)_2$. Ideally, the $Ti(Si_{1-x}Ge_x)_2$ films would form below melt fluence to determine the feasibility of the technique. A successful formation would enable the extent of Ge segregation as compared with Aldrich et al.[176, 180] A successful reaction could also yield the first observation of a metastable $Ti(Si_{1-x}Ge_x)_2$ C40 structure.[132] These approaches include fluence and number of laser pulses, which all attempts did not produce a film. The failed reaction is supported from sheet resistance measurements and micrographs. In a last attempt, the fluence and number of pulses induced laser surface effects of the $Si_{1-x}Ge_x$ surface.

One possible explanation is the total anneal time is too short for germanosilicide formation. The undercooling of laser annealing causes rapid heat dissipation. Also, the 5 nm Ti thickness is much shorter than the laser wavelength, so the layer is mostly transmissive into the $Si_{1-x}Ge_x$ layer. Thus, the dominant energy absorber is the $Si_{1-x}Ge_x$ layer, and the heat dissipation rate is accelerated with additional cooling from the Ti layer. Successful formations of silicide with laser anneals have been performed in the millisecond regime.[182, 184, 185, 199] Though the heating profile lasts beyond the exposure, the total heating time of nanosecond annealing will be significantly shorter than millisecond regime. The heating time is important for bilayer films because the metal and semiconductor must interdiffuse into a critical concentration. Based on the calculated diffusion limited model, the transformation thickness of a 45 ns pulse is 0.14 angstrom, which is a value much smaller than a single

unit cell. However, these calculations were performed assuming the heating time perfectly matched the laser pulse exposure time. A next step would be to implement heating models for a single laser pulse. These heating models would enable a more accurate temperature profile for the diffusion-limited model.[196][198] A more accurate model would predict the minimum fluence and pulse widths necessary to observe a transformation. If minimum values cannot be discovered, the bilayer setup is not feasible for phase transformation. Following experiments should consider the co-sputtering of Ge, Si, and Ti films.

Another explanation for the failure of phase transformation is the choice of films. The Ti layer thickness is a significant contributor to the formation of C54 for silicides. The transformation temperature increases with decreased Ti thickness due to the fine-line effect. This relationship between transformation and film thickness has also been found important for $Ti(Si_{1-x}Ge_x)_2$ transformation. At 10% Ge concentration, Aldirch et al. determined the phase transformation temperature increased with decreasing Ti films down to 10 nm. Samples annealed to 770°C only formed C49. This work incorporated 5 nm Ti films, so the fluence required to observe a phase transformation also increases along with temperature. A 5 nm Ti layer may require a fluence beyond the capability of this work's system. Even if higher fluences could be achieved, a higher fluence increases the thermal gradient in the film enabling the formation of multiple phases, and a higher fluence increases the risk of laser surface effects. Thus, experiments with 5 nm of Ti may be outside the scope of laser annealing. Currently, the lasers' fluence level relationship with Ge segregation is unknown, so a relationship between increased sheet resistance and increased Ge segregation from requiring higher fluences cannot be stated.

The $Si_{1-x}Ge_x$ layer itself contributes to the transformation temperature. Cheng et al.[200] coated the backside of a Si (001) wafer with SiO_2 and $CoSi_2$. The SiO_2 induced a compressive strain while $CoSi_2$ introduced tensile strain. The front side of the wafer was coated with 30 nm of Ti for RTA heat treatments between 600°C to 1000°C. The work concluded that films under a tensile strain showed thicker silicide films as apposed to films under compressive strain.

The compressive strain was found to hinder the mobility of Si into the Ti film. The relationship between compressive strain and phase transformation was also observed with Lai et al.(see Fig. 7-1)[125] In a three layer sample, the top $Si_{1-x}Ge_x$ layer is fully relaxed with a $Si_{1-y}Ge_y$ layer inducing compressive strain. Figure 1 shows the lowest sheet resistance shifts from 600°C to 800°C due to compressive strain. Relating to the Ti-$Si_{1-x}Ge_x$ reaction, The Ge concentration in Si is well known to introduce compressive strain.[8] Therefore, the compressive strain is retarding the mobility of Si and Ge atoms into the Ti layer. This problem is exaggerated for laser annealing since the energy absorber is the $Si_{1-x}Ge_x$. The laser does not deposit heat into the Ti layer for Ti atom mobility into the $Si_{1-x}Ge_x$. The Si and Ge atoms are the only mobile atoms for interdiffusion, so a retardation of these atoms mobility hinders the phase transformation more significantly. Future experiments should perform the nanosecond laser anneal experiments on Si wafers with 5 nm Ti films. A successful transformation of $TiSi_2$ would strongly suggest the Ge hinders Ti-$Si_{1-x}Ge_x$ reaction.

7.7 Chapter Summary

In this chapter, computational and experimental first attempts are made for the $Ti(Si_{1-x}Ge_x)_2$ phase. The computational work focused on the equilibrium thermodynamics from first-principles. The enthalpy of formation for $Ti(Si_{1-x}Ge_x)_2$ is calculated with ordered and quasirandom structures of the C40, C49, and C54 allotropes. This work found the C40 and C54 structures are more likely to be disordered. The C49 structure is more likely to be ordered due to ordered structures near the 0 eV line for PBE-GGA, and these structures calculated as ground state structures with the SCAN functional. Due to the choice of reference energy, the work could not be directly compared with experiment. However, this work does suggest the Ge atoms segregate, which is observed for $Ti(Si_{1-x}Ge_x)_2$ films.

This work performed the first attempt on nanosecond laser annealing of Ti-$Si_{1-x}Ge_x$ reaction. A solid rection of the bilayers was not observed to form any $Ti(Si_{1-x}Ge_x)_2$ allotrop or any Ti-Si-Ge ternary phase. The lack of reaction is attributed to three major contributors. Due to undercooling, the heat dissipation is too great for the diffusion to reach a critical

concentration. The choice of Ti thickness increases the activation barrier and temperature for phase transformation. Lastly, the compressive strain introduced with the Ge atoms may retards the mobility of Si and Ge. Further work is necessary to understand the rat limiting step.

CHAPTER 8
CONCLUSION

This dissertation focused on two material systems for enhancing device performance to keep pace with Moore's Law. These materials are the highly doped (HD) Si:P and the $Ti(Si_{1-x}Ge_x)_2$ films. Both films reduce the contact resistance between metal-semiconductor contacts, and the HD Si:P also introduces tensile strain for electron mobility enhancement. The $Ti(Si_{1-x}Ge_x)_2$ films are studied from the perspective of DFT and nanosecond laser annealing.

For the highly doped films, the origin of the strain is unsettled science with different perspectives as to the origin of the strain. One perspective suggests the strain is due to a Si_3P_4 nanophase within the HD Si:P film, and the strain is caused by the smaller lattice constant of this nanophase. If the Pseudocubic Si_3P_4 phase is viewed as a single unit cell within a Si matrix, the system is reduced to a P_4V cluster defect, which is a vacancy surrounded by four P atoms. Whether the nanophase or defect cluster contributes to strain directly, or Si-P bonds cause the strain only is currently unknown. However, this work introduces new evidence for whether the system exists as a nanophase or defect cluster. Epitaxial and precipitate strain is introduced to pseudocubic phases so that metastability can be studied in these growth environments. The pseudocubic phases of the Si:P, Si:As, Ge:P, and Ge:As systems (e.g., Si_3P_4, Si_3As_4, Ge_3P_4, and Ge_3As_4) are studied due to their relevance to the semiconductor industry. Each pseudocubic phase has different lattice constants and thus introduce adjustable amounts of semiconductor strain. Since strain alters the band structure, these phases have the potential for property engineering in such applications as optoelectronics. The pseudocubic and ground state phases of these systems are strained and referenced to the works of Sun et al. to test metastability. From the study, it is found that the ordered pseudocubic phase of Si_3P_4 is unlikely metastable under precipitate and epitaxial conditions. It is also predicted that the pseudocubic Ge_3As_4 and Ge_3P_4 phases are not energetically favorable in the unstrained bulk case. Though the Si_3As_4 phase shows some promise for metastability,

the enthalpy of formation is close to the 0 eV line, so the potential for instability cannot be ruled out. This work shows from the perspective of DFT that the nanophase of Si_3P_4 is unlikely to form. However, an experimental perspective is still preferred to observe this prediction directly. Therefore, a technique that can detect local bonding structure is utilized to distinguish whether the system exists as a nanophase or defect cluster. STEM mode EELS is the technique used for this work Since the EXELFS region of the measurement is known for local structure information. A Nion 100, VASP, and FEFF9 are the three tools for comparing experimental and theoretical EELS spectra. The conclusion was that the instrument was able to detect the presence of P atoms only; the local structure could not be determined using the comparison of EXELFS and simulation. The reason being, the Z number of P and Si are one atom apart, so the spectra are superimposed, making deconvolution impossible for this work. Therefore, the most persuasive evidence this dissertation can present for determining the presence of a nanophase or cluster defect is computational formation energies.

The $Ti(Si_{1-x}Ge_x)_2$ phase is separated into $TiSi_2$ and $TiGe_2$ phases to simplify the study. The Ge atoms reduce the formation temperature of $Ti(Si_{1-x}Ge_x)_2$ C54, and the reasoning behind the reduction is studied by comparing the $TiSi_2$ and $TiGe_2$ phases. The ground state structure for $TiSi_2$ is found to be the C49, while the ground state for $TiGe_2$ is C54. These ground states suggest the Ge atom prefers the C54 structure, so it lowers the formation temperature for the C54 allotrope. To understand the mechanism, the extended born model is presented to justify the study of these systems bonding components. The $TiSi_2$ C54 structure shows instability from the density of states (DOS) that is from the Fermi level suggesting unfilled bond orbitals. The $TiGe_2$ C54 structure suggests fully occupied orbitals from the DOS plots. Therefore, the C54 is the ground state structure for $TiGe_2$, and not $TiSi_2$ can be explained from covalent bond stability. Bader analysis is performed to determine if charge transfer is relevant for these systems. The charge transfer was similar for both $TiGe_2$ and $TiSi_2$, which suggests Ge does not make different ionic bonding behavior for changing the enthalpy of formation. Finally, the charge density difference (CDD) plots are applied to provide

an additional qualitative agreement for the results of the DOS and Bader analysis. The CDD shows both charge transfer and hybridization for the $TiSi_2$ and $TiGe_2$. The CDD suggested a hybridization between the Ti and Ge while hybridization was not observed in $TiSi_2$. Therefore, the further hybridization between the Ge and Ti atoms lower the enthalpy of formation of the C54 structure.

The final chapter of this work attempted a pseudobinary study of $Ti(Si_{1-x}Ge_x)_2$ from first-principles and nanosecond laser annealing of Ti-$Si_{1-x}Ge_x$ bilayers. The pseudobinary study is performed with VASP and ATAT to determine the enthalpy of formation of different Ge concentrations. The work found that C40 and C54 structures are more likely to prefer disordering of Ge while C49 prefer ordered structures. Temperature is introduced to these structures with a parabolic fit of the ideal solution model, assuming truly random ordering. Since C54 is more likely to be disordered, the model suggests phase segregation into a Si-rich $Ti(Si_{1-y}Ge_y)_2$ and Ge-rich $Ti(Si_{1-z}Ge_z)_2$. Phase segregation is observed in the $Ti(Si_{1-x}Ge_x)_2$ phase experimentally segregates into a Si-rich $Ti(Si_{1-y}Ge_y)_2$ and Ge-rich $Si_{1-z}Ge_z$. More work is needed to include the chemical potential of $Si_{1-x}Ge_x$ concentrations so that this computational work can be directly related to the experimental works of Aldrich et al. Finally, the nanosecond laser annealing of Ti-$Si_{1-x}Ge_x$ bilayers is the first attempt in this dissertation. A solid reaction is not observed between the layers, which suggests the processing windows of this work should be avoided in future works.

APPENDIX
LIST OF ACCOMPLISHMENTS

D.L. Brown, Maxwell Gregoire, Spencer Olson, Smaller mode waist, higher finesse, and birefringence for enabling a portable Bose-Einstein condensate interferometer from atom-cavity chip technology, Proposal Accepted, National Research Council Research Associate Program (RAP) Fellowship, (Sep 2019)

D.L. Brown, K.S. Jones, S.R. Phillpot, Stability of Epitaxial Pseudocubic Group IV-V Semiconductors, Journal of Vacuum Sciences and Technology B, 37, 5, (Sep 19, 2019), https://doi.org/10.1116/1.5111715

D.L. Brown, K.S. Jones, S.R. Phillpot, Stability of Epitaxial Pseudocubic Group IV-V Semiconductors, Accepted, Oral contribution at American Ceramic Society Conference on Electronic Materials and Applications, (Jan 2019)

D.L. Brown, K.S. Jones, S.R. Phillpot, Lattice Stability and Point Defect Formation Energy of $TiSi_2$ and $TiGe_2$ allotropes from First-Principles, in preparation for Journal of Applied Physics

D.L. Brown, J. Johnson, S.R. Phillpot, K.S. Jones, Laser annealing of pseudobinary $TiGe_2$-$TiSi_2$ for synthesizing low resistance C54 structure, Invited talk at Air Force Research Lab

D.L. Brown, K.S. Jones, Electron energy loss spectroscopy identification of Si_3P_4 in highly doped silicon, Proposal Accepted, Center for Nanophase Materials Sciences Oakridge National Labs, (2017)

REFERENCES

[1] W. F. Brinkman, D. E. Haggan, and W. W. Troutman, "A history of the invention of the transistor and where it will lead us," *IEEE Journal of Solid-State Circuits*, vol. 32, no. 12, pp. 1858–1865, 1997.

[2] ITRS More Moore, "ITRS 2.0," 2015.

[3] B. Razavi, *Design of Analog CMOS Integrated Circuits*, 1st ed. McGraw Hill, 2001.

[4] J. M. Rabaey, A. Chandrakasan, and B. Nikolic, *Digital IntegratedCircuits*, 2nd ed., ser. A Design Perspective. Pearson Education, 2003.

[5] J. Sun, R. C. Remsing, Y. Zhang, Z. Sun, A. Ruzsinszky, H. Peng, Z. Yang, A. Paul, U. Waghmare, X. Wu, M. L. Klein, and J. P. Perdew, "Accurate first-principles structures and energies of diversely bonded systems from an efficient density functional," *Nature Chemistry*, vol. 8, pp. 831 EP –.

[6] M. Horstmann, A. Wei, T. Kammler, J. Hntschel, H. Bierstedt, T. Feudel, K. Frohberg, M. Gerhardt, A. Hellmich, K. Hempel, J. Hohage, P. Javorka, J. Klais, G. Koerner, M. Lenski, A. Neu, R. Otterbach, P. Press, C. Reichel, M. Trentsch, B. Trui, H. Salz, M. Schaller, H. J. Engelmann, O. Herzog, H. Ruelke, P. Hubler, R. Stephan, D. Greenlaw, M. Raab, and N. Kepler, "Integration and optimization of embedded-sige, compressive and tensile stressed liner films, and stress memorization in advanced SOI CMOS technologies," in *IEEE InternationalElectron Devices Meeting, 2005. IEDM Technical Digest.* IEEE, pp. 233–236.

[7] E. Ungersboeck, V. Sverdlov, H. Kosina, and S. Selberherr, "Strain engineering for CMOS devices," in *2006 8th International Conference on Solid-State and Integrated Circuit Technology Proceedings*. IEEE, pp. 124–127.

[8] Y. Sun, S. E. Thompson, and T. Nishida, *Strain Effect in Semiconductors*. Boston, MA: Springer US, 2010.

[9] K.-W. Ang, K.-J. Chui, C.-H. Tung, N. Balasubramanian, G. S. Samudra, and Y.-C. Yeo, "Performance Enhancement in Uniaxial Strained Silicon-on-Insulator N-MOSFETs Featuring Silicon–Carbon Source/Drain Regions," *IEEE Transactions on Electron Devices*, vol. 54, no. 11, pp. 2910–2917.

[10] M. Bauer, V. Machkaoutsan, Y. Zhang, D. Weeks, J. Spear, S. Thomas, P. Verheyen, C. Kerner, F. Clemente, H. Bender, D. Shamiryan, R. Loo, A. Hikavyy, T. Hoffmann, P. Absil, and S. Biesemans, "SiCP Selective Epitaxial Growth in Recessed Source/Drain Regions yielding to Drive Current Enhancement in n-channel MOSFET," in *214th ECS Meeting*. ECS, Oct. 2008, pp. 1001–1013.

[11] Z. Ye, S. Chopra, R. Lapena, Y. Kim, and S. Kuppurao, "High Tensile Strained In-Situ Phosphorus Doped Silicon Epitaxial Film for nMOS Applications," *ECS Transactions*, vol. 50, no. 9, pp. 1007–1011, Mar. 2013.

[12] H.-D. Chiou, "Phosphorus Concentration Limitation in Czochralski Silicon Crystals," *Journal of The Electrochemical Society*, vol. 147, no. 1, pp. 345–349, 2000.

[13] M. Bauer and S. G. Thomas, "Low temperature Si:C co-flow and hybrid process using Si3H8/Cl2," *Thin Solid Films*, vol. 520, no. 8, pp. 3133–3138, Feb. 2012.

[14] M. Bauer and S. Thomas, "Low temperature catalyst enhanced etch process with high etch rate selectivity for amorphous silicon based alloys over single-crystalline silicon based alloys," *Thin Solid Films*, vol. 520, no. 8, pp. 3139–3143, Feb. 2012.

[15] G. Borot, L. Rubaldo, L. Clement, R. Pantel, D. Dutartre, K. Kuitunen, J. Slotte, F. Tuomisto, X. Mescot, M. Gri, and G. Ghibaudo, "Tensile strain in arsenic heavily doped Si," *Journal of Applied Physics*, vol. 102, no. 10, p. 103505, Nov. 2007.

[16] H. Yu, M. Schaekers, A. Peter, G. Pourtois, E. Rosseel, J.-G. Lee, W.-B. Song, K. M. Shin, J.-L. Everaert, S. A. Chew, S. Demuynck, D. Kim, K. Barla, A. Mocuta, N. Horiguchi, A. V.-Y. Thean, N. Collaert, and K. De Meyer, "Titanium Silicide on Si:P With Precontact Amorphization Implantation Treatment: Contact Resistivity Approaching 1×10^{-9} Ohm-cm2," *IEEE Transactions on Electron Devices*, vol. 63, no. 12, pp. 4632–4641.

[17] S. Choi, J. Kim, J. Choi, S. Cho, M. Lee, E. Ko, I. C. Rho, C. H. Kim, Y. Kim, D.-H. Ko, and H. Kim, "Microstructural properties of Ni-silicide films formed on epitaxially grown strained Si:P layer," *Microelectronic Engineering*, vol. 165, pp. 1–5, Nov. 2016.

[18] Z. N. Weinrich, X. Li, S. Sharma, V. Craciun, M. Ahmed, E. A. C. Sanchez, S. Moffatt, and K. S. Jones, "Dopant-defect interactions in highly doped epitaxial Si:P thin films," *Thin Solid Films*, vol. 685, pp. 1–7, Sep. 2019.

[19] S. K. Dhayalan, J. Kujala, J. Slotte, G. Pourtois, E. Simoen, E. Rosseel, A. Hikavyy, Y. Shimura, R. Loo, and W. Vandervorst, "On the Evolution of Strain and Electrical Properties in As-Grown and Annealed Si:P Epitaxial Films for Source-Drain Stressor Applications," *ECS Journal of Solid State Science and Technology*, vol. 7, no. 5, pp. P228–P237, May 2018.

[20] S. K. Dhayalan, J. Kujala, J. Slotte, G. Pourtois, E. Simoen, E. Rosseel, A. Hikavyy, Y. Shimura, S. Iacovo, A. Stesmans, R. Loo, and W. Vandervorst, "On the manifestation of phosphorus-vacancy complexes in epitaxial Si:P filmsOn the manifestation of phosphorus-vacancy complexes in epitaxial Si:P films," pp. 1–5, May 2016.

[21] R. W. Olesinski, N. Kanani, and G. J. Abbaschian, "The P−Si (Phosphorus-Silicon) system," *Bulletin of Alloy Phase Diagrams*, vol. 6, no. 2, pp. 130–133, Apr. 1985.

[22] X. Li, A. Dube, Z. Ye, S. Sharma, Y. Kim, and S. Chu, "Selective Epitaxial Si:P Film for nMOSFET Application: High Phosphorous Concentration and High Tensile Strain," *ECS Transactions*, vol. 64, no. 6, pp. 959–965, Aug. 2014.

[23] Z. N. Weinrich, "DOPANT-DEFECT INTERACTIONS IN EPITAXIALLY GROWN HIGHLY DOPED SI:P ," 2018.

[24] P. Hohenberg and W. Kohn, "Inhomogeneous Electron Gas," *Physical Review*, vol. 136, no. 3B, pp. B864–B871, Nov. 1964.

[25] G. K. Hafner and J, "Ab initio molecular dynamics for liquid metals," pp. 1–4, Mar. 2011.

[26] G. Kresse and J. Furthmüller, "Efficiency of ab-initio total energy calculations for metals and semiconductors using a plane-wave basis set," *Computational Materials Science*, vol. 6, no. 1, pp. 15–50, Jul. 1996.

[27] G. Kresse and D. Joubert, "From ultrasoft pseudopotentials to the projector augmented-wave method," *Physical Review B*, vol. 59, no. 3, pp. 1758–1775, Jan. 1999.

[28] R. G. Parr and W. Yang, Density-Functional Theory of Atoms and Molecules. Oxford University Press, 1994.

[29] J. P. Perdew, K. Burke, and M. Ernzerhof, "Generalized Gradient Approximation Made Simple," *Physical Review Letters*, vol. 77, no. 18, pp. 3865–3868, Oct. 1996.

[30] X. Zheng, A. J. Cohen, P. Mori-Sánchez, X. Hu, and W. Yang, "Improving Band Gap Prediction in Density Functional Theory from Molecules to Solids," *Physical Review Letters*, vol. 107, no. 2, p. 026403, Jul. 2011.

[31] N. Mardirossian and M. Head-Gordon, "Thirty years of density functional theory in computational chemistry: an overview and extensive assessment of 200 density functionals," *Molecular Physics*, vol. 115, no. 19, pp. 2315–2372, Apr. 2017.

[32] J. P. Perdew, A. Ruzsinszky, J. Sun, and K. Burke, "Gedanken densities and exact constraints in density functional theory," *The Journal of Chemical Physics*, vol. 140, no. 18, p. 18A533, May 2014.

[33] R. Ahlrichs, F. Furche, and S. Grimme, "Comment on "Assessment of exchange correlation functionals" [A.J. Cohen, N.C. Handy, Chem. Phys. Lett. 316 (2000) 160–166]," *Chemical Physics Letters*, vol. 325, no. 1-3, pp. 317–321, Jul. 2000.

[34] J. Tao, J. P. Perdew, V. N. Staroverov, and G. E. Scuseria, "Climbing the Density Functional Ladder: Nonempirical Meta–Generalized Gradient Approximation Designed for Molecules and Solids," *Physical Review Letters*, vol. 91, no. 14, p. 146401, Sep. 2003.

[35] J. P. Perdew, "Jacob's ladder of density functional approximations for the exchange-correlation energy," in *Density functional theory and its application to materials*. AIP, Aug. 2001, pp. 1–20.

[36] E. H. Lieb and S. Oxford, "Improved lower bound on the indirect Coulomb energy," *International Journal of Quantum Chemistry*, vol. 19, no. 3, pp. 427–439, Mar. 1981.

[37] J. Sun, R. C. Remsing, Y. Zhang, Z. Sun, A. Ruzsinszky, H. Peng, Z. Yang, A. Paul, U. Waghmare, X. Wu, M. L. Klein, and J. P. Perdew, "Accurate first-principles structures and energies of diversely bonded systems from an efficient density functional," *Nature Chemistry*, vol. 8, no. 9, pp. 831–836, Jun. 2016.

[38] J. Sun, A. Ruzsinszky, and J. P. Perdew, "Strongly Constrained and Appropriately Normed Semilocal Density Functional," *Physical Review Letters*, vol. 115, no. 3, p. 64, Jul. 2015.

[39] S. H. Vosko, L. Wilk, and M. Nusair, "Accurate spin-dependent electron liquid correlation energies for local spin density calculations: a critical analysis," *Canadian Journal of Physics*, vol. 58, no. 8, pp. 1200–1211, Aug. 1980.

[40] K. Hui and J.-D. Chai, "SCAN-based hybrid and double-hybrid density functionals from models without fitted parameters," *The Journal of Chemical Physics*, vol. 144, no. 4, p. 044114, Jan. 2016.

[41] H. Peng, "SCAN+rVV10: A promising van der Waals density functional."

[42] R. C. Remsing, M. L. Klein, and J. Sun, "Dependence of the structure and dynamics of liquid silicon on the choice of density functional approximation," *Physical Review B*, vol. 96, no. 2, p. 530, Jul. 2017.

[43] C. Kittel, *Introduction to Solid State Physics* , 8th ed. Hoboken, NJ: John Wiley & Sons, Inc, 2005.

[44] A. Togo and I. Tanaka, "First principles phonon calculations in materials science," *Scripta Materialia*, vol. 108, no. C, pp. 1–5, Nov. 2015.

[45] M. T. Dove, *Introduction to Lattice Dynamics*. Cambridge: Cambridge University Press, 2009.

[46] Y. Tojo, R. Matsumura, H. Yokoyama, M. Kurosawa, K. Toko, T. Sadoh, and M. Miyao, "High-quality formation of multiply stacked SiGe-on-insulator structures by temperature-modulated successive rapid-melting-growth," *Applied Physics Letters*, vol. 102, no. 9, p. 092102, Mar. 2013.

[47] A. Togo and I. Tanaka, "First principles phonon calculations in materials science," *Scripta Materialia*, vol. 108, no. C, pp. 1–5, Nov. 2015.

[48] K. Jorissen and J. J. Rehr, "Calculations of electron energy loss and x-ray absorption spectra in periodic systems without a supercell," *Physical Review B*, vol. 81, no. 24, p. 245124, Jun. 2010.

[49] M. S. Moreno, K. Jorissen, and J. J. Rehr, "Practical aspects of electron energy-loss spectroscopy (EELS) calculations using FEFF8," *Micron*, vol. 38, no. 1, pp. 1–11, Jan. 2007.

[50] K. Jorissen, J. J. Rehr, and J. Verbeeck, "Multiple scattering calculations of relativistic electron energy loss spectra," *Physical Review B*, vol. 81, no. 15, p. 155108, Apr. 2010.

[51] B. Ravel, "Muffin-tin potentials in EXAFS analysis," *Journal of Synchrotron Radiation*, vol. 22, no. 5, pp. 1258–1262, Sep. 2015.

[52] M. S. Moreno, K. Jorissen, and J. J. Rehr, "Practical aspects of electron energy-loss spectroscopy (EELS) calculations using FEFF8," *Micron*, vol. 38, no. 1, pp. 1–11, Jan. 2007.

[53] J. M. Sanchez, F. Ducastelle, and D. Gratias, "Generalized cluster description of multicomponent systems," *Physica A: Statistical Mechanics and its Applications*, vol. 128, no. 1-2, pp. 334–350, Nov. 1984.

[54] C. G. Van de Walle and J. Neugebauer, "First-principles calculations for defects and impurities: Applications to III-nitrides," *Journal of Applied Physics*, vol. 95, no. 8, pp. 3851–3879, Apr. 2004.

[55] A. Zunger, S. H. Wei, L. G. Ferreira, and J. E. Bernard, "Special quasirandom structures," *Physical Review Letters*, vol. 65, no. 3, pp. 353–356, Jul. 1990.

[56] J. P. P. Zunger and Alex, "Self-interaction correction to density-functional approximations for many-electron systems," pp. 1–32, Apr. 2011.

[57] A. van de Walle, P. Tiwary, M. de Jong, D. L. Olmsted, M. Asta, A. Dick, D. Shin, Y. Wang, L. Q. Chen, and Z. K. Liu, "Efficient stochastic generation of special quasirandom structures," *Calphad*, vol. 42, pp. 13–18, Sep. 2013.

[58] E. Sanville, S. D. Kenny, R. Smith, and G. Henkelman, "Improved grid-based algorithm for Bader charge allocation," *Journal of Computational Chemistry*, vol. 28, no. 5, pp. 899–908, 2007.

[59] M. Yu and D. R. Trinkle, "Accurate and efficient algorithm for Bader charge integration," *The Journal of Chemical Physics*, vol. 134, no. 6, p. 064111, Feb. 2011.

[60] G. Henkelman, A. Arnaldsson, and H. Jónsson, "A fast and robust algorithm for Bader decomposition of charge density," *Computational Materials Science*, vol. 36, no. 3, pp. 354–360, Jun. 2006.

[61] W. Tang, E. Sanville, and G. Henkelman, "A grid-based Bader analysis algorithm without lattice bias," *Journal of Physics: Condensed Matter*, vol. 21, no. 8, p. 084204, Jan. 2009.

[62] H.-Y. Chen and F.-H. Lu, "Oxidation behavior of titanium nitride films," *Journal of Vacuum Science & Technology A: Vacuum, Surfaces, and Films*, vol. 23, no. 4, pp. 1006–1009, Jul. 2005.

[63] D. B. Williams and C. B. Carter, Transmission Electron Microscopy: A Textbook for Materials Science , 2nd ed. Springer, 2009, vol. 1-4.

[64] L. A. Giannuzzi and F. A. Stevie, Eds., *Introduction to Focused Ion Beams*. Boston, MA: Springer US, 2005.

[65] M. Schaffer, B. Schaffer, and Q. Ramasse, "Sample preparation for atomic-resolution STEM at low voltages by FIB," *Ultramicroscopy*, vol. 114, pp. 62–71, Mar. 2012.

[66] R. F. Egerton, *Electron Energy-Loss Spectroscopy in the Electron Microscope*, 3rd ed. Springer, 2014.

[67] E. Okunishi, H. Sawada, Y. Kondo, and M. Kersker, "Atomic Resolution Elemental Map of EELS with a Cs Corrected STEM," *Microscopy and Microanalysis*, vol. 12, no. S02, pp. 1150–1151, Jul. 2006.

[68] P. Cueva, R. Hovden, J. A. Mundy, H. L. Xin, and D. A. Muller, "Data Processing for Atomic Resolution Electron Energy Loss Spectroscopy," *Microscopy and Microanalysis*, vol. 18, no. 4, pp. 667–675, Jun. 2012.

[69] V. Grill, H. Drexel, W. Sailer, M. Lezius, and T. D. Märk, "The working principle of the trochoidal electron monochromator revisited," *International Journal of Mass Spectrometry*, vol. 205, no. 1-3, pp. 209–226, Feb. 2001.

[70] B. K. Agarwal, *X-Ray Spectroscopy*, ser. Springer Series in Optical Sciences. Berlin, Heidelberg: Springer Berlin Heidelberg, 1991, vol. 15.

[71] D. K. Schroder, *Semiconductor Material and Device Characterization*, 3rd ed. Wiley-IEEE Press, 2015.

[72] D. K. Bowen and B. K. Tanner, *X-ray Metrology in Semiconductor Manufacturing*, 1st ed. CRC Press, 2006.

[73] M. Bauer, V. Machkaoutsan, Y. Zhang, D. Weeks, J. Spear, S. Thomas, P. Verheyen, C. Kerner, F. Clemente, H. Bender, D. Shamiryan, R. Loo, A. Hikavyy, T. Hoffmann, P. Absil, and S. Biesemans, "SiCP Selective Epitaxial Growth in Recessed Source/Drain Regions yielding to Drive Current Enhancement in n-channel MOSFET," in *214th ECS Meeting*. ECS, Oct. 2008, pp. 1001–1013.

[74] E. Rosseel, H. B. Profijt, A. Y. Hikavyy, J. Tolle, S. Kubicek, G. Mannaert, C. L'abbe, K. Wostyn, N. Horiguchi, T. Clarysse, B. Parmentier, S. Dhayalan, H. Bender, J. W. Maes, S. Mehta, and R. Loo, "Characterization of Epitaxial Si:C:P and Si:P Layers for Source/Drain Formation in Advanced Bulk FinFETs," *ECS Transactions*, vol. 64, no. 6, pp. 977–987, Sep. 2014.

[75] C. N. Ni, X. Li, S. Sharma, K. V. Rao, M. Jin, C. Lazik, V. Banthia, B. Colombeau, N. Variam, A. Mayur, H. Chung, R. Hung, and A. Brand, "Ultra-low contact resistivity with highly doped Si:P contact for nMOSFET," in *2015 Symposium on VLSI Technology*. IEEE, pp. T118–T119.

[76] M. Huang, Y. P. Feng, A. T. L. Lim, and J. C. Zheng, "Structural and electronic properties of Si3P4," *Physical Review B*, vol. 69, no. 5, p. 311, Feb. 2004.

[77] T.-Y. Lü and J.-C. Zheng, "Electronic properties of pseudocubic IV–V compounds with 3:4 stoichiometry: Chemical trends," *Chemical Physics Letters*, vol. 501, no. 1-3, pp. 47–53, Dec. 2010.

[78] B. Sahli, K. Vollenweider, N. Zographos, and C. Zechner, "Ab initio calculations of phosphorus and arsenic clustering parameters for the improvement of process simulation models," *Materials Science and Engineering: B*, vol. 154-155, pp. 193–197, Dec. 2008.

[79] B. Sahli, K. Vollenweider, and W. Fichtner, "Ab initiocalculations for point defect clusters with P, As, and Sb in Si," *Physical Review B*, vol. 80, no. 7, p. 075208, Aug. 2009.

[80] R. W. Olesinski and G. J. Abbaschian, "The As−Ge (Arsenic-Germanium) system," *Bulletin of Alloy Phase Diagrams*, vol. 6, no. 3, pp. 250–254, Jun. 1985.

[81] R. Olesinski and G. Abbaschian, "The As−Si (Arsenic-Silicon) system," *Bulletin of Alloy Phase Diagrams*, vol. 6, no. 3, pp. 254–258, Jun. 1985.

[82] T. Wadsten, M. Vikan, C. Krohn, Å. Nilsson, H. Theorell, R. Blinc, S. Paušak, L. Ehrenberg, and J. Dumanović, "The Crystal Structures of SiP2, SiAs2, and GeP." *Acta Chemica Scandinavica*, vol. 21, pp. 593–594, 1967.

[83] A. Jain, G. Hautier, C. J. Moore, S. Ping Ong, C. C. Fischer, T. Mueller, K. A. Persson, and G. Ceder, "A high-throughput infrastructure for density functional theory calculations," *Computational Materials Science*, vol. 50, no. 8, pp. 2295–2310, Jun. 2011.

[84] A. Jain, G. Hautier, S. P. Ong, C. J. Moore, C. C. Fischer, K. A. Persson, and G. Ceder, "Formation enthalpies by mixing GGA and GGA +Ucalculations," *Physical Review B*, vol. 84, no. 4, p. 66, Jul. 2011.

[85] C. G. Beck and R. Stickler, "Crystallography of SiP and SiAs Single Crystals and of SiP Precipitates in Si," *Journal of Applied Physics*, vol. 37, no. 13, pp. 4683–4687, Dec. 1966.

[86] A. Armigliato, D. Nobili, M. Servidori, and S. Solmi, "SiP precipitation within the doped silicon lattice, concomitant with phosphorus predeposition," *Journal of Applied Physics*, vol. 47, no. 12, pp. 5489–5491, Dec. 1976.

[87] B. Huang, "Highly stable two-dimensional silicon phosphides: Different stoichiometries andexotic electronic properties," *Physical Review B*, vol. 91, no. 12, 2015.

[88] W. Sun, S. T. Dacek, S. P. Ong, G. Hautier, A. Jain, W. D. Richards, A. C. Gamst, K. A. Persson, and G. Ceder, "The thermodynamic scale of inorganic crystalline metastability," *Science Advances*, vol. 2, no. 11, p. e1600225, Nov. 2016.

[89] F. Shojaei, J. R. Hahn, and H. S. Kang, "Electronic structure and photocatalytic band offset of few-layer GeP 2," *J. Mater. Chem. A*, vol. 5, no. 42, pp. 22 146–22 155, 2017.

[90] C. Hu and Y. P. Feng, "First-principles study of structural and electronic properties of group IV arsenides with 3:4 stoichiometry," *Physical Review B*, vol. 74, no. 10, p. 841, Sep. 2006.

[91] Z. Charifi, H. Baaziz, and B. Hamad, "Theoretical prediction of the structural and electronic properties of pseudocubic X3As4 (X=C, Si, Ge and Sn) compounds," *Physica B: Condensed Matter*, vol. 404, no. 12-13, pp. 1632–1637, Jun. 2009.

[92] Y. P. Feng, A. T. L. Lim, M. Huang, F. Ding, and J. C. Zheng, "Relative stability and electronic properties of group IV phosphides and nitrides," *Computational Materials Science*, vol. 36, no. 1-2, pp. 65–72, May 2006.

[93] F. D. Murnaghan, "The Compressibility of Media under Extreme Pressures," *Proceedings of the National Academy of Sciences*, vol. 30, no. 9, pp. 244–247, Sep. 1944.

[94] W. Setyawan and S. Curtarolo, "High-throughput electronic band structure calculations: Challenges and tools," *Computational Materials Science*, vol. 49, no. 2, pp. 299–312, Aug. 2010.

[95] M. S. Moreno, K. Jorissen, and J. J. Rehr, "Practical aspects of electron energy-loss spectroscopy (EELS) calculations using FEFF8," *Micron*, vol. 38, no. 1, pp. 1–11, Jan. 2007.

[96] P. Pichler, *Intrinsic Point Defects, Impurities, and Their Diffusion in Silicon*, ser. Computational Microelectronics. Vienna: Springer Vienna, 2004.

[97] G. Borot, L. Rubaldo, L. Clement, R. Pantel, D. Dutartre, K. Kuitunen, J. Slotte, F. Tuomisto, X. Mescot, M. Gri, and G. Ghibaudo, "Tensile strain in arsenic heavily doped Si," *Journal of Applied Physics*, vol. 102, no. 10, p. 103505, Nov. 2007.

[98] R. Milazzo, G. Impellizzeri, D. Piccinotti, A. La Magna, G. Fortunato, D. De Salvador, A. Carnera, A. Portavoce, D. Mangelinck, V. Privitera, and E. Napolitani, "Impurity and defect interactions during laser thermal annealing in Ge," *Journal of Applied Physics*, vol. 119, no. 4, p. 045702, Jan. 2016.

[99] R. Milazzo, G. Impellizzeri, D. Piccinotti, D. De Salvador, A. Portavoce, A. La Magna, G. Fortunato, D. Mangelinck, V. Privitera, A. Carnera, and E. Napolitani, "Low temperature deactivation of Ge heavily n-type doped by ion implantation and laser thermal annealing," *Applied Physics Letters*, vol. 110, no. 1, p. 011905, Jan. 2017.

[100] T. F. Retajczyk Jr. and A. K. Sinha, "Elastic stiffness and thermal expansion coefficients of various refractory silicides and silicon nitride films," *Thin Solid Films*, vol. 70, no. 2, pp. 241–247, Aug. 1980.

[101] T. Sonehara, A. Hokazono, H. Akutsu, T. Sasaki, H. Uchida, M. Tomita, S. Kawanaka, S. Inaba, and Y. Toyoshima, "Mechanism of Contact Resistance Reduction in Nickel Silicide Films by Pt Incorporation," *IEEE Transactions on Electron Devices*, vol. 58, no. 11, pp. 3778–3786.

[102] E. Rosseel, S. K. Dhayalan, A. Y. Hikavyy, R. Loo, H. B. Profijt, D. Kohen, S. Kubicek, T. Chiarella, H. Yu, N. Horiguchi, D. Mocuta, K. Barla, A. Thean, G. Bartlett, J. Margetis, N. Bhargava, and J. Tolle, "(Invited) Selective Epitaxial Growth of High-P Si:P for Source/Drain Formation in Advanced Si nFETs," *ECS Transactions*, vol. 75, no. 8, pp. 347–359, Sep. 2016.

[103] P. H. Keys, J. H. Li, E. Heitman, P. A. Packan, M. E. Law, and K. S. Jones, "Effect of Extended Defects on the Enhanced Diffusion of Phosphorus Implanted Silicon," *MRS Proceedings*, vol. 568, p. 295, Feb. 2011.

[104] J. Li, P. Keys, J. Chen, M. E. Law, K. S. Jones, and C. Jasper, "Transient Enhanced Diffusion of Phosphorus and Defect Evolution in P +Implanted Si," *MRS Proceedings*, vol. 568, p. 175, Feb. 2011.

[105] O. L. Krivanek, N. Dellby, M. F. Murfitt, M. F. Chisholm, T. J. Pennycook, K. Suenaga, and V. Nicolosi, "Gentle STEM: ADF imaging and EELS at low primary energies," *Ultramicroscopy*, vol. 110, no. 8, pp. 935–945, Jul. 2010.

[106] J. J. Rehr, J. J. Kas, F. D. Vila, M. P. Prange, and K. Jorissen, "Parameter-free calculations of X-ray spectra with FEFF9," *Physical Chemistry Chemical Physics*, vol. 12, no. 21, pp. 5503–5513, 2010.

[107] Y. Wang, Y. E. Suyolcu, U. Salzberger, K. Hahn, V. Srot, W. Sigle, and P. A. van Aken, "Correcting the linear and nonlinear distortions for atomically resolved STEM spectrum and diffraction imaging," *Microscopy*, vol. 67, no. suppl_1, pp. i114–i122, Jan. 2018.

[108] J. L. Allain, J. R. Regnard, A. Bourret, A. Parisini, A. Armigliato, G. Tourillon, and S. Pizzini, "Extended x-ray-absorption fine-structure study of the local atomic structure in As+heavily implanted silicon," *Physical Review B*, vol. 46, no. 15, pp. 9434–9445, Oct. 1992.

[109] D. Giubertoni, G. Pepponi, M. A. Sahiner, S. P. Kelty, S. Gennaro, M. Bersani, M. Kah, K. J. Kirkby, R. Doherty, M. A. Foad, F. Meirer, C. Streli, J. C. Woicik, and P. Pianetta, "Deactivation of submelt laser annealed arsenic ultrashallow junctions in silicon during subsequent thermal treatment," *Journal of Vacuum Science & Technology B*, vol. 28, no. 1, pp. C1B1–C1B5, Jan. 2010.

[110] R. Hovden, P. Cueva, J. A. Mundy, and D. A. Muller, "The Open-Source Cornell Spectrum Imager," *Microscopy Today*, vol. 21, no. 1, pp. 40–44, Dec. 2012.

[111] J. S. Johannessen, W. E. Spicer, J. F. Gibbons, J. D. Plummer, and N. J. Taylor, "Observation of phosphorus pile-up at the SiO 2-Si interface," *Journal of Applied Physics*, vol. 49, no. 8, pp. 4453–4458, Aug. 1978.

[112] "EELS Atlas," Gatan Corporation.

[113] S. P. Murarka, D. B. Fraser, A. K. Sinha, and H. J. Levinstein, "Refractory Silicides of Titanium and Tantalum for Low-Resistivity Gates and Interconnects," *IEEE Journal of Solid-State Circuits*, vol. 15, no. 4, pp. 474–482.

[114] G. Ottaviani and C. Nobili, "Silicide formation," *Thin Solid Films*, vol. 163, pp. 111–121, Sep. 1988.

[115] F. M. d'Heurle, S. L. Zhang, C. Lavoie, P. Gas, C. Cabral Jr., and J. M. E. Harper, "Formation of C54 TiSi2: Effects of niobium additions on the apparent activation energy," *Journal of Applied Physics*, vol. 90, no. 12, pp. 6409–6415, Dec. 2001.

[116] R. Beyers and R. Sinclair, "Metastable phase formation in titanium-silicon thin films," *Journal of Applied Physics*, vol. 57, no. 12, pp. 5240–5245, Jun. 1985.

[117] D. B. Aldrich, H. L. Heck, Y. L. Chen, D. E. Sayers, and R. J. Nemanich, "Film thickness effects in the Ti–Si 1− xGe xsolid phase reaction," *Journal of Applied Physics*, vol. 78, no. 8, pp. 4958–4965, Oct. 1995.

[118] U. Gösele and K. N. Tu, "Growth kinetics of planar binary diffusion couples: ''Thin-film case'' versus ''bulk cases'','' *Journal of Applied Physics*, vol. 53, no. 4, pp. 3252–3260, Apr. 1982.

[119] S. Motakef, J. M. E. Harper, F. M. d'Heurle, T. A. Gallo, and N. Herbots, "Stability of C49 and C54 phases of TiSi 2under ion bombardment," *Journal of Applied Physics*, vol. 70, no. 5, pp. 2660–2666, Sep. 1991.

[120] F. M. d'Heurle and P. Gas, "Kinetics of formation of silicides: A review," *Journal of Materials Research*, vol. 1, no. 01, pp. 205–221, Mar. 2011.

[121] A. Mouroux, S. L. Zhang, W. Kaplan, S. Nygren, M. Östling, and C. S. Petersson, "Enhanced formation of the C54 phase of TiSi 2by an interposed layer of molybdenum," *Applied Physics Letters*, vol. 69, no. 7, pp. 975–977, Aug. 1996.

[122] H. K. Park, J. Sachitano, M. McPherson, T. Yamaguchi, and G. Lehman, "Effects of ion implantation doping on the formation of TiSi 2," *Journal of Vacuum Science & Technology A: Vacuum, Surfaces, and Films*, vol. 2, no. 2, pp. 264–268, Apr. 1984.

[123] H. Jeon, C. A. Sukow, J. W. Honeycutt, G. A. Rozgonyi, and R. J. Nemanich, "Morphology and phase stability of TiSi 2on Si," *Journal of Applied Physics*, vol. 71, no. 9, pp. 4269–4276, May 1992.

[124] W. Freiman, A. Eyal, Y. L. Khait, R. Beserman, and K. Dettmer, "Kinetics of processes in the Ti–Si 1− xGe xsystems," *Applied Physics Letters*, vol. 69, no. 25, pp. 3821–3823, Dec. 1996.

[125] J. B. Lai and L. J. Chen, "Effects of composition on the formation temperatures and electrical resistivities of C54 titanium germanosilicide in Ti–Si1−xGex systems," *Journal of Applied Physics*, vol. 86, no. 3, pp. 1340–1345, Aug. 1999.

[126] H. Yu, M. Schaekers, J. Zhang, L.-L. Wang, J.-L. Everaert, N. Horiguchi, Y.-L. Jiang, D. Mocuta, N. Collaert, and K. De Meyer, "TiSi(Ge) Contacts Formed at Low Temperature Achieving Around 2×10^{-9}~Ω cm2 Contact Resistivities to p-SiGe," *IEEE Transactions on Electron Devices*, vol. 64, no. 2, pp. 500–506.

[127] J. B. Lai and L. J. Chen, "Effects of composition on the formation temperatures and electrical resistivities of C54 titanium germanosilicide in Ti–Si1−xGex systems," *Journal of Applied Physics*, vol. 86, no. 3, pp. 1340–1345, Aug. 1999.

[128] H. Yu, M. Schaekers, A. Hikavyy, E. Rosseel, A. Peter, K. Hollar, F. A. Khaja, W. Aderhold, L. Date, A. J. Mayur, J. G. Lee, K. M. Shin, B. Douhard, S. A. Chew, S. Demuynck, S. Kubicek, D. Kim, A. Mocuta, K. Barla, N. Horiguchi, N. Collaert, A. V. Y. Thean, and K. De Meyer, "Ultralow-resistivity CMOS contact scheme with pre-contact amorphization plus Ti (germano-)silicidation," in *2016 IEEE Symposium on VLSI Technology*. IEEE, pp. 1–2.

[129] O. Thomas, S. Delage, F. M. d'Heurle, and G. Scilla, "Reaction of titanium with germanium and silicon-germanium alloys," *Applied Physics Letters*, vol. 54, no. 3, pp. 228–230, Jan. 1989.

[130] Q. Z. Hong, K. Barmak, and F. M. d'Heurle, "Formation of a C49 TiGe 2phase during annealing a coevaporated Ti 0.33Ge 0.67alloy," *Applied Physics Letters*, vol. 62, no. 26, pp. 3435–3437, Jun. 1993.

[131] K. Li, S. Y. Chen, and Z. X. Shen, "Identification of refractory-metal-free C40 TiSi2 for low temperature C54 TiSi2 formation," *Applied Physics Letters*, vol. 78, no. 25, pp. 3989–3991, Jun. 2001.

[132] S. Y. Chen, Z. X. Shen, K. Li, A. K. See, and L. H. Chan, "Synthesis and characterization of pure C40 TiSi2," *Applied Physics Letters*, vol. 77, no. 26, pp. 4395–4397, Dec. 2000.

[133] T. Yu, S. C. Tan, Z. X. Shen, L. W. Chen, J. Y. Lin, and A. K. See, "Structural study of refractory-metal-free C40 TiSi2 and its transformation to C54 TiSi2," *Applied Physics Letters*, vol. 80, no. 13, pp. 2266–2268, Apr. 2002.

[134] S. C. Tan, L. Liu, Y. P. Zeng, A. See, and Z. X. Shen, "The Effect of Film Thickness on the C40 TiSi[sub 2] to C54 TiSi[sub 2] Transition Temperature," *Journal of The Electrochemical Society*, vol. 152, no. 10, pp. G754–G756, 2005.

[135] G. Kresse and J. Hafner, "Norm-conserving and ultrasoft pseudopotentials for first-row and transition elements," *Journal of Physics: Condensed Matter*, vol. 6, no. 40, pp. 8245–8257, Jan. 1999.

[136] M. Modrzejewski, G. Chalasinski, and M. M. Szczesniak, "Assessment of Newest Meta-GGA Hybrids for Late Transition Metal Reactivity: Fractional Charge and Fractional Spin Perspective," *The Journal of Physical Chemistry C*, p. acs.jpcc.8b07394, Nov. 2018.

[137] P. Wisesa, K. A. McGill, and T. Mueller, "Efficient generation of generalized Monkhorst-Pack grids through the use of informatics," *Physical Review B*, vol. 93, no. 15, p. 155109, Apr. 2016.

[138] H. T. Stokes and D. M. Hatch, "FINDSYM: Program for Identifying the Space Group Symmetry of a Crystal." *Journal of Applied Crystallography*, vol. 38, pp. 237–238, 2005.

[139] P. E. Blöchl, O. Jepsen, and O. K. Andersen, "Improved tetrahedron method for Brillouin-zone integrations," *Physical Review B*, vol. 49, no. 23, pp. 16 223–16 233, Jun. 1994.

[140] M. Methfessel and A. T. Paxton, "High-precision sampling for Brillouin-zone integration in metals," *Physical Review B*, vol. 40, no. 6, pp. 3616–3621, Aug. 1989.

[141] K. Mathew, A. K. Singh, J. J. Gabriel, K. Choudhary, S. B. Sinnott, A. V. Davydov, F. Tavazza, and R. G. Hennig, "MPInterfaces: A Materials Project based Python tool for high-throughput computational screening of interfacial systems," *Computational Materials Science*, vol. 122, pp. 183–190, Sep. 2016.

[142] S. N. Sun, N. Kioussis, S.-P. Lim, A. Gonis, and W. H. Gourdin, "Impurity effects on atomic bonding in Ni3Al," *Physical Review B*, vol. 52, no. 20, pp. 14 421–14 430, Nov. 1995.

[143] P. A. Korzhavyi, L. V. Pourovskii, H. W. Hugosson, A. V. Ruban, and B. Johansson, "Ab InitioStudy of Phase Equilibria in TiCx," *Physical Review Letters*, vol. 88, no. 1, p. 177, Dec. 2001.

[144] J. Liu, E. Tennessen, J. Miao, Y. Huang, J. M. Rondinelli, and H. Heinz, "Understanding Chemical Bonding in Alloys and the Representation in Atomistic Simulations," *The Journal of Physical Chemistry C*, vol. 122, no. 26, pp. 14 996–15 009, May 2018.

[145] H. Heinz and U. W. Suter, "Atomic Charges for Classical Simulations of Polar Systems," *The Journal of Physical Chemistry B*, vol. 108, no. 47, pp. 18 341–18 352, Nov. 2004.

[146] C. Colinet, W. Wolf, R. Podloucky, and A. Pasturel, "Ab initiostudy of the structural stability of TiSi2 compounds," *Applied Physics Letters*, vol. 87, no. 4, p. 041910, Jul. 2005.

[147] T. Wang, Y. B. Dai, S. K. Ouyang, H. S. Shen, Q. K. Wang, and J. S. Wu, "Investigation of vacancy in C54 TiSi2 using ab initio method," *Materials Letters*, vol. 59, no. 8-9, pp. 885–888, Apr. 2005.

[148] L. Miglio, M. Iannuzzi, P. Raiteri, and M. Celino, "Silicon diffusion in competitive TiSi2 phases by molecular dynamics simulations," *Microelectronic Engineering*, vol. 55, no. 1-4, pp. 83–92, Mar. 2001.

[149] G. Frenking and N. Fröhlich, "The Nature of the Bonding in Transition-Metal Compounds," *Chemical Reviews*, vol. 100, no. 2, pp. 717–774, Feb. 2000.

[150] H. Ehrenreich, "The Physics of Metals. Vol. 1, Electrons. J. M. Ziman, Ed. Cambridge University Press, New York, 1969. xviii + 436 pp., illus. $14.50,$" *Science*, $vol.168, no.3928, pp.237 - -237, Apr.1970.$

[151] A. Pasturel, C. Colinet, and P. Hicter, "Strong chemical interactions in disordered alloys," *Physica B+C*, vol. 132, no. 2, pp. 177–180, Jul. 1985.

[152] C. D. Gelatt, A. R. Williams, and V. L. Moruzzi, "Theory of bonding of transition metals to nontransition metals," *Physical Review B*, vol. 27, no. 4, pp. 2005–2013, Feb. 1983.

[153] A. J. Freeman, T. Hong, W. Lin, and J.-H. Xu, "Phase Stability and Role of Ternary Additions on Electronic and Mechanical Properties of Aluminum Intermetallics," *MRS Proceedings*, vol. 213, p. 14, Feb. 2011.

[154] J.-H. Xu and A. J. Freeman, "Bandfilling and structural stability of trialuminides: YAl 3, ZrAl 3, and NbAl 3," *Journal of Materials Research*, vol. 6, no. 6, pp. 1188–1199, Jan. 2011.

[155] C. Colinet, "Ab-initio calculation of enthalpies of formation of intermetallic compounds and enthalpies of mixing of solid solutions," *Intermetallics*, vol. 11, no. 11-12, pp. 1095–1102, 2003.

[156] J. H. Xu, T. Oguchi, and A. J. Freeman, "Crystal structure, phase stability, and magnetism in Ni3V," *Physical Review B*, vol. 35, no. 13, pp. 6940–6943, May 1987.

[157] C. Colinet and J.-C. Tedenac, "Structural stability of intermetallic phases in the Si–Ti system. Point defects and chemical potentials in D88-Si3Ti5 phase," *Intermetallics*, vol. 18, no. 8, pp. 1444–1454, Aug. 2010.

[158] P. Ravindran, G. Subramoniam, and R. Asokamani, "Ground-state properties and relative stability between the L12and DOaphases of Ni3Al by Nb substitution," *Physical Review B*, vol. 53, no. 3, pp. 1129–1137, Jan. 1996.

[159] P. Ravindran, L. Fast, P. A. Korzhavyi, B. Johansson, J. Wills, and O. Eriksson, "Density functional theory for calculation of elastic properties of orthorhombic crystals: Application to TiSi2," *Journal of Applied Physics*, vol. 84, no. 9, pp. 4891–4904, Nov. 1998.

[160] M. Ekman and V. Ozoliņš, "Electronic structure and bonding properties of titanium silicides," *Physical Review B*, vol. 57, no. 8, pp. 4419–4424, Feb. 1998.

[161] A. R. Miedema, F. R. d. Boer, and P. F. d. Chatel, "Empirical description of the role of electronegativity in alloy formation," *Journal of Physics F: Metal Physics*, vol. 3, no. 8, pp. 1558–1576, Aug. 1973.

[162] D. M. Bylander, L. Kleinman, K. Mednick, and W. R. Grise, "Self-consistent energy bands and bonding of Ni Si2," *Physical Review B*, vol. 26, no. 12, pp. 6379–6383, Dec. 1982.

[163] C. I. Fonseca Guerra, J.-W. Handgraaf, E. J. Baerends, and F. M. Bickelhaupt, "Voronoi deformation density (VDD) charges: Assessment of the Mulliken, Bader, Hirshfeld, Weinhold, and VDD methods for charge analysis," *Journal of Computational Chemistry*, vol. 25, no. 2, pp. 189–210, 2003.

[164] T. A. Manz and N. G. Limas, "Introducing DDEC6 atomic population analysis: part 1. Charge partitioning theory and methodology," *RSC Advances*, vol. 6, no. 53, pp. 47 771–47 801, 2016.

[165] N. G. Limas and T. A. Manz, "Introducing DDEC6 atomic population analysis: part 2. Computed results for a wide range of periodic and nonperiodic materials," *RSC Advances*, vol. 6, no. 51, pp. 45 727–45 747, 2016.

[166] J. Tersoff and D. R. Hamann, "Bonding and structure of Co Si2and Ni Si2," *Physical Review B*, vol. 28, no. 2, pp. 1168–1170, Jul. 1983.

[167] Z. Ma and L. H. Allen, "Kinetic mechanisms of the C49-to- C54 polymorphic transformation in titanium disilicide thin films: A microstructure-scaled nucleation-mode transition," *Physical Review B*, vol. 49, no. 19, pp. 13 501–13 511, May 1994.

[168] F. La Via, F. Mammoliti, and M. G. Grimaldi, "Influence of defects on the kinetic of C49–C54 TiSi2 transformation," *Applied Physics Letters*, vol. 85, no. 23, pp. 5577–5579, Dec. 2004.

[169] T. C. Chou, C. Y. Wong, and K. N. Tu, "Lattice imaging of metastable TiSi 2," *Journal of Applied Physics*, vol. 62, no. 6, pp. 2275–2279, Sep. 1987.

[170] M. H. Wang and L. J. Chen, "Phase formation in the interfacial reactions of ultrahigh vacuum deposited titanium thin films on (111)Si," *Journal of Applied Physics*, vol. 71, no. 12, pp. 5918–5925, Jun. 1992.

[171] ——, "Simultaneous occurrence of multiphases in interfacial reactions of ultrahigh vacuum deposited Ti thin films on (111)Si," *Applied Physics Letters*, vol. 59, no. 19, pp. 2460–2462, Nov. 1991.

[172] O. Chaix-Pluchery, B. Chenevier, I. Matko, J. P. Sénateur, and F. La Via, "Investigations of transient phase formation in Ti/Si thin film reaction," *Journal of Applied Physics*, vol. 96, no. 1, pp. 361–368, Jul. 2004.

[173] F. L. Via, F. Mammoliti, and M. G. Grimaldi, "Reaction of the Si/Ta/Ti system: C40 TiSi2 phase formation and in situkinetics," *Journal of Applied Physics*, vol. 91, no. 2, pp. 633–638, Jan. 2002.

[174] G. L. Vick and K. M. Whittle, "Solid Solubility and Diffusion Coefficients of Boron in Silicon," *Journal of The Electrochemical Society*, vol. 116, no. 8, pp. 1142–1144, 1969.

[175] C. G. Van de Walle and R. M. Martin, "Theoretical calculations of heterojunction discontinuities in the Si/Ge system," *Physical Review B*, vol. 34, no. 8, pp. 5621–5634, Oct. 1986.

[176] D. B. Aldrich, Y. L. Chen, D. E. Sayers, R. J. Nemanich, S. P. Ashburn, and M. C. Öztürk, "Stability of C54 titanium germanosilicide on a silicon-germanium alloy substrate," *Journal of Applied Physics*, vol. 77, no. 10, pp. 5107–5114, May 1995.

[177] S. Zaima, "Study of reaction and electrical properties at Ti/SiGe/Si(100) contacts for ultralarge scale integrated applications," *Journal of Vacuum Science & Technology B: Microelectronics and Nanometer Structures*, vol. 16, no. 5, p. 2623, Sep. 1998.

[178] O. Thomas, S. Delage, F. M. d'Heurle, and G. Scilla, "Reaction of titanium with germanium and silicon-germanium alloys," *Applied Physics Letters*, vol. 54, no. 3, pp. 228–230, Jan. 1989.

[179] D. A. Grützmacher, T. O. Sedgwick, A. Powell, M. Tejwani, S. S. Iyer, J. Cotte, and F. Cardone, "Ge segregation in SiGe/Si heterostructures and its dependence on deposition technique and growth atmosphere," *Applied Physics Letters*, vol. 63, no. 18, pp. 2531–2533, Nov. 1993.

[180] D. B. Aldrich, Y. L. Chen, D. E. Sayers, and R. J. Nemanich, "Titanium Germanosilicide Phase Formation During The Ti-Si1-xGex Solid Phase Reactions," *MRS Proceedings*, vol. 402, p. 53, Feb. 2011.

[181] D. B. Aldrich, H. L. Heck, Y. L. Chen, D. E. Sayers, and R. J. Nemanich, "Film thickness effects in the Ti–Si 1— xGe xsolid phase reaction," *Journal of Applied Physics*, vol. 78, no. 8, pp. 4958–4965, Oct. 1995.

[182] E. D'Anna, G. Leggieri, and A. Luches, "Laser synthesis of thin films of metal silicides," *Thin Solid Films*, vol. 218, no. 1-2, pp. 95–108, Oct. 1992.

[183] M. von Allmen, S. S. Lau, M. Mäenpää, and B. Y. Tsaur, "Metastable phases in laser-irradiated Pt-Si and Pd-Si thin films," *Applied Physics Letters*, vol. 37, no. 1, pp. 84–86, Jul. 1980.

[184] S. Y. Chen, Z. X. Shen, Z. D. Chen, L. H. Chan, and A. K. See, "Laser-induced direct formation of C54 TiSi2 films with fine grains on c-Si substrates," *Applied Physics Letters*, vol. 75, no. 12, pp. 1727–1729, Sep. 1999.

[185] L. Lu and M. O. Lai, "Laser induced transformation of TiSi2," *Journal of Applied Physics*, vol. 94, no. 7, pp. 4291–4295, Oct. 2003.

[186] G. Kresse and M. Marsman. (2018) VASP Manual. [Online]. Available: https://cms.mpi.univie.ac.at/wiki/index.php/The_VASP_Manual

[187] A. van de Walle, "Multicomponent multisublattice alloys, nonconfigurational entropy and other additions to the Alloy Theoretic Automated Toolkit," *Calphad*, vol. 33, no. 2, pp. 266–278, Jun. 2009.

[188] A. v. d. Walle and M. Asta, "Self-driven lattice-model Monte Carlo simulations of alloy thermodynamic properties and phase diagrams," *Modelling and Simulation in Materials Science and Engineering*, vol. 10, no. 5, pp. 521–538, Jul. 2002.

[189] A. Walle and G. Ceder, "Automating first-principles phase diagram calculations," *Journal of Phase Equilibria*, vol. 23, no. 4, pp. 348–359, Aug. 2002.

[190] F. Schäffler, "High-mobility Si and Ge structures," *Semiconductor Science and Technology*, vol. 12, no. 12, pp. 1515–1549, Jan. 1999.

[191] J. W. Cahn, "Phase Separation by Spinodal Decomposition in Isotropic Systems," *The Journal of Chemical Physics*, vol. 42, no. 1, pp. 93–99, Jan. 1965.

[192] D. B. Aldrich, Y. L. Chen, D. E. Sayers, R. J. Nemanich, S. P. Ashburn, and M. C. Öztürk, "Stability of C54 titanium germanosilicide on a silicon-germanium alloy substrate," *Journal of Applied Physics*, vol. 77, no. 10, pp. 5107–5114, May 1995.

[193] J. B. Lai and L. J. Chen, "Effects of composition on the formation temperatures and electrical resistivities of C54 titanium germanosilicide in Ti–Si1−xGex systems," *Journal of Applied Physics*, vol. 86, no. 3, pp. 1340–1345, Aug. 1999.

[194] S. Lany, "Semiconductor thermochemistry in density functional calculations," *Physical Review B*, vol. 78, no. 24, p. 2, Dec. 2008.

[195] B. N. Chichkov, C. Momma, S. Nolte, and F. Von Alvensleben, "Femtosecond, picosecond and nanosecond laser ablation of solids," *Applied Physics A*, vol. 63, pp. 109–115, 1996.

[196] Y. Xu, C. J. Dibble, N. G. Petrik, R. S. Smith, A. G. Joly, R. G. Tonkyn, B. D. Kay, and G. A. Kimmel, "A nanosecond pulsed laser heating system for studying liquid and supercooled liquid films in ultrahigh vacuum," *The Journal of Chemical Physics*, vol. 144, no. 16, p. 164201, Apr. 2016.

[197] M. E. Levinshteĭn, S. L. Rumyantsev, and M. Shur, *Properties of Advanced Semiconductor Materials: GaN, AlN, InN, BN, SiC, SiGe*. New York: Wiley, 2001.

[198] G. Bomchil, D. Bensahel, A. Golanski, F. Ferrieu, G. Auvert, A. Perio, and J. C. Pfister, "Formation kinetics of MoSi 2induced by cw scanned laser beam," *Applied Physics Letters*, vol. 41, no. 1, pp. 46–48, Jul. 1982.

[199] H. S. Lee, "Growth Kinetics of Mo, W, Ti, and Co Silicides Formed by Infrared Laser Heating," *Journal of The Electrochemical Society*, vol. 137, no. 2, pp. 684–690, 1990.

[200] S. L. Cheng, H. Y. Huang, Y. C. Peng, L. J. Chen, B. Y. Tsui, C. J. Tsai, and S. S. Guo, "Effects of stress on the growth of TiSi2 thin films on (001)Si," *Applied Physics Letters*, vol. 74, no. 10, pp. 1406–1408, Mar. 1999.

BIOGRAPHICAL SKETCH

David Brown enjoys many physical hobbies ranging from hunting to competitive boxing, but his true hobby will always be the scientific pursuit. Born in San Diego, California, his single parent mother moved to Clearwater, Florida when he was five years old. David attended Gibbs Senior High School in south-side St. Petersburg, Florida. He was accepted into a collegiate scholar program skipping his senior year of high school for college. In his college years, David has been in several lab groups from the University of Rochester to University of Florida. These groups ranged from biomedical to RADAR, but his true passion has always been photonic research and laser systems. He recieved his Ph.D. from the University of Florida in 2020.
In his next life's chapter, David is an awardee of the National Research Council Research Associate Program fellowship for postdoctoral research at the Air Force Research Laboratory in Albuquerque, New Mexico.